U.S. Coast Guard Research and Development Center
1082 Shennecossett Road, Groton, CT 06340-6048

---

**Report No. CG-D-01-2006**

# INTEGRATION OF COASTAL OCEAN DYNAMICS APPLICATION RADAR (CODAR) AND SHORT-TERM PREDICTIVE SYSTEM (STPS) SURFACE CURRENT ESTIMATES INTO THE SEARCH AND RESCUE OPTIMAL PLANNING SYSTEM (SAROPS)

**FINAL REPORT**
November 2005

This document is available to the U.S. public through the
National Technical Information Service, Springfield, VA 22161

Prepared for:

U.S. Department of Homeland Security
United States Coast Guard
Operations (G-O)
Washington, DC 20593-0001

# N O T I C E

Marc B. Mandler, Ph.D
Technical Director
United States Coast Guard
Research & Development Center
1082 Shennecossett Road
Groton, CT 06340-6048

Technical Report Documentation Page

**1. Report No.**
CG-D-01-2006

**2. Government Accession Number**

**3. Recipient's Catalog No.**

**4. Title and Subtitle**
Integration of Coastal Ocean Dynamics Application Radar (CODAR) and Short-Term Predictive System (STPS) Surface Current Estimates into the Search and Rescue Optimal Planning System (SAROPS)

**5. Report Date**
November 2005

**6. Performing Organization Code**
Project No. 1013

**7. Author(s)**
J. O'Donnell, D. Ullman, M. Spaulding, E. Howlett, T. Fake, P. Hall, T. Isaji, C. Edwards, E. Anderson, T. McClay, J. Kohut, A. Allen, S. Lester, C. Turner, and M. Lewandowski

**8. Performing Report No.**
R&DC 671

**9. Performing Organization Name and Address**

U.S. Coast Guard
Research & Development Center
1082 Shennecossett Road
Groton, CT 06340-6048

Anteon Corporation
240 Oral School Road
Suite 105
Mystic, CT 06355-1208

**10. Work Unit No. (TRAIS)**

**11. Contract or Grant No.**
DTCG39-00-D-R00008/
HSCG32-04-J-100052

**12. Sponsoring Organization Name and Address**

U.S. Department of Homeland Security
United States Coast Guard
Operations (G-O)
Washington, DC 20593-0001

**13. Type of Report & Period Covered**
Final Report

**14. Sponsoring Agency Code**
Commandant (G-OPR)
U.S. Coast Guard Headquarters
Washington, DC 20593-0001

**15. Supplementary Notes**
The R&DC's technical point of contact is Chris Turner, 860-441-2623, email: A.Chris.Turner@uscg.mil.

**16. Abstract (MAXIMUM 200 WORDS)**

The CODAR-based surface current prediction model (Short-Term Predictive System – STPS) previously demonstrated in Block Island Sound was extended to an existing long-range CODAR area in the Middle Atlantic Bight (MAB) and upgraded to incorporate the effects of wind forcing. Signal processing and data reduction refinements were also incorporated in the CODAR scheme.

To test these improvements, conventional methods of determining SAR target drift (e.g. NOAA tidal data or climatological data) were compared to Self-Locating Datum Marker Buoy (SLDMB) trajectories and STPS generated trajectories in the MAB. Techniques were also developed to estimate the velocity variance, dispersion coefficient, and autocorrelation time scales necessary as input to random walk (RW) and random flight (RF) models from CODAR, STPS, and SLDMB data.

An operational T&E was conducted to determine the accuracy and user-friendliness of incorporating CODAR and STPS information in the new SAROPS planning tool and Environmental Data Server framework.

**17. Key Words**
CODAR, dispersion, drift trajectory, forecasts, Monte Carlo, random flight, random walk, SAR, SAROPS, Search and Rescue, SLDMB, surface currents, uncertainty, variance

**18. Distribution Statement**
This document is available to the U.S. public through the National Technical Information Service, Springfield, VA 22161.

**19. Security Class (This Report)**
UNCLASSIFIED

**20. Security Class (This Page)**
UNCLASSIFIED

**21. No of Pages**

**22. Price**

(This page intentionally left blank.)

# EXECUTIVE SUMMARY

Coastal Ocean Dynamics Application Radar (CODAR) is a shore-based high-frequency (HF) surface wave radar system that can be used to measure surface currents up to 200 km from shore. Because of CODAR's ability to provide real-time surface current data, the U. S. Coast Guard (CG) is investigating the utility of CODAR in Search and Rescue (SAR) mission planning.

In 2003, the University of Connecticut (UCONN) developed a Short-Term Predictive System (STPS) that used CODAR data to make surface current predictions 24 hours into the future. The STPS was initially developed using CODAR data from the standard CODAR system covering Block Island Sound (BIS). CODAR-based STPS predictions were found to be significantly more accurate than those developed using National Oceanic and Atmospheric Association (NOAA) tide data. Based on this initial success, additional CODAR development was pursued. Specific development initiatives included in the present study were to:

- Extend the STPS to an existing long-range CODAR system that is not dominated by tidal flow (i.e., Mid-Atlantic Bight (MAB). Apply and evaluate the effect of geometric dilution of precision (GDOP) filtering of CODAR data in the enhanced version of the STPS. In this instance, GDOP filtering was found to substantially decrease STPS current prediction errors.
- Upgrade STPS by adding the capability to incorporate the effects of wind forcing and evaluate the impact of including wind forcing. In addition, the STPS was enhanced by the use of covariance estimates in the Gauss-Markov procedure. Adding forecast winds improved the average accuracy of current forecasts by approximately 10 to 20 percent in the first 5 hours of the forecast in the MAB region depending on the quality of the CODAR data used to make the prediction. The improvement was less for longer prediction times. This limited impact of the wind component may reflect the lack of significant wind events during the study period or inadequacies in the statistical approach to incorporate winds.
- Further investigate the accuracy and sources of error in using CODAR data and STPS to determine drift trajectories as compared to more conventional methods of estimating surface drift (including NOAA tidal data, Mariano climatology data, and last known position). This was accomplished for both Block Island Sound and the Middle Atlantic Bight by computing separation distance between model-predicted and actual Self-Locating Datum Marker Buoys (SLDMB) positions. In both the BIS and MAB, the evaluation showed that trajectories calculated from real-time CODAR data provided some improvement in predicting SLDMB locations relative to conventional prediction approaches. The STPS provided a measurable improvement over conventional techniques only in BIS.
- Investigate methods of determining and incorporating error and sub-grid uncertainty terms into Monte Carlo trajectory models derived from the comparison of CODAR and SLDMB trajectory data. In this part of the study, random walk (RW) and random flight (RF) methods were compared for simulating the transport of surface drifters. Differences in RW and RF search area size are small when comparable input parameters were used. Both models were highly sensitive to the effect of uncertainties in dispersion.

- Identify the current quality and utility of HF radar products for SAR. For the MAB in summer, it was determined that CODAR improvements did reduce drifting body prediction error by approximately 20 percent relative to present techniques. Improvements in the processing and filtering of CODAR returns provided the largest benefit in this study, suggesting that additional work in this area may be called for. The time series analysis techniques employed in this study produced smaller and less consistent improvements.
- Evaluate the capabilities of the prototype SAROPS environmental data server (EDS), which was extended to retrieve CODAR and STPS surface current data and forecasts from the MAB CODAR region. This effort demonstrated that the SAROPS EDS is capable of collecting and disseminating CODAR current data and STPS predictions.
- Conduct an operational test and evaluation (T&E) at CG Group Moriches, in which CODAR and STPS data were utilized in actual SAR mission planning. The T&E showed that STPS and CODAR data could be effectively acquired, interpreted, and used by CG SAR mission planners.

CODAR and STPS are maturing technologies that have demonstrated the ability to improve CG operational planning. Presently, however, CODAR and STPS are not ready for operational use in SAROPS. The following recommendations are provided to make them viable for operational use in SAROPS.

- Through Oceans.US, the CG should
    a. Encourage initiatives to improve the accuracy and coverage of HF radar arrays,
    b. Encourage development of enhancements to STPS in HF radar coverage regions.
    c. Partner with the HF radar community to ensure that the CG requirements are recognized.
- In the SAROPS development process, G-OPR should include methodologies in the EDS to fill the gaps where no data or invalid surface current data exist.
- In conjunction with the Operations System Center, G-OPR should develop an archive to store SLDMB data, and periodically calculate and store regionally representative dispersion coefficients from SLDMB trajectories. Archived SLDMB data could also be matched with seasonal and environmental conditions to provide better historical current estimates in areas where CODAR/STPS is not available.
- G-OPR should support further research on the impact of forecast wind change on STPS current estimates.

# TABLE OF CONTENTS

# LIST OF FIGURES

# LIST OF TABLES

# LIST OF ACRONYMS

| | |
|---|---|
| AOI | Area of Interest |
| AOR | Area of Responsibility |
| ArcGIS | Integrated collection of GIS software Program |
| ASA | Applied Science Associate |
| ASCII | American Standard Code for Information Exchange |
| BIS | Block Island Sound |
| C2PC | Command and Control Personal Computer |
| CASP | Computer-Assisted Search Planning |
| CG | United States Coast Guard |
| CJMTK | Commercial Joint Mapping Tool Kit |
| CODAR | Coastal Ocean Dynamics Application Radar |
| CTF | Coastmap Text Format |
| DMB | Datum Marker Buoy |
| EDS | Environmental Date Server |
| ESRI | Environmental Systems Research Institute, Inc. |
| FTP | File Transfer Protocol |
| GDOP | Geometric Dilution of Precision |
| GIS | Geographical Information System |
| GMT | Greenwich Mean Time |
| GRUMOR | CG Group Moriches |
| GUI | Graphical User Interface |
| HF | High Frequency |
| HTML | Hypertext Markup Language |
| HTTP | Hypertext Transfer Protocol |
| IAMSAR | International Aeronautical and Maritime Search and Rescue |
| JAWS | Joint Automated Worksheets |
| LKP | Last Known Position |
| MAB | Mid-Atlantic Bight |
| NDBC | National Data Buoy Center |
| NetCDF | Network Common Data Form |
| nmi | Nautical miles |
| NOAA | National Oceanic and Atmospheric Association |
| OPCEN | Operations Center |
| OPeNDAP | Open-source Project for a Network Data Access Protocol |
| OSC | Operations System Center |
| OSCAR | Ocean Surface Currents Analysis-Real Time |
| PIW | Person in the Water |
| POS | Probability of Success |
| R&DC | Research and Development Center |
| RDT&E | Research Development Testing and Evaluation |
| RF | Random Flight |
| RMS | Root-Mean-Squared |
| RW | Random Walk |
| SAP | Search Action Plan |
| SAR | Search and Rescue |

| | |
|---|---|
| SARMAP | Search and Rescue Model System |
| SAROPS | Search and Rescue Optimal Planning System |
| SLDMB | Self-Locating Datum Marker Buoys |
| SNR | Signal to Noise Ratio |
| SOAP | Simple Object Access Protocol |
| SRU | Search and Rescue Unit |
| STPS | Short-Term Predictive System |
| T&E | Test and Evaluation |
| URI | University of Rhode Island |
| UCONN | University of Connecticut |
| WERA | WEllen Radar |
| XML | Extensible Markup Language |

# 1. INTRODUCTION

## 1.1. Background

The U.S. Coast Guard (CG) Research and Development Center (R&DC) conducted research, development, testing, and evaluation (RDT&E) to evaluate high frequency (HF) surface wave radar systems that exploit the Doppler shift in the Bragg scatter of the sea surface to measure surface currents in real time. Several surface current mapping systems (e.g. Coastal Ocean Dynamics Application Radar (CODAR), WEllen Radar (WERA), and Ocean Surface Currents Analyses-Real time (OSCAR)) have been developed and are now commercially available (Teague, Vesecky, & Fernandez, 1997). CODAR SeaSonde systems are the HF surface wave radar systems currently used in the Block Island Sound (BIS) and Mid-Atlantic Bight (MAB) regions covered in this report. Although the name "CODAR" is used throughout this report, other brands of hardware could have been used had they been available for the study area. CODAR systems are owned and operated by university oceanographers and provide surface current data for many areas adjacent to the U.S. coastline via the Internet. With recent advances in processing speed and Internet-based data dissemination, ocean current measurements provided by CODAR may improve CG mission effectiveness and efficiency in carrying out search and rescue (SAR) cases.

In 2002, the R&DC funded a study (Ullman, O'Donnell, Edwards, Fake, Morschauser, Sprague, Allen, & Krenzien, 2003) with participation by the University of Connecticut (UCONN) and University of Rhode Island (URI) to investigate more closely the application of data from the Block Island Sound (BIS) CODAR system in Search and Rescue (SAR) planning. The BIS CODAR system is a standard-range 25-MHz CODAR system, owned and operated by URI and UCONN. It operates from three stations: Montauk Point, NY; Southeast Light House, Block Island, RI; and Misquamicut, RI. The locations of the BIS CODAR transmitters and the approximate operating ranges of each transmitter are shown in Figure 1-1. Using direction- and range-finding algorithms, each station measures radial surface current velocities every 10 minutes. These radial velocities are filtered and used to calculate the surface current velocities for the BIS, a region approximately 40 x 40 kilometers (km), with grid cells every 1.5 km. The depth of the water column over which currents are measured is dependent on the transmitter frequency: at 25-MHz, surface currents in the upper 0.5 meters of the water column are measured. Theoretically, the current field is resolved in areas where the arcs of at least two of the transmitters intersect. Coverage is lost, however, in the shadow of a land mass, such as Block Island, or in the line of sight between two stations, or at the outer range of each transmitter. The system produces surface current maps at one hour intervals. A map depicting surface current typical coverage of the BIS system is shown in Figure 1-2.

Ullman, et al, (2003) focused on the following three tasks. (1) develop a Short-term Predictive System (STPS) based upon surface current fields estimated from CODAR data in the Block Island Sound (BIS) region; (2) develop an environmental data server (EDS) Web site for collecting and disseminating CODAR data fields and forecast fields from the STPS; and (3) compare the actual trajectories of surface drifters with predicted trajectories based upon CODAR, STPS, and the nearest National Oceanographic and Atmospheric Administration (NOAA) tidal current prediction stations.

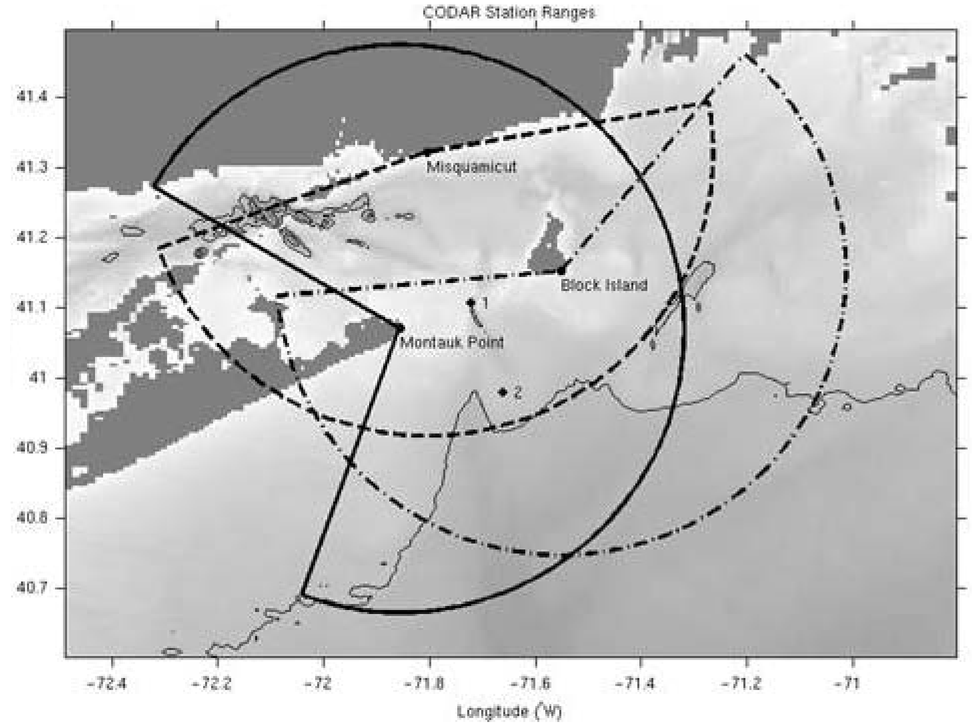

Figure 1-1. The coastline and bathymetry of Block Island Sound with the location and approximate observation areas of three CODAR sites.

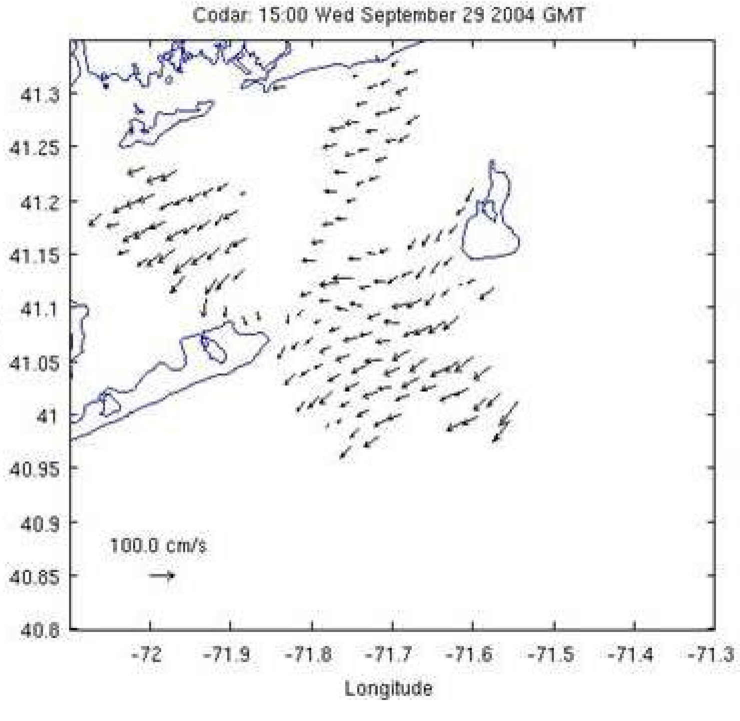

Figure 1-2. The typical spatial coverage of the BIS CODAR system operated by URI and UCONN.

In the present project, the features of the BIS CODAR system is extended to the CODAR network for the Middle Atlantic Bight (MAB). The MAB CODAR system is a long-range system consisting of ten stations operated by Rutgers University. Six of these stations are lower-resolution, long-range sites. With an approximate 5-MHz operating frequency, these sites measure surface currents within the upper 2.4 meters of the water column (Stewart and Joy, 1974). Typical spatial resolutions are on the order of 6 km (grid cell size) with maximum ranges exceeding 200 km. A cluster of four sites along the coast of New Jersey extending between Wildwood and Sandy Hook form the MAB CODAR network for this study, which provides hourly surface current maps over an area approximately 150 x 100 km off the New Jersey coast. These sites use global positioning system (GPS) time synchronization so that each site operates at the same frequency and is bi-statically linked to the other sites in the network. The CODAR system samples data continuously and outputs a 4-hour running average every hour. Processing of the CODAR data performed by Rutgers University is further outlined in Appendix A. Figure 1-3 shows the MAB CODAR coverage for July/August 2004. The black line in the figure bounds the 50 percent contour coverage for the length of the deployment, i.e., grid points inside the black line had returns more than 50 percent of the time; grid points outside of the black line had returns less than 50 percent of the time. The 50 percent contour coverage is based on data from the 27 July to 31 August 2004 deployment period.

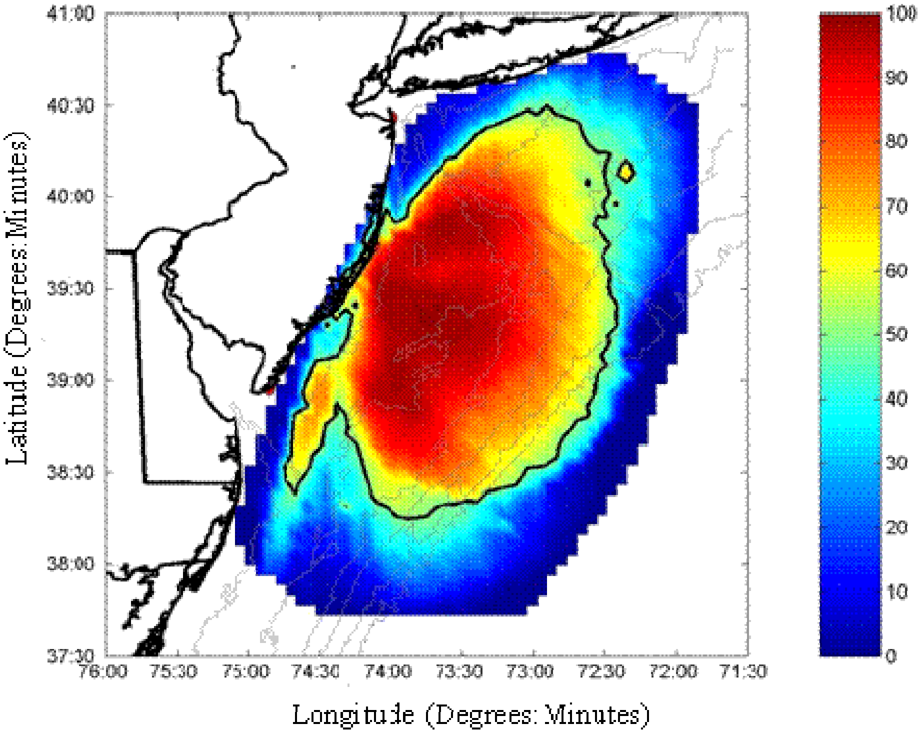

Figure 1-3. MAB CODAR coverage for July/August 2004.

In a separate effort, the CG has been developing a system for search planners, called Search and Rescue Optimal Planning System (SAROPS). SAROPS is intended to replace both of the CG's presently fielded search planning tools, Command and Control Personal Computer (C2PC) SAR Tools and Computer-Assisted Search Planning (CASP). A prototype graphical user interface

(GUI) has been provided by the SAROPS developer as part of this study to see how SAR controllers could utilize the current fields provided by CODAR in SAROPS to plan search efforts. Procedures and results are presented in Section 6 of this report.

## 1.2. Project description

The goal of this project is to resolve the potential benefits to SAR Planning of adapting the STPS to a larger and more generalized CODAR network. The elements of this project are (1) modify the STPS developed for the tidally-dominated BIS to the larger MAB where circulation is dominated by winds and other processes; (2) develop and exercise new analysis procedures to incorporate wind forcing into STPS; (3) identify the processes or factors that affect the performance of the CODAR-based surface current predictions in the MAB; and finally (4) conduct an operational test of the system to identify its skill and to identify the direction and potential benefits of future work in this area.

# 2. MODIFICATIONS TO STPS FOR THE MAB APPLICATION

The STPS developed in Ullman et al, (2003) is based on the decomposition of the CODAR measured currents into tidal and non-tidal components (i.e., wind-driven motion and motion associated with ocean density variations and very low frequency waves). At each grid point, tidal currents are predicted using tidal constituents derived from a harmonic analysis of a one-month record of CODAR surface currents. A Gauss-Markov estimator is used to predict the non-tidal component of currents. The current prediction is the sum of the predicted tidal and non-tidal currents.

The Gauss-Markov estimator, based on auto- and cross-covariance functions, is used to predict the non-tidal component of current (Ullman, O'Donnell, Kohut, Fake, Allen, 2005). The covariance function is a series that measures how similar a time series signal is to a time-shifted version of itself or another series of values. For example, in a tidally-dominated area, the autocovariance series will have a high value at time lags corresponding to tidal periodicities (e.g. 12.4 hours). The Gauss-Markov estimator calculates filter weights that also are a function of time lag, which are then used to generate a prediction of future values based on a memory effect created from previous values through the covariance function. Predictions are produced on an hourly basis and extend for 25 hours into the future.

The Gauss-Markov estimator is used in two ways in this study. In the first application, it derives a series of weights that are calculated from the autocovariance of previous current data that are then applied to recent values to predict future currents (i.e. for the next 25 hours). In the second application, the cross-covariance between previous surface wind measurements and surface currents derived from CODAR will be used to estimate future currents.

The STPS developed for BIS did not explicitly account for wind forcing in the BIS because its circulation is considered to be tidally dominated. In exercising the STPS and comparing the results to SLDMB trajectories in the Middle Atlantic Bight, it seemed likely that a second generation model that included wind forcing could improve forecast accuracy in areas where there is a significant wind-driven surface current component.

The STPS algorithm was extended to accommodate data from the MAB between southern Long Island and the mouth of Delaware Bay. The following modifications were implemented and tested in STPS:

- Covariance calculated for each grid point, instead of a region-wide average, was used in the Gauss-Markov procedure to account for local geographic and bathymetric effects.
- Covariance was calculated between the east and north velocity components of current at each grid point to account for the Coriolis effect.
- Improvements were incorporated into the MAB CODAR processing algorithm, including geometric dilution of precision (GDOP) and percentage return filtering.
- Measured wind data from a moored buoy in the vicinity of the CODAR coverage area was used to calculate the covariance function with the CODAR data. The wind data were used in two ways. First, wind observations prior to each time step were used to predict

future surface currents and second, “predicted” winds, (actually wind observations) were used to predict future surface currents.

The incorporation of local covariance and east and north velocity component covariance into the Gauss-Markov estimator (items 1 and 2 above) did not provide significant improvements to the model’s predictive skill. These improvements were retained in the STPS, but are not discussed further. Details of the STPS enhancements in the BIS region are described in detail in Appendix B.

## 2.1. Enhancements adopted from the MAB algorithm

To further refine the CODAR data for the present project, Rutgers University implemented a new algorithm for combining CODAR radials that incorporated two improvements: a 50 percent return mask and GDOP filtering (Kohut, Roarty, Glenn, 2004). Each hour, the available radial vector maps were combined into a single total vector map. All radial component vectors within 10 km were used to calculate the vector at each grid point, but a total vector was generated only if at least three radial vectors from at least two remote sites were used in the combination. The uncertainty of the combined totals was separated into radial vector uncertainty based on the number of radials in the 4-hour average, signal to noise ratio (SNR), and geometric dilution of precision (GDOP) (e.g. see Riddles, 2003). Scalar values (Chapman and Graber, 1997) were calculated based on the intersection angles of radial vectors within 10 km of each grid point and compared with a scalar threshold. The expected error in the surface current vector due to GDOP calculated from two radials increases as their intersection angle diverges from the orthogonal. For this project, the scalar GDOP threshold was calculated to be 1.25, corresponding to intersection angles less than 30 degrees or greater than 150 degrees. These filters reduced the size of the CODAR coverage area, but they improved the quality of the data.

Figure 2-1 shows MAB CODAR coverage when the filtering algorithm was used for July/August 2004. The black line in the figure bounds the 50 percent contour coverage for the length of the deployment. The 50 percent contour coverage is based on data from the 27 July to 31 August 2004 deployment period. When the GDOP and percent return constraints were used to filter the set of CODAR data used to generate current predictions (referred to below as the “New Gauss-Markov” predictor), the root-mean-squared (RMS) error of the predictions was reduced by approximately 20 percent.

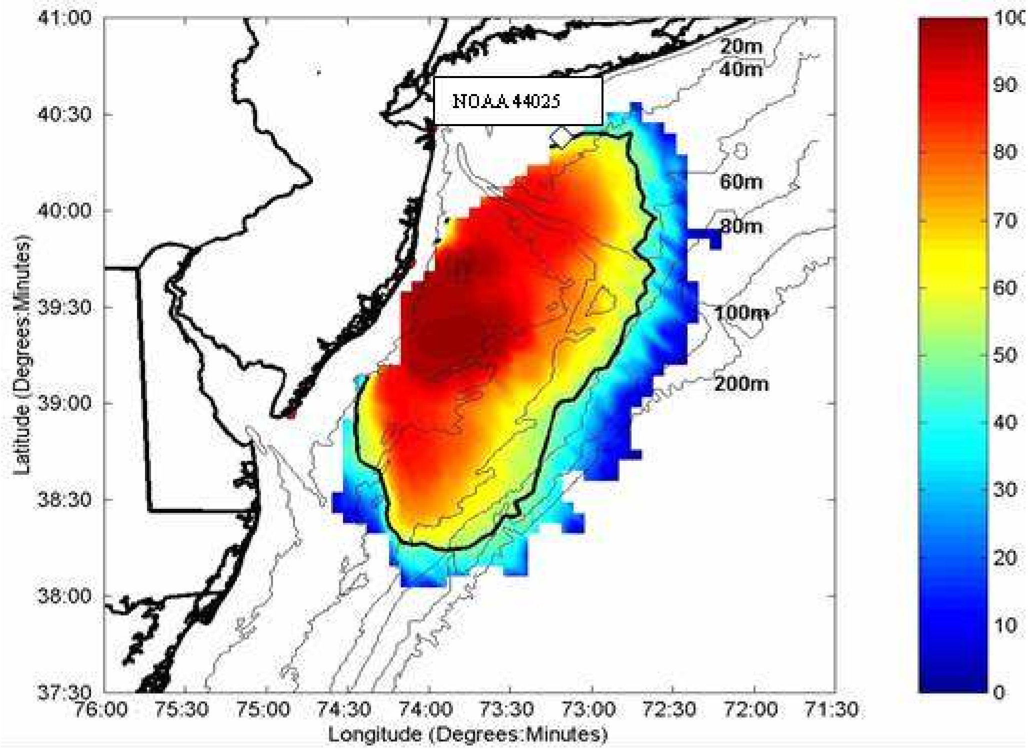

Figure 2-1. MAB CODAR coverage for July/August 2004, showing percent radar return percentages (color coded) and using the GDOP-filtered data. (Note: The approximate location of NOAA buoy 44025 is at the top of the 50 percent coverage area.)

## 2.2. Incorporation of NOAA buoy data into STPS

The first attempt to incorporate wind data into STPS involved the use of previous wind observations to construct predictions of near future non-tidal residual currents. Wind data from the closest operating NOAA buoy (#44025) were used for this exercise. We chose a seven day period during August 2004 when winds were highest (~5 m/s) to maximize the influence of wind. First, previous winds and CODAR current fields were used to establish filter weights for the Gauss-Markov estimator. Next, at each time step, the wind-driven residual current was predicted for the upcoming 24 hour period. This prediction was made with the Gauss-Markov estimator using observed winds and CODAR current fields from the previous 24 hour period. For the purpose of identifying the degree of improvement, an initial run was made where winds were set to zero, such that only the basic features of the STPS, tides plus a residual current estimated using the Gauss-Markov estimator, were in play.

The improvement provided by using recent buoy winds with the basic STPS for August 2004 is summarized in Figure 2-2 by plotting the spatially-averaged RMS differences between the STPS and CODAR surface current components versus forecast time for the August study period. The "New Gauss-Markov" titles in the figure signify that the CODAR return processing algorithms described in Section 2-1 were being used. The no-wind case differences are shown as a function of forecast time for the east (u-component, blue solid line) and north (v-component, red solid line) current components. Where the wind-driven residual is not incorporated, the RMS differences start at 9 cm/s at the t=0 forecast and increase, then level off at 12 cm/s for the east component and 13 cm/s for the north component at approximately 5 hours forecast time. The dashed blue line (u-component) and dashed red line (v-component) show the corresponding RMS difference plots incorporating the wind-driven residual current based on observed wind.

The reductions in RMS error vs. time plots at the bottom of the figure show that a reduction 1 to 2 cm/s (20 percent) was realized for the present time analysis, but the reduction dropped off rapidly to 1cm/s or less at forecast times of a few hours or more.

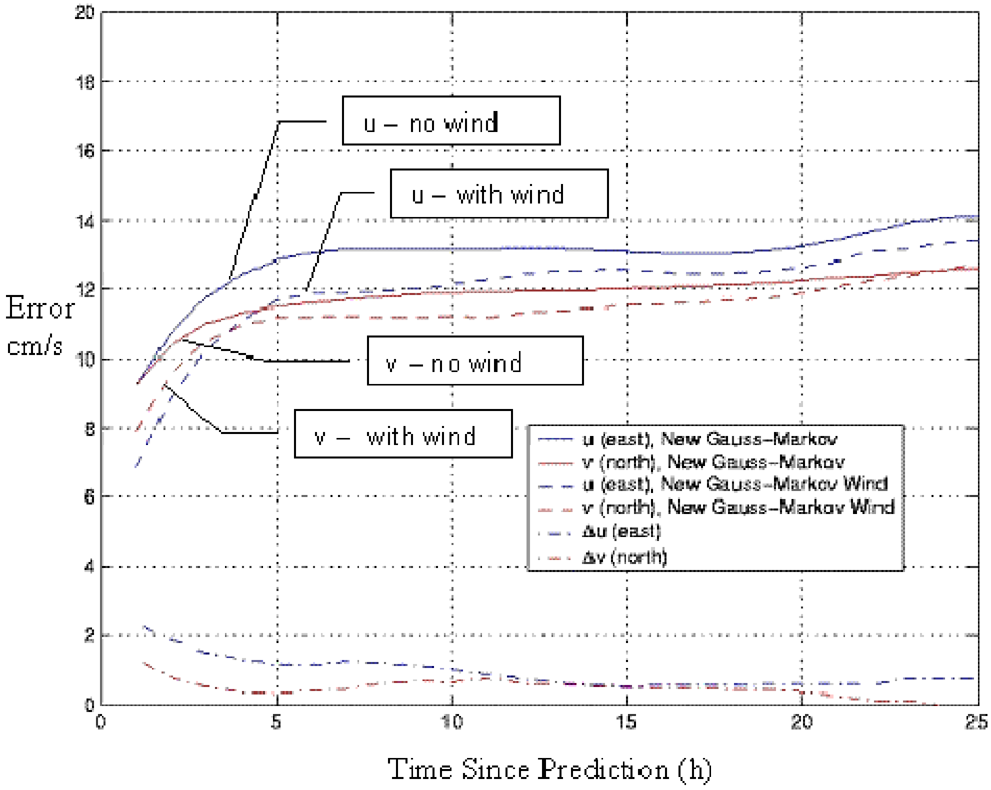

Figure 2-2. The RMS difference (cm/s) between area-averaged MAB CODAR east (u-blue lines) and north (v-red lines) components of surface current for August 2004 as a function of current forecast period (hrs) using measured wind (dashed lines) and no wind forcing (solid lines). The reductions (Δu, Δv) in RMS error at the bottom of the figure represent the error reduction realized by the use of buoy winds.

## 2.3. Use of "forecast" winds derived from NOAA buoy data

An experiment was performed in which observed winds from NDBC buoy #44025 were included as "forecast" winds during the same period in August 2004. In this test winds from times following each present time (i.e. as simulated predictions of future winds) were included in the Gauss-Markov estimator. In making predictions for planning an actual SAR case, these "future wind values" would of course be replaced by model predictions. In a sense, this provided a "perfect prediction" of future winds for the time period considered to establish an upper limit of the potential value of including wind forecasts. At each time step, the "New Gauss-Markov Forecast" approach was used to construct an estimate of the surface current based on measured buoy winds during the 48 hour period centered on the present time (e.g. t = 0 in Figure 2-3). As before, the basic features of the STPS (Gauss-Markov tidal and residual currents) were included in the prediction. The improvement provided by using present buoy winds relative to the basic STPS using only observations (made prior to t=0) is shown by plotting RMS difference as a function of forecast time in Figure 2-3 for the August 2004 time period. The area-averaged east (blue) and north (red) RMS velocity component errors are plotted as a function of the forecast period (hrs). The solid lines represent predictions based on measured and forecast winds; dashed lines correspond to predictions based only on measured winds. The results suggest that the use of wind forecasts produces a negligible improvement in prediction skill. The low magnitude and variability of the wind during the test period may not have produced a significant response from the model because surface currents were not well correlated with local winds during that time. Other explanations may be that surface currents are forced by other processes, or that another analysis approach to quantifying the wind-driven circulation is called for.

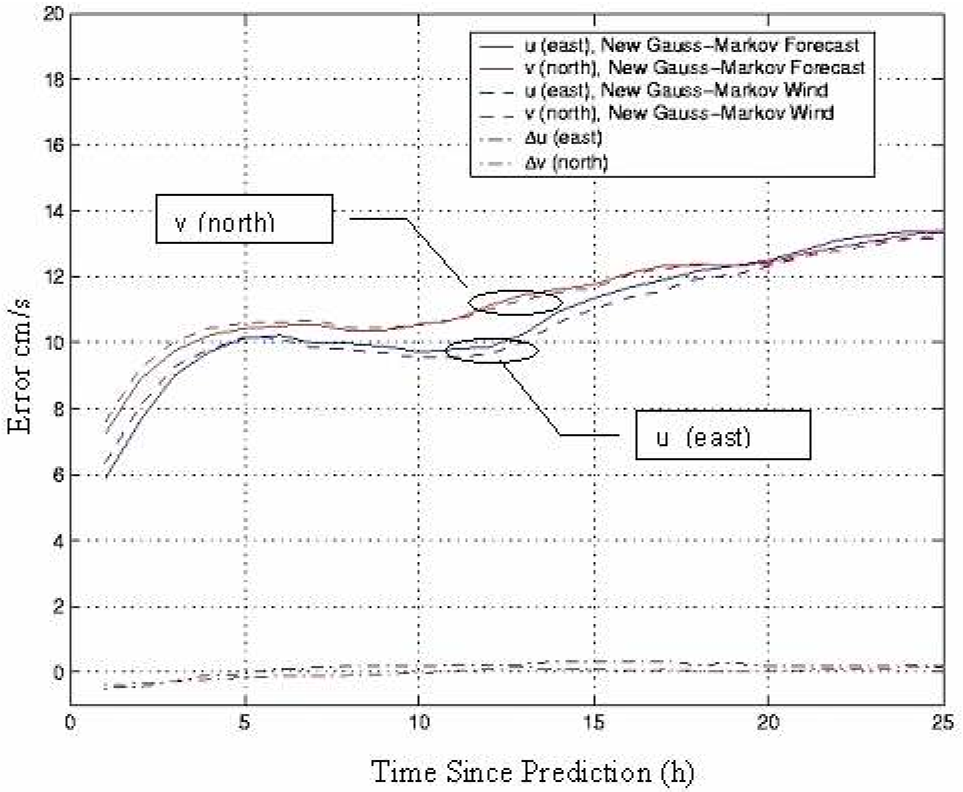

Figure 2-3. The evolution of the area-averaged RMS difference between the forecast current components using the enhanced STPS algorithm with measured wind (dashed lines) and with measured and forecast wind (solid lines) in the MAB area. The reductions (Δu, Δv) in RMS error at the bottom of the figure represent the error reduction realized by the use of buoy winds.

## 2.4. Summary of STPS extension efforts

A series of changes were made to the STPS as it was adapted from the BIS area to the MAB area. The changes fell into two categories: modifications to the processing of the CODAR data to enhance data quality prior to use by STPS, and application of new techniques to predict surface currents incorporating a wind-driven component based on actual observed and forecast winds. The exercises determined that changes to the processing of CODAR returns had the largest influence on the agreement of subsequent CODAR-derived surface current data with STPS predictions. The use of currents derived from the GDOP and percent return filters reduced RMS errors by approximately 20 percent.

The introduction of wind data into the Gauss-Markov estimator as incorporated into the MAB STPS algorithm provided a small improvement in the RMS differences between predictions and future CODAR data. The reductions in RMS prediction error varied between 2 cm/s at the one hour forecast time to less than 1 cm/s at prediction times of a few hours, or approximately 10 percent.

Potential reasons for the minimal contribution of the wind-driven component may be that the low magnitude and variability of the wind during the test period may not have produced a significant response from the model because surface currents were not well correlated with local winds during that time. Other reasons may be that the statistical approach chosen did not represent the effect of wind. Additional testing and a different conceptual approach are needed, particularly for the 0 to 6 hour interval, a time period of significant operational interest to the CG.

In summary, the greatest improvement in the STPS performance was due to improved CODAR data processing than to adding the effect of forecast winds to the STPS.

# 3. EVALUATION OF PREDICTIVE METHODS IN ESTIMATING DRIFTER TRAJECTORIES

Through this study and previous work, investigators had access to actual SLDMB trajectory information in the Mid-Atlantic Bight (MAB) and Block Island Sound (BIS) dating from December 2002 through September 2004. These trajectories were used to evaluate the performance of the extended STPS with wind forcing, and their underlying CODAR surface-current maps with improved processing, and compare the CODAR/STPS performance against traditional CG search planning methods for determining surface currents.

## 3.1. Mid-Atlantic bight SLDMB deployments

Figure 3-1 and Figure 3-2 show the trajectories of SLDMBs launched in the MAB study area. The thin dark line shows the area for which CODAR coverage was available more than 90 percent of the time. The thick lines represent the drifter trajectories.

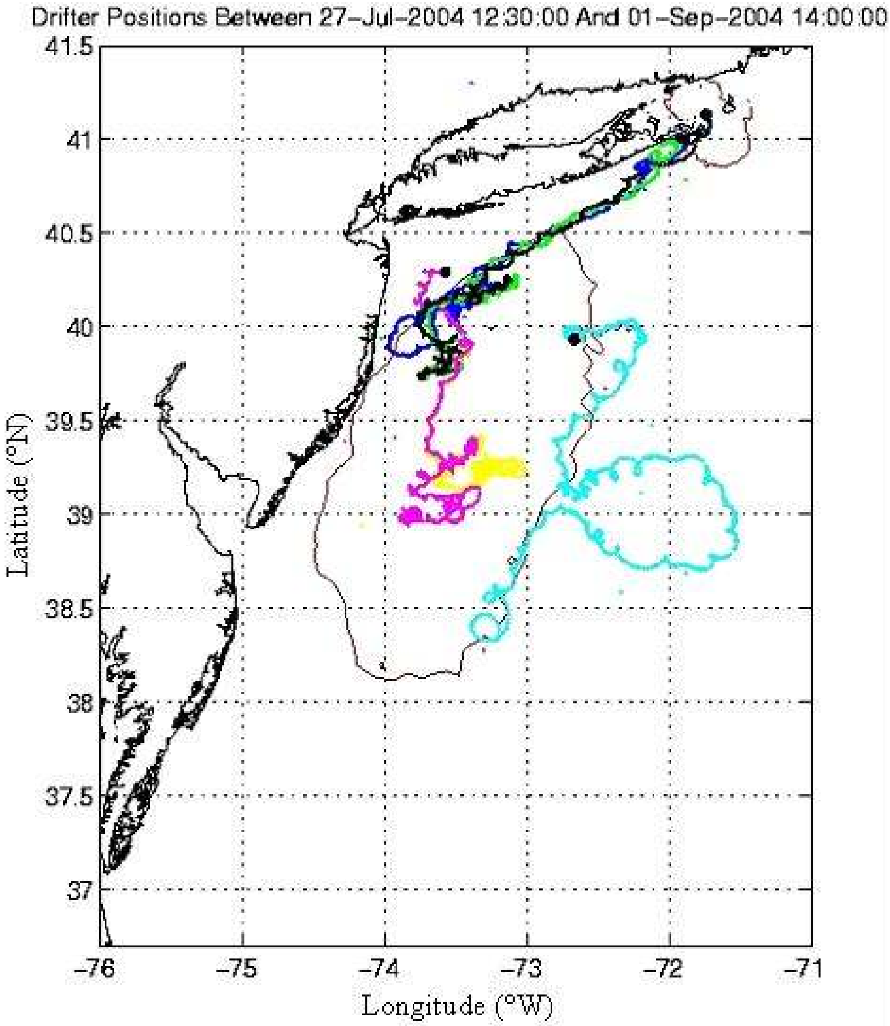

Figure 3-1. Drifter trajectories in the MAB study area in July–Sept 2004 (Black dots represent the start point for each trajectory).

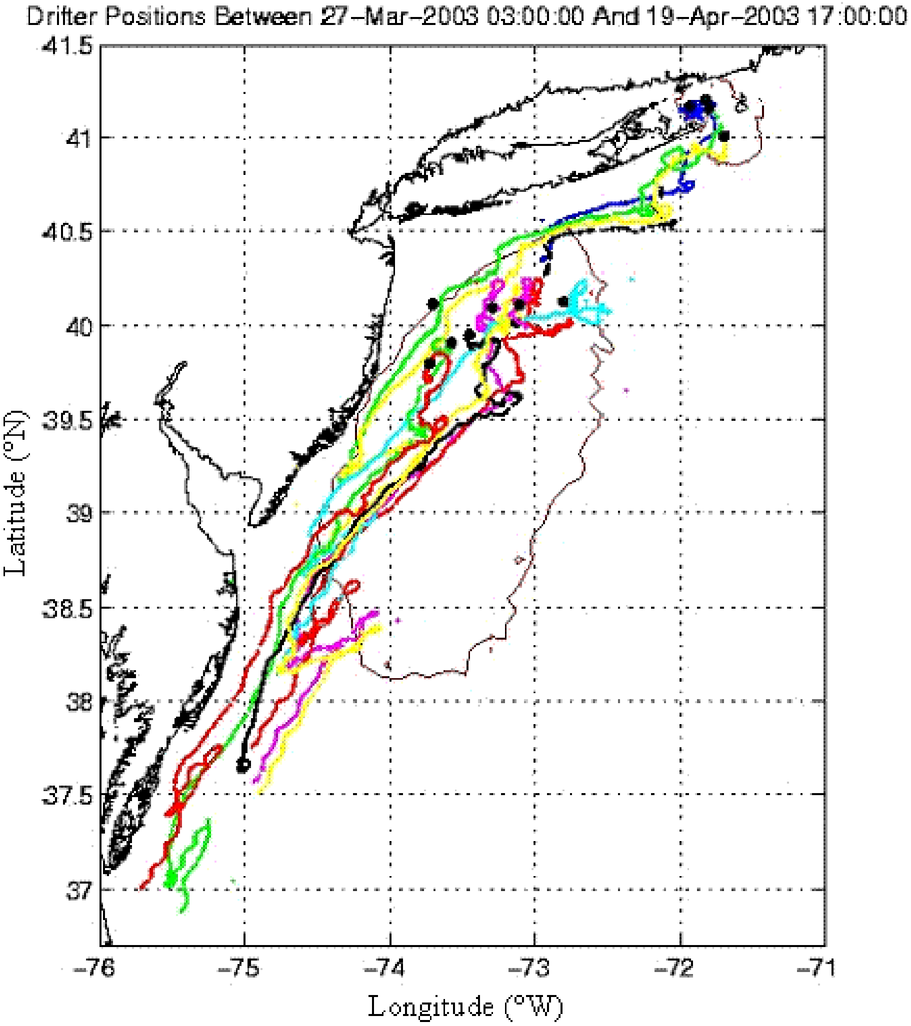

Figure 3-2. Trajectories in the MAB study area in March–April 2003 (Black dots represent the start point for each trajectory).

The drifter trajectories were divided into 24-hour segments, creating approximately 200 independent sample tracks. The frequency distribution of separation distances (position errors) between drifter location and positions computed using the CODAR current estimates at 3, 6, 12, and 24 hours is shown in the left column of Figure 3-3. The second column shows the same information with the drifter locations predicted using the STPS currents. Measured wind data from NDBC buoy #44025 were used in the STPS predictions to incorporate a wind-driven component as described in Section 2.2. Because the CG currently uses a climatological mean current specified at 1-degree intervals to estimate the drift of search targets in most of this area, the third column shows the separation distances between the drifter location and the positions predicted using the Mariano climatology (Mariano, Ryan, Perkins, Smithers, 1995). Finally, the LKP column shows the distribution of separation distances between the actual position of the drifter and its initial location (i.e., if we assumed that the object did not drift from its initial position over the 24-hour period). At 3 and 6 hours, the distributions of the separations in the left two columns (CODAR and STPS) are slightly more skewed to lower values than the right two columns, indicating that these two approaches are somewhat more accurate.

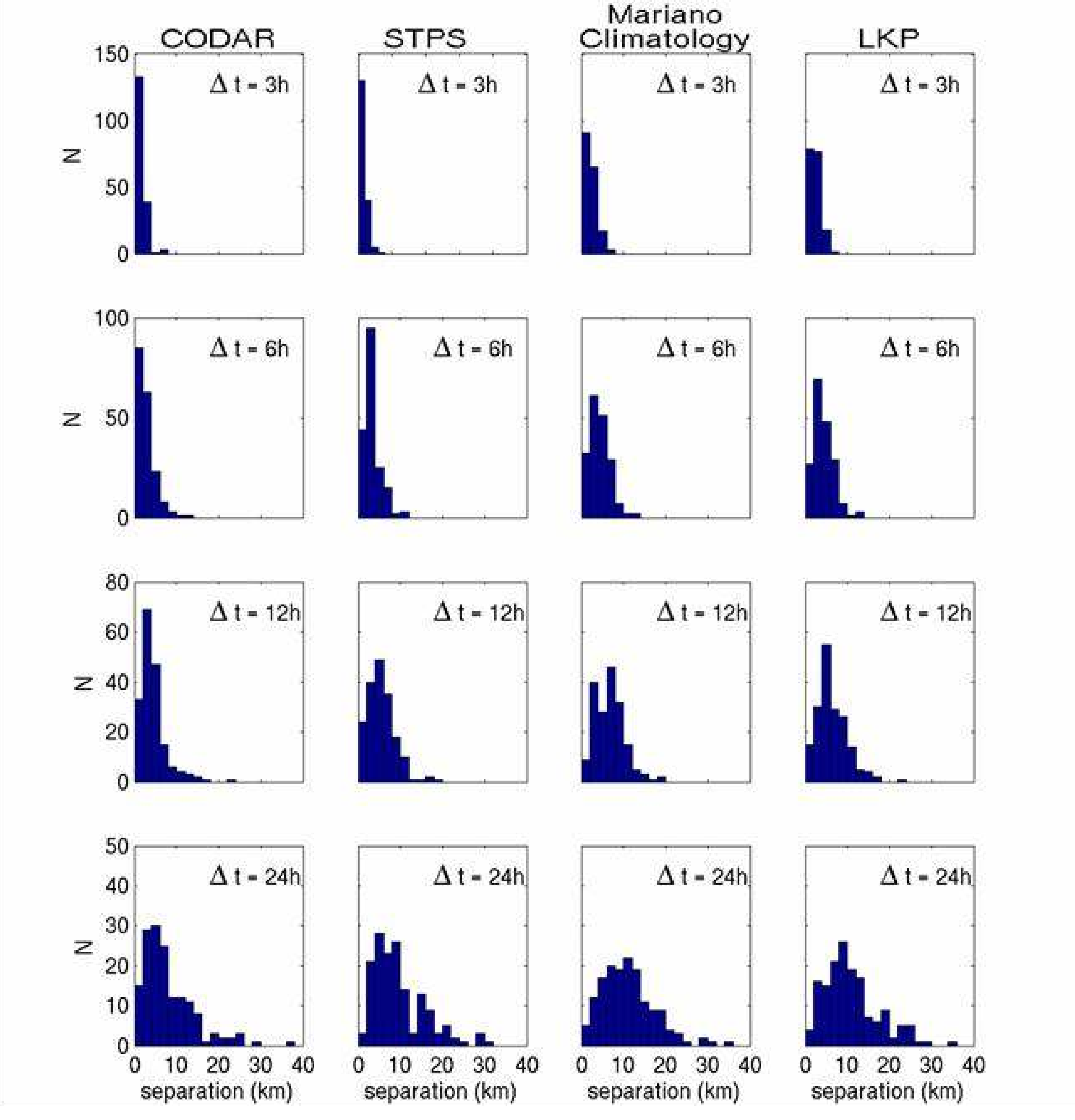

Figure 3-3. Histograms of the separation between the predicted and actual locations of SLDMBs in the MAB study area, shown as the number of endpoints (N) vs separation distance (km) at 3, 6, 12, and 24 hours. From left to right, the predicted positions are obtained by integrating observed CODAR velocities, STPS-predicted currents, velocities estimated using the Mariano climatology data, and the LKP.

Distances corresponding to the 95th percentile of the separation distance distributions at each time step are shown in Figure 3-4. The differences are relatively similar in this case. At 24 hours, the difference between the four methods is less than 5 km. As shown in Figure 3-4, CODAR and STPS have slightly smaller separation distances than the Mariano climatology or LKP estimates, but the difference is not significant.

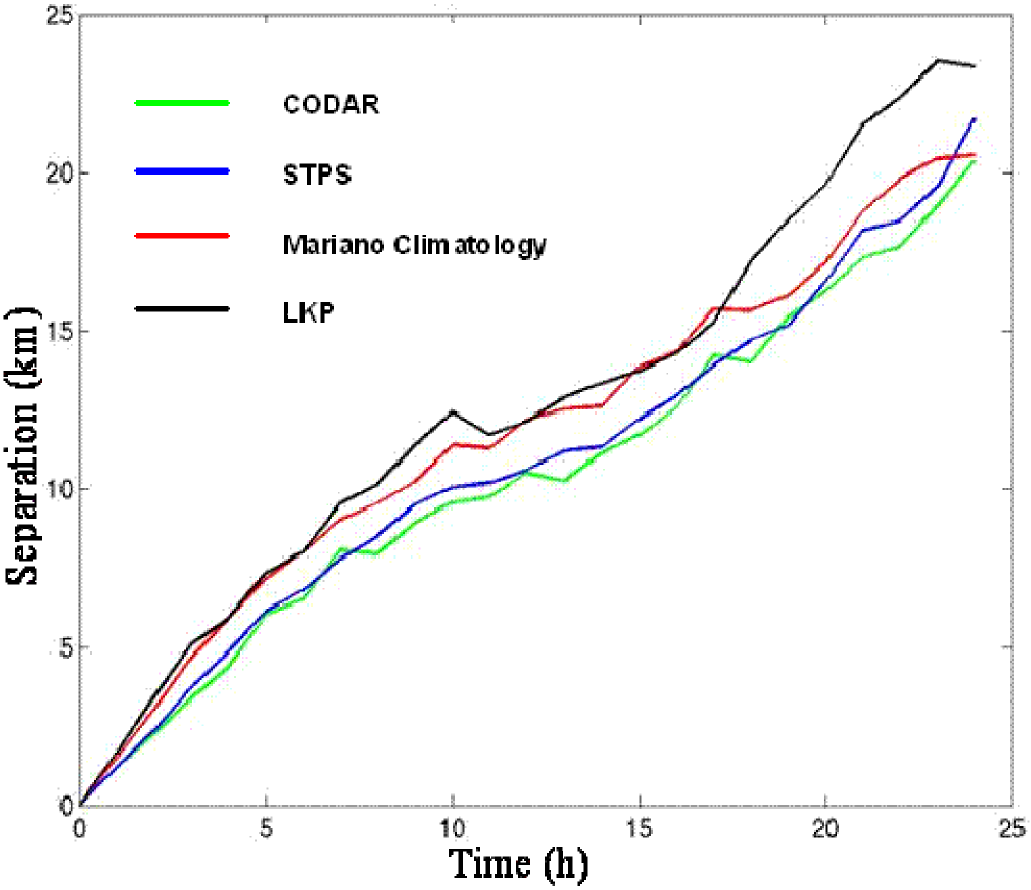

Figure 3-4. The evolution of the 95th percentile value of separation distance between drifters and simulated trajectories in the MAB based on CODAR data (green line), the STPS algorithm (blue line), LKP (black line), and Mariano climatology (red line).

To provide a more realistic comparison of the CODAR and STPS predictions with the more conventional predictions, data from the MAB area were reprocessed to exclude data outside of the 90 percent availability line (i.e., excluding lower percent return CODAR areas). The results are provided in Figure 3-5 and Figure 3-6. The data are similar to those without screening except for CODAR. The CODAR errors decrease approximately 20 to 25 percent when the lower-quality data are excluded, and STPS errors decrease by roughly 10 percent. The outcome illustrates the value gained by preprocessing and use of higher quality CODAR returns implemented in the MAB processing algorithm, in improving the performance of these approaches for predicting drift body motion.

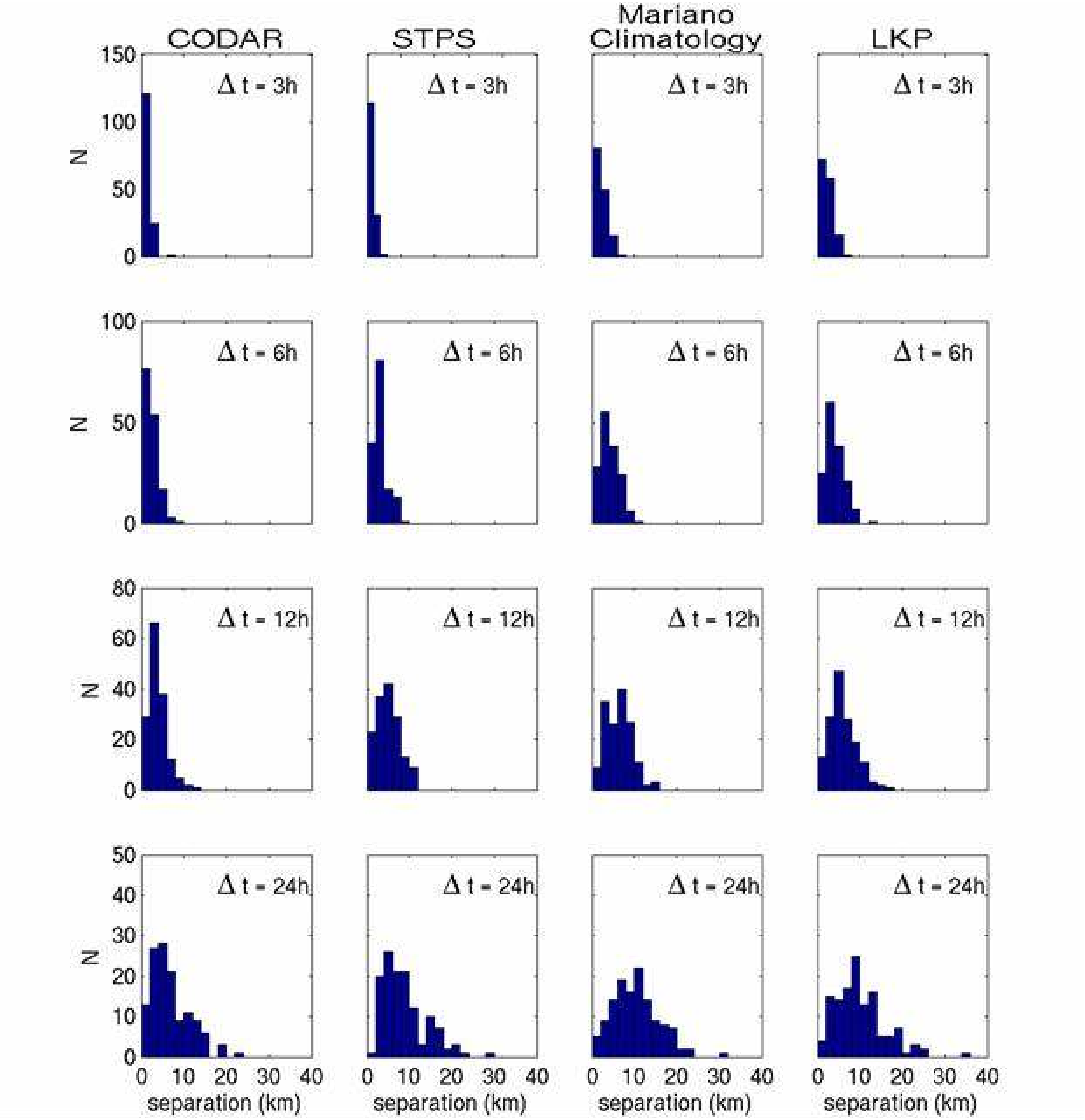

Figure 3-5. Histograms of the separation between the predicted and actual locations of SLDMBs in the MAB study area, shown as the number of endpoints (N) vs separation distance (km) at 3, 6, 12, and 24 hours. From left to right, the predicted positions are obtained by integrating observed CODAR velocities, STPS-predicted currents, velocities estimated using the Mariano climatology, and the LKP. These results were obtained using only drifter trajectories that were always inside the CODAR 90 percent availability line.

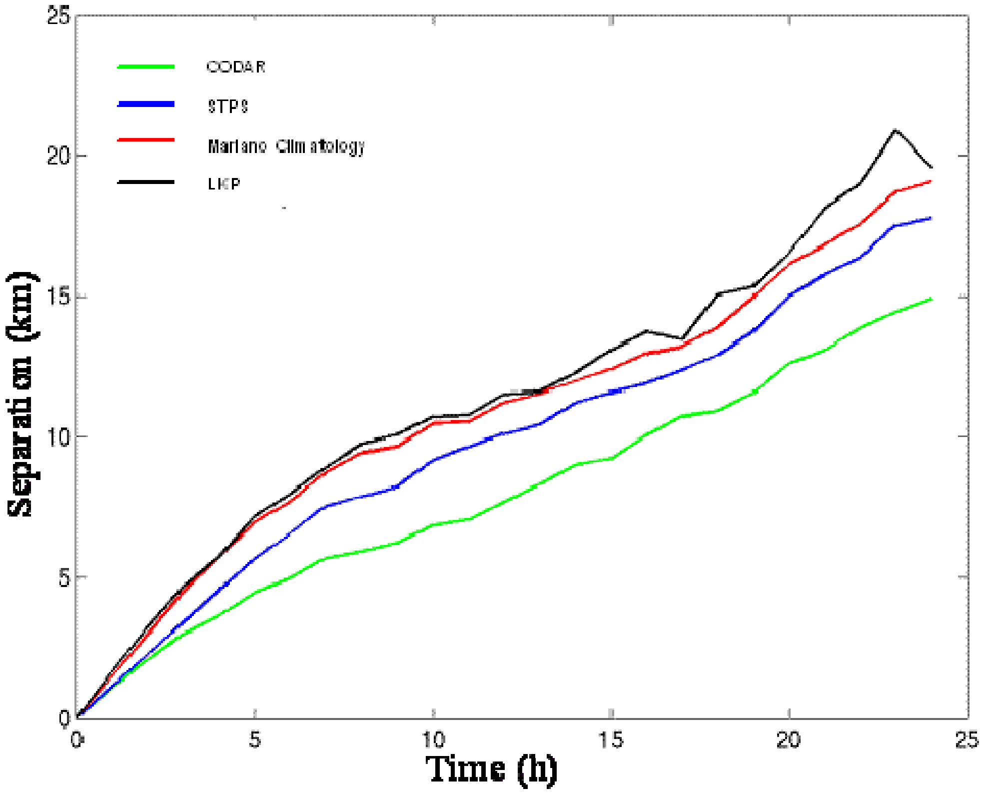

Figure 3-6. The evolution of the 95th percentile separation distance between drifters and simulated trajectories in the MAB based on CODAR data (green line), the STPS predictions (blue line), LKP (black line), and Mariano climatology (red line). These results were obtained using only drifter trajectories that were always inside the CODAR 90 percent availability line.

## 3.2. Block Island Sound SLDMB deployments

The four predictive approaches were applied to the BIS for the purpose of comparing their performance in a tidally-dominated region. The SLDMB deployments also included trajectories inside the area covered by the BIS CODAR system. Figure 3-7 shows the locations of the release points (red dots) of the drifters and the subsequent tracks (blue). Two obvious features of these trajectories deserve comment.

- The drifters launched in the northern half of the BIS moved to the east and exit the sound between Block Island and the Rhode Island shore. In contrast, those released in the southern half moved almost directly to the south between Montauk and Block Island into the Atlantic. Thus, knowing the initial position and the spatial structure of the circulation is critical to knowing where drifters will go.
- Within BIS, large reversals occur in the trajectories where the tidal currents are strong.

The drifter trajectories were divided into 24-hour segments overlapped by 12 hours, which resulted in a total of 140 independent sample tracks within the area monitored by the BIS CODAR system. The modified STPS was used to make 24-hour trajectory predictions to compare with the subsequent SLDMB tracks along with predictions based on actual CODAR data (without the MAB pre-processing steps) and the NOAA tidal current forecasts. Position difference from the LKP was used as a reference. In each case, the observed (SLDMB) and predicted (CODAR, STPS, NOAA Tide, and LKP) velocity fields were converted to trajectories using simple predictor-corrector integration combined with bi-linear interpolation of point velocity data at nearby locations to the locations of the drifters.

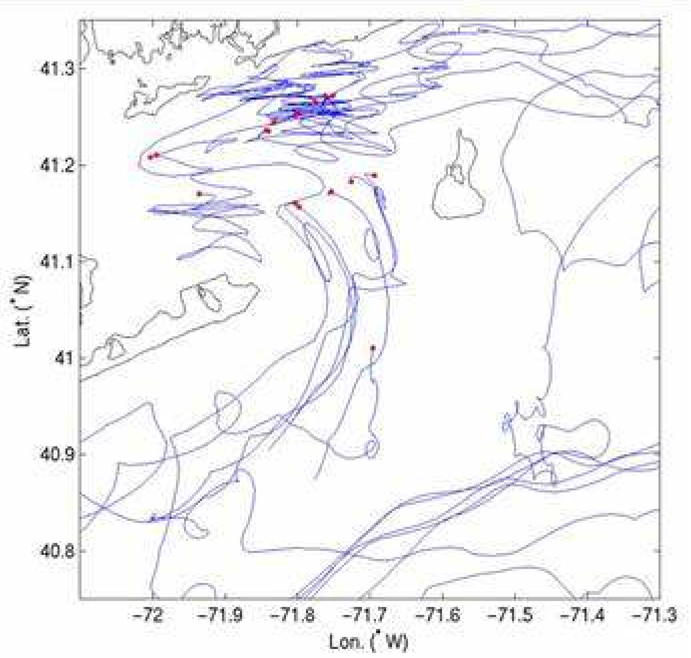

Figure 3-7. Deployment locations of SLDMBs (red dots) and their subsequent trajectories (blue lines) in BIS.

The distributions of position errors as represented by separation distances between observed and predicted drifter locations are shown at 3, 6, 12, and 24 hour forecast times in Figure 3-8. Separation distances between actual SLDMB locations and CODAR predicted locations are shown in the left column. The second column shows the separation distances between actual SLDMB locations and STPS predicted locations. Because the CG currently uses NOAA tidal current station information to estimate the drift of search targets in most of this area, the third column shows the separation distances between the SLDMB locations and predictions made using the NOAA information. (Note: data from the NOAA tidal station nearest to the position at the beginning time segment was applied for the duration of the 24-hour trajectory.) Finally, to evaluate the assumption that an object did not drift from its last known position (LKP), the right column shows the separation distances between the actual position of the drifter and its initial location estimate (LKP).

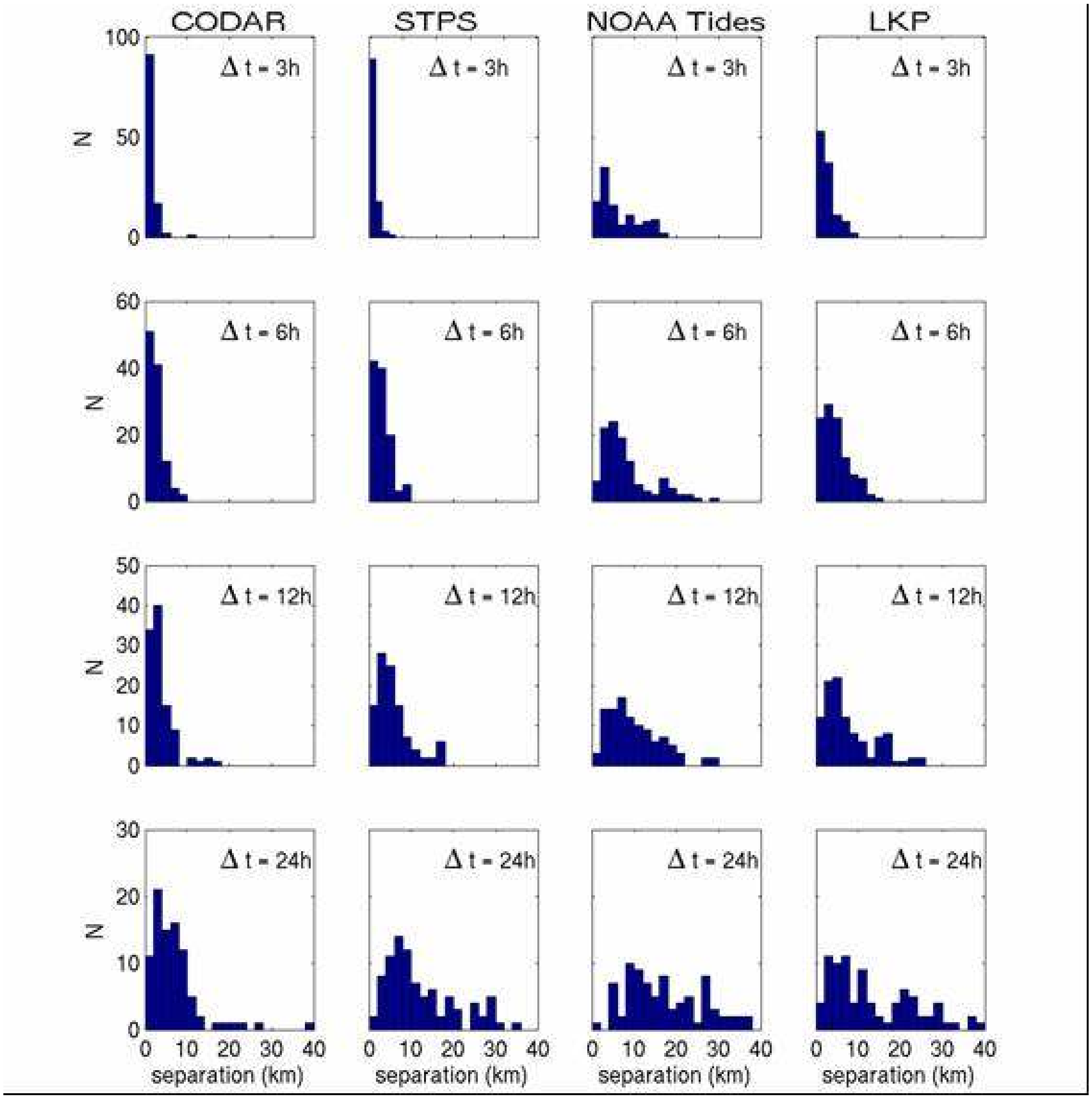

Figure 3-8. Histograms of the separation between the predicted and actual locations of SLDMBs in the MAB study area, shown as the number of endpoints (N) vs. separation distance (km) at 3, 6, 12, and 24 hours. From left to right, the predicted positions are obtained by integrating observed CODAR velocities, STPS-predicted currents, velocities estimated using the NOAA tides, and the LKP.

The NOAA tide and LKP separation histograms are more widely distributed, particularly as the prediction time increases, indicating that position errors will be larger for these approaches. The CODAR and STPS separation distance distributions show smaller separation distances (position errors), particularly within the first 6 hours, indicating that these approaches have higher predictive skill. At 3 and 6 hours, the separation distance is 0 to 2 km with almost all values less than 5 km for both the CODAR and STPS distributions. At 12 and 24 hours, the modal values increase to 4 km and the distribution of the STPS separations is obviously wider than that in the first column, reflecting the decrease in the predictive skill with increasing forecast time for STPS.

Figure 3-9 provides another view of the separation by showing the increase in the 95th percentile of each distribution in Figure 3-8 as a function of prediction time. The CODAR analysis trajectories and STPS predictions produce nearly equivalent separation distance (position errors) between 0 and 5 hours with an approximate RMS separation error of 5 km at 5 hours. On the other hand, the separation based on the NOAA tidal current predictions was approximately 20 km at 5 hours, a factor of 4 higher. Of the four methods, the NOAA tidal current predictions provided the least accurate estimate of drifter location. This result is partially due to the distance and position of the drifters relative to the nearest NOAA tidal station and because the NOAA tidal stations used for estimates were not updated during the drift. The no-motion drifter displacement (LKP) error is lower than the NOAA tides prediction with a separation of approximately 7.5 km at 5 hours but is less accurate than the STPS forecast. Beyond the 5-hour prediction time, the STPS prediction diverges from the CODAR-derived positions, and is much larger at the 24-hour prediction time. The separation distance in SLDMB positions associated with the use of CODAR data is approximately 16 km after a 24-hour period.

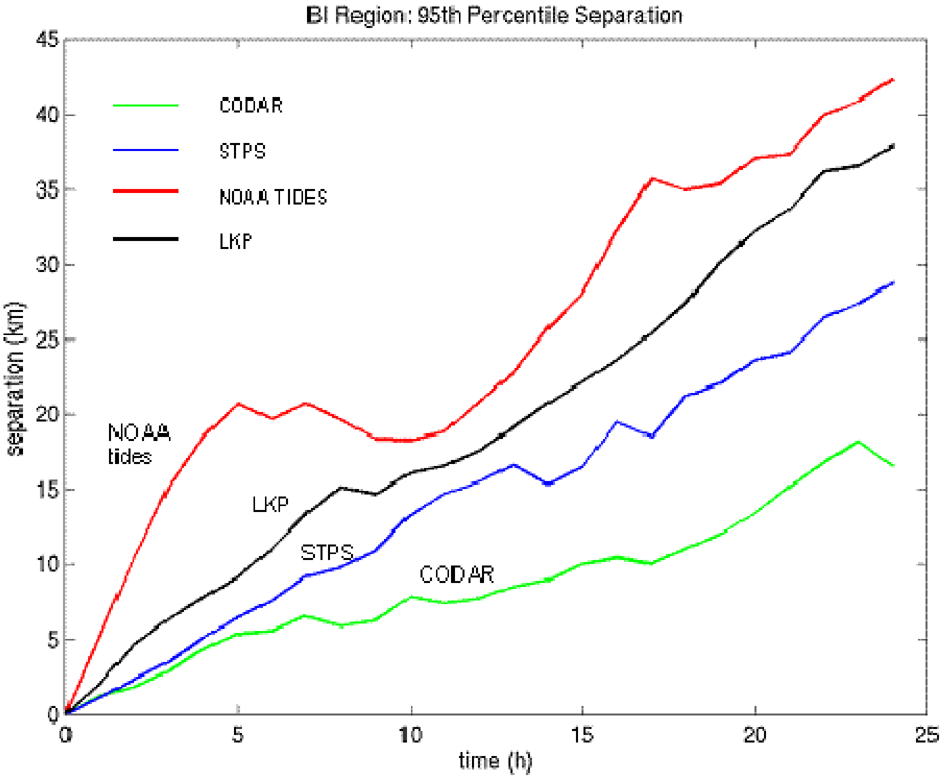

Figure 3-9. The evolution of the 95th percentile separation distance between drifters and simulated trajectories in the BIS based on CODAR data, the STPS algorithm, last known position (LKP), and NOAA tidal current predictions.

## 3.3. Summary of results

In both BIS and MAB, the CODAR systems provided the most accurate estimates of the four methods selected. This result validates the usefulness of CODAR, but is tempered somewhat by the fact that CODAR is a real-time observation and cannot be used as a predictive tool for these exercises. In both areas, the STPS produced larger separation distances than the CODAR analysis velocities and provided only a modest improvement in prediction accuracy over conventional methods. Use of the Mariano currents (standard CG procedure) in the MAB provided a prediction of SAR object drift that was functionally identical to the STPS. This result is reasonable because winds were relatively light over the period of the test. For the MAB, trajectory errors derived from CODAR data improved the skill of the prediction, reducing the separation error by 20 to 25 percent when CODAR data outside of the 90 percent availability line were not used for trajectory calculations. In BIS, trajectory predictions based on the NOAA tidal current predictions produced the largest prediction errors of any method. This is caused by the spatial variability of tidal currents in that area and because current estimates were used only from the closest operational NOAA station to the study area at the start of the period of drift. The signal processing and use of wind data in STPS did not improve or change its predictive skill in BIS.

CODAR therefore represented a modest improvement over the present Mariano current data tool in this area. The use of STPS produced only a minor improvement over those derived from the LKP and NOAA tidal current predictions. The incorporation of the MAB CODAR filtering algorithms produced the largest improvement in system accuracy.

# 4. OTHER FACTORS AFFECTING USABILITY OF CODAR AND STPS FOR SEARCH PLANNING

This section focused on the characterization of uncertainties in the surface current field using CODAR and STPS, and the subsequent incorporation of these parameters into trajectory simulations. Errors in the measurement of velocity at the sampling scale were considered. Dispersion due to surface water currents occurring at scales smaller than the sampling scale (i.e., turbulence) was also considered. Methods were developed to quantify the error and determine dispersion components of CODAR-derived velocities. Random walk (RW) and random flight (RF) Monte Carlo models were analyzed and compared. SLDMB trajectories were then modeled incorporating CODAR and STPS velocity data using both the RW and RF models.

## 4.1. Surface current dispersion

The motion of particles (including SAR drift objects) is caused by processes that vary over a wide range of scales. In SAR problems, for example, processes may be on the scale of the continental shelf or down to the scale of the SAR drift object itself. Because methods are not available to solve for motion at all scales simultaneously, it is still common practice (Taylor, 1921) to describe the velocity of a particle in terms of a mean field component and a turbulent component.

Surface current mapping radars such as CODAR can provide estimates of the mean field velocity at temporal scales of 1 hour and spatial scales of approximately 1.5 km and 6 km for standard-range and long-range systems, respectively. This radar-derived mean field velocity is subject to significant uncertainties and errors, which effectively constitute a separate 'error' component of the total velocity. The turbulent component of velocity incorporates velocity fluctuations on all scales smaller than the scale of the CODAR-derived mean field velocity. For a detailed description of these three components of the total velocity, see (O'Donnell, Ullman, Edwards, Fake, Allen, 2005) and Ullman et al, (2005)) Appendices C and D.

For reasons of practicality, the 'error' component of the total CODAR-derived velocity is combined with the turbulent component of the velocity. This combination is partly motivated by the fact that there is no easy way to separate the two components when comparing the radar-based mean velocity with similar estimates from drifters. This report will assume that this combined error plus the turbulent velocity component can still be described by models of turbulence, and it is treated as such in this study.

The dispersion of an array of drifters is the increase in mean separation of neighboring drifters over time due to the effects of turbulence and spatial gradients (shear) in the velocity field. To the first approximation, dispersion is defined in terms of the dispersion coefficient, $K$, the velocity variance, $\sigma^2$, and the autocorrelation time of the velocity field, $\tau$, according to the following equation (Csanady, 1973):

$$K = \sigma^2\tau .$$

The value of K chosen for a search case has a significant impact on the size of the containment area. As an example, results of a vertical person in the water (PIW) 3-hour drift using the RW Monte Carlo method and dispersion coefficients of 5 $m^2/s$ (the value originally recommended for the operational T&E) and 140 $m^2/s$ (Ullman's estimate based on data from the MAB region) were simulated during the operational test and evaluation (T&E). The results are shown in Figure 4-1. The containment area was 1.8 square nmi when $K$ was 5 $m^2/s$ and 34 square nmi when $K$ was 140 $m^2/s$.

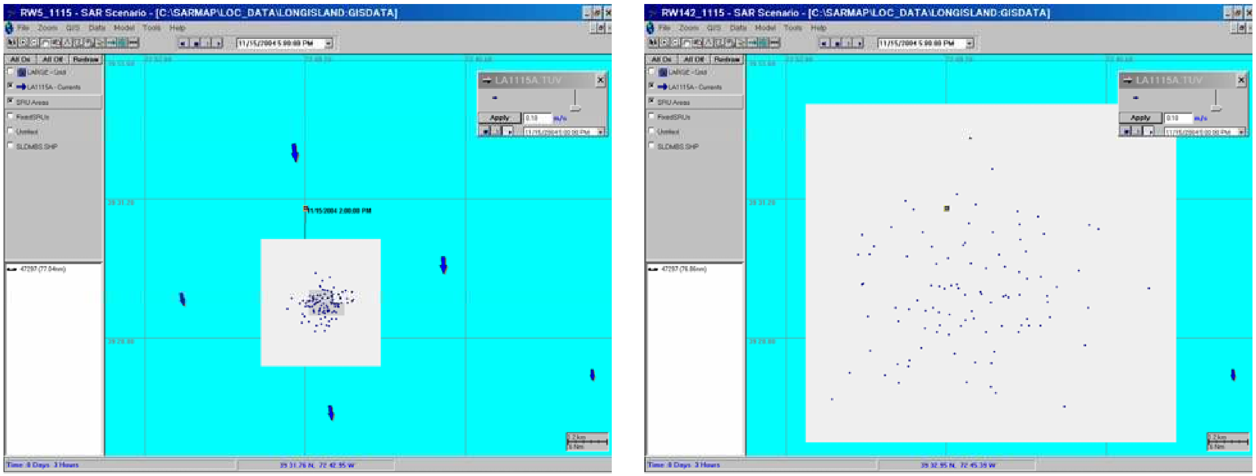

$K = 5$ $m^2/s$ $K = 140$ $m^2/s$

Figure 4-1. Containment areas resulting from different dispersion coefficients.

In practice, dispersion is difficult to measure directly. Several approaches were taken to quantify dispersion in the BIS and the MAB CODAR regions. The dispersion coefficient was estimated directly through analysis of the spread of individual clusters of SLDMBs with time. The dispersion coefficient can also be calculated as the product of the velocity variance and the velocity autocorrelation time. Dispersion coefficients were calculated in this way using variance computed for CODAR velocities and variance computed for the differences between CODAR and SLDMB velocities. Dispersion was also estimated retrospectively using the results of Monte Carlo simulations of SLDMB trajectories. These various methods resulted in estimates of the dispersion coefficient ranging from approximately 40 $m^2/s$ to 700 $m^2/s$ as reported in (Spaulding, Isaji, Hall, Allen, 2005) Appendix E. Ullman et al, (2005) used the variance of the difference between SLDMB and CODAR velocities (see Appendix B) to produce estimates of K for the BIS and the MAB regions that are presented in Table 4-1. This approach using differences between CODAR and SLDMB velocities is considered advantageous conceptually because it most closely characterizes the sub-grid scale velocity field and includes the measurement error from the CODAR system.

Table 4-1. Summary of Dispersion Coefficients *K* for BIS and MAB regions calculated using the variance of the difference between SLDMB and CODAR velocities in the BIS and the MAB regions.

| Region | *K*–East-West ($m^2/s$) | *K*–North-South ($m^2/s$) | *K*–Average ($m^2/s$) |
|---|---|---|---|
| BIS | 110 | 80 | 90 |
| MAB | 120 | 160 | 140 |

## 4.2. Monte Carlo characterization of dispersion

The random walk characterization of surface current dispersion is based on the assumption that the non-tidal residual component of the surface current vector is randomly distributed. This process adds random noise to the surface current vector fields to reproduce the effects of dispersion. This method is easily implemented and has seen frequent use in past Monte Carlo search planning tools. In the Random Flight characterization of surface currents, dispersion is modeled by drawing values that are random, yet are partially dependent on the previous value of the surface current vector. Each new vector calculated by the RF approach is therefore partially correlated with the previous value. As new vectors are calculated on succeeding time steps, positions at later time steps become less dependent on earlier values. The system "decorrelates", approximately at an exponential rate with the number of time steps. The characteristic time corresponding to that exponential decay rate, is referred to as the "e-folding" time or autocorrelation time.

In practice, the RW model treats dispersion through the dispersion coefficient, *K*. The RW approach handles dispersion ($S^2$), or the mean squared separation of particles, as linear growth with time (t) at the rate $S^2 = 2Kt$. With the RF model, for a given value of dispersion, the mean squared particle separation grows at a slower rate of time, $S^2 = 2Kt - 2KT(1-e^{-t/T})$, where T is the characteristic autocorrelation time of the velocity field (Spaulding et al, 2005). For a given K, the dispersion of a particle field predicted by the RW approach will be larger than one predicted by the RF approach. For detailed methodologies of these models, also see Griffa (1996) or Berloff and McWilliams (2002).

A comparison of analytical solutions for the RW and RF models shows that for a given value of *K*, the RW model results in more dispersion (and a larger predicted search area) than the RF model (Figure 4-2). This difference is particularly pronounced at times shorter than the velocity autocorrelation time (T=3 hr). During this period, the size of the search area predicted by the RW model increases more rapidly than the size predicted by the RF model. At times greater than the velocity autocorrelation time, the search areas predicted by the two models increase at the same rate.

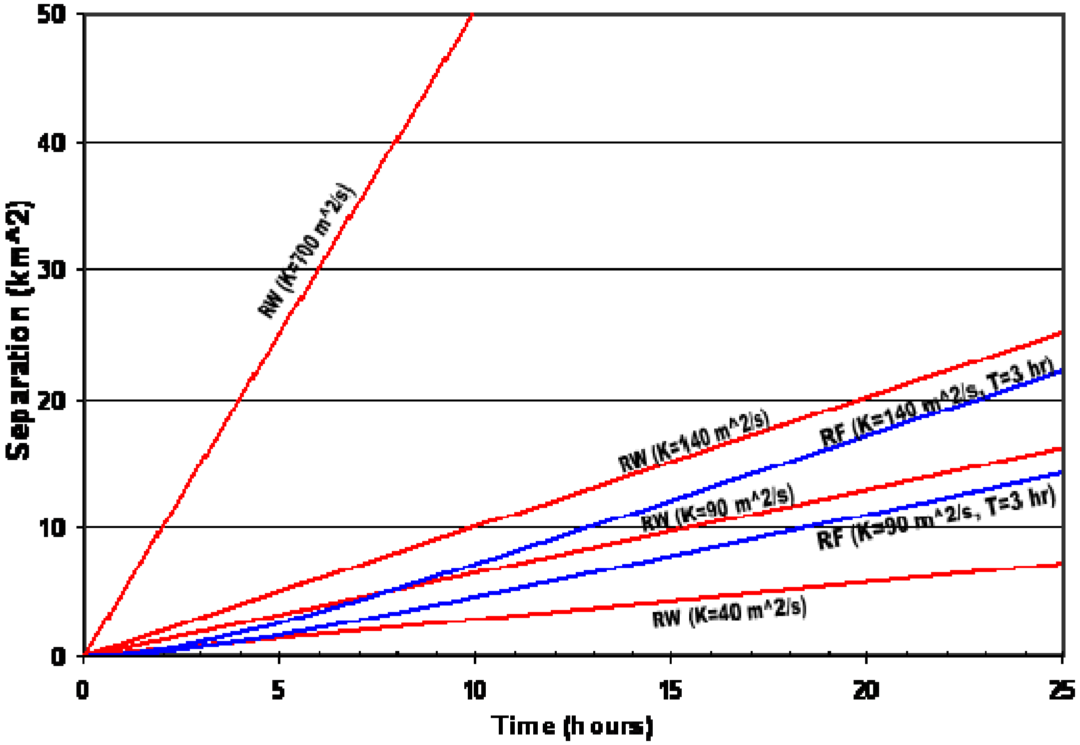

Figure 4-2. Analytical solution of predicted search areas (separation) as a function of time for the RW and RF models. The difference in search areas predicted by the two models is small relative to the overall range of potential search areas due to uncertainty in K. For example, RW and RF separation initially increases, but levels off at a constant value for a given K.

While the RF approach is conceptually better, the difference between the search areas obtained from RW and RF models is small relative to the difference resulting from uncertainty in dispersion (*K*). The value selected for K emerges as the critical factor in defining the size and growth of the search area in a SAR case. Figure 4-2 therefore underscores the significance of having a representative value of K for SAR planning. If K is overestimated, the search area will be too large, resulting in a waste of search effort. If K is underestimated, the search area will be too small, increasing the probability that the search object will be outside of the search area and increasing the potential that the search object will not be found.

## 4.3. Monte Carlo simulation results

Simulations were conducted to evaluate the ability of the two Monte Carlo models to predict search areas using CODAR and STPS velocity data in conjunction with the dispersion parameters obtained from this study (using the East-West and North-South dispersion coefficients for BIS and MAB in Table 4-1). Search areas were predicted for the individual 24-hour BIS SLDMB trajectories. A total of 159 independent drifter trajectories were modeled in the MAB; 72 drifter trajectories were modeled in the BIS. Figure 4-3 shows an example of an actual SLDMB trajectory with a predicted search area derived from pseudo-drifter trajectories derived from a RF simulation. The 95 percent containment region (predicted search area) was estimated by computing a two-dimensional histogram of the pseudo-drifter locations, sorting the spatial bins based on the number of pseudo-drifters contained, and then summing over the bins until 95 percent of the total was obtained. This approach allowed the containment area to be more closely tailored to the distribution of the modeled pseudo-drifters than a simple circular area would be. The performance of the RW and RF approaches was compared by calculating the percent of cases when the actual SLDMB was located in the predicted search area between 1 and 24 hours. If the SLDMB was located within the predicted search area (defined as the 95 percent containment region), the prediction was considered a success.

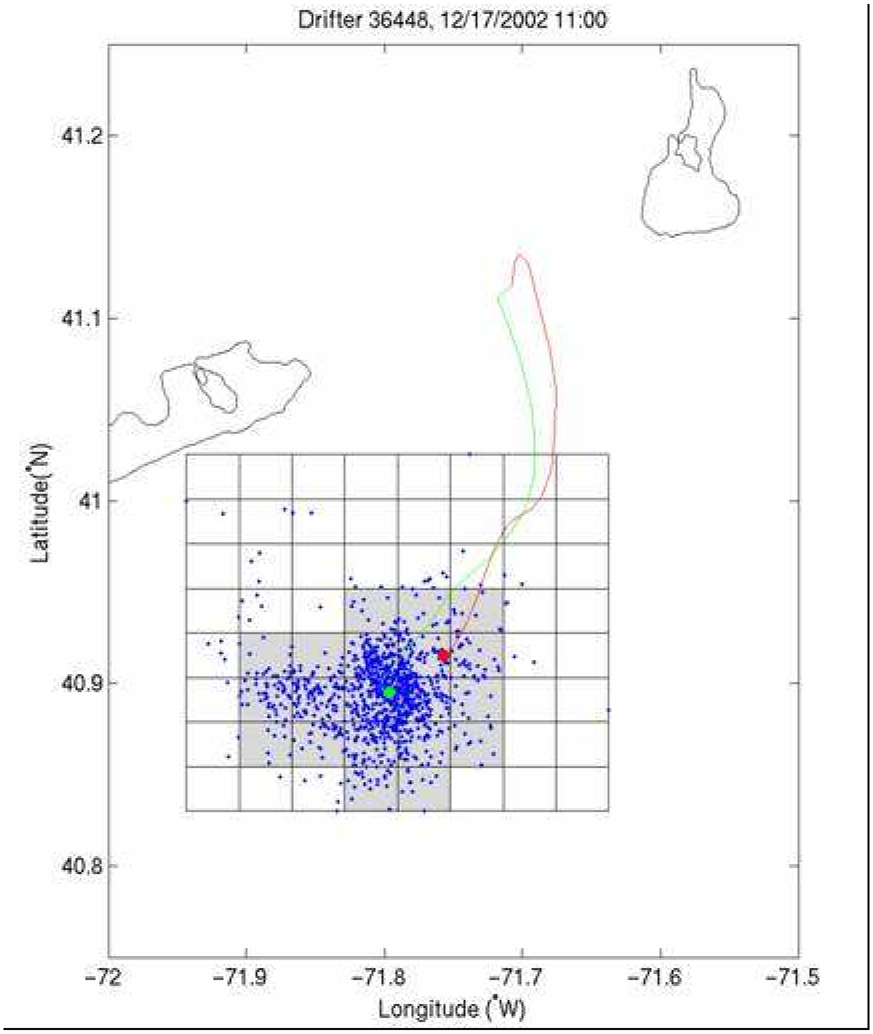

Figure 4-3. Illustration showing actual 24 hr SLDMB track (red) and predicted drifter trajectory (green). Small blue dots represent the positions of the individual particles used in a series of Random Flight Monte Carlo simulations. The 95 percent containment region is shown as gray-shaded rectangles.

Using the drifter trajectories described above and corresponding CODAR data, Ullman et al, (2005) calculated dispersion coefficients for RF and RW trajectory simulations in BIS and MAB. The dispersion coefficients were based on the variance and autocorrelation times of the nontidal velocity plus measurement error time series. Ullman et al, (2005) found that the area containing

95 percent of SLDMB trajectories predicted by the RF approach contained drifters with a probability of about 90 percent. On the other hand, a much smaller 95 percent containment area was predicted by the RW approach that contained the drifter in only 60 percent to 80 percent of the cases. The disparity was attributed to an underestimate of the autocorrelation time estimate used for K in the RW calculations. When K was changed to a value consistent with the one used for the RF simulations, the two approaches provided consistent results (Figure 4-4), particularly at times greater than the velocity autocorrelation time. This behavior was demonstrated in the analytic solutions for the two models (Figure 4-2).

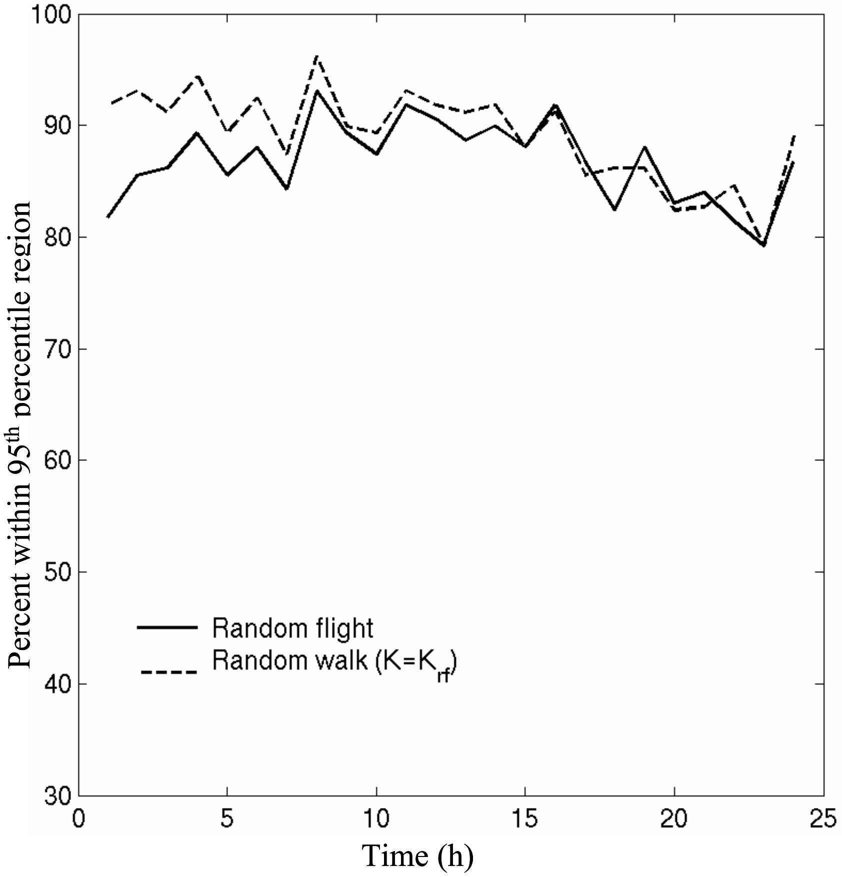

Figure 4-4. A comparison of RW and RF Monte Carlo simulation results for the MAB region. For each hourly prediction time, the percent of cases where the actual drifter location at that time fell within the estimated 95 percent confidence region is plotted.

## 4.4. Discussion of Monte Carlo modeling results

The Monte Carlo exercises were somewhat inconclusive in that there was some disagreement over the relative merits of the Random Walk and Random Flight approaches. For short Search Action Plan drifts (i.e., on the order of the autocorrelation time), the RW model produced a larger predicted search area than the RF model and consequently was more likely to contain the target. As drift times lengthen, the relative difference in predicted search area between the two models decreased, and the performance of the two models was approximately equivalent.

The overarching issue, however, appears to be that the value selected for K exerts a major influence on the outcome of the initial search area that would be estimated. Values of K between 40 to 700 $m^2/s$ produced separation estimates from 7 to 120 square kilometers in 24 hours, based upon Spaulding et al, (2005) (Appendix E), equation 4 (RW Separation area = 2 x K x time). Using the difference between SLDMB and CODAR velocities in the BIS region, *K* was estimated to be 90 $m^2/s$. In the MAB region, *K* was estimated to be 140 $m^2/s$. Thus, the separation area after 24 hours of drift for the BIS area is expected to be 16 square kilometers and 24 square kilometers for the MAB region.

The most practical ways to estimate *K* are determining the dispersion parameters (i.e., velocity variance and autocorrelation time) from CODAR velocity data, SLDMB velocity data, or from the difference between CODAR and SLDMB velocities. Using the difference between CODAR and SLDMB velocities most closely characterizes the sub-grid scale velocity field and includes the measurement error from the CODAR system. While analyzing the dispersion of the individual SLDMB clusters is the most direct way to measure dispersion, this process is problematic in that large numbers of SLDMBs (i.e., on the order of 10) need to be deployed and allowed to drift for a significant period of time in order for the resulting statistics to be truly robust. Completing this task for the CG's area of responsibility would be a large task.

Dispersion parameters vary both spatially and temporally, and the degree to which dispersion parameters can be usefully differentiated depends on both the spatial and temporal density of data used to estimate them. Improved estimates of dispersion, including the possibility of some spatial refinement, can be achieved incrementally through additional SLDMB deployments. A system could be established to catalog SLDMB and CODAR data for individual CODAR regions. By maintaining a database with all SLDMB trajectories through a given CODAR region, along with concurrent CODAR velocities, estimates could be refined as necessary in the future. Calculations could be performed on a periodic basis (e.g., annually). As new data are added to the calculations, the accuracy of the estimates of K would approach their representative mean values over a period of several years.

(This page intentionally left blank.)

# 5. EXTENSION OF THE PROTOTYPE SAROPS ENVIRONMENTAL DATA RETRIEVAL SUBSYSTEM TO EXTRACT STANDARD CODAR DATA FIELDS AND THEIR ASSOCIATED STPS FORECASTS

## 5.1. Prototype SAROPS EDS

SAROPS is the new CG SAR system currently being developed by Northrop Grumman, Applied Science Associates (ASA), and Metron. SAROPS contains three main components: ArcGIS/Commercial Joint Mapping Tool Kit (CJMTK)-based graphical user interface (GUI), Environmental Data Server (EDS), and Simulator engine that performs the particle motion and search optimization.

At the time of this project, SAROPS was still under development; the alpha version of SAROPS was delivered in March 2005, and final release is not expected until 2006. As a replacement for the SAROPS application, a modified version of SARMAP, a commercially available SAR application used by international CG agencies, was substituted. SARMAP includes geographic information system (GIS)-based tools for developing SAR cases, gathering and entering environmental data, running International Aeronautical and Maritime Search and Rescue (IAMSAR) or Monte Carlo simulations, visualizing SAR results, and adding Search and Rescue Unit (SRU) patterns.

Even though SAROPS was not available, a preliminary version of the SAROPS EDS was available for evaluation. SARMAP was customized to connect to the EDS to access environmental data. This connection enabled evaluation of the SAROPS client communications with the EDS by using the modified SARMAP software as a proxy for SAROPS.

Primary data served by the EDS are current and wind data. Additional environmental parameters are expected to be available in the future. Environmental data are based on the SAR case information. SAROPS determines the area of interest (AOI) and time of interest before making a request to the EDS for data (currents and winds) that meet the AOI and time of interest.

The initial developmental prototype EDS version retrieved, archived, and distributed data from NOAA PORTS sites, NOAA CO-OPS, selected NDBC stations, and selected New England USGS river gauges. As part of the continuing SAROPS development effort, the EDS was modified to add CODAR and SLDMB data. The EDS is made up of two main components: a catalog server and an EDS Web server.

### 5.1.1. Catalog server

The catalog component of the EDS contains the data sources available to the EDS. Both HyperText transfer protocol (HTTP) and file transfer protocol (FTP) were required to retrieve information from the data sources. The significant information contained in the catalog are:

- Geographic extent of the data source,
- Time window of data available for a data source, and
- Structure and format of the source files.

On a routine basis, based on source data update frequency, the catalog server retrieves data from different sources and makes these data available to the SAROPS user. As new data are collected and stored, the catalog is updated to reflect the most recent "time-stamp" of available data. Archives are kept so that SAROPS users can retrieve up to six months of historical data for case reconstruction.

Environmental data are highly heterogeneous; data providers supply their data in a variety of formats. In some cases, the catalog server converts the incoming data to make access and archiving simpler and to provide compatibility with common units, coordinates, etc.

The modified EDS collects and distribute four data products:

- UCONN CODAR and STPS data
  The EDS catalog retrieved the BIS CODAR and STPS files on an hourly basis from the UCONN server using FTP and stored files on the EDS.
- Rutgers CODAR and STPS data
  The EDS catalog retrieved the MAB CODAR files on an hourly basis from the Rutgers server using FTP and stored files on the EDS. The MAB STPS files were retrieved on an hourly basis from the UCONN server-using FTP, and files were stored on the EDS.
- Selected northeast NDBC wind station data
  The catalog stored uniform resource locator (URL) information for selected NDBC stations (Table 5-1) and collected the data using HTTP on an hourly basis, parsed the HyperText markup language (HTML) data, and appended data for each station into a delimited text file.

Table 5-1. NDBC stations accessed by prototype EDS.

| NDBC Station List |
|---|
| 44004 – HOTEL |
| 44005 – GULF OF MAINE |
| 44007 – PORTLAND, ME |
| 44008 – NANTUCKET |
| 44009 – DELAWARE BAY |
| 44011 – George's Bank |
| 44013 – BOSTON, MA |
| 44017 – Montauk Point, NY |
| 44018 – SE Cape Cod |
| 44025 – LONG ISLAND |
| 44027 – Jonesport, ME |
| ABAN6 – Alexandria Bay, NY |
| ALSN6 – Ambrose Light, NY |
| BUZM3 – Buzzard's Bay, MA |
| IOSN3 – Isle of Shoals, NH |
| MDRM1 – Mt Desert Rock, ME |
| MISM1 – Matinicus Rock, ME |
| SUPN6 – Superior Shoals, NY |
| THIN6 – Thousand I Bridge, NY |
| TPLM2 – Thomas Point, MD |

- SLDMB tracks (from Operations System Center (OSC) Martinsburg).
  The catalog retrieved the latest SLDMB tracks from an American Standard Code for

Information Exchange (ASCII) comma-delimited text file stored on an FTP site at OSC Martinsburg.

The EDS version implemented for this project is the first draft (alpha) of the EDS that will be installed for the SAROPS project. Evaluation of the EDS shows that the use of Network Common Data Form (NetCDF) as a data transport format is quite efficient and also allows the EDS to transition to use of Open-source Project for a Network Data Access Protocol (OPeNDAP) in the future. There are many issues involved in the long-term evolution and improvement of the EDS including:

- Server side filtering (spatial and temporal) based on user data requests;
- Server side aggregation to combine data across space and time;
- Server side quality assurance/quality control (QA/QC) processes; and
- Server side data blending, objective analysis, and data assimilation techniques.

### 5.1.2. EDS Web Services

The EDS Web services (.NET based) wait for requests from the SAROPS client. The requests come in eXtensible Markup Language (XML) format through Simple Object Access Protocol (SOAP). When a request is received for meteorological and oceanographic data for a particular area of interest (AOI) and time of interest, the Web service processes the appropriate data from the catalog and returns data to the SAR client. A schematic of this process is included in Figure 5-1. The modified EDS Web services manage the following: CODAR/STPS, NDBC winds, and SLDMB data.

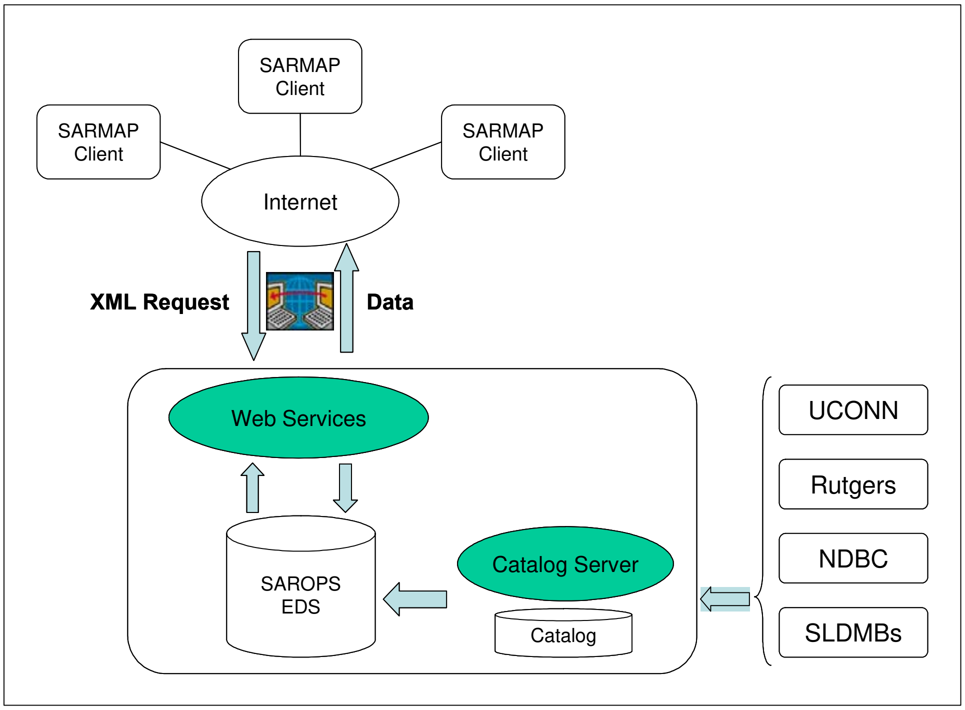

Figure 5-1. Schematic of SARMAP (SAROPS) clients connecting to EDS for environmental data needs.

## 5.2. CODAR/STPS

A user requesting water current data from the EDS can select from one of three choices as shown in Figure 5-2.

- CODAR
  This process gives the user the "best" available data by combining the latest available CODAR (observation) data with STPS data for a forecast period. Although these data are uniform, the operational test and evaluation (T&E) users noted that this solution did not allow them to know whether a particular time step was represented by CODAR (actual observation) or STPS (forecast). As a result, the users were uncertain as to how much confidence to put in the results.
- CODAR RAW
  This process gives the user only CODAR data and does not fill any gaps with STPS or provide STPS forecast data.
- STPS
  This process gives the user only STPS data; no actual CODAR observation data are used.

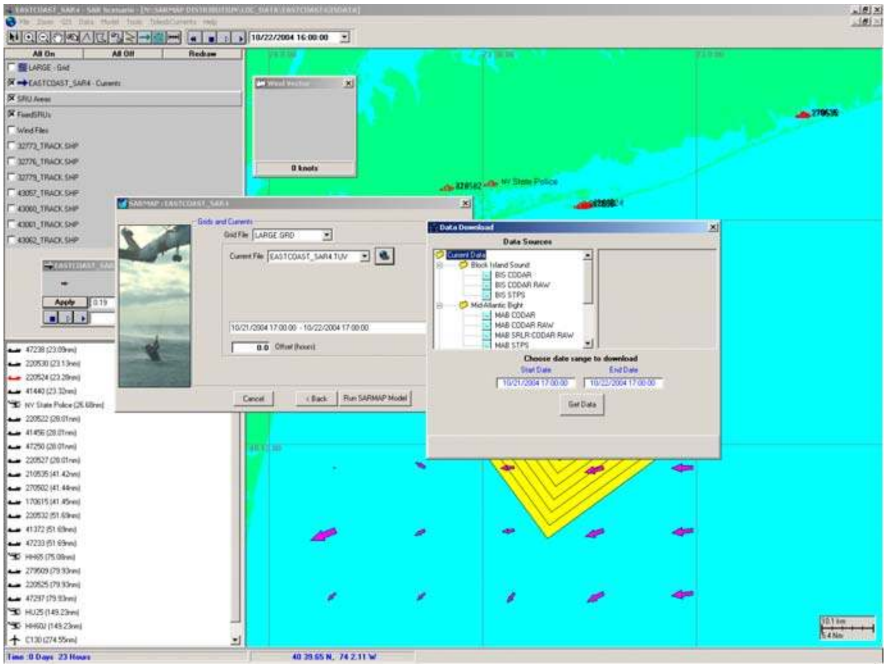
Grid File: LARGE.GRD
Current File: EASTCOAST_SAR4.TUV
10/21/2004 17:00:00 - 10/22/2004 17:00:00
0.0 Offset (hours)
Start Date: 10/21/2004 17:00:00
End Date: 10/22/2004 17:00:00

Figure 5-2. Example SARMAP Graphical User Interface (GUI) connecting to EDS for user selection of environmental data.

## 5.3. NDBC winds

In response to a user request for wind data, the EDS provides a list of NDBC wind stations in the region (Figure 5-3). The user selects a wind station, and the wind time series for a SAR case is automatically loaded from the NDBC data.

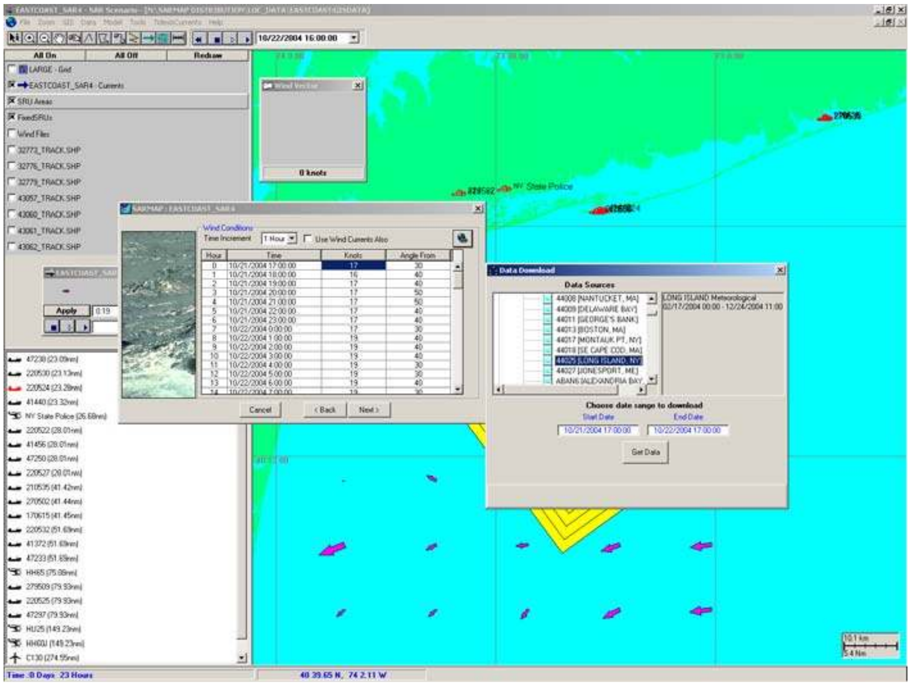

Wind Conditions

Time Increment: 1 Hour ☐ Use Wind Currents Also

| Hour | Time | Knots | Angle From |
|---|---|---|---|
| 0 | 10/21/2004 17:00:00 | 17 | 30 |
| 1 | 10/21/2004 18:00:00 | 16 | 40 |
| 2 | 10/21/2004 19:00:00 | 17 | 40 |
| 3 | 10/21/2004 20:00:00 | 17 | 50 |
| 4 | 10/21/2004 21:00:00 | 17 | 50 |
| 5 | 10/21/2004 22:00:00 | 17 | 40 |
| 6 | 10/21/2004 23:00:00 | 17 | 40 |
| 7 | 10/22/2004 0:00:00 | 17 | 30 |
| 8 | 10/22/2004 1:00:00 | 19 | 40 |
| 9 | 10/22/2004 2:00:00 | 19 | 40 |
| 10 | 10/22/2004 3:00:00 | 19 | 40 |
| 11 | 10/22/2004 4:00:00 | 19 | 30 |
| 12 | 10/22/2004 5:00:00 | 19 | 30 |
| 13 | 10/22/2004 6:00:00 | 19 | 40 |

Data Download

Data Sources

44008 [NANTUCKET, MA]
44009 [DELAWARE BAY]
44011 [GEORGE'S BANK]
44013 [BOSTON, MA]
44017 [MONTAUK PT, NY]
44018 [SE CAPE COD, MA]
44025 [LONG ISLAND, NY]
44027 [JONESPORT, ME]
ABAN6 [ALEXANDRIA BAY

LONG ISLAND Meteorological
02/17/2004 00:00 - 12/24/2004 11:00

Choose date range to download

Start Date: 10/21/2004 17:00:00

End Date: 10/22/2004 17:00:00

Figure 5-3. Example SARMAP Graphical User Interface (GUI) connecting to the EDS for user selection of NDBC wind data.

The NDBC data are stored on the EDS as Coastmap Text Format (CTF) files, are parsed for the time of interest, and then returned to the client as a binary wind file (.WNE). The CTF file format is a flexible space-delimited test format useful for storing time series data (e.g., wind speed and direction, tide height, water temperature) for a single geographic location. Metadata are included in the file header, and all data at a given time are listed on single lines with a date and time stamp.

## 5.4. SLDMB data

In response to a user request for SLDMB data, the EDS processes the ASCII file containing all of the SLDMB locations in near real time and returns an Environmental Systems Research Institute, Inc. (ESRI) shape (SHP) file containing the buoy tracks for the time of interest. This SHP file is then displayed on the SARMAP chart/map.

## 5.5. Conclusions on extension of the prototype SAROPS environmental data retrieval subsystem

This task demonstrated that it will be possible for the SAROPS EDS to collect and distribute CODAR current data and STPS current predictions from UCONN and Rutgers, wind observations from NDBC buoy sites, and SLDMB data from OSC Martinsburg. It will also be possible for remote users to request and download these data in near real-time for use in Search Action Plans (SAPs).

(This page intentionally left blank.)

# 6. OPERATIONAL TEST AND EVALUATION

CODAR and STPS forecasts offer greater temporal and spatial resolution than those used in C2PC/CASP/joint automated worksheets (JAWS) software and may be useful in developing SAPs that confine searches to smaller areas and increase the probability of success (POS).

During the operational T&E, controllers had the opportunity to compare SAP data developed from CODAR/STPS current data with comparable data from C2PC/JAWS. They also had opportunities to provide suggestions for improvements to CODAR/STPS products and the software that accessed these products.

The two objectives of the 30-day operational T&E were:

1) Validate the utility of using near-real-time CODAR and STPS forecast data interpolated to a small geographic area to develop a search action plan, and
2) Assess the level of confidence that CG operations personnel (i.e., controllers) have in using CODAR/STPS data to develop a search action plan.

## 6.1. Test description

CG Group Moriches (GRUMOR) hosted the operational T&E. Operations Center (OPCEN) controllers were trained on the use of the modified SARMAP software and its wind and data retrieval functions to access the EDS where CODAR/STPS data are posted. All Group controllers participated during the 30-day evaluation period by accessing CODAR/STPS data to execute simulated test cases, complete data forms, and share their comments and suggestions during interviews with the test observer.

Pretest training was provided from 20-31 October 2004 on an ad hoc basis at times convenient to the controllers. Each controller received approximately four hours of one-on-one instruction during the initial week of training. During the first week of the operational T&E, additional follow-on training was conducted to ensure that the controllers were using the software correctly, had no questions, and understood their roles during the test period.

The operational T&E was conducted from 1-29 November 2004. During this period, four separate predefined six-hour observation/interview sessions were conducted by a test observer/data collector.

During the operational T&E, the following three SLDMBs were deployed as illustrated in Figure 6-1 to provide simulated zero-leeway search objects.

1) #38968 on 27 October 2004 at 041° 07.00′ N, 071° 42.00′ W.
2) #38708 on 3 November 2004 at 040° 37.90′ N, 072° 28.90′ W.
3) #39001 on 18 November 2004 at 040° 26.23′ N, 073° 18.18′ W.

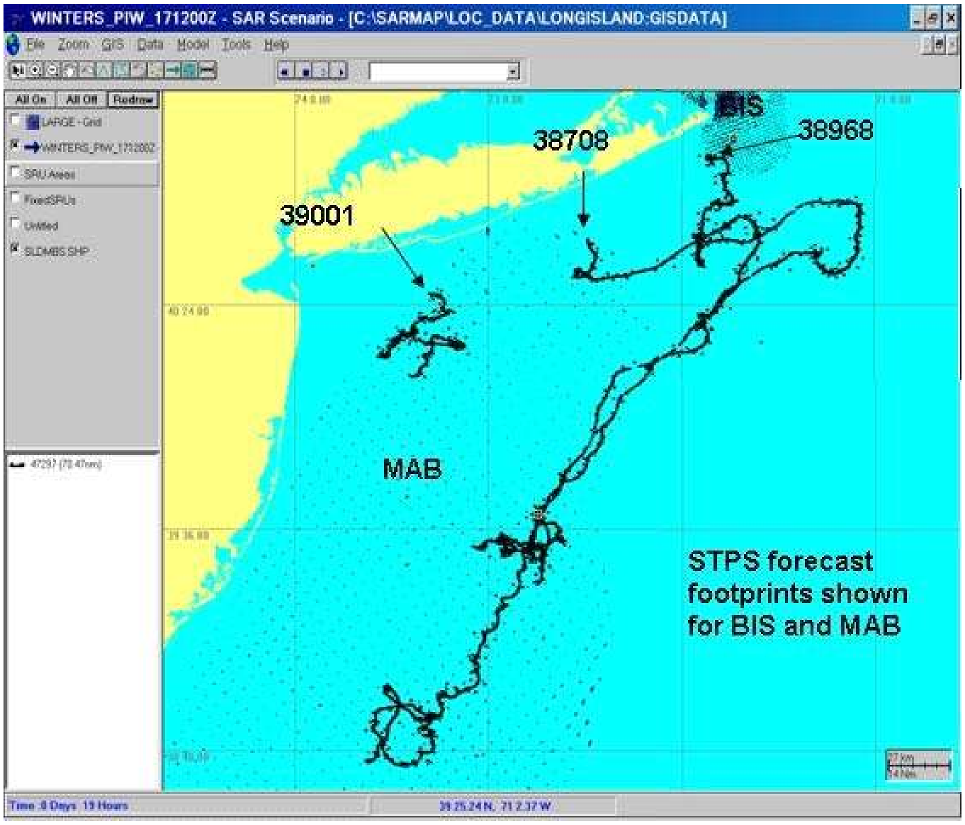

Figure 6-1. Three SLDMBs deployed as targets.

SLDMB #38968 stayed in the BIS CODAR region from 27–31 October, drifted south then east during a period of high wind, and continued southwest until it entered the MAB region on 15 November. SLDMB #38968 then remained in the MAB region for the duration of the test. SLDMB #38708 remained on the northeast edge of the MAB region from 3–5 November, then drifted east during a period of high wind, continued southeast until it re-entered the MAB region on 14 November, and then remained in the MAB region for the duration of the test. SLDMB #39001 remained on the northern border of the MAB region from its deployment on 18 November throughout the operational T&E period.

GRUMOR OPCEN was contacted once per shift and supplied with simulated case data that could be used to exercise the modified SARMAP software and the C2PC/JAWS software. The data were developed from the SLDMB data and specified the target, the Greenwich Mean Time (GMT) of the LKP to be used, the latitude/longitude of the LKP, and the length of time of the drift for the test case.

All watchstanders were asked to run the simulated case twice, once using modified SARMAP and once using C2PC/JAWS. They were requested to archive all computer-generated files required by the modified SARMAP software so that the cases could be reconstructed following the test, and to save case summaries in text file format from both the C2PC/JAWS and the modified SARMAP software. After running a simulated SAR case, and waiting for the SLDMB trajectory for the time period of interest to be completed, the controller could access the SLDMB data to determine the accuracy of the modeled containment area.

In addition, controllers were also asked to use SARMAP to develop a search action plan for any actual offshore SAR cases that developed during their watch. These cases could be run whenever it was convenient. As it turned out, there were no cases appropriate to this purpose during the operational T&E period.

## 6.2. Controller feedback

In general, the GRUMOR controllers were positive and enthusiastic about accessing CODAR/STPS data using the modified SARMAP software. Collected feedback is presented in Table 6-1.

Table 6-1. Controller feedback.

| Feedback Applicability | Feedback |
|---|---|
| Modified SARMAP | Simple to use.<br>Requires fewer clicks of the mouse; clickable functions save time.<br>There are fewer data to input. |
| CODAR/STPS data | Not appropriate for surf-zone SAR cases.<br>MAB and BIS regions do not provide sufficient coverage for the GRUMOR area of responsibility (AOR).<br>CODAR data encompassed the target intermittently because the size and shape of the CODAR coverage area varied with time.<br>It is impossible to tell if the displayed current data are from CODAR or from STPS. |
| Wind data | When predicted wind is applied to STPS forecast current data, it is also inappropriately applied to CODAR currents. |
| Current data | Cannot mix CODAR analysis with tidal predictions or datum marker buoy (DMB) data with STPS forecasts. |
| Search area results | The SARMAP containment area is small compared with the C2PC/JAWS Total Probable Error (TPE).<br>The target was not always contained in the containment area. |
| Display | The ability to view the object drift on the map and display the surrounding current vectors are good features. |
| Modified SARMAP/EDS interaction | When the incident site is outside of a CODAR analysis coverage area, the software should let the user know that the data may not be appropriate.<br>Modified SARMAP uses the four nearest vectors (regardless of how far away they are) to define the current field. |

## 6.3. SAROPS and EDS interaction

Decision automation was an item of particular interest. The controllers recommend that the SAP software should suggest an NDBC station, a CODAR analysis area, and parameter values (such as dispersion, safety, and drift) based on the incident location to be used as input to the SAP processing. At the same time, they pointed out that C2PC/JAWS currently allows them to select and view the NDBC buoy to ensure that it is operational and that the data from the buoy are in the expected range before the data are imported to the SAR software.

## 6.4. Test case comparisons

### 6.4.1. STPS forecast versus CODAR analysis

The procedures described in Section 6.1 yielded 47 test cases for evaluation. All test cases were later reviewed to compare separation distances to the SLDMB drifter when the different models were used and to associate the quality of the modified SARMAP results with the proximity to valid CODAR/STPS data. Watchstander workloads during the tests precluded an accurate comparison of the two models. Time expended accessing the SLDMB data, developing case parameters, reporting the case to the OPCEN, and executing the case at an opportune time often caused cases to be run later in or after the STPS prediction period. Once the prediction time became a CODAR observation, STPS values for that time were overwritten as CODAR data and a new set of STPS values were created. When this occurred, these cases were based only on CODAR data and not on any STPS predictions, preventing an accurate comparison of the two approaches.

Some cases were based on time periods when the target SLDMB was not in the CODAR/STPS data coverage area. For most of the cases, the target SLDMB was in the area, but the CODAR data coverage area only intermittently included it. This was because returns measured from the HF radar sensors propagate in the atmosphere inconsistently, especially at night and cause the reported current field size to vary by the hour. The STPS forecast data, based on averaged CODAR data, has a larger area of consistent coverage.

### 6.4.2. CODAR/STPS versus C2PC/JAWS comparisons inside the CODAR/STPS coverage area

Eleven simulated SAR cases were completely inside the CODAR analysis/STPS forecast area. The International Aeronautical and Maritime Search and Rescue (IAMSAR) model was used to match the C2PC/JAWS model currently used at GRUMOR. Note: One case is included twice (once for STPS, and once for CODAR). Modified SARMAP predictions from these cases were compared with C2PC/JAWS predictions. Results are shown in Figure 6-2. Statistical parameters are provided in Table 6-2. The average ranges (separation distances) from the centers of the left and right IAMSAR-modeled position estimates to the SLDMB positions at the ends of the drifts was 1.3 nmi when the modified SARMAP with CODAR/STPS data were used compared with 2.8 nmi when C2PC/JAWS was used. More variability was also evident using the C2PC/JAWS model: 11.0 nmi compared with 1.4 nmi (SARMAP value).

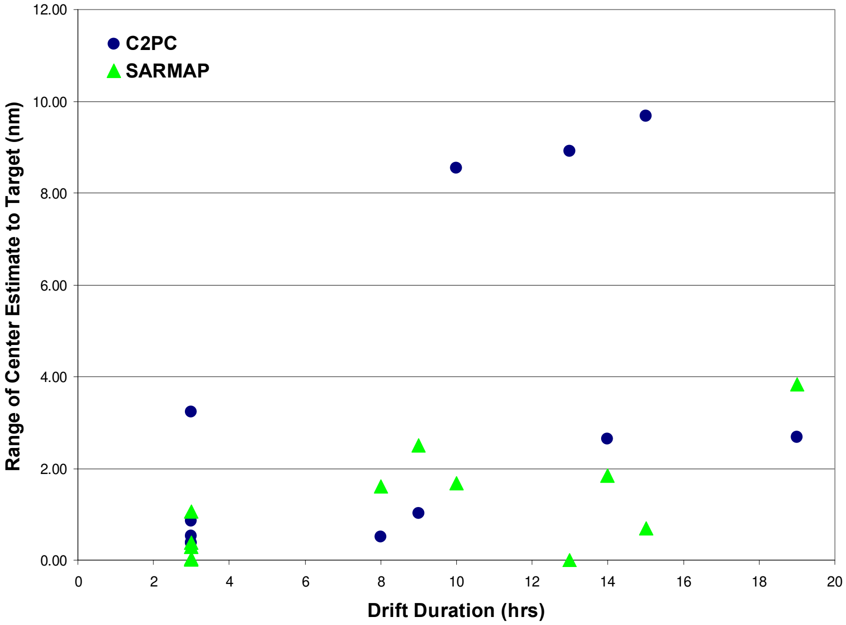

Figure 6-2. Comparison of CODAR/STPS and C2PC/JAWS results inside the CODAR/STPS coverage area.

Table 6-2. Statistical comparison of CODAR/STPS versus C2PC/JAWS inside the CODAR/STPS coverage area.

| Model | Mean Range to Drifter (nmi) | Standard Deviation (nmi) |
|---|---|---|
| CODAR/STPS | 1.3 | 1.4 |
| C2PC/JAWS | 2.8 | 11.0 |

### 6.4.3. CODAR/STPS versus C2PC/JAWS comparisons outside the CODAR/STPS coverage area

Fourteen simulated SAR cases were completely outside the CODAR analysis/STPS forecast area. The IAMSAR model was used to match the C2PC/JAWS model currently used at GRUMOR. When the drifter was outside the CODAR/STPS coverage area, the modified SARMAP software extrapolated from the nearest available CODAR/STPS data. Trajectories predicted outside of the CODAR/STPS coverage are expected to be less accurate because the current field is not spatially uniform and because the CODAR data used in the extrapolation most likely had higher associated uncertainties as they are on the fringe of the coverage area. Modified SARMAP predictions from these cases were compared with C2PC/JAWS predictions. Results are shown in Figure 6-3. Statistical parameters are provided in Table 6-3. The average range from the centers of the left and right IAMSAR-modeled position estimates to the SLDMB positions at the ends of the drifts was 2.4 nmi when the modified SARMAP with CODAR/STPS data were used compared with 2.6 nmi when C2PC/JAWS was used. More variability was evident using the CODAR/STPS data, 2.8 nmi compared with 0.7 nmi.

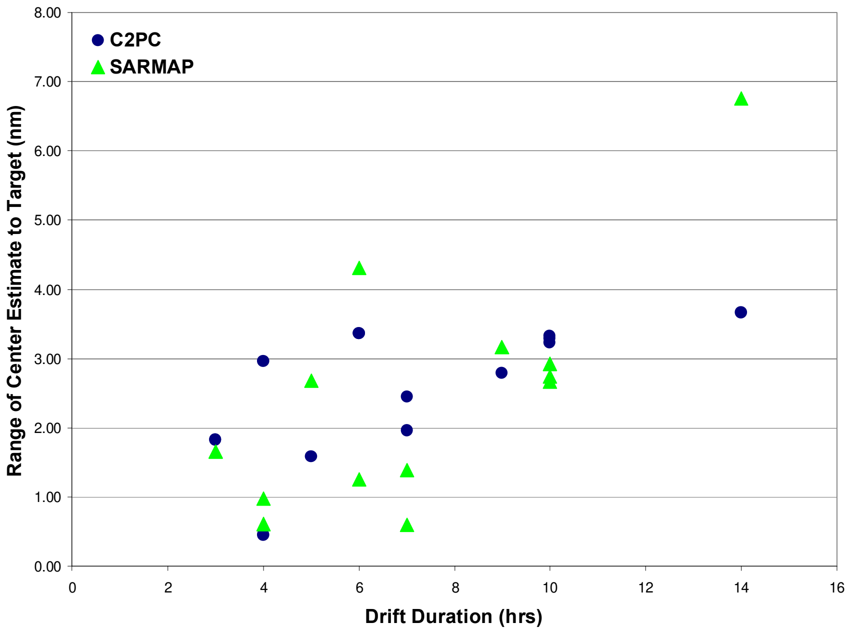

Figure 6-3. Comparison of CODAR/STPS and C2PC/JAWS results outside the CODAR/STPS coverage area.

Table 6-3. Statistical comparison of CODAR/STPS versus C2PC/JAWS outside the CODAR/STPS coverage area.

| Model | Mean Range to Drifter (nmi) | Standard Deviation (nmi) |
|---|---|---|
| CODAR/STPS | 2.4 | 2.8 |
| C2PC/JAWS | 2.6 | 0.7 |

## 6.5. Summary of the CODAR/STPS operational T&E

- The BIS and the MAB CODAR sites were fully functional during the entire operational T&E period. This demonstrated the operational reliability of these automated processing systems.
- CG GRUMOR controllers demonstrated interest and confidence in using CODAR surface currents measured in near real time and STPS estimated currents developed from CODAR data to develop SAPs.
- Use of the modified SARMAP to interface with the EDS raised issues that should be considered in the development of SAROPS, e.g., decision automation.
- On the basis of a very limited data set, the modified SARMAP model using CODAR and STPS data predicted target drift of simulated PIW targets more accurately than the C2PC/JAWS model. Caution should be used when the drifter is outside the CODAR/STPS coverage area as the results may be based on incorrect current data both because the current may be very different at the drift location than it is within the CODAR/STPS coverage area and also because the extrapolated data probably have higher associated uncertainties than more included data.

# 7. SUMMARY AND RECOMMENDATIONS

## 7.1. STPS modifications

The STPS, which had been developed for the BIS where surface currents were considered to be tidally dominated, was adapted to the MAB, where local winds were considered to dominate circulation. Several enhancements were made to the STPS. The calculations were modified to factor in the localized wind-current relationships at each grid point, instead of a region-wide average. The cross-correlations between the east and north velocity components of current at each grid point were factored in to account for the Coriolis effect. Measured wind data from a moored buoy in the vicinity of the CODAR coverage area were used to calculate the covariance function with the CODAR data. Winds were incorporated in two ways. First, wind observations prior to each time step were used to predict future surface currents. Next, actual wind observations for times after the current time were used as "predicted" winds to evaluate the extent to which including the wind-driven component would improve performance.

Of these enhancements, the addition of the wind contributed to a marginal improvement in the predictive skill of the STPS, when surface current fields predicted by STPS were compared to subsequent CODAR measurements. The incorporation of winds into STPS produced reductions in RMS prediction error ranging from 2 cm/s at the one hour forecast time to less than 1 cm/s at prediction times of a few hours, or approximately 10 percent. The weight of this conclusion is tempered by the fact that winds were relatively light during the study period. The impact of the wind on the prediction skill may be underestimated in this test, and further study may be warranted using data from time periods when winds are stronger or show a large change in direction (e.g. during frontal passages) and have more of an impact on surface flow.

## 7.2. STPS and CODAR prediction of SLDMB trajectories

Surface currents fields derived from the modified STPS and the CODAR data were used to generate pseudo-trajectories in MAB and BIS. The small-scale random component of motion was simulated using Monte-Carlo RW and RF models. Trajectories predicted using the RW and RF models were compared against actual SLDMB trajectories. The method used to calculate dispersion was found to affect the size and skill of the RW and RF approaches relative to the SLDMB trajectories. The magnitude of the dispersion coefficient used had a principal effect on the search area size and the success of the RW versus RF models.

A modification not envisioned during the planning of this project was to incorporate processing features used in the MAB CODAR processing algorithm. This modification to STPS included the incorporation of Geometric Information System (GDOP) and percentage return filtering, along with other modifications. The incorporation of the MAB processing algorithm produced the most significant improvement in the skill of STPS, reducing the RMS error of the STPS predictions by approximately 20 percent. The quality of the returns is related to the geometry of the transmitter arrays and the orientation of transmitters relative to the predominant directions of surface current flow. These results may indicate that future efforts to improve the usability of this technology should also examine signal processing and siting issues. In summary, the greatest improvement to the usability of the CODAR system resulted from an improvement to the processing of CODAR data rather than from adding the effect of forecast winds to the STPS.

The exercise showed that CODAR is better at hindcasting drifter motion in these areas relative to the methods currently in use. The most significant improvements in CODAR skill resulted from CODAR data processing and filtering steps. Further improvements in accuracy may be realized in improved processing of returns and spatial configuration of CODAR networks. The time series analysis techniques employed in this study produced smaller and less consistent improvements. Modifications to the time series analysis approach used by STPS may also be beneficial.

Future improvements to the predictive performance of both methods will also require more accurate estimates of the dispersion coefficients and correlation time scale. As SLDMBs are deployed in a region, current velocity data could be saved and utilized, in conjunction with CODAR current velocity data, to improve dispersion parameter estimates in the region.

## 7.3. Factors affecting usability of HF radar products

A Monte-Carlo simulation task was undertaken to focus on improving the characterization of uncertainties in the CODAR and STPS surface current fields. Random walk (RW) and random flight (RF) Monte Carlo models were used to simulate CODAR/STPS error and dispersion due to turbulence in the surface current field. The RW and RF models were used to model SLDMB trajectories in the MAB and BIS. Dispersion coefficients were computed using variance of CODAR field velocities and from differences between CODAR and SLDMB velocities. Dispersion was estimated retrospectively using the results of Monte Carlo simulations of SLDMB trajectories. These various methods resulted in estimates of the dispersion coefficient ranging from 40 $m^2/s$ to 700 $m^2/s$.

The differences between search areas obtained from RW and RF models was found to be minor relative to the differences in search area sizes resulting from uncertainty in dispersion ($K$). The value selected for the dispersion coefficient (K) emerges as the critical factor in defining the size and growth of the search area in a SAR case, and subsequently the usefulness of the CODAR and STPS products.

## 7.4. Operational demonstration of SAROPS

A preliminary version of SAROPS EDS was used to collect CODAR current data and STPS current predictions from UCONN and Rutgers, wind observations from NDBC buoy sites, and SLDMB data from OSC Martinsburg. This initial test of the retrieval system concluded that remote users will be able to request and download these data in near-real time for use in Search Area Plans (SAPs). The following issues, however, need to be considered for operational use.

- The SAR operators possessed an understanding of the marine environment and want more information on the data that they use for SAR cases. They need information on the quality and reliability of the environmental data that they use.

- The user could manually select data sources available from the EDS, but the system should automatically recommend data sources and parameters such as regional dispersion/turbulence based on the AOI.

A 30-day evaluation operational test and evaluation was then conducted was at CG Group Moriches (GRUMOR). SLDMBs deployed during this period were used as search targets. Trajectory predictions were made using STPS and CODAR. Both the BIS and MAB systems were fully functional during the T&E period. Operators expressed interest and confidence in the CODAR/STPS predictions. When SLDMB trajectories were inside the CODAR/STPS coverage area, the mean value and variability of SLDMB-prediction errors using CODAR/STPS were measurably lower than those from C2PC/JAWS. When the drifter was outside the CODAR/STPS coverage area, the mean errors were comparable, although the variability of SLDMB-prediction errors obtained from CODAR/STPS were lower. In spite of this result, caution is recommended when using data collected outside of the coverage area.

Significant issues that emerged were:

- Use of the modified SARMAP to interface with the EDS raised issues that should be considered in the development of SAROPS, e.g., decision automation.
- The lack of near coastal CODAR coverage was a concern for operators. Future versions of the EDS will need to blend data sources such as CODAR with other data sources to provide complete data coverage for a SAR case.

The demonstration project had no method to assimilate drift data from the SLDMB tracks into SARMAP. The tracks could be visualized, but the forecast (and hindcast) solutions did not exploit the SLDMB data. A system could be established to catalog SLDMB and CODAR data for individual CODAR regions. Simply maintaining a database with all SLDMB trajectories through a given CODAR region along with concurrent CODAR velocities will allow better estimates of prediction error and dispersion coefficients for a specific region. The necessary calculations could be performed on a regular basis (e.g., annually or seasonally).

## 7.5. Recommendations for the U.S. Coast Guard

CODAR and STPS are maturing technologies that have demonstrated the ability to improve CG operational planning. Presently however, CODAR and STPS are not ready for operational use in SAROPS. The following recommendations are provided to make them viable for operational use in SAROPS.

1) Through Oceans.US, the CG should
    a. Encourage initiatives to improve the accuracy and coverage of HF radar arrays,
    b. Encourage development of enhancements to STPS in HF radar coverage regions.
    c. Partner with the HF radar community to ensure that the CG requirements are recognized.

2) In the SAROPS developments process, G-OPR should include methodologies in the EDS to fill the gaps where no or invalid surface current data exist. This applies to the use of model

data as well as HF radar data. In areas where there is no HF radar coverage, alternative current estimates, such as historical files or datum marker buoy (DMB) data, should be available.

3) In conjunction with the Operations Systems Center, G-OPR should develop an archive to store SLDMB data and periodically calculate and store regionally representative dispersion coefficients from SLDMB trajectories. Archived SLDMB data could also be matched with seasonal and environmental conditions to provide better historical current estimates in areas where CODAR/STPS is not available.
4) G-OPR should support further research on the impact of forecast wind change on STPS current estimates.

## 7.6. CODAR/HF radar community specific recommendations

The following recommendations are provided for HF radar operators.

1) Add standard-range HF radar sites to fill in gaps in areas closer to shore and in approaches to harbors, especially in areas where spatial variability is high. Consider site development by frequency of SAR cases.
2) Document the software that is used to process data in each area. Meet with operators in other regions to develop standards for combining radials, filling in missing spatial and temporal data, and eliminating low quality data. Develop data sharing standards to facilitate interfacing with STPS and SAROPS.
3) Develop standard quality control and uncertainty estimates so that search areas can be modeled more effectively.
4) Explore schemes to use stored HF radar data to compute and regularly update regionally appropriate dispersion coefficients. To the CG user, CODAR surface current mapping credibility is contingent on reliable updates to dispersion coefficients.

# 8. REFERENCES

Berloff, P. & McWilliams, J. C. (2002). Material transport in ocean gyres: Part II hierarchy of stochastic models. Journal of Physical Oceanography, Vol. 32, p. 797-830.

Csanady, G. T. (1973). Turbulent diffusion in the environment. D. Reidel Publishing Company, Boston, MA.

Chapman, R. D. & Graber, H. C. (1997). Validation of HF radar measurements. Oceanography, Vol. 10, p. 76-79.

Griffa, A. (1996). Applications of stochastic particle models to oceanographic problems, in *Stochastic Modeling in Physical Oceanography,* edited by Adler, R., Mueller, P., & Rozovski, B. Boston, MA: Birkhauser, p. 114-140.

Kohut, J. T., Roarty, H. J., & Glenn, S. M. (2004). Characterizing observed environmental variability with HF Doppler radar surface current mappers and acoustic Doppler current; profilers. Manuscript submitted for publication. IEEE Journal of Ocean Engineering.

Mariano, A. J., Ryan, E. H., Perkins, B. D. and Smithers, S. (1995). The Mariano Global Surface Velocity analysis 1.0, U.S. Coast Guard Report (CG-D-34-95). Groton, CT: USCG Research & Development Center. (NTIS# AD-A302245).

O'Donnell, J., Ullman, D., Edwards, C., Fake, T., & Allen, A. (2005). The operational prediction of circulation and Lagrangian trajectories in the coastal ocean. Unpublished work. University of Connecticut at Avery Point.

Riddles, H., (2003). Geometric Dilution of Precision of HF Radar Data in 2+ Station Networks.

Spaulding, M., Isaji, T, Hall, P., & Allen, A. (2005). A hierarchy of stochastic particle models for Search and Rescue (SAR): Application to predict surface drifter trajectories using HF radar current forcing. Unpublished work. University of Rhode Island.

Stewart, R. H. & Joy, J. W. (1974). HF radio measurement of surface currents. Deep-Sea Research, Vol. 21, p. 1039-1049.

Taylor, G. I. (1921). Diffusion by continuous movement. Proceedings of the London Mathematical Society, Vol. 20, p. 196-212.

Teague, C. C., Vesecky, J. F., & Fernandez, D. M. (1997). HF radar instruments, past and present. Oceanography, Vol. 10, No. 2, p. 40-44.

Ullman, D., O'Donnell, J., Edwards, C., Fake, T., Morschauser, D., Sprague, M., Allen, A., & Krenzien, LCDR B. (2003). Use of coastal ocean dynamics application radar (CODAR) technology in U.S. Coast Guard search and rescue planning (CG-D-09-03). Groton, CT: USCG Research and Development Center.

Ullman, D., O'Donnell, J., Kohut, J., Fake, T., & Allen, A. (2005). Trajectory prediction using HF radar surface currents: Monte-Carlo simulations of prediction uncertainties. Unpublished work. University of Connecticut at Avery Point.

# APPENDIX A.

# DESCRIPTION OF THE RUTGERS UNIVERSITY CODAR DATA PROCESSING

## A.1 Introduction

High frequency radar systems, typically deployed along the coast (Figure A-1), use Bragg peaks within a signal (3 ~ 30 MHz) scattered off the ocean surface to calculate radial components of the total surface velocity at a given location (Barrick, Evens, Weber, 1977). Crombie (1955) recognized that these peaks were the result of an amplification of a transmitted wave by surface gravity waves with a wavelength equal to half that of the transmitted signal. A signal scattered off a wave and back toward the antenna will be in phase with a signal that traveled to the next surface wave (½ transmit wavelength further) and returned to the original wave (another ½ transmit wavelength). The frequency of the backscattered signal will be shifted depending on the velocity of the scattering surface. Using linear wave theory, the phase speed of the surface waves can be separated from the total frequency shift, leaving only that shift due to the surface current. Over a given time period, sites along the coast generate radial component maps of the surface current with typical resolutions on the order of 1 to 6 km in range and 5 degrees in azimuth (Figure A-2). Because the Doppler shift can only resolve the component of the current moving toward or away from the site, information from at least two sites must be geometrically combined to generate total surface current maps.

Figure A-1. Transmit (left) and receive (right) antennas for a typical CODAR-type long-range system.

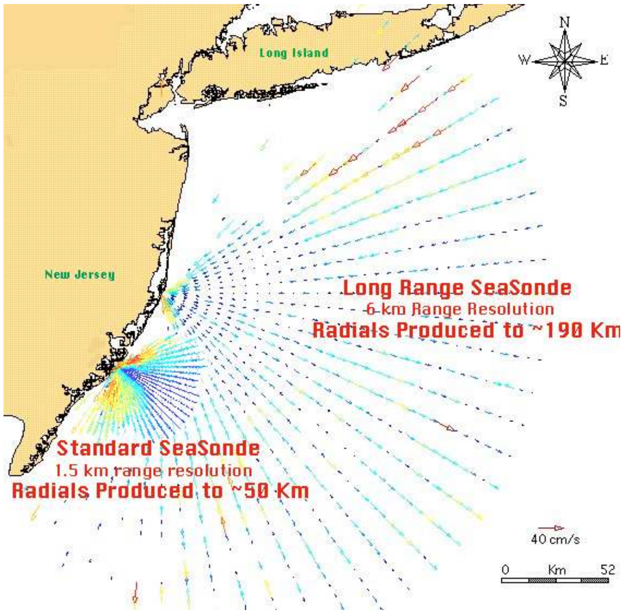

Figure A-2. Sample radial vector coverage for a long-range and standard-range HF radar system.

Rutgers University operates an array of 10 CODAR-type HF radar systems, 6 of which are lower resolution, long-range sites. With an operating frequency around 5 MHz, these sites measure surface currents within the upper 2.4 meters of the water column (Stewart and Joy, 1974). Typical spatial resolutions are on the order of 6 km, with maximum ranges exceeding 200 km. Four sites along the coast of New Jersey from Wildwood to Sandy Hook provide hourly surface current maps over the New Jersey Shelf (Figure A-3). These four sites form one cluster of systems within the North East Observing System (NEOS). These sites use global positioning system (GPS) synchronization so that each site is operating at the same frequency and bistatically linked to the other sites within the network.

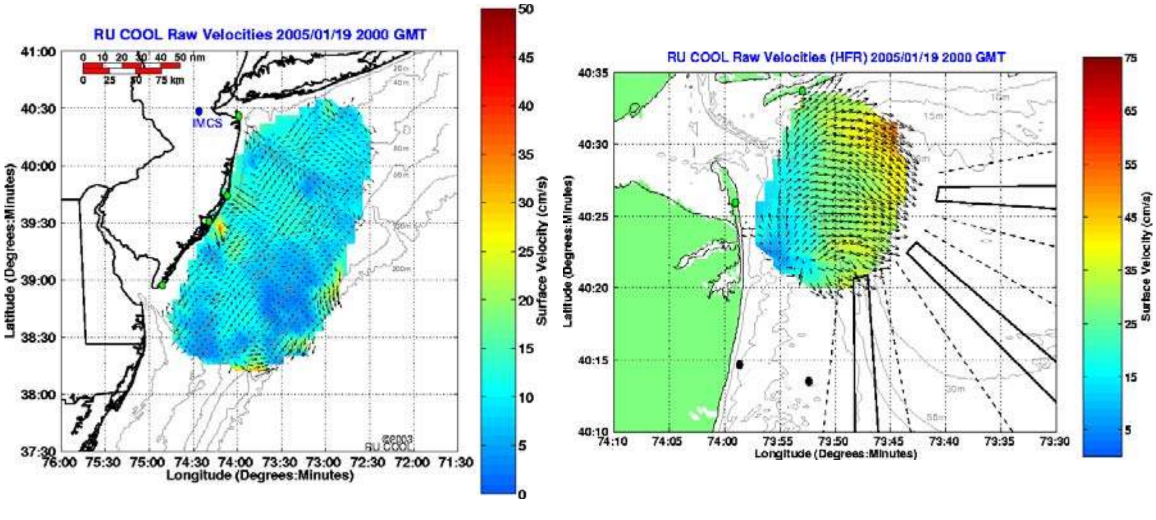

Figure A-3. Surface current map of January 19, 2005 at 20:00 GMT. Coverage is shown for the long-range (left) and standard-range (right) systems.

Two standard-range systems, currently deployed on opposite sides of the entrance to New York Harbor (Figure A-3), are nested within the New Jersey long-range cluster. With an operating frequency of 25 MHz, these systems measure the current within the upper 50 cm of the water column. Typical spatial resolutions are on the order of 1 km with maximum ranges out to 40 km. The two sites were recently moved from their original location along the southern coast of New Jersey to the New York Bight apex to support (1) a National Science Foundation (NSF)-funded project focusing on the Hudson River outflow and (2) the development of ship-tracking capabilities near the harbor entrance. On 26 January 2005, a third standard range site operated by Stevens Institute was deployed within the lower harbor. This site paired with the two Rutgers sites brings existing high-resolution coverage into the harbor.

## A.2 Radial data processing

These CODAR-type systems are direction-finding systems that use a three-element receive antenna mounted on a single post to determine the direction of the incoming signals. The angular resolution, set in the processing, is typically 5 degrees (Teague, Vesecky, Fernandez, 1997; Barrick and Lipa, 1996). For the radial vector map processing, raw time series from each element are transformed into cross-spectra with a 1024-point fast Fourier transform (FFT). For the long-range systems, these data are created every 17 minutes and averaged hourly, centered on each half hour. For each range bin, spectra are run through a multiple signal classification (MUSIC) algorithm with the measured beam patterns (Kohut and Glenn, 2003) to calculate the bearing of each radial velocity within the first-order Bragg region (Schmidt, 1986; Barrick and Lipa, 1999). This first-order region was limited to signal to noise ratios (SNR) of at least 5.0 dB. Each hour, seven of these hourly velocity estimates, each overlapped by half an hour, are averaged to get a 4-hour running average for the center time. This file is input to the vector combination procedure to generate the total vector file described in section A.3.

The number of radial vectors in any given range cell depends on (1) the digitization interval determined by the FFT length, operating frequency, and sweep rate and (2) the number of antenna elements in the receive array. The digitization interval controls how many radial velocity vectors are available, and the number of antenna elements determines the number of possible MUSIC solutions for each radial velocity. For our setup with three-receive antenna elements, a radial velocity every 3.22 cm/s can be placed in up to two angular bins. Consequently, if there are more than two angles with a given radial velocity or periods of weak surface currents, data coverage will be reduced. Based on these constraints, an interpolation was done in azimuth. The scheme linearly interpolated radial data across angular gaps of 15 degrees or less (Kohut, Roarty, Glenn, 2004; Kohut and Glenn, 2003).

## A.3 Total vector combination

Every hour, the available radial vector maps were geometrically combined into a single total vector map. All radial component vectors within 10 km of each grid point were used in the combination. A total vector was generated only if at least three radial vectors from at least two remote sites were used in the combination. When the orthogonal velocity components are combined into total vector estimates, errors are introduced. The uncertainty of the combined totals can be separated into radial vector uncertainty and geometric uncertainty. The geometric uncertainty is based on the angles of the radial component vectors. The farther the radials are from orthogonal, the greater the uncertainty. This uncertainty is described by Chapman and Graber (1997) as geometric dilution of precision (GDOP). These uncertainties increase along the baseline between the coastal sites as well as offshore. In these regions, the radial component vectors are resolving the along-shore and cross-shore velocity components, respectively. The relative magnitude of the geometric uncertainty was calculated at each grid point for every current map (Gurgel, 1994). Using this scalar as an indicator of the magnitude of the geometric contribution to the uncertainty, data subject to poor geometry were eliminated. This was done by eliminating all data above a threshold of 1.25. This 1.25 threshold was chosen based on qualitative analysis of previous data. Drifter deployments offer an excellent opportunity to better define this threshold and apply it to future system operation. For the duration of the project, total vector fields were made with and without the geometric filter (Figure A-4). For the purpose of this analysis, the unfiltered data was used to evaluate the filter, and the filtered data was used for all direct comparisons to drifter velocities.

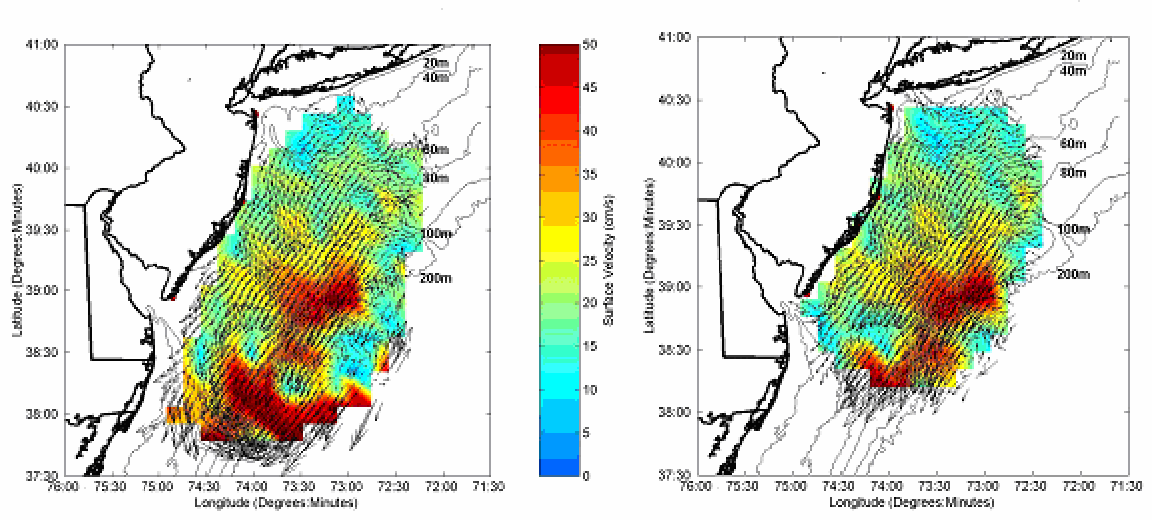

Figure A-4. Surface current map combined with (right) and without (left) the geometric filter.

## A.4 Drifter velocities

The drifter position data were used to evaluate the CODAR observations. The drifter data used here are from the deployment during the summer of 2004 (July 27th to August 31st). Throughout the deployment, drifter positions were reported every half hour (Figure A-5). SLDMBs #32773, #32776, and #32779 were deployed in the BIS and moved southwest along the southern Long Island coast. SLDMBs #43057 and #43060 were deployed in the upper Hudson Canyon and moved south into the center of the coverage, and SLDMBs #43061 and #43062 were deployed farther offshore and moved in and out of the coverage through the deployment. Drifter velocities were calculated to match the averaging of the CODAR processing. Velocities based on two drifter positions one hour apart were calculated every half hour. Each hour seven of these hourly velocity estimates, each overlapped by half an hour, were averaged to get a 4-hour running average for the center time. These drifter data were compared to CODAR observations. At each time step, the CODAR data were linearly interpolated to the drifter position. Because only radial data within 10 km of a grid point were combined to create the total vector grid, comparisons were limited to times when the drifter was no more than 10 km from the closest CODAR grid point.

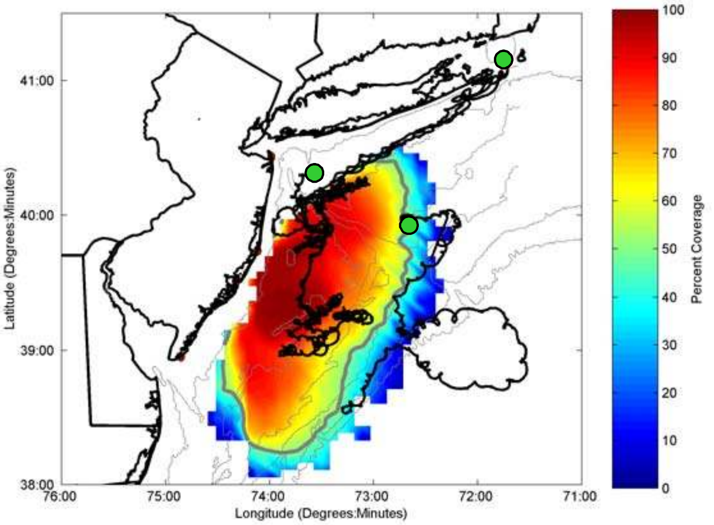

Figure A-5. Tracks of the seven drifters (black line) deployed between July 27, 2004 and August 31, 2004. The deployment sites (green circle) and the 50 percent CODAR coverage contour (gray line) are also shown.

## A.5 CODAR/drifter comparisons

CODAR data were validated against seven drifters deployed in the summer of 2004. For each drifter within the CODAR coverage (Figure A-5), comparisons were drawn between spatially interpolated CODAR observations and climatological estimates. Because the CODAR data sampled the surface current over different horizontal and spatial scales than the drifter, the current estimates differed in the absence of instrument uncertainty. Therefore, the contribution to the RMS difference includes CODAR uncertainty, drifter uncertainty, and sub-grid scale uncertainty. The standard deviation of the drifter data calculated with the seven half-hourly data averaged each hour was used as an estimate of the sub-grid scale uncertainty. For reference, the average standard deviation for all drifters through the entire deployment was 7.2 cm/s for the east component and 6.2 cm/s for the north component.

The average RMS difference among all available drifter and CODAR velocities was 9.1 cm/s in the east component and 12.1 cm/s in the north component. The same drifter data were compared to Mariano climatology giving an RMS difference of 17.3 cm/s in the east direction and 15.9 cm/s in the north direction (Table A-1).

Table A-1. Comparison statistics among drifter velocity, Mariano climatology, and CODAR observations. For reference, the standard deviation of the drifter data was 7.2 cm/s for the east direction and 6.2 cm/s for the north component.

| SLDMB Number | Velocity Component | SLDMB/CODAR RMS (cm/s) | SLDMB/ Mariano Climatology RMS (cm/s) |
|---|---|---|---|
| 32773 | East | 7.7 | 18.1 |
| 32773 | North | 11.0 | 13.5 |
| 32776 | East | 10.1 | 19.4 |
| 32776 | North | 12.4 | 15.3 |
| 32779 | East | 7.6 | 17.3 |
| 32779 | North | 10.4 | 13.3 |
| 43057 | East | 8.1 | 16.9 |
| 43057 | North | 11.3 | 14.9 |
| 43060 | East | 9.6 | 16.6 |
| 43060 | North | 10.1 | 15.2 |
| 43061 | East | 12.2 | 17.9 |
| 43061 | North | 16.9 | 22.7 |
| 43062 | East | 8.6 | 15.2 |
| 43062 | North | 12.6 | 16.1 |
| **Average** | **East** | **9.1** | **17.3** |
| **Average** | **North** | **12.1** | **15.9** |

For each drifter, the RMS difference with the CODAR observations was lower than that with Mariano climatology. In addition, the east component of the CODAR data had a lower RMS difference than the north component for all drifters. This difference is evidence of the additional uncertainty in the north component due to site geometry. All the sites in this network were deployed along the New Jersey coast. Given the drifter location and the radial coverage of these sites, the east component of the total vectors was better resolved by the radial vectors than the north component. SLDMB #32773 clearly illustrated the geometric uncertainty in the vector combination (Figure A-6). Early on in the deployment, the drifter was south of Long Island where the radial vectors measured at the CODAR sites better resolved the east velocity component. The time series clearly shows better agreement between the east component of the CODAR and drifter observations compared to the north component. As the drifter moved closer to the sites and better geometry, the north component was better resolved and the agreement improved. SLDMB #43060 spent more time in the coverage area with better geometry, and the agreement was good throughout the time series. The CODAR data are an improvement to existing Mariano climatology when compared to drifter velocity estimates. Future work will focus on refining the geometric filter and processing algorithms to improve both the geometric and CODAR uncertainties.

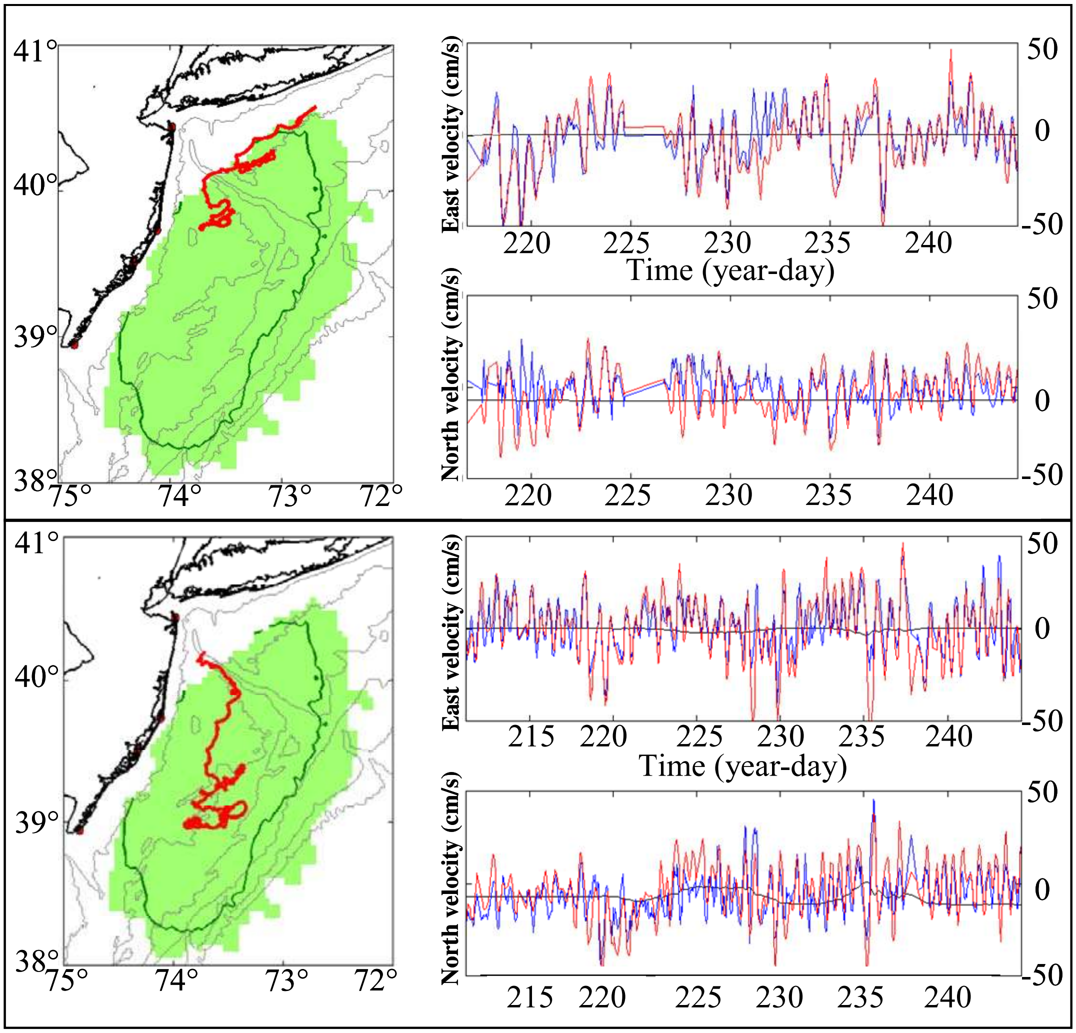

Figure A-6. Drifter track (red line) (left), CODAR coverage area (green) (left), and time series of the east and north velocity components from drifter locations (red trace), CODAR (blue trace), and Mariano climatology (black line). The upper panel is for SLDMB #32773, and the lower panel is for SLDMB #43060.

## A.6 References

Barrick, D. E., Evens, M. W., & Weber, B. L. (1977). Ocean surface currents mapped by radar. Science, Vol. 198, p. 138-144.

Barrick, D. E. & Lipa, B. J. (1996). Comparison of direction-finding and beam-forming in HF radar ocean surface current mapping. Phase 1 SBIR final report. Rockville, MD: National Oceanic and Atmospheric Administration. (Contract No. 50-DKNA-5-00092).

Barrick, D. E. & Lipa, B. J. (1999). Radar angle determination with MUSIC direction finding. United States Patent, No. 5,990,834.

Chapman, R. D. & Graber, H. C. (1997). Validation of HF radar measurements. Oceanography, Vol. 10, p. 76-79.

Crombie, D. D. (1955). Doppler spectrum of sea echo at 13.56 Mc/s. Nature, Vol. 175, p. 681-682.

Gurgel, K. W. (1994). Shipborne measurement of surface current fields by HF radar. L'Onde Electrique, Vol. 74, p. 54-59.

Kohut, J. T. & Glenn, S. M. (2003). Improving HF radar surface current measurements with measured antenna beam patterns. Journal of Atmospheric and Oceanic Technology, Vol. 20, p. 1303-1316.

Kohut, J. T., Roarty, H. J., & Glenn, S. M. (2004). Characterizing observed environmental variability with HF Doppler radar surface current mappers and acoustic Doppler current; profilers. Manuscript submitted for publication. IEEE Journal of Ocean Engineering.

Schmidt, R.O. (1986). Multiple emitter location and signal parameter estimation. IEEE Transactions on Antennas and Propagation, Vol. AP-34, p. 276-280.

Stewart, R. H. & Joy, J. W. (1974). HF radio measurement of surface currents. Deep-Sea Research, Vol. 21, p. 1039-1049.

Teague, C. C., Vesecky, J. F., & Fernandez, D. M. (1997). HF radar instruments, past and present. Oceanography, Vol. 10, No. 2, p. 40-44.

(This page intentionally left blank.)

# APPENDIX B.
# STPS ENHANCEMENTS IN THE BIS REGION

## B.1 Enhanced STPS with no wind in the BIS region

Using CODAR data for the December 2003 to January 2004 period, the period when drifter data were available in the BIS area, there was no substantial improvement to the performance of the algorithm when local covariance estimates and the covariance of the current components were used. Figure B-1 shows a comparison of the area-averaged error in the forecasts of the original algorithm with that of the new algorithm in support of this conclusion. The difference in root-mean-squared (RMS) errors is less than 0.25 cm/s.

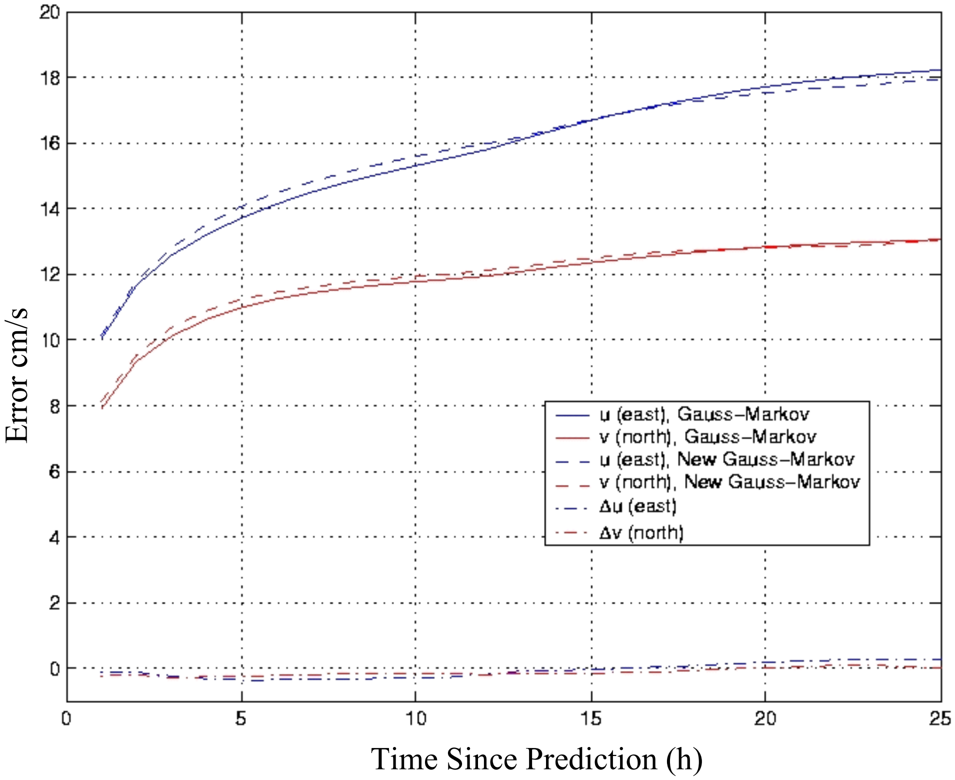

Figure B-1. Area-averaged RMS error in the east (blue lines) and north (red lines) components of the surface currents estimated by the original (solid lines) STPS algorithm and the enhanced STPS algorithm with local covariance and covariance component modifications (dashed lines) in the BIS region.

The spatial structure of the errors at the 6-hour forecast time is presented in Figure B-2. The distribution and magnitude of the errors are very similar in large areas where the error is approximately 10 cm/s and areas of slightly higher error where the geometry of the CODAR system degrades the precision of the vector estimates. The top figures, the east components, have more areas of green and yellow, corresponding to higher RMS errors.

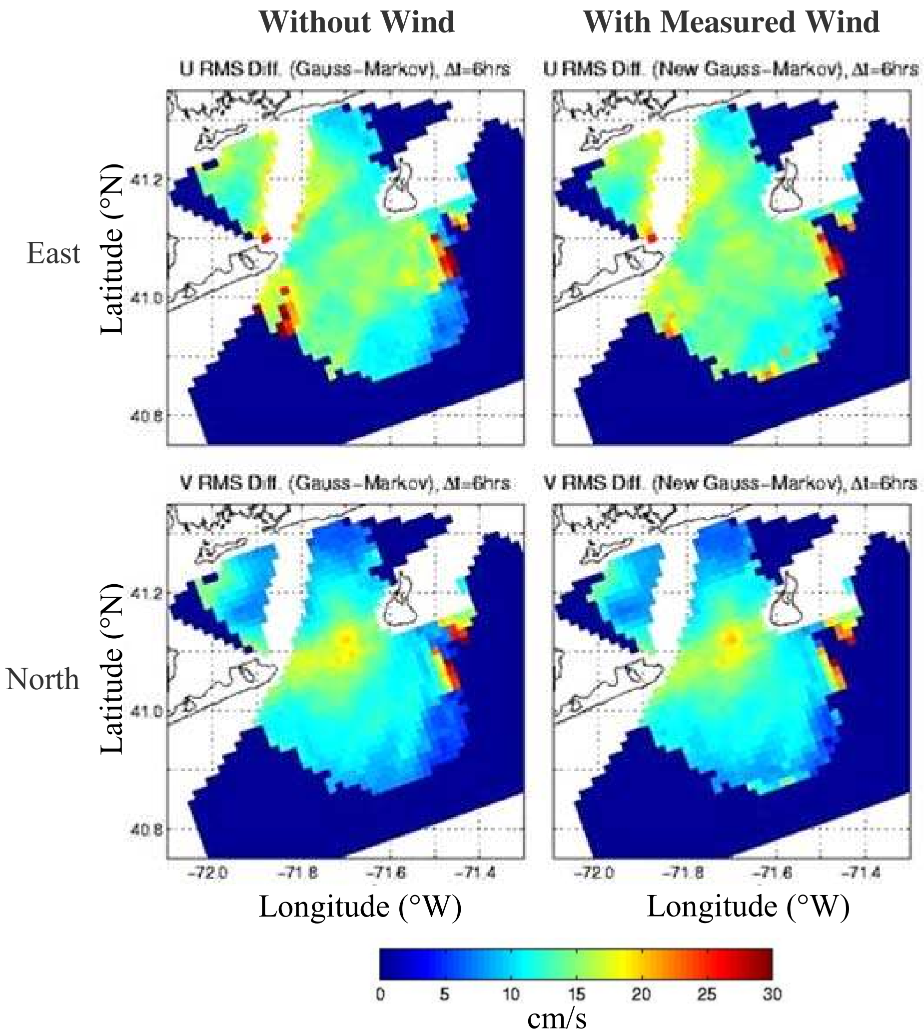

Figure B-2. The distribution of the time-averaged RMS error in the surface current predictions of original (left two frames) and new STPS (right frames) in the BIS area. The errors in the east components are presented in the top two frames and the north component in the lower frames.

## B.2 Enhanced STPS with measured wind in the BIS region

Measured wind data were included in the Gauss-Markov procedure to generate current forecasts. Note that wind forecasts were not included at this stage of the analysis. The wind data were acquired from NDBC buoy #44025. Figure B-3 displays a comparison of the area-averaged error. Again, there was no improvement in the prediction skill.

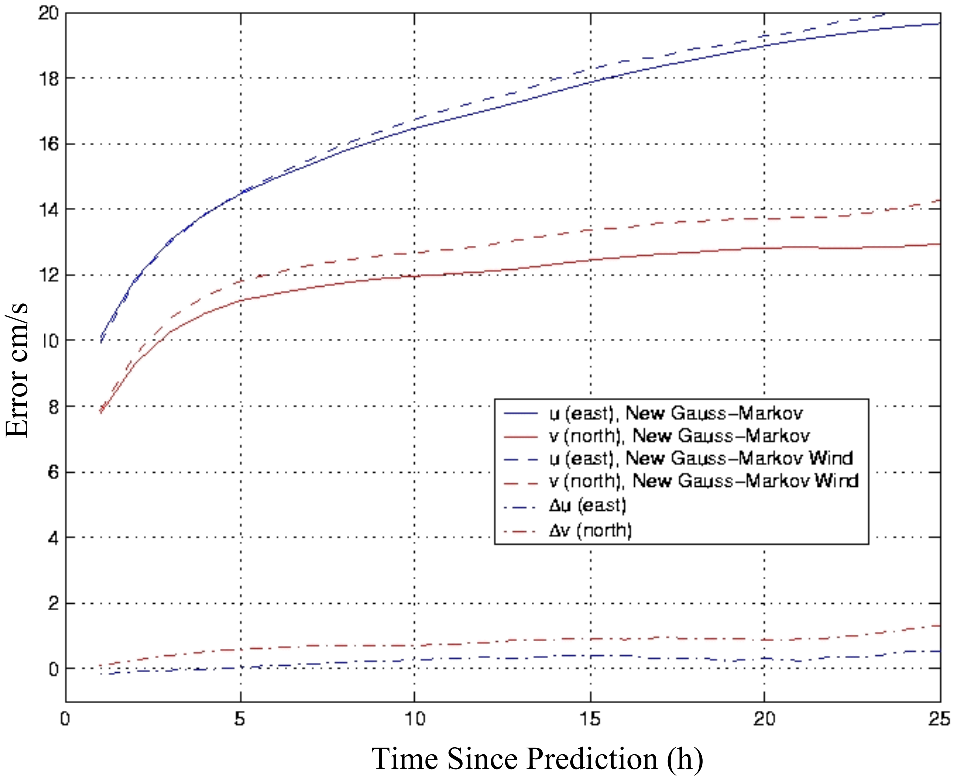

Figure B-3. Area-averaged RMS error in the predicted east (blue lines) and north (red lines) velocity components of the surface currents estimated by the enhanced STPS algorithm without wind data (dashed lines) and the enhanced algorithm with measured wind data (solid lines) in the BIS area.

(This page intentionally left blank.)

# APPENDIX C.
# THE OPERATIONAL PREDICTION OF CIRCULATION AND LAGRANGIAN TRAJECTORIES IN THE COASTAL OCEAN

February 2, 2005

James O'Donnell[1], David Ullman[2], Chris Edwards[3], Todd Fake[1], and Arthur Allen[4]

[1]Department of Marine Sciences, University of Connecticut, Groton, CT 06340
[2]Graduate School of Oceanography, University of Rhode Island, Narragansett, RI
[3]Department of Ocean Sciences, University of California, Santa Cruz, CA
[4]US Coast Guard Research and Development Center, Groton, CT 06340

## Abstract

The ability to predict the movement of particles drifting at the surface of the coastal ocean is of great value to agencies responsible for the management of oil spills, search and rescue operations, marine safety and coastal water quality. High frequency radio surface-current measuring systems that are capable of mapping wide areas can be exploited for this purpose. We present a simple statistical technique that exploits observations to extrapolate Eulerian velocity estimate 12 hours into the future. We then use these predictions in the Euler-Lagrange transformation to simulate the trajectories of drifting particle. The performance of both the Eulerian forecast and the trajectory forecast technique are evaluated by comparison to observations in Block Island Sound and the adjacent shelf. We also evaluate the performance to an algorithm similar to that in operational use to gauge the practical value of the system. We find that the surface current predictions have root mean square errors averaged over the ~800 km$^2$ area of less than 15 cm/s for forecasts up to 12 hours. The errors appear to be correlated with wind, suggesting that the algorithm could be further refined. When employed to forecast drifter trajectories we find that the root mean squared separation between predicted drifter locations and observations show that 95 percent of the differences are less that 7 km at 6 hours and 13 km at 12 hours. This is approximately a factor of two better than methods currently in operational use.

## C.1 Introduction

Several surface current mapping systems (e.g. CODAR, WERA, OSCAR) that exploit the Doppler shift in the Bragg scatter from high frequency radio transmissions have been developed and are now commercially available. We will refer to them collectively as SCMS. Though they differ in important technical characteristics, we believe our work is equally applicable to observations from all designs. Some installations have been operating for more than 7 years (Glenn and Schofield, 2003) and the data has been extensively used in science programs (Kohut et al, 2004). Though there is a variety of algorithms that transform the backscatter spectra to velocity and many technical improvements remain possible, system designs have become stable and very reliable in the last few years and are ready for operational use as a central component of an integrated ocean observing system.

The timely and accurate prediction of the motion of material floating at the ocean surface is a critical limitation to the effective response to marine safety emergencies and the accidental release of pollutants. In particular, the availability of SCMS has the potential to offer substantial advantage to the CG, which currently relies on sparse network stations at which tidal current harmonics have been estimated. As has been well established (see, for example, Ridderinkof and Zimmerman, 1992), the interaction of tidal currents with spatially varying mean flows can create extremely rapid Lagrangian dispersion. Since SCMS can reveal the spatial structure of the circulation, they offer the potential of substantial improvement in the effectiveness of search planning. Because of the shape of the coastline, harbors and estuaries have complex currents, a lot of boat traffic, and frequent marine accidents. SCMS could, therefore, help save lives in the immediate future.

The spectral averaging, data telemetry and processing required by SCMS delays the availability of observations. The most recent observations currently available can be 1 to 3 hours old. The integration of surface current measuring infrastructure to operational safety and management systems, therefore, requires that a forecast capability be developed for the Eulerian currents and that an algorithm be developed that can effectively exploit forecasts to predict Lagrangian trajectories (particle paths).

In this paper our intent is to describe the development and performance of an algorithm that exploits data to produce short term (0-24 hour) forecasts. The approach we adopted makes no assumptions about the underlying dynamics and ignores the coastal geometry and bathymetry. The primary advantage of this approach is that the algorithm can be readily applied in any area with an operational SCMS with limited effort and expense. It is unlikely that this will be the best approach in the long run. However, it is easily implemented and it establishes a benchmark against which more sophisticated algorithms can be evaluated.

We use the Eulerian forecast algorithm to predict Lagrangian trajectories in Block Island Sound and the adjacent continental shelf. To evaluate the effectiveness of the approach we deployed surface drifters. To establish the relative importance of the limitation imposed by the data and the prediction system we simulated the drifter trajectories using data and the forecast system. We also evaluated the performance of the system that is currently in use that neglects much of the spatial structure in the flow field. We demonstrate that the SCMS-based system is limited by data quality but is substantially better than the available technology in the test area.

In the next section we describe the characteristics of the flow in the area of Block Island Sound where a standard range CODAR system has been in operation since 2000. We deployed a flotilla of GPS tracked CODE-style drifters to assess the effectiveness of the system and describe this data in Section 3. We then define the empirical forecasting algorithm in Section 4 and assess its performance by comparing predictions to SCMS observations in Section 5. The effectiveness of the simulation of drifter trajectories using both the observed and forecast currents is assessed in Section 6 by comparing them to drifter tracks. We summarize the results and comment on potential developments in Section 7.

## C.2 Block Island Sound current observations

In 2000 the National Ocean Partnership Program (NOPP) sponsored the development of an experimental coastal ocean observatory at the approaches to Block Island Sound, an area of strong tides and significant buoyancy driven circulation on the Southern New England Shelf. Figure C-1. The coastline and bathymetry of Block Island Sound with the location and approximate observation areas of three CODAR sites. shows a map of the area with the bathymetry. Ullman and Cornillion's (1999) analysis of surface temperature observations demonstrated that this is an area with persistent and complicated fronts. O'Donnell and Allen (1992) used drifter observations and data from a moored current meter to demonstrate that there is substantial mean exchange flow through Block Island Sound associated with the estuarine outflow from Long Island Sound. They showed the surface motion is to the east and south at approximately 10 cm/s carrying the brackish effluent to the adjacent continental shelf. Salty shelf water flows north and west into Long Island Sound along the relic river channel that is apparent in the isobaths.

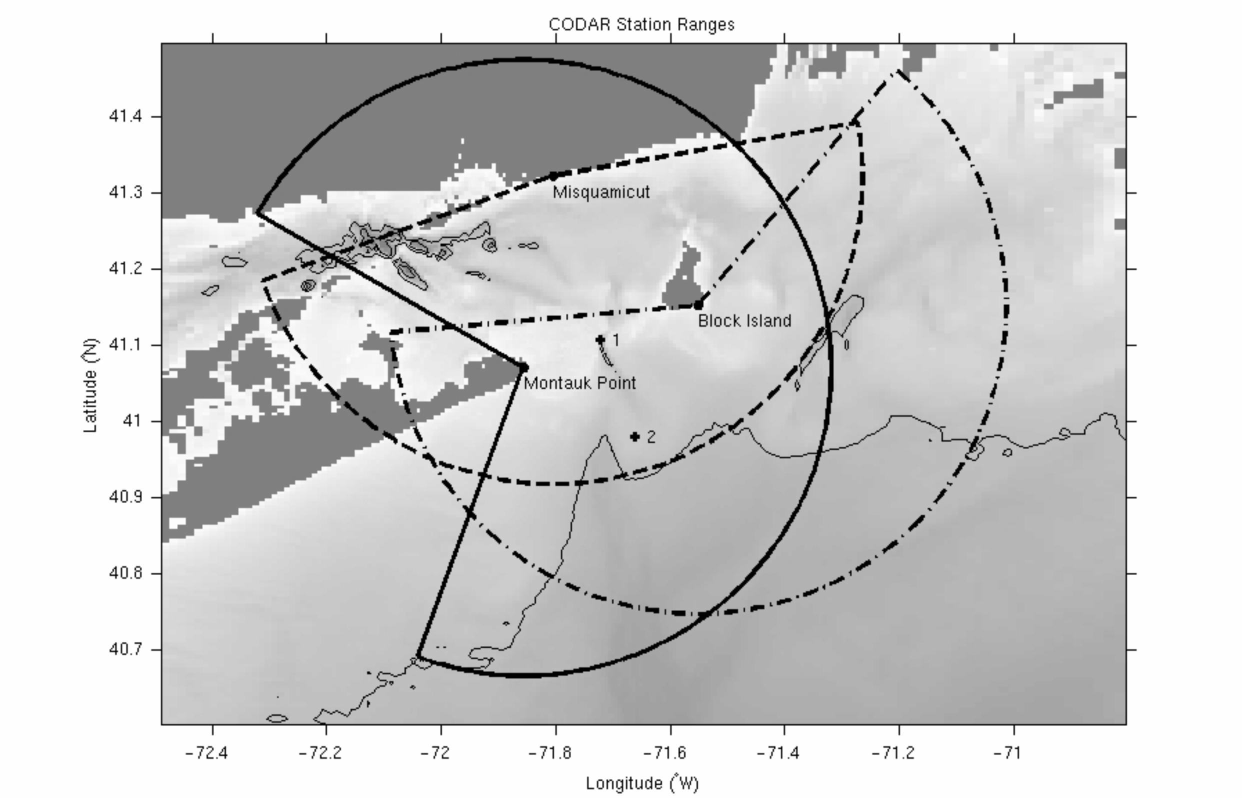

Figure C-1. The coastline and bathymetry of Block Island Sound with the location and approximate observation areas of three CODAR sites.

Figure C-1 also shows the location of the three standard range CODAR SeaSondes© that were deployed in 2000 at Misquamicut, RI, Montauk Point, NY, and Block Island, RI, also displayed with their approximate areas of coverage. HF radio frequency backscatter observations by these instruments can be combined to obtain estimates of the near surface, approximately the top 2 meters, velocity component in the radial direction towards the receivers in 2 km range and 5 degree azimuth cells every hour. At the FRONT site the “radials” from all three sites are combined by weighted area averaging to form east and north components of the velocity at the points indicated by the “+” symbols in Figure C-1. Ullman and Codiga (2004) present an analysis of the mean and seasonal variation of the circulation in the area using observations from this system.

## C.3 Drifter Data

The RV Connecticut deployed four CODE-style surface drifters (see Davis, 1985) equipped with GPS navigation and Argos data telemetry systems in Block Island Sound during December 2002 within the coverage area of the FRONT CODAR system. The four rectangular drag elements (sails) of the drifter were 0.7m by 0.3m and were suspended 0.3m below the surface. Several of these drifters were recovered and redeployed, while one failed to return useful data. Subsequently, in March 2003, CG helicopters air-deployed an additional 12 drifters, of which 4 were deployed in the FRONT region and 8 off the New Jersey shore for a study that will be described elsewhere. The drifters reported their positions at 0.5-hour intervals via the Argos network. The time series of drifter position were decimated to hourly intervals to align with the hourly CODAR current estimates. Each drifter track was broken up into a series of 24-hour segments that were treated as independent trajectories for the analysis of errors in drift prediction performance (Figure C-2). The start times of the segments were offset by 12 hours. Thus the first trajectory for a given drifter starts at the time of the first good position ($t_0$) with subsequent pseudo-independent trajectories starting at $t_0$+12, $t_0$+24, etc.

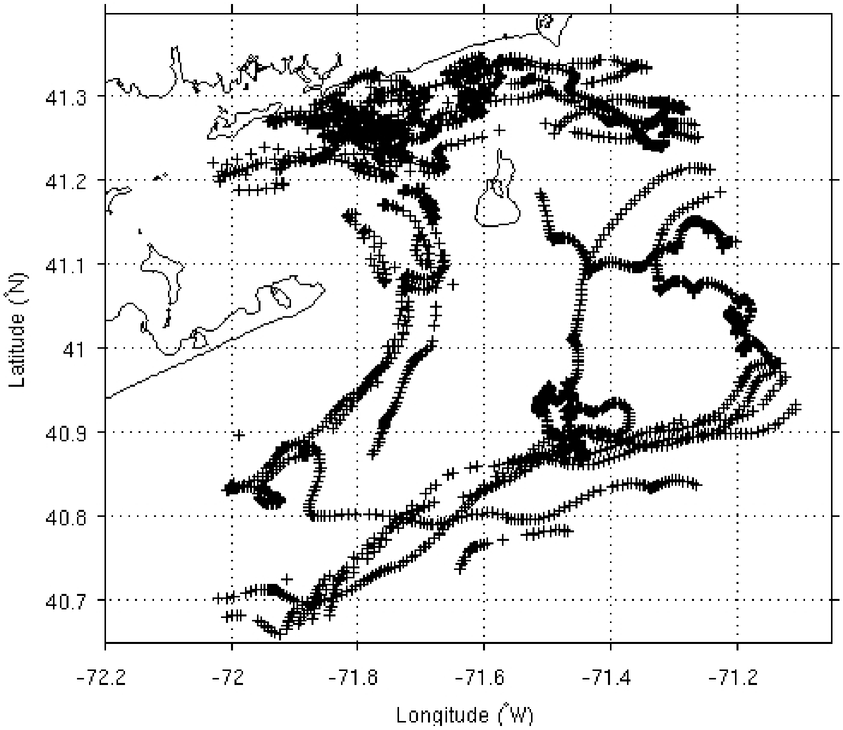

Figure C-2. Trajectories of drifters launched in the area of Block Island Sound in December 2002 and March 2003.

## C.4 Eulerian Current Forecast Algorithm

### C.4.1 Overview

The surface current forecast algorithm is based on an empirical decomposition of the currents into three components. As in most of the coastal ocean, a strong component of the motion is due to tides, a weaker and more slowly varying component is driven by winds, and a more persistent motion associated with ocean density variations and very low frequency waves. The tidal circulation is periodic and, therefore, easy to forecast. The largest five tidal constituents in the FRONT region are listed in Table C-1. Three are semidiurnal and two are diurnal. Least-squares harmonic analysis method is used to compute the amplitude and phase of these constituents at each CODAR grid point. In our forecast algorithm the harmonic analysis is performed each week using the observations acquired during the prior month. The constituents are used to predict the tidal component of the circulation for the next week.

### C.4.2 Tidal Circulation

The least-squares method for determination of the harmonic constituent amplitudes and phases also provides estimated uncertainties in these parameters (Press, et al., 1992). Using standard propagation of errors techniques (Emery and Thomson, 1997) these uncertainties can be used to estimate the error in a tidal prediction made with the harmonic constituents. The prediction errors are independent of time, but exhibit some variation with location as shown in Figure C-3.

Generally, the errors are less than 3-4 cm/s. In a small region southeast of Block Island, however, they reach 5-10 cm/s.

Table C-1. Major tidal constituents in FRONT area.

| **Constituent** | **Period (hours)** |
|---|---|
| $S_2$ | 12.00 |
| $M_2$ | 12.42 |
| $N_2$ | 12.66 |
| $K_1$ | 23.93 |
| $O_1$ | 25.82 |

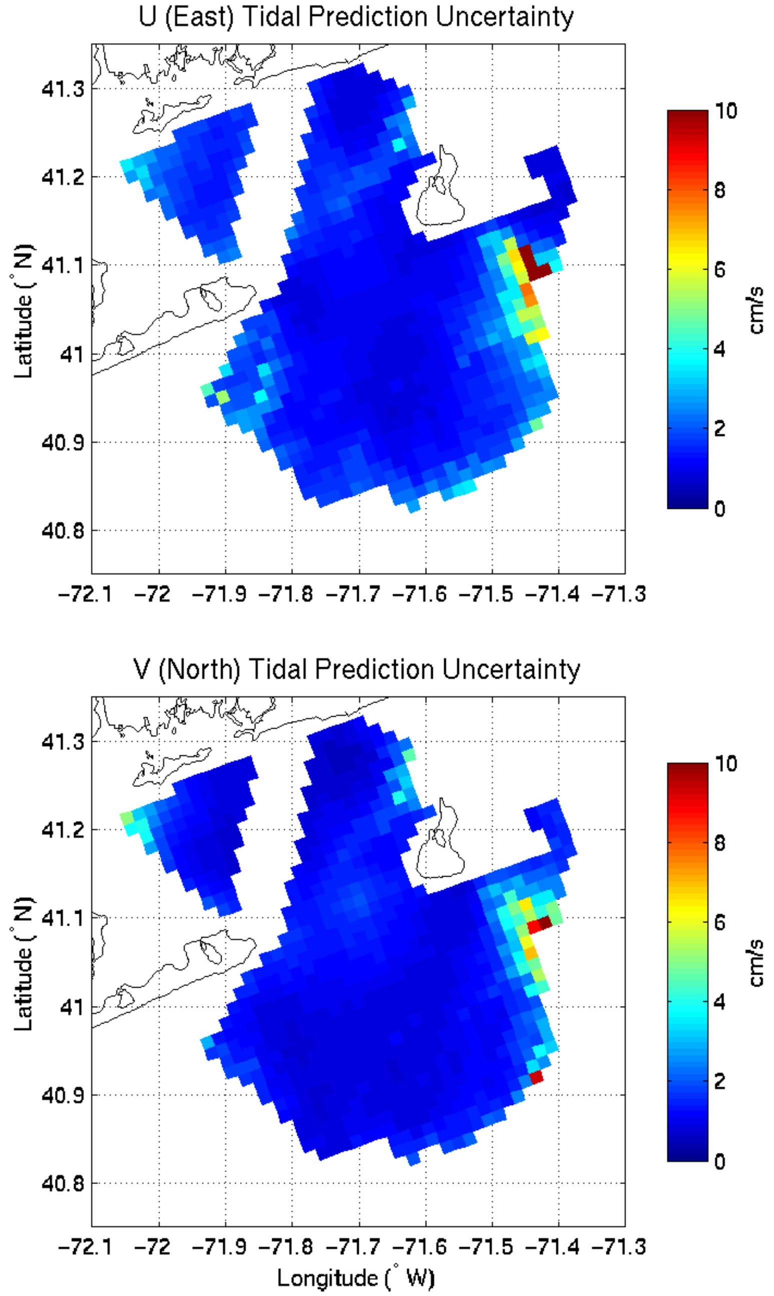

Figure C-3. Uncertainty in the eastward (top) and northward (bottom) components of the tidal current predictions. The predictions are made using constituents derived from harmonic analysis of 1-month time series.

### C.4.3 Non-tidal Motion: Hedging

Two methods for predicting the non-tidal current component were tested. We refer to the first as the "hedging" method. In it we assume that the non-tidal current observed for the last $T_H$ persists throughout the prediction interval. The second method exploits the archived data to characterize the structure of the correlation in the data. It is essentially an application of Gauss-Markov estimation (Wunsch, 1996).

The hedging method requires the estimation of the non-tidal current, $u'_{NT}$, at the time of prediction, $t_p$. The simplest approach is to subtract the predicted tidal current, $u_T$, from the observed current, $u_{OBS}$, at the time of the prediction. However, to reduce noise, some averaging is desirable. Our hedging estimate of the non-tidal flow is computed as

$$u_{NT}(t_p) = \frac{1}{M}\sum_{m=1}^{M} u'_{NT}(t_{p-m}) \tag{1}$$

where $u'_{NT} = u_{OBS} - u_T$ and M is the number of samples in the averaging interval $T_H$. The choice of $T_H$ is somewhat arbitrary but should reflect the timescale of autocorrelation. We have tested the values of 25 and 49 hours. The predictions derived from the 25-hour average were more accurate for short-term predictions (i.e. 24 hours or less) and we used it in the operational evaluation discussed below.

### C.4.4 Non-tidal Motion: Gauss-Markov

It has been well established that the non-tidal motion in this area is autocorrelated (Pettigrew, 1981) as it is elsewhere in the coastal ocean (see, for example, Kundu and Allen, 1976). This correlation can be exploited by representing the desired prediction at time $t_p+\delta t$ as a linear combination of previous measurements, i.e.

$$u_{NT}(t_p + \delta t) = \sum_{m=1}^{M} \alpha_m u'_{NT}(t_{p-m}), \tag{2}$$

where $\alpha_m$ represent weights and the sum is taken over the M prior data values. Unlike the hedging method defined in equation (1), the predicted non-tidal current is not constant during the prediction interval since (2) is evaluated for each $t_p+\delta t$. The Gauss-Markov theorem states that appropriately chosen weights, based on knowledge of both the measurement errors and the autocovariance of the data, produce a solution that minimizes the variance of the difference between the estimate and the true value. For a data series with zero-mean, this estimate is unbiased and is referred to as the best linear unbiased estimate (Wunsch, 1996).

Our procedure assumes that measurement errors have zero mean, are uncorrelated, and are normally distributed with standard deviation distributed as in the maps of Figure C-4. Autocovariance functions, are calculated at each location from one month of data and averaged over the entire CODAR domain. The autocovariance functions ($R_{xx}$), shown in Figure C-5, describe the degree of temporal correlation in the data time series. If we define $R_{nn}=\sigma I$, the weights are found to be

$$\alpha_i = \sum_{j=1}^{J} \left\{ R_{xx}(t_p,t_j)\left[R_{xx}(t_i,t_j)+R_{nn}(t_i,t_j)\right]^{-1} \right\}. \tag{3}$$

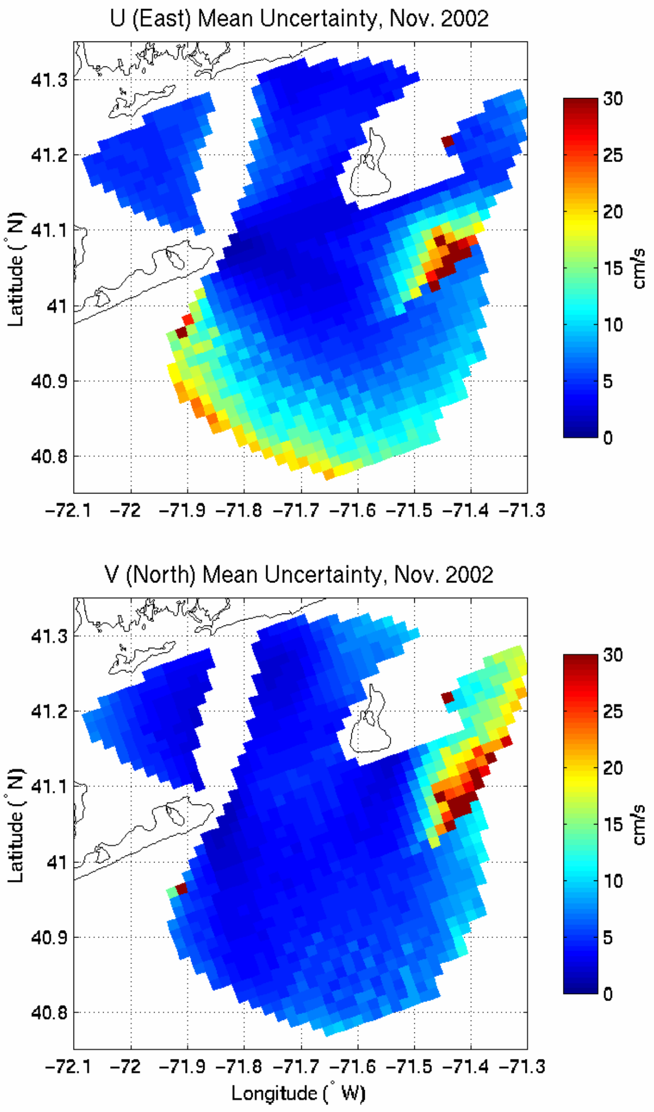

Figure C-4. Estimated uncertainty in CODAR current observations.

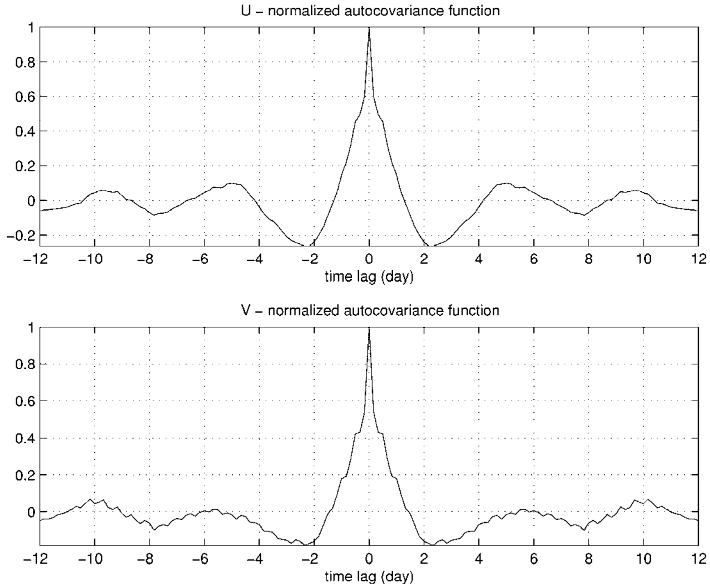

Figure C-5. Autocovariance functions for *u* (top) and *v* (bottom), averaged over the entire CODAR domain for the month of November 2002.

Data statistics are assumed to be stationary in time, but in operational mode this calculation could be repeated regularly, perhaps once a month, to ensure that long-term variations of the statistical character of the fields are captured.

An attractive advantage of the Gauss-Markov approach is that it also produces estimates of the uncertainty in the prediction. At short time scales, and in cases where the measurement signal to noise ratio is high, this uncertainty is approximately equal to the measurement noise. As the time of the prediction extends, the uncertainty approaches the data variance. This estimate of the uncertainty can be very useful for a short-term predictive modeling system, and its consistency is evaluated below.

## C.5 Evaluation of Forecasts

The algorithm is evaluated by comparing the predicted surface currents to subsequent measurements. The two methodologies are tested using a 28-day period starting December 1, 2002. The measure of the prediction error is the root-mean-square (RMS) difference between predicted and observed currents, defined for the eastward component as:

$$U_{RMS} = \sqrt{\frac{1}{N}\sum_{n=1}^{N}\left(u_p(t_n) - u_{obs}(t_n)\right)^2}, \qquad (4)$$

where $u_p(t_n)$ is the predicted eastward current, and $u_{obs}(t_n)$ is the corresponding measurement at time $t_n$, and the average is spatial over $N$ pairs of observations/predictions. $U_{RMS}$ is expected to depend on the time since the prediction was made, $t_n - t_p$, the forecast lag. Equation (4) and the corresponding equation for the northward velocity component, are evaluated separately for each forecast lag up to a maximum lag of 25 hours.

### C.5.1 Region-Averaged Differences

Evaluation of the differences averaged over the entire FRONT domain provides an assessment of the performance of the algorithm. Figure C-6 shows the dependence of $U_{RMS}$ for both the hedging and Gauss-Markov methods functions of the forecast lag. Note that the same tidal prediction method is used for both cases. As expected, the errors increase with the forecast lag, rapidly at first, and then approach constant values (approximately 15 cm/s for $v$ and 20 cm/s for $u$) at large lags. Forecasts of the northward component are more accurate than those of the eastward component for all forecast lags, with the difference being of the order of 3-6 cm/s. This is likely a regional effect, resulting from the fact that the wind-driven currents are predominantly in the east-west direction, whereas the more easily predicted tidal currents are oriented more north-south. The performance of the Gauss-Markov method is clearly superior to the hedging method at all forecast lags by approximately 2-3 cm/s.

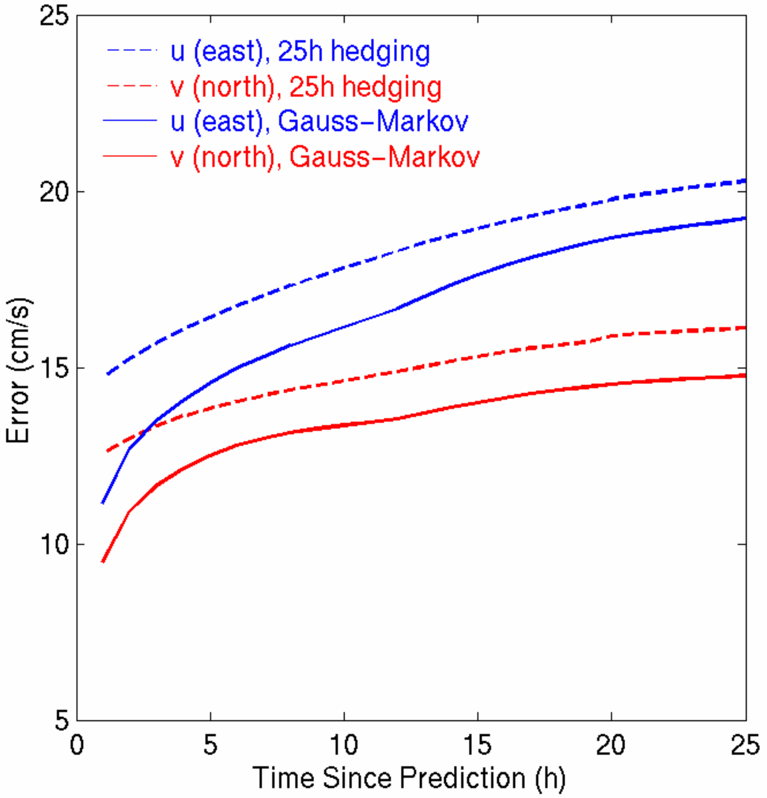

Figure C-6. $U_{RMS}$ differences averaged over the entire domain as a function of forecast lag. The dashed and solid curves are the results respectively of using the hedging method and the Gauss-Markov technique for estimating the non-tidal current.

### C.5.2 Spatial Structure of the Differences

In the FRONT region the dynamics and geometry conspire to create substantial spatial variations in the magnitude of the tidal and non-tidal current components. It is important, therefore, to investigate how the algorithm performs in different parts of the region. This is accomplished by evaluating the $U_{RMS}$ at each CODAR grid point by setting $N=1$ in and $t_n$ = 6, 12 and 24 hours in equation (4). Maps of the structure of $U_{RMS}$ are presented in Figure C-7, Figure C-8 and Figure C-9.

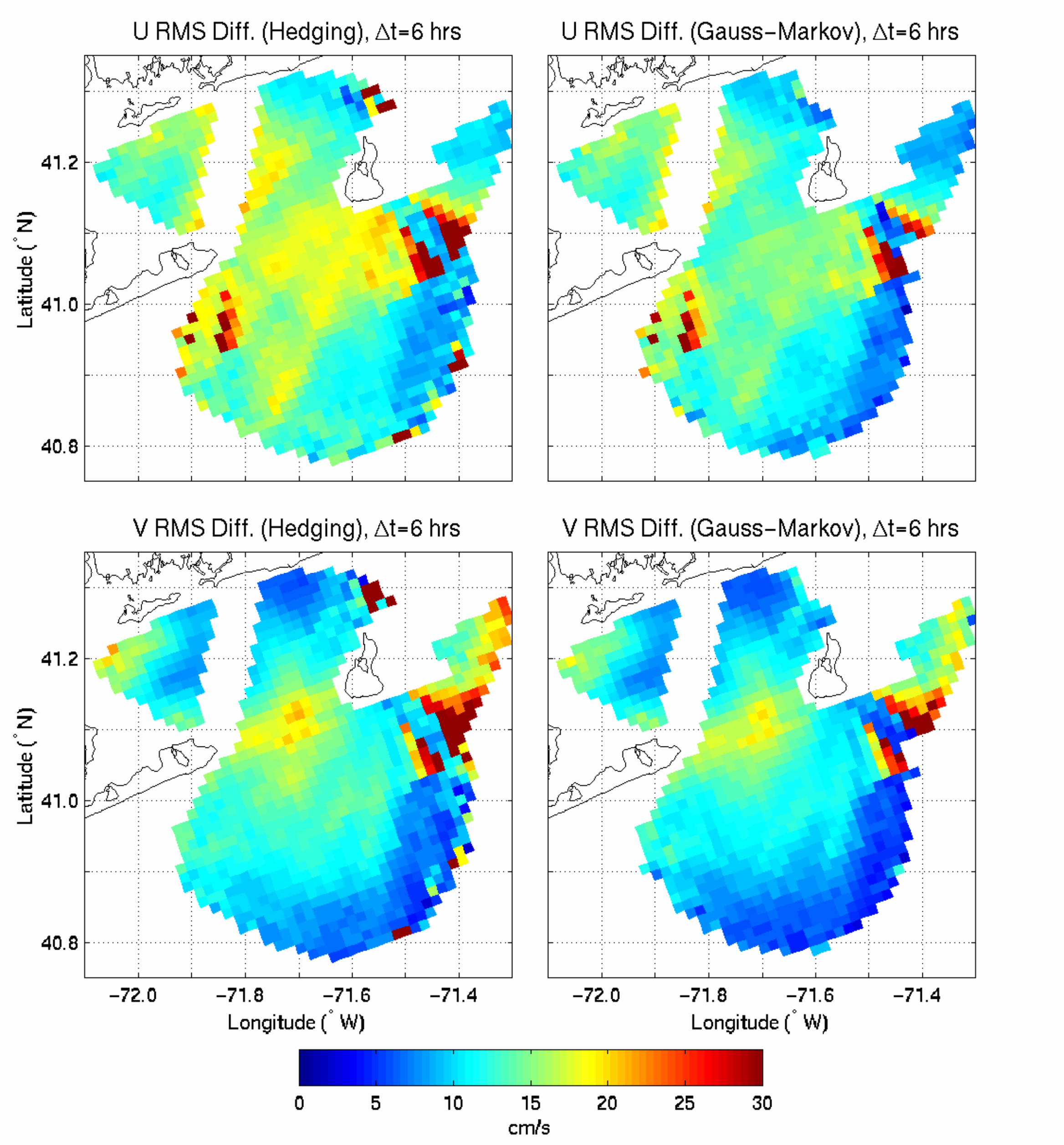

Figure C-7. Spatial structure of the RMS differences for predictions made using the hedging method (left) and the Gauss-Markov method (right), evaluated 6 hours after the prediction was made.

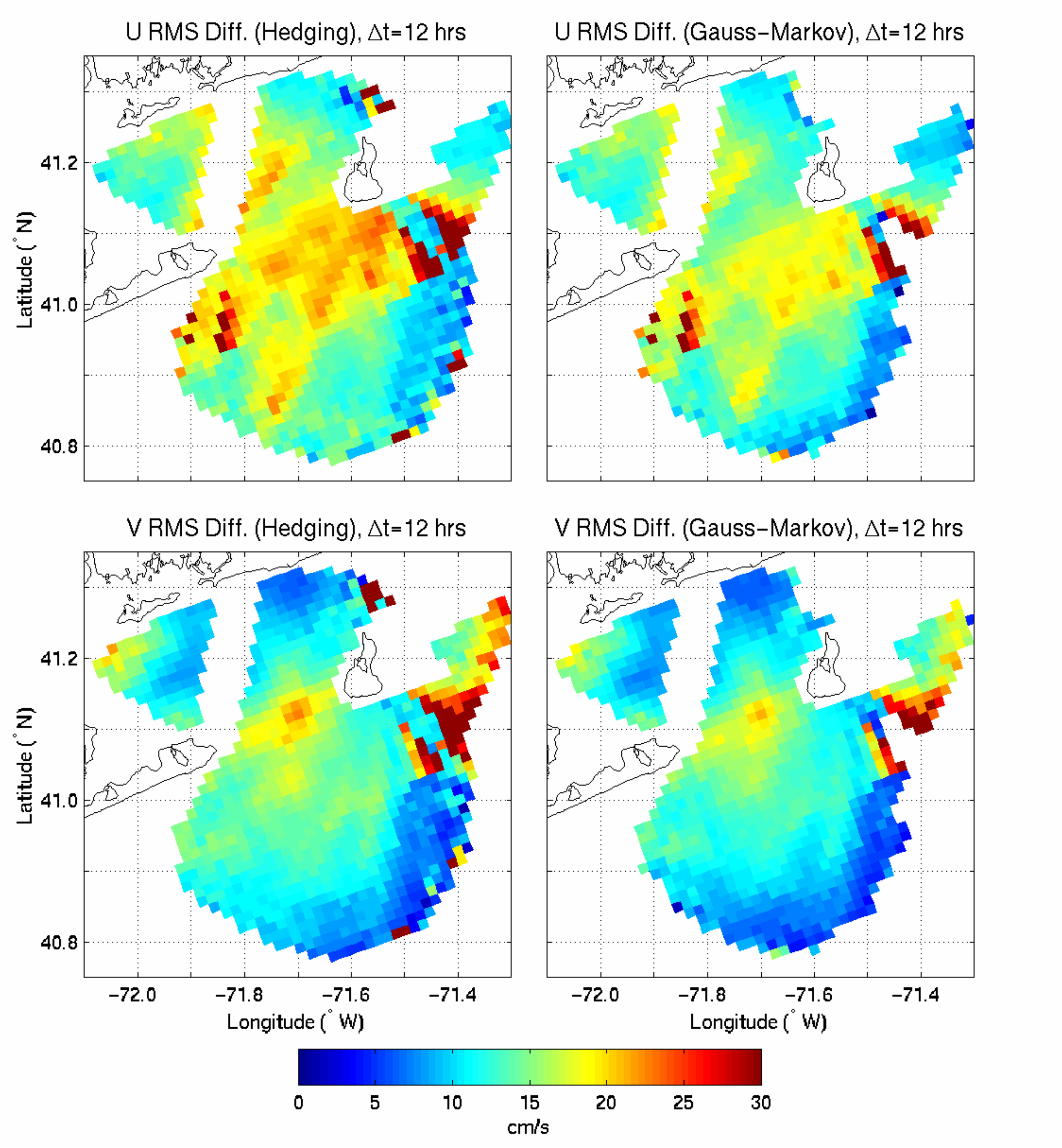

Figure C-8. Spatial structure of the RMS differences for predictions made using the hedging method (left) and the Gauss-Markov method (right), evaluated 12 hours after the prediction was made.

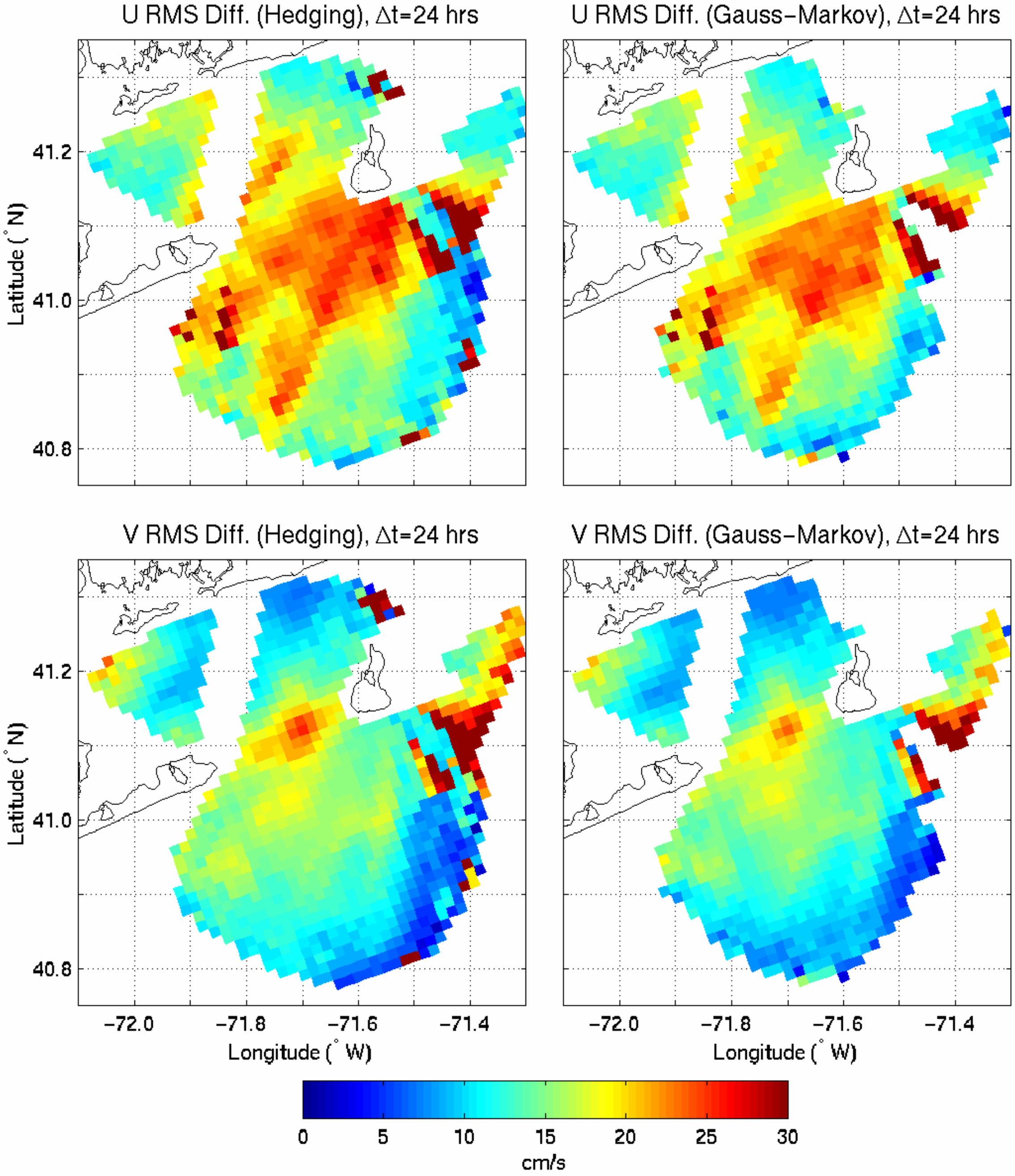

Figure C-9. Spatial structure of the RMS differences for predictions made using the hedging method.

It is immediately apparent from Figure C-7, Figure C-8 and Figure C-9 that the spatial structures in the error maps for the two methods are quite similar. As noted above, differences in magnitude are observed at all lags with the Gauss-Markov method performing somewhat better for both components. The largest errors in the eastward component occur along the edges of the domain, especially the areas south of Montauk Point and Block Island. These are regions where the CODAR measurements themselves are least accurate with respect to the eastward component (see Figure C-4, top). As will be discussed below, the increased measurement uncertainty damages both the prediction itself and its evaluation. The spatial structure of the error in the predicted northward component is quite different. Although predictions are poor at a few CODAR grid points along the edge of the coverage region southeast of Block Island, generally the largest errors occur in the zone between Montauk Point and Block Island. Because of the coastal geometry, the strongest north-south non-tidal currents and vertical stratification occur in this area, suggesting a linkage between current magnitude and the prediction error.

### C.5.3 Consistency of the Uncertainty estimates

For the current predictions to be useful for the prediction of Lagrangian trajectories and the uncertainty of the target location, it is essential that the uncertainties in the predicted current *at the time that the predictions are made* be established. Because of the superior performance of the Gauss-Markov technique and the fact that it provides error estimates as well, we focus in the following on the predictions made using this method.

The RMS differences between the predicted and observed surface currents result from three contributions. The observations themselves are uncertain, and there are errors associated with the prediction of the tidal and the non-tidal motions. Mathematically, this can be expressed:

$$U_{RMS} = \sqrt{\sigma_{obs}^2 + \sigma_{tidal}^2 + \sigma_{gm}^2}\ , \qquad (5)$$

where $U_{RMS}$ is the difference between the observations and predictions, and $\sigma_{obs}$, $\sigma_{tidal}$, and $\sigma_{gm}$ are the uncertainties in the observations, the tidal predictions, and the Gauss-Markov predictions of the non-tidal current, respectively. To evaluate the consistency of the observations and the assumptions, we compare the left-hand side of (5) with the right-hand side for both east and north components in Figure C-10. The fact that the points generally fall along line of unit slope, (the red lines in Figure C-10), is evidence that the prediction errors are consistent with the assumptions and estimates of the measurement and algorithm errors.

Equation 5 can be rearranged to provide an expression for the total prediction error in terms of the actual RMS difference and the estimated observational error:

$$\sigma_{pred} = \sqrt{\sigma_{tidal}^2 + \sigma_{gm}^2} = \sqrt{U_{RMS}^2 - \sigma_{obs}^2}\ . \qquad (6)$$

$\sigma_{pred}$ provides an *a posteriori* estimate of the true forecast performance since the prediction can not be better than the observations. Figure 11 shows the evolution of $\sigma_{pred}$ for the Gauss-Markov method averaged over the whole domain. The prediction error is only about 2 cm/s less than the RMS observation/prediction difference, reflecting the fact that $\sigma_{obs}^2$ in Figure C-4 is much smaller than $U_{RMS}^2$ in Figure C-7, Figure C-8 and Figure C-9. There is, therefore, considerable scope for improvement in the forecast model by the inclusion of dynamical constraints. The prediction errors for *u* and *v* are 10 cm/s or less at lags less than 2 hours and increase to 18 cm/s and 13 cm/s for *u* and *v* respectively at forecast lag of 25 hours.

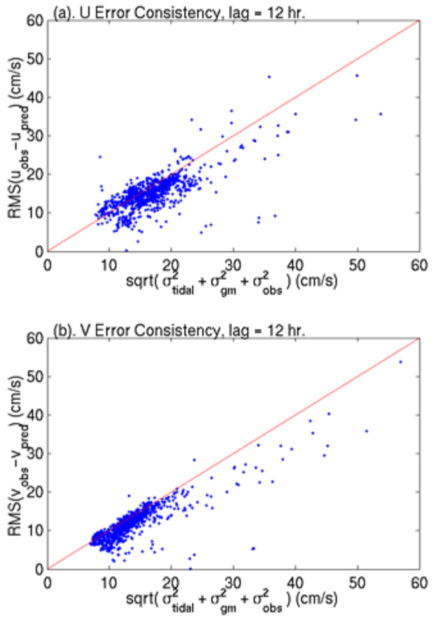

Figure C-10. Observed RMS difference between observed and predicted currents at 12 hours versus the sum of the errors in the observations and in the predictions (tidal and non-tidal) (a), for the eastward component and (b), for the northward component.

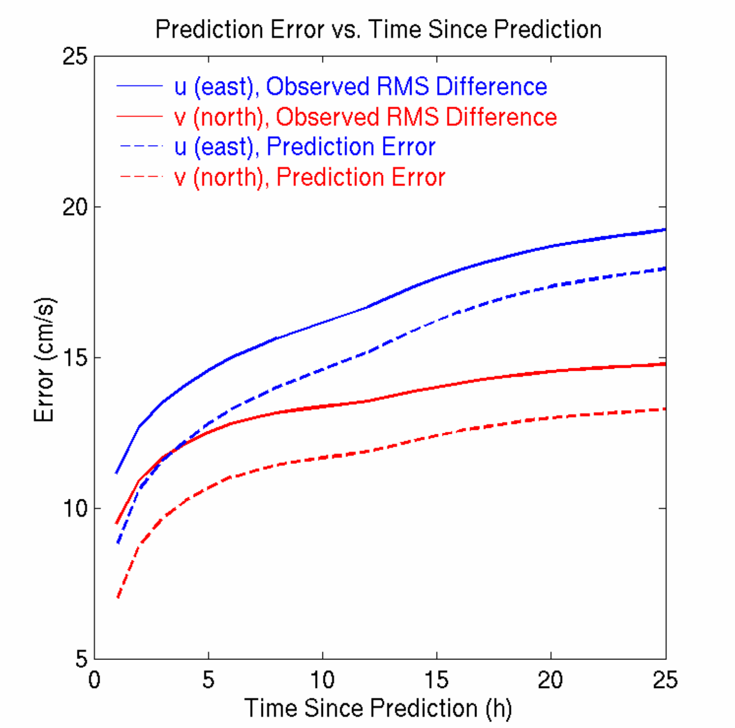

Figure C-11. The solid curves are the root mean square (RMS) difference between predicted and observed current, averaged over the entire CODAR domain, as a function of the time since the prediction using the Gauss-Markov method. The dashed curves are the estimated prediction errors.

### C.5.4 Sources of Error

The observations and predictions at the two CODAR grid points shown in Figure 1 will now be studied to examine the sources of error in the predictions. Figure C-12 (a) shows the evolution of the east component of the current observed at station 1 in blue and the predicted current with a forecast lag of 12 hours (i.e. the forecast computed at time t-2 hours) in red. The corresponding north components are shown in (c). Station 1 was chosen to represent the areas where tides dominate. In contrast, station 2 is representative of areas in which tides are weak and the motion is dominated by fluctuations at longer time scales. Figure C-12 (e) and (g) compare the east and north components respectively.

Time series of differences between the observations and predictions at station 1 (Figure C-12b and d) do not exhibit the strong tidal fluctuations present in the observations (Figure C-12a and c). This suggests that the tidal prediction is working well. This is consistent with the estimated tidal prediction errors in Figure C-4. Major errors arise from the non-tidal prediction. Visual comparison of the difference time series at the two stations (Figure C-12, b and f, and d and h), indicates a correlation, implying similar errors tend to occur simultaneously at the two stations and that there is a common source.

Prior analysis of the CODAR observations has shown that the wind is effective in driving surface current fluctuations over the whole domain (Ullman and Codiga, 2004). To examine this mechanism we obtained wind measurements from the NDBC Buoy 44017, located approximately 23 miles southwest of Montauk Point. Figure C-13 shows the dependence of the prediction-observation differences (with a forecast lag of 12 hours) on the wind at the time of the current observation. Positive correlations between the differences in the eastward currents and the eastward wind velocity, and between the northward wind and northward velocity components are apparent. For example, strong eastward winds tend to produce an eastward flow that is stronger than the predicted eastward flow. This results in a positive difference ($u_{obs} - u_{pred}$). The behavior is similar for northward winds.

We performed a similar analysis using the observation-prediction differences at a forecast lag of 3 hours. These display weaker correlation with the wind. This can be understood by noting that the Gauss-Markov prediction tends toward the time series mean as the forecast lag increases. So for 12-hour forecast lag, the prediction is closer to the mean than for the 3-hour case, so the wind-driven current fluctuations will produce larger differences that are correlated with the wind.

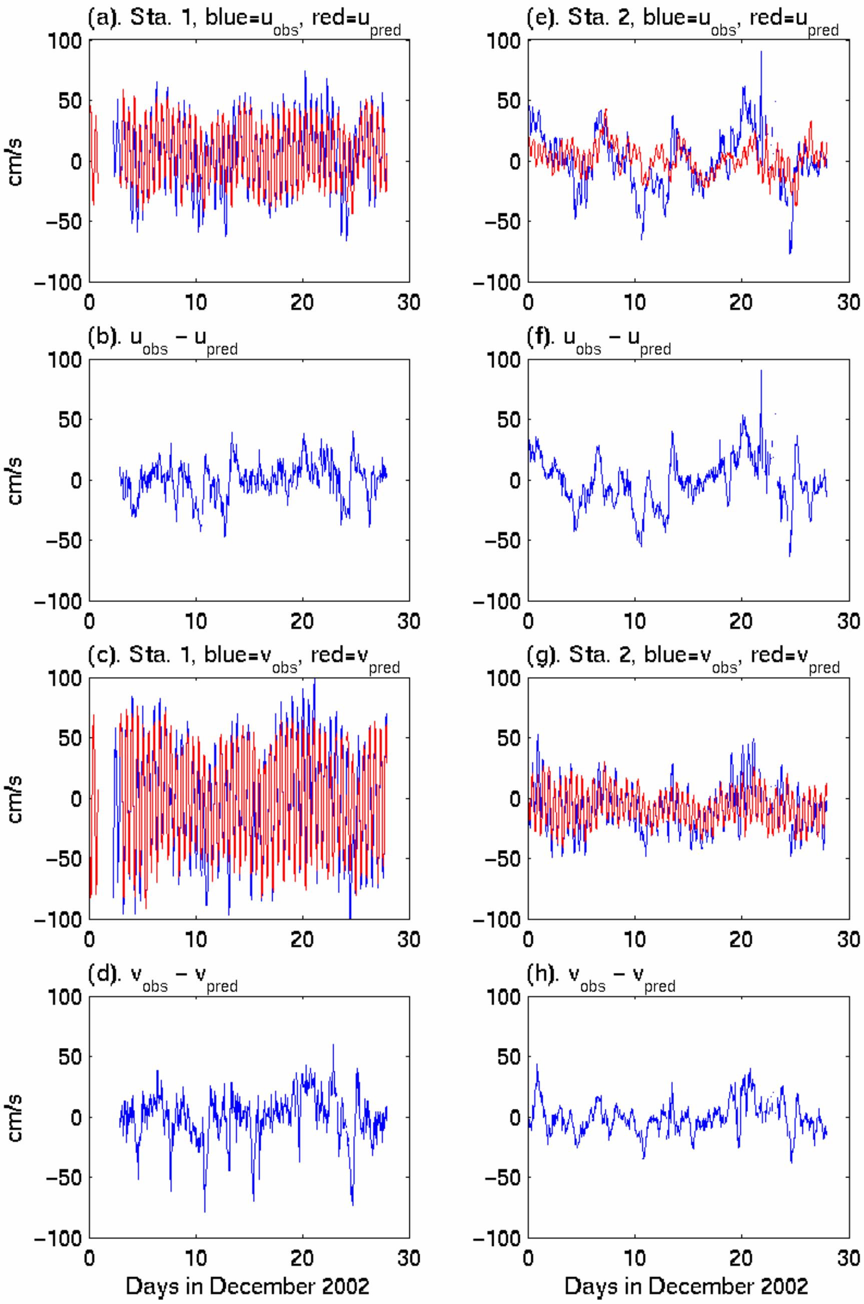

Figure C-12. Comparison of CODAR currents in December 2002 with predicted currents using the Gauss-Markov method 12 hours prior to the observation times. Shown are results from stations 1 (a-d) and 2 (e-h) in Figure C-1. Panels (a) and (e) show the observed and predicted *u* (east); (b) and (f) show the difference between the observed and predicted *u*; (c) and (g) show the observed and predicted *v* (north); (d) and (h) show the difference between the observed and predicted *v*.

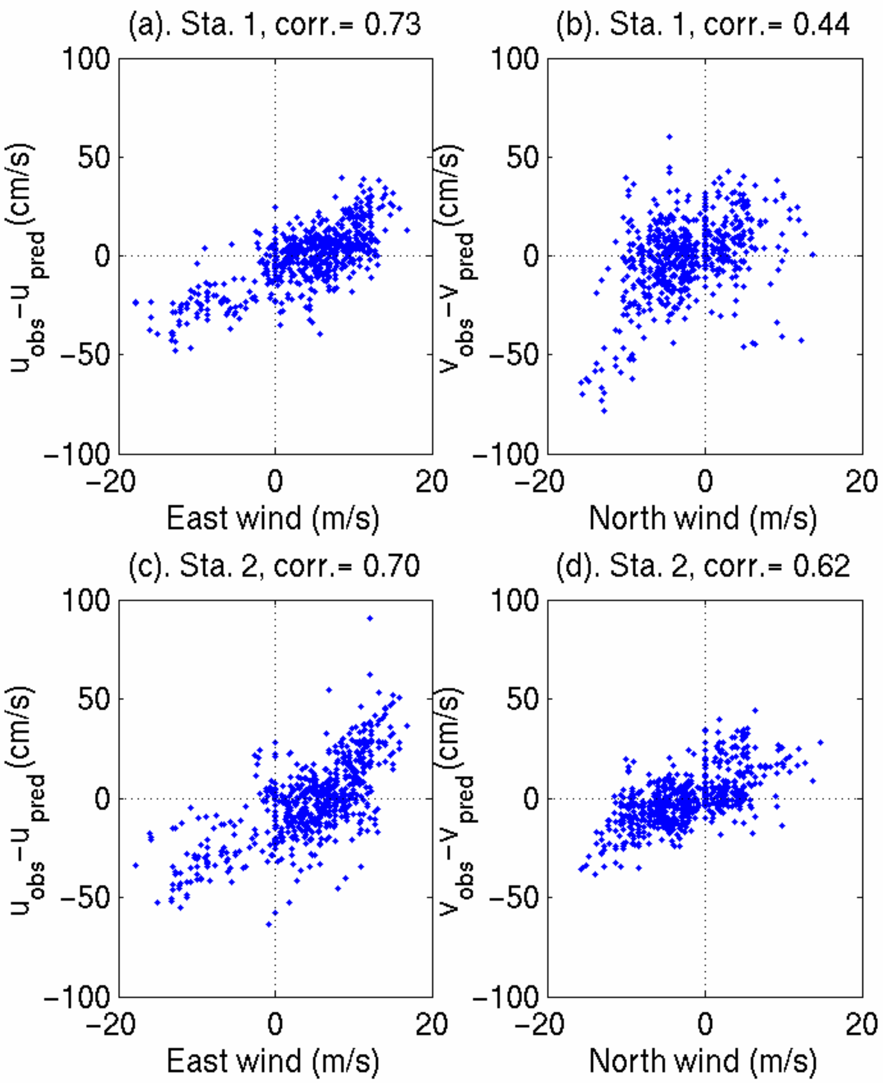

Figure C-13. Differences between observed and predicted (using the Gauss-Markov method and evaluating at forecast lag of 12 hours) currents versus the wind measured at National Data Buoy Center buoy 44017. (a, c) eastward currents at stations 1 and 2 (Figure B-1) versus the eastward wind. (b, d) northward currents at stations 1 and 2 versus the northward wind. Correlation coefficients are given above each plot.

## C.6 Trajectory Predictions Using CODAR data and Current Predictions

To demonstrate the potential practical utility of our empirical forecast approach, we now show its performance in a problem of significant importance. The ability to predict the trajectory of an object released in the ocean at a known time and location is critical to effective marine search and rescue operations. It also has application in the management of oil spill and some military operations. Since we have developed a forecast capability for the Eulerian currents, we now evaluate its utility in the prediction of particle motion. We first introduce the method we employ for the Euler-Lagrange transformation and then test the approach by comparing drifter tracks to trajectory predictions based on forecast currents, and ones based on current observations. These comparisons allow us to estimate the expected errors and the relative contributions of the uncertainty in the data and the forecast algorithm. We also evaluate the effectiveness of an algorithm like that used at the moment to quantitatively establish the magnitude of the improvement that could be achieved with an SCMS.

### C.6.1 Trajectory Prediction

By definition, the Eulerian and Lagrangian velocity at any particular point, $\mathbf{x}_p$, and time, $t$, the Lagrangian velocity and Eulerian velocity, $\mathbf{u}(\mathbf{x}_p, t)$, must be equal, i.e.,

$$\frac{d\mathbf{x}_p}{dt} = \mathbf{u}(\mathbf{x}_p, t) \qquad (7)$$

The SCMS system provides us with $\mathbf{u}_{\mathbf{obs}}(\mathbf{x}, t)$ at hourly intervals and the forecast algorithm allows us to compute $\mathbf{u}_{\mathbf{pred}}(\mathbf{x}, t)$ for a short time into the future. We can use either of these to approximate the right-hand side of (7). Obviously the forecast must be used operationally, but since the predicted currents can not be shown to be any more accurate than the observations, use of the data,

$$\mathbf{u}=\mathbf{u}_{\mathbf{obs}}(\mathbf{x}, t), \qquad (8)$$

in (7) establishes the upper bound for the performance of the prediction of the Lagrangian trajectory.

The numerical integration of (7) is quite straightforward and we employed a simple second-order predictor-corrector scheme (Press et al, 1992). The velocity must be interpolated from the data/prediction grid to $\mathbf{x}_p$ and we employed a nearest neighbor averaging scheme. The velocity components at the closest four grid points are weighted inversely as the square of the distance from $\mathbf{x}_p$. This is a robust method in the sense that it will provide an interpolated velocity in the presence of data gaps. In the absence SCMS data, archived tidal constituents at the nearest station available, $\mathbf{x}_\mathrm{N}$, could be used to estimate the right side of (7). This is equivalent to the approximation

$$\mathbf{u}(\mathbf{x}_p, t) = \mathbf{u}(\mathbf{x}_N, t) = \mathbf{u}_N(t) \qquad (9)$$

which ignores the spatial structure of the circulation. Since this is all that is available to the CG at this time we compare the consequences approximation (9) to our approach, $\mathbf{u}(\mathbf{x}_\mathrm{p}, t) = \mathbf{u}_{\mathbf{pred}}(\mathbf{x}_\mathrm{p}, t)$, and to the best prediction possible with SCMS data, (8). Note that the tidal constituents used in this study were obtained from the National Oceanic and Atmospheric Administration for the location located 41°2.9′ N, 071° 57.6′ W.

An example of 24-hour trajectories predicted using $\mathbf{u}_N$ and $\mathbf{u}_\mathrm{obs}$ in (7), together with the track of a drifter released near $\mathbf{x}_\mathrm{N}$ at 00:00 on 16 December, 2002 are shown in Figure C-14. The release point is shown by the black X. The surface velocity field at the end of the 24 hours is also shown to illustrate the spatial structure of the flow in the region. The drifter trajectory is represented by

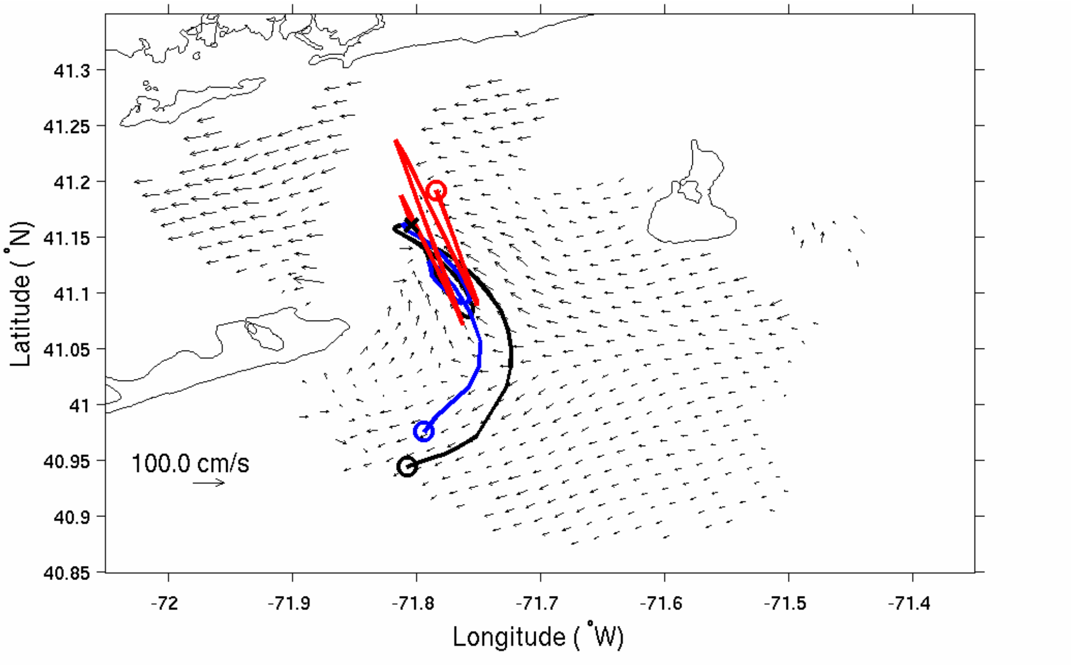

Figure C-14. Sample Trajectory Predictions.

the black line, and the simulated tracks using $\mathbf{u}_N$ and $\mathbf{u}_{\text{obs}}$ are colored red and blue respectively. The open circles denote the final positions. In this example the trajectory predicted using $\mathbf{u}_N(t)$ has a large error after 24 hours. The separation between the prediction and the drifter location is approximately 25 km. In contrast, the trajectory predicted using the $\mathbf{u}_{\mathbf{obs}}(\mathbf{x},t)$ is only 3 km. This case clearly illustrates the consequences of neglecting the spatial structure of the circulation. Of course, in the performance of the trajectory, simulations are sensitive to the release location and the Figure 14 is an extreme case. We explore the statistics of the errors in the next section.

### C.6.2 Trajectory Error Statistics

As Section C.3, each drifter trajectory was segmented into 24-hour segments with the beginning of each segment offset by 6 hours. Current predictions were generated for 24 hours for each drifter segment. Each segment was then treated like an independent drifter release and trajectory predictions computed using three estimates of the Eulerian current, $\mathbf{u}_N(t)$, $\mathbf{u}_{\text{obs}}(\mathbf{x},t)$, and $\mathbf{u}_{\text{pred}}(\mathbf{x},t)$. This approach allowed 140 release points to be sampled throughout the FRONT CODAR domain. At each time step, the separation between the actual and predicted SLDMB positions was computed and stored. The resulting database of separation versus time was used to produce the histograms of separation at 3, 6, 12 and 24 hours presented in Figure C-15. We then computed the separation value that was greater than 95 percent of the estimates and present it as a time series in Figure C-16.

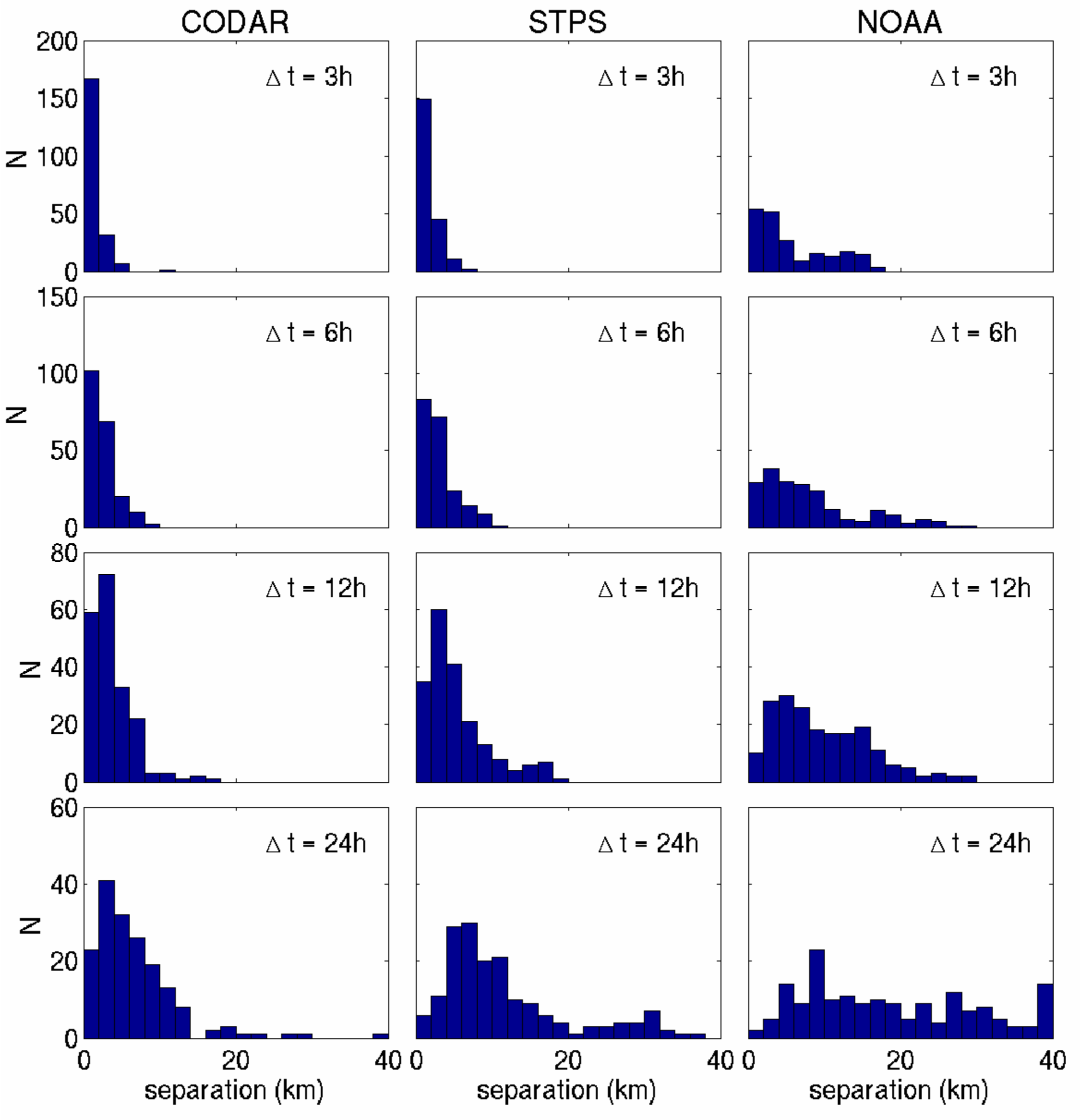

Figure C-15. Block Island Region Trajectory Error Histograms.

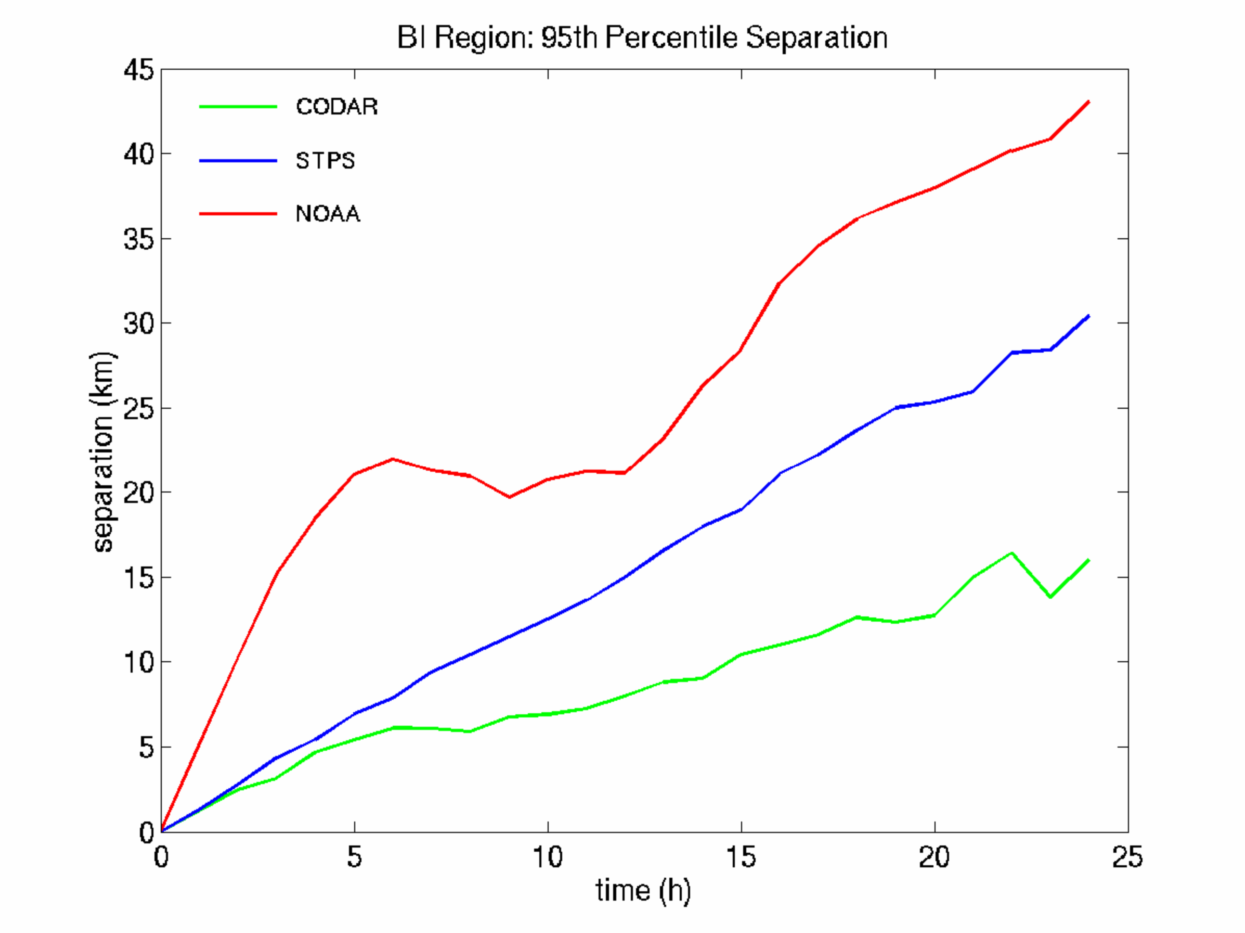

Figure C-16. Block Island Region 95th Percentile Separation.

The left column in Figure C-15 shows histograms of the separation between drifters and the simulations (the target error) using observed currents, $\mathbf{u}_{\mathrm{obs}}(\mathbf{x},t)$. The center and right columns show the performance of the simulations based in the forecast currents $\mathbf{u}_{\mathrm{pred}}(\mathbf{x},t)$, and $\mathbf{u}_{\mathrm{N}}(t)$ respectively. The rows show results at prediction times of 3, 6, 12, and 24 hours.

Comparison of the histograms at any time shows that the lowest modal values of the target errors occur when observed velocities are used (left column). The central and right columns show that the modal target error and width of the histogram are both substantially smaller when the forecast algorithm is employed. For example, at an elapsed time of 3 hours, the $\mathbf{u}_{\mathrm{pred}}(\mathbf{x},t)$ predicted positions are always within 10 km of the actual drifter position, whereas a significant number of the $\mathbf{u}_{\mathrm{N}}(t)$ based predictions are in error by 10-20 km.

The evolution of the target error statistics is most clearly summarized in Figure 16 by the time series of the 95 percentiles. The three curves represent the three current sources. The green, blue and red lines show the values obtained with $\mathbf{u}_{\mathrm{obs}}(\mathbf{x},t)$, $\mathbf{u}_{\mathrm{pred}}(\mathbf{x},t)$, and $\mathbf{u}_{\mathrm{N}}(t)$. At all times, the predictions made using data are the best and those made using $\mathbf{u}_{\mathrm{N}}(t)$ are the worst, with trajectories predicted using the forecast currents intermediate in accuracy. The 95th percentile separation value increases monotonically for the $\mathbf{u}_{\mathrm{obs}}(\mathbf{x},t)$, and $\mathbf{u}_{\mathrm{pred}}(\mathbf{x},t)$ based trajectory predictions with values at 24 hours of 15 and 30 km respectively. Using $\mathbf{u}_N(t)$, the separation decreases slightly between about 6 and 12 hours before rising again to a 24-hour value of 40-45 km. The reason for this decrease at intermediate times is due to the fact that the $\mathbf{u}_N(t)$ currents are mainly tidal with a period of 12.4 hours. If applied in a region where tidal currents are actually weak (station 2 in Figure C-1 for example), the predicted drifter motion will show a large oscillation with this period, whereby the actual drifter will move slowly more or less in one direction. At the end of 12.4 hours in this case, the simulated drifter will have almost returned to its starting point and therefore be closer to the actual drifter position.

### C.6.3 Trajectory Errors versus Wind

CODE-type drifters are thought to exhibit negligible windage (motion relative to the surface water driven because of wind). This was investigated empirically by comparing drifter prediction errors, in the Block Island region, with winds measured at a nearby NOAA buoy (44017). The separation between predicted and actual drifter position after 24 hours was plotted versus the mean wind magnitude over the 24-hour prediction interval, as shown in Figure C-17. The three panels show, from top to bottom, the comparisons of wind speed to separation for predictions using $\mathbf{u}_{obs}(\mathbf{x},t)$, $\mathbf{u}_{pred}(\mathbf{x},t)$, and $\mathbf{u}_N(t)$. The first comparison shows that prediction errors using observed currents, $\mathbf{u}_{obs}(\mathbf{x},t)$, for the prediction do not correlate with the wind. We interpret that this is because the CODAR observations include the real wind-driven surface current component, which is known from prior unpublished work to be large. In contrast, the drifter trajectories simulated by the predicted currents, $\mathbf{u}_{pred}(\mathbf{x},t)$ and $\mathbf{u}_N(t)$, tend to be more seriously in error under high wind conditions. Since $\mathbf{u}_N(t)$, does not include any subtidal frequency motion, it is not surprising that the target errors correlate with the wind speed. However, the CODAR observation, and the predictions based on them, $\mathbf{u}_{pred}(\mathbf{x},t)$, do have information about the wind driven current, though it appears that the algorithm could be improved by capturing the effect of wind more directly. Note however, that the drifters were in the region of FRONT CODAR coverage for only 10 days and we may not have adequately sampled the response to wind.

## C.7 Conclusions and Recommendations

The surface current forecast algorithm developed in this paper is based on the independent prediction of the tidal and non-tidal surface current components. Tidal currents are predicted using harmonic constituents derived from a 1-month record of CODAR estimated surface currents. Two methods for predicting the non-tidal component were tested: hedging and Gauss-Markov estimation. The Gauss-Markov method was clearly superior at all forecast lags up to 25 hours, the maximum lag that was tested. Since the calculation of the autocorrelation function for the Gauss-Markov method requires at least a 30-day archive of currents, the hedging approach may be useful at new SCMS locations. Either of these strategies is capable of turning data from a coastal current observing network into useful forecast products.

Analysis of the combined, tidal plus Gauss-Markov non-tidal, prediction algorithm over a 1-month period gives estimates of the region-averaged prediction error of 9-18 cm/s for the eastward component and 7-13 cm/s for the northward component. The range of prediction errors reflects the increase in prediction error with forecast lag. Note that the performance should be expected to be site-specific.

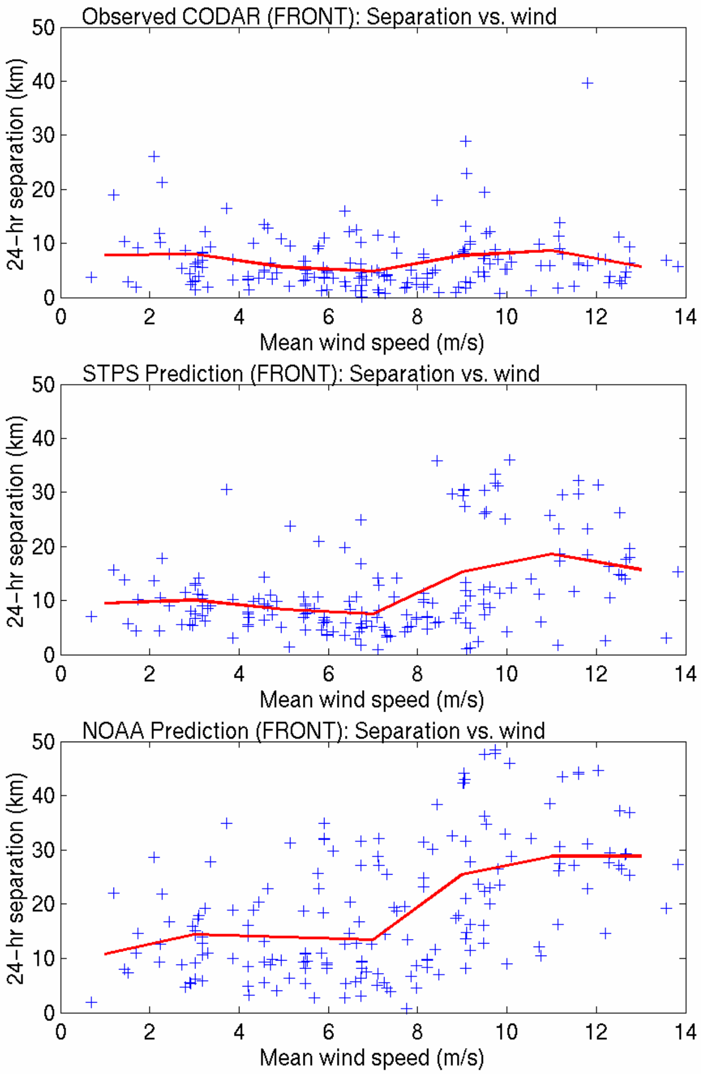

Figure C-17. Block Island Region 24-hour Separation versus Wind. A key component of the Short Term Predictive System (STPS) is the estimation, at the time of prediction, of the uncertainties associated with the forecast velocities. The magnitudes of the predicted uncertainties are consistent with the computed RMS differences and the estimated uncertainties in the observations themselves. This leads to the conclusion that the forecast uncertainties can be reliably used to characterize the statistics of errors in the predictions. The prediction uncertainties are essential to modeling Lagrangian dispersion.

The correlation of observation/prediction differences with wind, which is known to be the major forcing function for non-tidal fluctuations in the FRONT region, is somewhat surprising. It suggests that the relative weight placed on the data contributing to the prediction is not quite correct. This could result from incorrect characterization of either the observational errors in the velocity components or the data autocovariance functions. The observational errors are estimated by assuming that the uncertainty in the radial velocity from a given site is spatially and temporally constant, which has yet to be verified for the CODAR system. The autocovariance functions used in our implementation of the Gauss-Markov estimation procedure are averaged spatially over the CODAR domain and are then scaled by the actual data variance at each grid point. This spatial averaging is done to produce smoother autocovariance functions, the use of which helps to reduce the incidence of wild predictions at grid points with frequent data gaps. However, there is clearly some spatial structure present in the autocovariance functions and its neglect can lead to misrepresentation of the data covariance in some locations in the region. Further work is necessary to determine whether the use of more robust autocovariance functions derived from historical data records of say several months will produce more accurate predictions.

Although more work is necessary to confirm this point, preliminary work on the prediction methodology carried out using CODAR data from August 2001 resulted in somewhat lower prediction error during that time period as compared with the December 2002 period presented in this report. As the accuracy of the tidal prediction is unlikely to vary in a systematic manner over the seasons, this suggests that the non-tidal predictability may be reduced in winter. This may be due to increased non-tidal (wind-driven) current fluctuations driven by wintertime wind intensification.

Comparison of drifter trajectory predictions with observed trajectories demonstrates that the SCMS-based forecasts are clearly superior to current practice. This arises from two major improvements: a good representation of the spatial structure of the mean and tidal flow, and inclusion of an estimate of the low frequency variability. The simple Gauss-Markov approach results in mean drifter position errors after 6 hours of 7 km and 13 km after 12 hours. These errors are approximately half of that obtained using the tidal current predictions from the archives maintained by NOAA, as is currently the operational practice in the CG. Operational use of the currently available technology could, therefore, have the potential of reducing predicted search areas by a factor of four.

## C.8 Acknowledgements

We are grateful to the R&DC for the financial and operational support of this work through contract DTCG39-00-D-R300022, task order DTCG32-02-F-200004 to Microsystems Integration Inc. In particular, we thank Brian Krenzien and Jennifer O'Donnell who provided helpful guidance at the beginning of the project, and Mike Sprague of MSI who coordinated the project.

## C.9 References

Davis, R., 1985, Drifter Observations of Coastal Surface Currents During CODE: The Method and Descriptive View," Journal of Geophysical Research, 90 4741-4755.

Emery, W. J. and R. E. Thomson, *Data Analysis Methods in Physical Oceanography*, 1st ed., Elsevier, New York, 1997.

Glenn, S.M. and O. Schofield, 2003. Observing the Oceans from the COOL Room: Our History, Experience, and Opinions, Oceanography, V16, N4, pp. 37-52.

Kohut, J. T., Glenn, S. M., Chant, R. J. 2004. Seasonal current variability on the New Jersey inner shelf. Journal of Geophysical Research. 109, C07S07, doi: 10.1029/2003JC001963.

Kundu, P. K. and J. S. Allen, 1976, Some threee dimensional characteristics of low frequency current fluctuations near the Oregon coast. J. Phys. Oceanogr. 19, 1091-1101.

O'Donnell, J., and A. Allen, 1992. Observations of the hydrography and Lagrangian surface drift in Block Island Sound. Proceedings of the First Long Island Sound Research Conference, New Haven, Connecticut. October 23-24, 1992.

Pettigrew, N. R., 1981. The dynamics and kinematics of the coastal boundary layer off Long Island. Ph.D. Thesis, MIT-WHOI joint Program in Physical Oceanography.

Press, W. H., S. A. Teukolsky, W. T. Vetterling, and B. P. Flannery, *Numerical Recipes in FORTRAN: The Art of Scientific Computing*, 2nd ed., Cambridge University Press, Cambridge, U. K., 1992.

Ridderinkhof, H. & Zimmerman, J. T. F. 1992 Chaotic stirring in a tidal system. Science 258, 1107–1111.

Ullman, D. S. and D. L. Codiga, 2004: Seasonal variation of a coastal jet in the Long Island Sound outflow region based on HF radar and Doppler current observations. In press, *J. Geophys. Res.* 109, C07S06, doi:10.1029/2002JC001660.

Ullman, D.S. and P. C. Cornillon, 1999: Satellite-derived sea surface temperature fronts on the continental shelf off the northeast US coast. J. Geophys. Res., 104, 23,459-23,478.

Wunsch, C., *The Ocean Circulation Inverse Problem*, Cambridge University Press, Cambridge, U. K., 1996.

# APPENDIX D.
# TRAJECTORY PREDICTION USING HF RADAR SURFACE CURRENTS: MONTE-CARLO SIMULATIONS OF PREDICTION UNCERTAINTIES

February 2, 2005

David S. Ullman[1], James O'Donnell[2], Josh Kohut[3], Todd Fake[2], and Arthur Allen[4]

[1]Graduate School of Oceanography, University of Rhode Island, Narragansett, RI
[2]Department of Marine Sciences, University of Connecticut, Groton, CT
[3]Institute of Marine and Coastal Studies, Rutgers University, New Brunswick, NJ
[4]US Coast Guard Office of Search and Rescue, Groton, CT

## Abstract

An important aspect of trajectory modeling in support of search and rescue applications is the assessment of the uncertainty in the search target position. Many factors contribute to the uncertainty and spread of the final position distribution, including uncertainty in: initial position, initial time of incident, wind and leeway, and surface currents. This paper focuses on the contribution of the uncertainty in the surface currents to the search and rescue final probability distribution. Monte-Carlo particle trajectory simulations using surface currents derived from CODAR High Frequency (HF) radar systems were performed with sub-gridscale motions parameterized using random walk and random flight turbulence models, and the resulting trajectories were compared to the trajectories of surface drifting buoys. Velocity statistics for the turbulence models were derived from covariance functions of time series of differences between CODAR and drifter estimates of surface currents. Drifter positions, predicted over 24-hour periods using CODAR currents, were found to be more accurate predictors of the real drifter positions than were initial positions. The particle dispersion predicted by 24-hour Monte-Carlo simulations using the estimated fluctuation statistics was used to determine 95 percent confidence regions, which were subsequently tested using the real drifter location. Search areas determined from the 95 percent regions using the random flight model were found to be 80-90 percent effective, in reasonable agreement with the expected 95 percent success rate. On the other hand, search areas computed from random walk modeling were found to be inadequate unless the diffusion coefficient was increased to approximately the random flight value. The effectiveness of the random flight search areas lends support to the proposed methodology for estimating turbulence parameters from drifter-CODAR velocity differences.

## D.1 Introduction

The recent proliferation of coastal High Frequency (HF) surface wave radar installations for mapping surface ocean currents provides a rapidly expanding capability for real-time observation of surface currents. These data have the potential to dramatically improve the efficiency and success rate of search and rescue operations in coastal waters. For this reason, the R&DC has initiated a program to assess the effectiveness of trajectory predictions using currents derived from HF radar, and if warranted, to implement the use of this technology on an operational basis. Preliminary work toward this end was reported by Ullman, O'Donnell, Edwards, Fake, Morschauser, Sprague, Allen, Krenzien, (2003).

Trajectory modeling applied for search and rescue operations must provide a measure of the uncertainty in the surface current portion of drift of the search and rescue object in order for an optimal search area to be delineated. The identification of a search area is based on a balance between the need to define a large enough area to ensure that the target is within the search area and the reality that search resources are finite. The size of an operational search area is related to the magnitude of various uncertainties including those introduced by poorly known initial target position and time, velocity errors, and target leeway. This paper focuses on the estimation of a search area due only to uncertainties in the drifter advective velocity provided by HF radar systems.

Search areas are estimated in this paper using a Monte-Carlo approach whereby the trajectories of an ensemble of 1,000 particles are modeled over 24 hours. The advective velocity is decomposed into a deterministic, large-scale component measured by the CODAR plus a non-deterministic component representing a combination of sub-gridscale motion and errors in the CODAR velocity. We make use of the hierarchy of stochastic particle models outlined by Griffa (1996), testing the first two of these, the random walk and random flight models, in the present work.

## D.2 Data and Methodology

### D.2.1 Drifter Trajectories

A number of drifter releases in the Mid Atlantic Bight were performed by the R&DC over the period 2002-2004 with the objective of providing a data set with which to assess trajectory predictions. Drifters were released in Block Island Sound within the coverage region of the standard-range CODAR system operated by the Universities of Rhode Island and Connecticut (Figure D-1). A number of these drifters eventually passed through the coverage region of Rutgers University's long-range CODAR system and a number of additional drifters were released within that zone as well (Figure D-2). The CODE-type drifters (Allen, 1996) recorded Global Positioning System (GPS) fixes on one-half hour intervals and transmitted positions via Argos. With one-half hour sampling and a nominal GPS position uncertainty of 10 m, the uncertainty in the velocity of the drifter is O(1 cm/s), which will be seen to be small compared to the observed differences between drifter and radar-derived velocities.

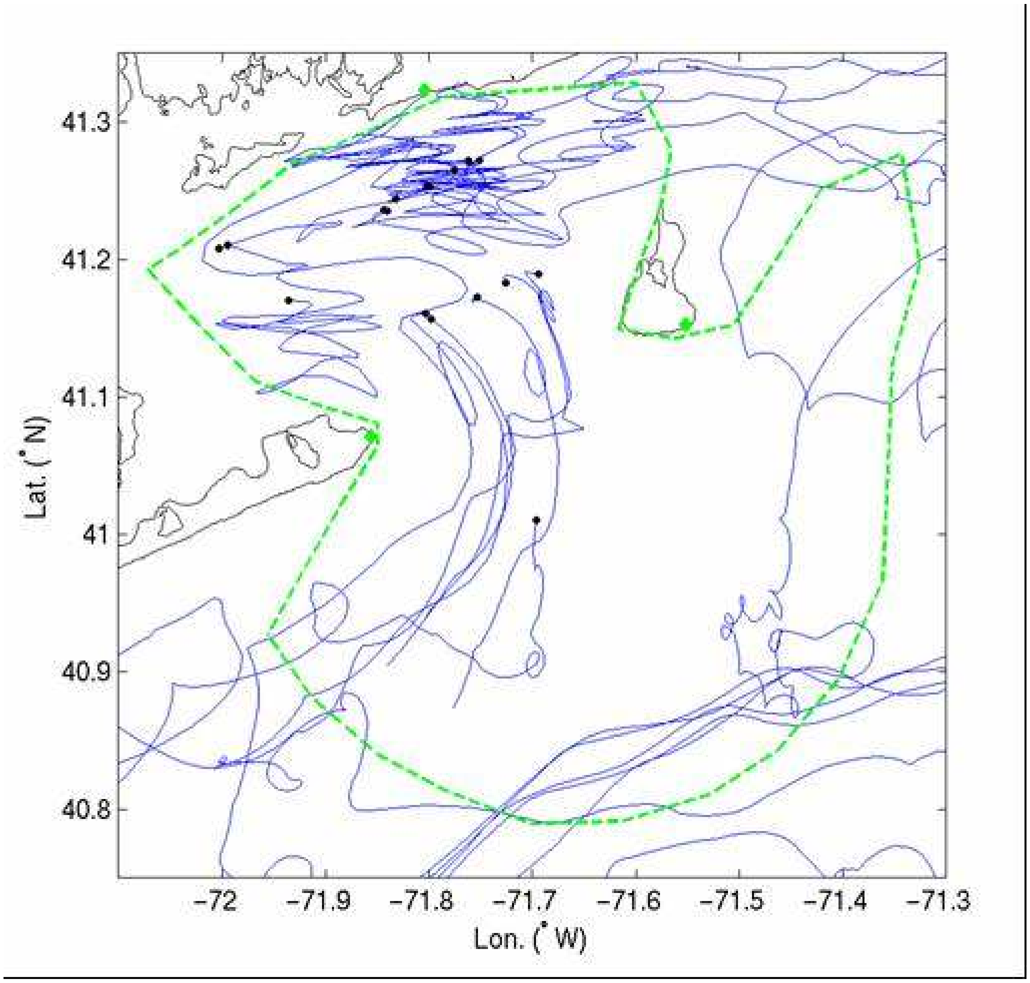

Figure D-1. Trajectories of surface drifters deployed during December 2002 and March 2003 in the Block Island CODAR region. The black dots show the release points of each drifter (note that some were retrieved and redeployed). The green diamonds show the locations of the CODAR sites, and the dashed line shows the approximate 10 percent coverage region.

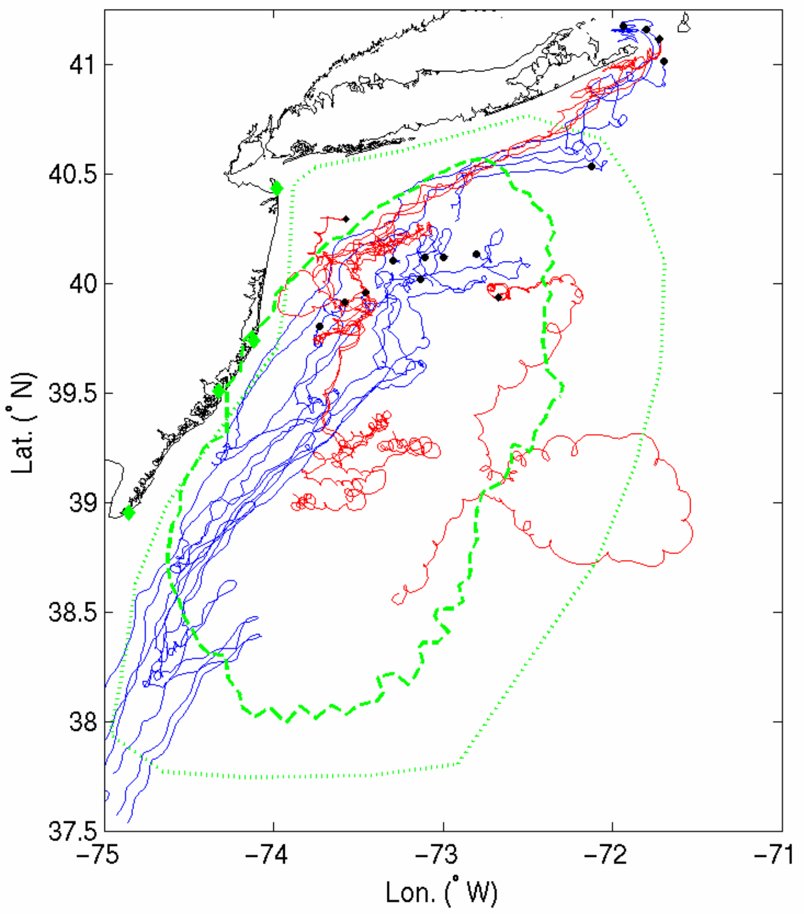

Figure D-2. Trajectories of surface drifters deployed during March 2003 (blue) and July 2004 (red) that passed through the New Jersey shelf CODAR domain. The black dots show the release points of each drifter. The green diamonds show the locations of the CODAR sites. The dotted line shows the nominal coverage zone and the dashed line shows the approximate 10 percent coverage region.

Drifters were deployed in December 2002 in the Block Island region and again in March 2003. A number of the latter group subsequently moved southwest on the shelf and passed through the New Jersey shelf CODAR coverage region. A deployment of drifters was also made in March 2003 within the New Jersey shelf domain. A final set of deployments was made during July 2004 in both regions; however the drifters released in the Block Island region rapidly exited that domain and did not provide significant trajectory segments. Table D-1 summarizes the drifter deployments. Initial analysis focused on drifters within the Block Island region during 2002-2003 and on those within the New Jersey shelf region during 2004. The New Jersey shelf drifters from 2003 were subsequently used for the purpose of verifying the choice of turbulence parameters made using the 2004 data.

Table D-1. R&DC Mid Atlantic Bight drifter releases during 2002-2004.

| Date | Region | Number | Notes |
|---|---|---|---|
| Dec. 16-18, 2002 | Block Island | 9 | Retrieved and redeployed several. |
| Mar. 27, 2003 | Block Island | 4 | Passed through NJ Shelf region. |
| Mar. 27, 2003 | NJ Shelf | 8 | |
| Jul. 27, 2004 | Block Island | 3 | Rapidly left domain.<br>Passed through NJ Shelf region. |
| Jul. 27, 2004 | NJ Shelf | 4 | |

### D.2.2 CODAR Surface Currents

HF radar surface currents were obtained with CODAR SeaSonde systems located in the Mid Atlantic Bight in the region around Block Island and on the shelf east of New Jersey. A three-site standard-range (25 MHz) system in the Block Island region provided hourly surface currents at 1.5 km resolution over the region shown in Figure D-1. Radial velocities observed at each of the three sites were obtained with the Multiple Signal Classification (MUSIC) algorithm (Schmidt, 1986) using measured antenna patterns; and combining into vector velocities was performed using the manufacturer's (CODAR Ocean Sensors) software. The New Jersey shelf surface currents with spatial resolution of 6 km were provided by a four-site long-range (5 MHz) system in the area shown in Figure D-2. Radial velocities, averaged over 3-hour periods using measured antenna patterns, were output on an hourly basis and were combined using the Naval Postgraduate School's HF Radar Toolbox. A screening methodology, utilizing a threshold on the estimated geometric dilution of precision (GDOP) (Gurgel, 1994), was used to remove current vectors derived from combinations of radials from sites with poor geometry. Vectors for which the GDOP was greater than an empirical threshold of 1.25 were eliminated from consideration.

Estimates of the uncertainties associated with surface currents derived from CODAR systems have been provided using *in situ* velocity observations from Acoustic Doppler Current Profilers (ADCPs). Chapman and Graber (1997) cite differences of O(15 cm/s) between HF radar current estimates and *in situ* current measurements. However, as Kohut et al. (2004) point out, these error estimates include a large component that is due to the different spatial scales and depths sampled by HF radar and ADCPs. They estimate the intrinsic CODAR radial uncertainty to be of O(5 cm/s) for the New Jersey shelf long-range systems used in the present study. Vector uncertainties for the Block Island region were estimated to be 3-15 cm/s with the larger values observed along the outer boundaries of the coverage regions where the combining geometry is non-optimal and where signal to noise ratios increase (Ullman and Codiga, 2004).

Interpolation of velocities from the CODAR grid to the location of a drifter was performed using a weighted, nearest-neighbor scheme in which velocities from the four nearest-neighbor grid points were weighted inversely with distance. This method is more robust than bi-linear interpolation because it is more forgiving of missing CODAR vectors and allows for extrapolation beyond the instantaneous zone of CODAR coverage. Although velocities could be extrapolated to any distance beyond the coverage zone, in practice, we restrict the trajectory prediction to those trajectory segments that start within the nominal coverage zones shown in Figures D-1 and D-2. Also shown in Figure D-2 is the 10 percent coverage zone. This is the region within which CODAR vectors are obtained at least 10 percent of the time, computed over the drifter deployment period. Note that in the Block Island region, the 10 percent coverage region and the nominal coverage region were the same. The 10 percent coverage regions were used to perform more stringent screening of the trajectories to regions of more reliable CODAR currents.

### D.2.3 Monte-Carlo Trajectory Prediction

The motion of a particle in a two-dimensional velocity field can be described by the equation:

$$\frac{d\boldsymbol{r}}{dt} = \boldsymbol{u}(t,\boldsymbol{r}), \tag{1}$$

where $\boldsymbol{r}=(x,y)$ denotes the position of the particle and $\boldsymbol{u}=(u,v)$ is the Eulerian velocity at position $\boldsymbol{r}$ and time $t$. The velocity can be decomposed into a large-scale, slowly varying component, $\boldsymbol{U}$ and a component, $\boldsymbol{u_t}$ representing sub-gridscale deviations, which will be referred to as turbulence:

$$\boldsymbol{u} = \boldsymbol{U} + \boldsymbol{u}_t. \tag{2}$$

Surface current mapping radars such as CODAR can provide estimates of $\boldsymbol{U}$ at spatial scales of approximately 1.5 km (6 km) and temporal scales of 1 hr (3 hr) for standard-range (long-range) systems, thus the turbulent component represents velocity fluctuations on scales smaller than these. The radar-derived velocity is subject to significant uncertainties such that the large-scale component can be expressed as:

$$\boldsymbol{U} = \boldsymbol{U}_{Radar} + \delta\boldsymbol{u}, \tag{3}$$

where $\boldsymbol{U_{radar}}$ is the radar measurement and $\delta\boldsymbol{u}$ is the measurement error. Combining (2) and (3), the total Eulerian velocity can be written:

$$\boldsymbol{u} = \boldsymbol{U}_{radar} + \boldsymbol{u}_t + \delta\boldsymbol{u} = \boldsymbol{U}_{radar} + \boldsymbol{u}', \tag{4}$$

where $\boldsymbol{u}'$ includes both the turbulent velocity and the measurement error.

Prediction of particle trajectories in a region of HF radar coverage was achieved by integrating (1) using a predictor-corrector scheme with the velocity given by (4). A time-step of 1 hr was used and radar velocities were interpolated to the particle location using the weighted nearest-neighbor approach. The methodology for specifying $\boldsymbol{u}'$ is described in the following section.

### D.2.4 Sub-gridscale model

Although $\boldsymbol{u}'$ is a combination of radar measurement errors, unresolved motion, and true geophysical turbulent fluctuations, we hypothesize that its properties can still be described by models of turbulence. This is partly motivated by the fact that there is no easy way to separate the two components when comparing with velocity estimates from drifters. The fact that surface drifters are routinely launched in support of search and rescue operations motivates the development of a methodology to estimate the statistics of ***u'*** from drifter-derived velocities. The fluctuating velocity, ***u'*** will be referred to below as turbulence with the understanding that this quantity also contains a significant measurement error component.

Two models of turbulence were examined, both of which are members of the hierarchy of stochastic particle models reviewed by Griffa (1996). The so-called random walk and random flight models both assume that the particle position is Markovian and differ in that the latter also assumes that the particle velocity is a Markov variable. Physically, the difference is that the turbulence has a finite temporal scale and therefore temporal correlation in the random flight case whereas the random walk model assumes that the turbulent time scale is infinitesimal. For equal turbulent velocity variance, one therefore expects greater dispersion in the former case.

The two components of the vector velocity ***u'*** are assumed independent in both models. The random walk formulation for $u'$ can be expressed as:

$$u' = \sigma_u \frac{T^{\frac{1}{2}}}{dt} \cdot dw, \tag{5}$$

where $\sigma_u$ is the velocity standard deviation and $dw$ is a normally distributed random increment with zero mean and second moment $\langle dw \cdot dw \rangle = 2 \cdot dt$ with $dt$ the time step for the integration of (1). The turbulent time scale $T_u$ in the discrete problem is not actually infinitesimal but is constrained to equal $dt/2$ to obtain consistency of (5) and the definition of velocity variance (Griffa, 1996).

The evolution of the turbulent velocity in the random flight turbulence model is described by:

$$du' = -\frac{u'}{T_u} dt + \frac{\sigma_u}{T_u^{\frac{1}{2}}} dw. \tag{6}$$

The first term on the right of (6) represents the "memory" of the turbulence, decaying with time scale $T_u$ which is arbitrary in this case. The second term is a Gaussian random impulse as in the random walk case. The autocorrelation function of the turbulent velocity decays exponentially with an e-folding time or integral time scale equal to $T_u$ (Griffa, 1996).

It is important to note that the diffusion coefficient for particles in homogeneous turbulence at times large compared with $T_u$ is defined as:

$$K_x = \sigma_u^2 \cdot T_u. \tag{7}$$

(Csanady, 1973). Since for the random walk case, $T_u=dt/2$, the dispersion in numerical implementation of this model, for a given $\sigma^2$, is dependent on the time step employed.

### D.2.5 Estimating turbulent velocity statistics

Practical implementation of the aforementioned turbulence models to determine the random velocity components in (4) requires specification of the velocity variance, and for the random flight case the turbulent time scale $T_u$. One could prescribe the diffusion coefficient in both cases, but we argue that with relatively few drifters deployed and lacking large clusters, it is more appropriate to estimate the fluctuating velocity statistics than the diffusion coefficient. From (4), the fluctuating velocity is: $\boldsymbol{u}' = \boldsymbol{u} - \boldsymbol{U}_{radar}$, and we consider the drifter velocity to approximate the true velocity $\boldsymbol{u}$.

Time series of drifter positions at 1/2-hourly intervals were used with a central difference scheme to compute drifter velocities at times (hourly) corresponding to CODAR observations. CODAR velocities were then spatially interpolated to the drifter location using a weighted nearest-neighbor method. Velocities at locations outside of the 10 percent coverage zones were eliminated from consideration. Time series of $\boldsymbol{u}'$ for each drifter were then computed by differencing the drifter and CODAR velocities. These time series were used to estimate covariance functions, averaged over all drifters, for the $u'$ and $v'$ components (Figure D-3).

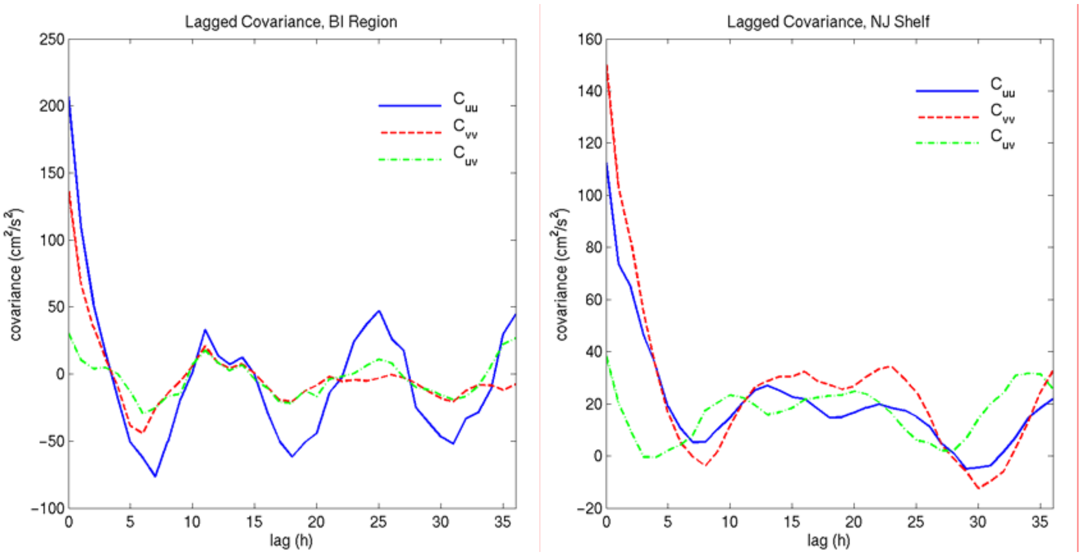

Figure D-3. Lagged covariance functions of time series of differences between drifter velocity and CODAR velocity averaged over all drifters within the Block Island region (left) and the New Jersey shelf region (right). The autocovariances of the eastward ($u$) and northward ($v$) components are shown by the blue solid and the red dashed lines, respectively. The green dash-dot line denotes the cross-covariance.

The autocovariance functions exhibit rapid decay at lags of several hours and display lower amplitude periodicities at the semi-diurnal period in the Block Island region and at approximately the inertial period in the New Jersey shelf region (Figure D-3). The cross-covariance is generally low, consistent with statistical independence between the two components. Turbulent variances were estimated as the zero-lag values of the autocovariance functions. The turbulent integral time scales were estimated as one half the time lag of the first zero crossing of the autocovariance functions. The estimates of these parameters are given in Table D-2.

Table D-2. Estimates of turbulence parameters from autocovariance functions of drifter-CODAR velocity differences for the two CODAR regions.

| Region | σu (cm/s) | Tu (h) | σv (cm/s) | Tv (h) |
|---|---|---|---|---|
| Block Island | 14.4 | 1.5 | 11.8 | 1.5 |
| NJ Shelf | 10.6 | 3 | 12.3 | 3 |

## D.3 Results

To evaluate the consistency of our approach to modeling dispersion and the estimates of the parameters, we compared observed drifter trajectories over 24 hours to those predicted retrospectively using CODAR velocities. The trajectory of each drifter was broken down into 24-hour segments with each segment overlapping the previous one by 12 hours for drifters within the Block Island region. An example simulation is shown in Figure D-4 where we show the 95th percentile region for the final psuedo-drifter location as a gray polygon. This region was estimated by computing the two-dimensional histogram of the pseudo-drifter location, sorting the spatial bins based on the number within and then summing over bins until 95 percent of the total (1000) was obtained. Trajectories were only computed for segments in which the starting position of the drifter was within the CODAR coverage region. In the analysis that follows, we present statistics for all computed trajectories as well as statistics of a screened subset of

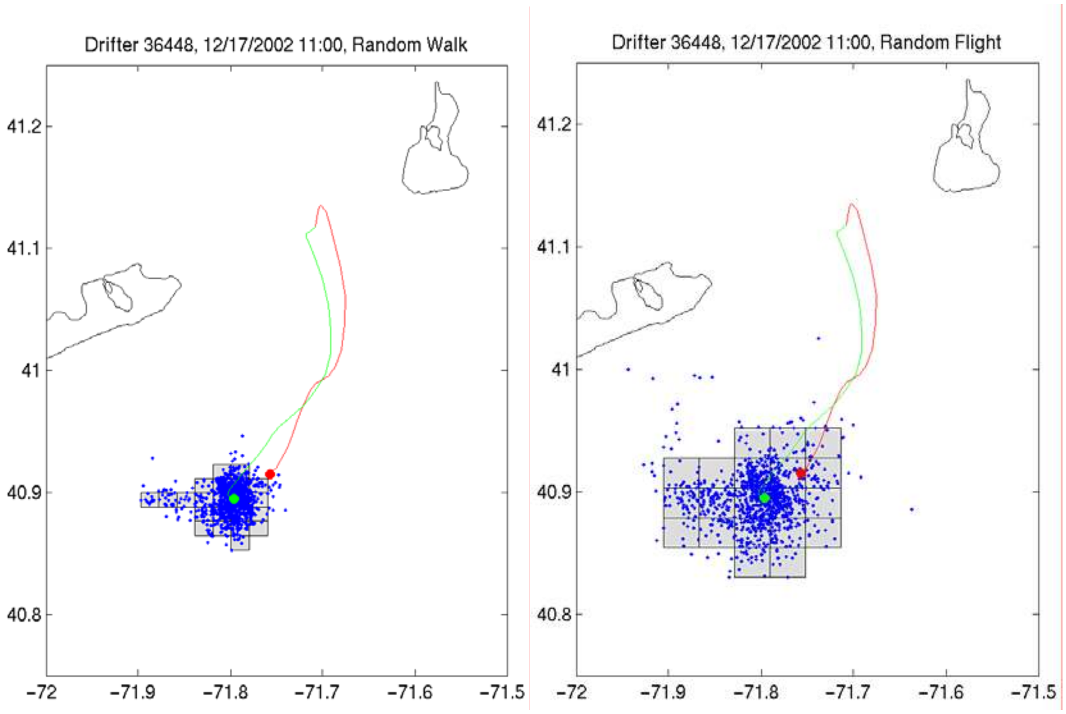

Figure D-4. Example drifter trajectory within the Block Island CODAR region showing the real drifter path over 24 hrs in red and the CODAR predicted position in green, with final positions denoted by the circles. The ensemble of trajectory prediction endpoints using the random walk (left) and random flight (right) models are shown as blue dots. The gray polygons denote the region within which 95 percent of the drifter final positions lie.

trajectory segments for which the end position is also located within the coverage region. The number of comparisons versus the time since the start of the prediction is shown in Figure D-5. The decrease in number with time in the Block Island region results from the retrieval and redeployment of drifters that left the CODAR domain; thus a number of "short" trajectories (< 24 hr) is present in the trajectory ensemble.

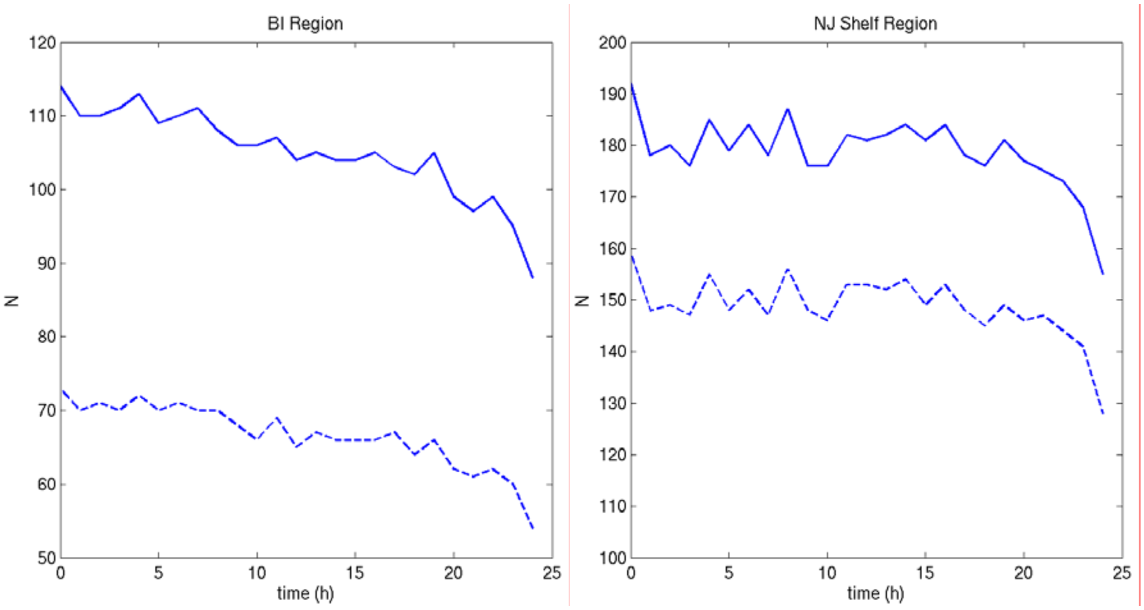

Figure D-5. The number of comparisons between predicted and true drifter position versus time for no screening (solid lines) and for screening using the 10 percent coverage zone (dashed lines) for the Block Island region (left) and New Jersey Shelf region (right).

### D.3.1 Accuracy of Predictions

The accuracy of a drifter trajectory prediction is measured by the distance between the real drifter and the pseudo-drifter. This was computed for each hour of each 24-hour trajectory segment. The ensemble mean separation and the 95th percentile separation is presented in Figure D-6 for all trajectories and for the screened subset. Mean separations in the two regions increase with time in a linear fashion with some indication that separations at short times increase at a slightly faster rate. After 24 hours, mean separation is approximately 7 km (6 km) for the Block Island unscreened (screened) ensembles and about 8 km (7 km) for the drifters in the New Jersey shelf region. The 95th percentile separation values are also slightly higher in the latter domain, for the unscreened subset, reaching 20 km at the end of 24 hours compared to about 18 km for the Block Island drifters. When drifters leaving the CODAR region are eliminated, the 95th percentile separations (24 hr) are about 12 km and 15 km in the two regions respectively. The general decrease in error with screening is not surprising, and is consistent with the occurrence of relatively large trajectory prediction error along the outer boundary of the CODAR domain where radar velocity errors increase.

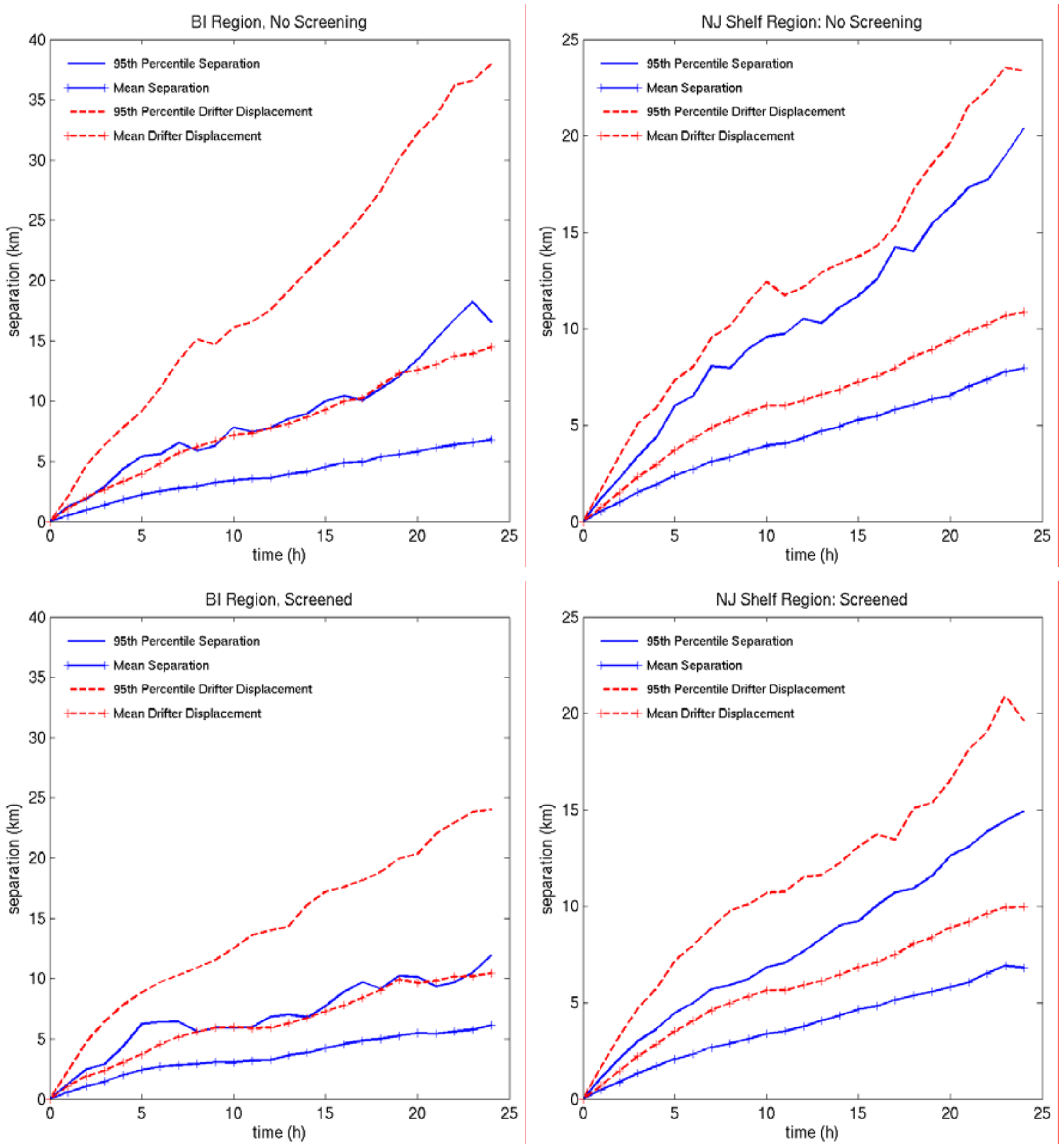

Figure D-6. Separation between actual and predicted drifter position as a function of time since start of prediction, averaged over all trajectory segments that start within the nominal coverage zone for the Block Island region (upper left) and the New Jersey shelf region (upper right). The blue curves show the mean separation (solid line and plusses) and the 95th percentile separation (solid line) of the real drifter and the predicted position. The red curves show the mean distance (dashed line and plusses) and the 95th percentile distance (dashed line) that the real drifter moved over the prediction time. The lower plots show the same statistical measures averaged over all segments that both start and end within the 10 percent coverage zone for the Block Island region (lower left) and New Jersey shelf (lower right).

To place the CODAR-based trajectory accuracies into context, and to evaluate whether CODAR predictions provide an improvement over the so-called persistence forecast (last known position), we also show, in Figure D-6, the mean and 95th percentile values of the distance traveled by the real drifters. Drifters released in the Block Island region tend to travel farther than those released on the open shelf. For the unscreened case, the mean (95th percentile) distance traveled after 24 hours in the Block Island region is 15 km (38 km) compared with about 11 km (23 km) in the New Jersey shelf region. The net result is that drifter locations predicted using CODAR currents in the Block Island region are on average approximately 50 percent closer to the real drifter position than are the last known positions. This effect is less pronounced on the New Jersey shelf where the mean distance from the predicted position to the real drifter is about 70 percent of the distance traveled. Similar conclusions are reached using the screened drifter subsets, although the screening can be seen to sharply reduce the 95th percentile separation value in the Block Island region.

### D.3.2 Uncertainty Bounds for Predictions

Monte-Carlo simulation of drifter trajectories provides an ensemble of final drifter locations that can be used to construct a search area. The search area was defined as the region in which 95 percent of the pseudo-drifters were located, estimated as discussed above. At each hour of each modeled trajectory, the search area was computed and the position of the real drifter checked to see whether it was inside or outside the search area. The number of real drifters within the search area was summed for each hour and divided by the number of trajectories so that the fraction ( percent) inside the predicted search area could be computed.

Comparison of the percent success measure for the two turbulence models tested shows clearly that the random flight method is superior in both regions (Figure D-7). Approximately 80-90 percent of all drifter search areas using this method enclosed the real drifter position and there was little variation with time. The comparison, using the screened drifter subset is improved somewhat, peaking above 90 percent in both regions. Search areas estimated using the random walk model of turbulence are severely underestimated with percent success, for the unscreened subset, dropping from about 70-80 percent at a prediction time of 1 hour to 35-60 percent after 24 hours. As for the random flight results, the comparison using the screened subset improves typically by about 5 percent at all prediction times. The discrepancy between the search areas produced using the two methods is most apparent for the simulations on the New Jersey shelf.

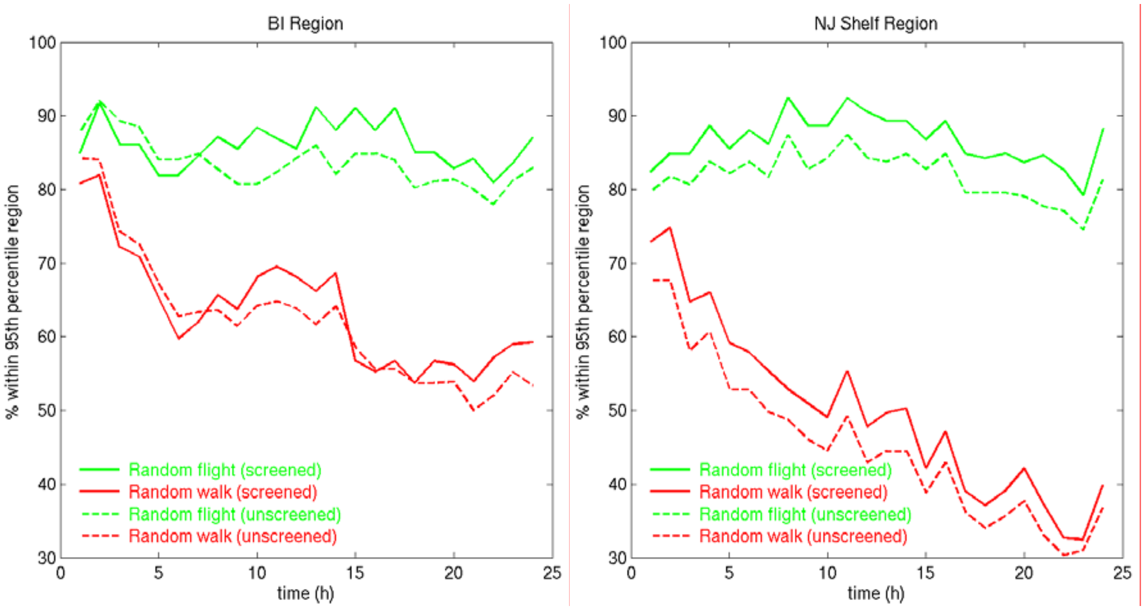

Figure D-7. Comparison of the uncertainty bounds for predicted drifter position using the random flight (green) and random walk (red) turbulence models for the Block Island region (left) and New Jersey shelf region (right). The solid curves are computed using only those trajectories that both start and end within the 10 percent coverage zone while the dashed curves are computed based on all trajectories that start within the nominal coverage zone. For each prediction time we plot the percent of cases where the actual drifter location at that time fell within the estimated 95 percent confidence region.

## D.4 Discussion

Drifter positions predicted over 24 hours using CODAR surface currents are clearly superior to the persistence forecast in estimating the final drifter location. The mean separation between predicted and observed drifter location is 50-70% of the separation using the persistence forecast. Using currents from a numerical circulation model, Thompson et al. (2003) simulated the trajectories of a number of surface drifters on the Scotian shelf. They estimated the 50th percentile separation value after 24 hours to be 6 km, which is very similar to the mean separation of 6-7 km found in the present study. This suggests that trajectory predictions using CODAR surface currents have comparable skill in predicting target trajectories as predictions using numerical model currents.

The search area evaluations can be used to assess the consistency of the turbulence models and their associated parameters. A consistent turbulence model would be expected to provide, for instance, a 95 percent confidence region that is successful (that is including the real drifter location) 95 percent of the time. The random flight method provides search areas that enclose the real drifter approximately 90 percent of the time, whereas the random walk formulation does significantly worse. This suggests that, with the parameter(s) estimated from the drifters, the random flight model is nearly self-consistent while the random walk model is definitely not self-consistent. The difference between the random flight success rate and the expected 95 percent suggests a slight underestimate of either the variance or the time scale. The latter seems the more likely candidate here, as we have estimated the turbulent time scale as half the value of the first zero crossing of the autocovariance function and not the true integral time scale. Note that evaluation of the integral time scale by integration of the autocovariance to infinite lags is problematic in the presence of the quasi-periodic motions evident in the covariance functions of Figure D-3.

The comparison of the effectiveness of random walk and random flight derived drifter dispersion is based on the case of equivalent turbulent velocity fluctuation variance. Alternatively, one could specify the diffusion coefficient and either the fluctuation variance or the turbulent time scale for the random flight model. In the case of equivalent $K_x$, the results of Zambianchi and Griffa (1994) show that, for homogeneous, stationary turbulence, the random walk model overestimates the particle dispersion for $t < T_u$. At times large compared to the turbulent time scale, the two models predict that the particle cloud dispersion increases at the same rate but the offset introduced by the initial overestimate persists. For turbulent time scales of 1-3 hours as determined in the present study, the difference is 10-20 percent at times after prediction of 12-24 hr. One could clearly increase the diffusion coefficient in the random walk case to produce more dispersion of the pseudo-drifter cloud, and if the diffusion coefficient were set to the random flight value ( $\sigma^2 T_u$) we would expect that the search areas would be at least as effective.

## D.5 Summary and Conclusions

Comparison of real drifter trajectories and trajectories predicted using CODAR-derived surface currents illustrates the value of these data for search and rescue operations. For prediction times of 1-24 hr, the mean (and 95th percentile) distance between the CODAR-predicted position and the real position is smaller than the distance traveled by the drifter. This indicates that predictions using CODAR velocities are more accurate than the so-called “persistence” forecast (zero drifter velocity). Although, not shown here, CODAR trajectory predictions are also superior to those produced using current CG practice, in which the advective velocity is obtained from NOAA tidal current predictions in nearshore waters and a surface current climatology offshore (O’Donnell, 2005).

The statistics of the combination of sub-gridscale velocity and CODAR velocity error that contribute to the dispersion of a cloud of pseudo-drifters have been estimated using the ensemble-averaged covariance functions of CODAR-drifter velocity differences. Approximate consistency of the estimates of turbulent velocity variance and timescale was demonstrated for the random flight turbulence model by evaluation of the resulting search areas, defined as the region in which 95 percent of the pseudo-drifters are located. The random flight search areas include the real drifter location in 80-90 percent of cases. Using the turbulent velocity variance estimated from the zero-lag autocovariance function, as for the random flight model, the random walk search areas were significantly less effective. This is due to the fact that the effective turbulent time scale in the random walk formulation is $dt/2$ or 0.5 hr with the time step used in this study. One could expect to achieve satisfactory search area predictions using the random walk model by specifying a diffusion coefficient equal to the random flight value.

## D.6 Acknowledgements

Funding for this study was provided by the R&DC through contract DTCG39-00-0-R00008 to Anteon Corporation. We thank Adam Houk and Hugh Roarty for their efforts in maintaining continuous operation of the CODAR systems during the drifter deployments. We also acknowledge the CG for the deployment of the drifters.

## D.7 References

Allen, A. A., 1996. Performance of GPS/Argos Self-Locating Datum Marker Buoys (SLDMBs), in *OCEANS 96*, MTS/IEEE Conference Proceedings, pp. 857-861.

Chapman, R. D. and H. C. Graber, 1997. Validation of HF radar measurements, *Oceanography,* 10: 76-79.

Csanady, G. T., 1973. *Turbulent Diffusion in the Environment,* D. Reidel, Boston, 248 pp.

Griffa, A., 1996. Applications of stochastic particle models to oceanographic problems, in *Stochastic Modelling in Physical Oceanography,* R. J. Adler , P. Müller, and B. L. Rozovskii, eds., Birkhäuser, Boston.

Gurgel, K. W., 1994. Shipborne measurement of surface current fields by HF radar. *L'Onde Electrique*, 74: 54-59.

Kohut, J. T., H. J. Roarty, and S. M. Glenn, 2004. Characterizing observed environmental variability with HF Doppler radar surface current mappers and acoustic Doppler current profilers, *IEEE J. Ocean. Eng.,* (submitted).

O'Donnell, J., E. Howlett, E. Anderson, and T. McClay, 2005. Integration of Coastal Ocean Dynamics Application Radar (CODAR) and Short-Term Predictive System (STPS) Surface Current Estimates into the Search and Rescue Optimal Planning System (SAROPS), Anteon Corporation.

Schmidt, R.O., 1986. Multiple emitter location and signal parameter estimation, *IEEE Trans. Antennas Propag*, AP-34: 276-280.

Thompson, K. R., J. Sheng, P. C. Smith, and L. Cong, 2003. Prediction of surface currents and drifter trajectories on the inner Scotian Shelf, *J. Geophys. Res.,* 108(C9), 3287, doi: 10.1029/2001JC001119.

Ullman, D. S. and D. L. Codiga, 2004. Seasonal variation of a coastal jet in the Long Island Sound outflow region based on HF radar and Doppler current observations, *J. Geophys. Res.*, 109, C07S06, doi: 10.1029/2002JC001660.

Ullman, D. J. O'Donnell, C. Edwards, T. Fake, D. Morschauser, M. Sprague, A. Allen, and B. Krenzien, 2003. Use of Coastal Ocean Dynamics Application Radar (CODAR) technology in CG SAR planning, CG Report CG-D-09-03.

Zambianchi, E. and A. Griffa, 1994. Effects of finite scales of turbulence on dispersion estimates. *J. Mar. Res.,* 52: 129-148.

# APPENDIX E.
# A HIERARCHY OF STOCHASTIC PARTICLE MODELS FOR SEARCH AND RESCUE (SAR): APPLICATION TO PREDICT SURFACE DRIFTER TRAJECTORIES USING HF RADAR CURRENT FORCING

February 2, 2005

Malcolm L. Spaulding[1], Tatsu Isaji[2], Paul Hall[2], and Art Allen[3]

[1]Ocean Engineering, University of Rhode Island, Narragansett, RI 02882
[2]Applied Sciences Associates, Inc., Narragansett, RI 02882
[3] US Coast Guard, Search and Rescue Center, Groton, CT 06340

## Abstract

This report summarizes a hierarchy of stochastic particle models, where the object's position, velocity, and acceleration are progressively represented as Markovian processes. Numerical implementation and testing of the first and second order models (random walk and random flight) against an analytic solution to the diffusion equation show very good agreement provided that 2,000 or more independent simulations are ensemble-averaged. The random flight model is shown to predict smaller search areas than the random walk model, with a long-term reduction in the area proportional to the dispersion coefficient times the velocity autocorrelation time scale. This offset ramps in immediately after the release, and occurs over the velocity autocorrelation time scale. The particle models were applied to predict the trajectories of seven CG, Self Locating Datum Marker Buoys (SLDMB) Argos tracked drifters (Davis like) deployed in three clusters: one located in western Block Island Sound, and the other two near the coast and shelf break in the New York Bight. The buoys were deployed for a 35-day period starting on July 27, 2004. High frequency coastal radar (CODAR) measurements were collected during the same time period by a short range system (50 km range and 5 km resolution) operated by the Universities of RI and Connecticut for the Block Island Sound and adjacent shelf area, and by the long range system (150 km range, 6 km resolution) operated by Rutgers University for the Mid Atlantic Bight. The motion of the buoys was dominated by a mean southwesterly shelf transport and inertial and semi-diurnal tidal oscillations. A cluster analysis of the very limited number of SLDMBs gives dispersion coefficients in the range of 40 to 80 $m^2$/sec. Analysis of the CODAR velocity errors and variances gives values in the range of 40 to 700 $m^2$/sec, with velocity autocorrelation time scales in the range of 4 to 7 hours, depending on the velocity component, the location, and whether the current record used to determine the autocorrelation time scale is de-tided. Comparison of the velocities derived from the drifters and the radar system shows differences comparable to the observed speeds. Scatter plots for the Block Island Sound (Mid Atlantic Bight) show a correlation of less than 0.1 (greater than 0.75) for the east/west component and greater than 0.6 (less than 0.4) for the north/south component. Correlation coefficients were observed to be much lower in areas where the percent data return was below 50 percent. Statistically independent simulations were performed using SARMAP, a search and rescue model, to predict the daylong trajectories at successive (non-overlapping) locations along the paths of the seven SLDMBs in the Mid Atlantic Bight. Model predicted and observed locations at the end of one day (typical search and rescue model prediction time scale) showed an averaged difference of 9.3 km, with an error in location comparable (about 80

percent) to the distance the drifter traveled in one day. Errors were significantly higher in areas where the CODAR data return rates were less than 50 percent. Estimates of the dispersion coefficients necessary as input to the search and rescue model, to ensure that the predicted and observed locations of the drifters were within the model predicted search area, were made and gave values ranging from 20 to 500 $m^2$/sec, with a median value of 90 $m^2$/sec. The largest dispersion coefficients were associated with areas where the radar data returns were lowest. The various estimates of the dispersion performed (cluster analysis, radar velocity variance, and trajectory analysis) gave values consistent with Okubo's relationship. Random flight models offered no improvement in predictive performance for any of the applications due to the substantial uncertainty in estimates of the dispersion coefficient.

## E.1 Introduction

In planning search and rescue operations, it is common practice to use Lagrangian (particle) trajectory models to predict the transport of objects (i.e. vessel, person in the water, life raft, etc.) at sea. The majority of the models employ random walk (Markovian in position) techniques to perform these simulations (Breivik et al, 2004; Spaulding and Howlett, 1996; Spaulding and Jayko, 1991; ASA, 2003). The current and wind fields used to force these models are derived from hindcasts, nowcasts, and forecasts, depending on the application, and are supplied by hydrodynamic and meteorological models or the direct use or interpolation/extrapolation of observations. The movement of the objects is typically approximated as the vector sum of the current field plus an empirically based down and cross (leeway) drift in response to wind forcing. Allen and Plourde (1999) and Allen (1999) provide empirical leeway drift factors (drift rate, down and cross wind, versus wind speed) and the associated uncertainties for 63 separate classes of objects.

The principal goal of search and rescue model simulations is to predict the location and size of the area where the lost object is most likely to be found (search area) as a function of time. Simulation periods typically extend from several days in the past to 1 or 2 days in the future. The search planner is typically faced with making critical assumptions about the initial release location and the conditions that existed at that time. (When and where did the vessel experience its initial distress? Was the vessel upside down? Does the life raft have a drogue deployed?). Stochastic simulations are then performed to predict the location of the search area. Once the simulation is complete and the search area estimated the search planner must determine how to allocate search resources (i.e. boats, helicopters, airplanes) to maximize the probability of success in the search. Wind and current induced advective processes can reasonably predict the center of the search area. The size of the search area however, depends on the evolution of the ocean turbulence fields and the shear in the mean current, normally parameterized in terms of the horizontal dispersion coefficient, over the duration of the simulation. If estimates of the search area are too small, the probability of detecting the object is reduced. On the other hand, if the search area is too large, it is likely that search resources will not be available to cover the search area, thus lowering the probability of detection, since some of the area will remain unsearched. Application of higher order stochastic models (e.g. random flight, Markovian in both position and displacement) offer the potential to reduce the size of the search area because the effective dispersion, compared to its random walk counterpart, is reduced. In spite of the potential improvements, none of the current operational search and rescue models currently employ higher order stochastic trajectory models.

In addition, the rapid development and implementation of high frequency, short and long range coastal radar systems for real-time measurements of surface currents provide a new source of near-real-time observations of the surface current field that could be used as input to search and rescue models. These systems have the potential of providing high spatial (1.5 to 6 km) and temporal (1 to 3 hr) resolution observations of surface current fields over ranges of 50 to 150 km. In addition, these systems can provide estimates of the surface velocity variances that might be exploited to improve estimates of the effective turbulent dispersion, and hence improve predictions of the size of the search area.

The first objective of this paper is to summarize a hierarchy of stochastic particle models from the literature that might be used in search and rescue models to predict the search area. The second objective is to apply random walk and flight models, driven by surface current data derived from short- and long-range high frequency radar systems, to understand the transport and dispersion of seven, 7/10 scale Davis (1985) like surface drifters deployed in Block Island Sound and the Mid Atlantic Bight by the CG over a 35-day period in July and August, 2004. Integral to both objectives is an assessment of the dispersion characteristics and autocorrelation time of the velocity variances of these coastal waters.

Section 2 provides a summary of the hierarchy of stochastic particle models, drawn from the literature on Lagrangian dynamics in the ocean and atmosphere, which might be used in search and rescue models. Numerical implementation and testing of the models against an analytic solution to the diffusion equation are also covered in this section. Application of random walk and flight models to the surface drifter data to estimate the turbulent dispersion and to assess their predictive performance is provided in Section 3. Anticipating the use of high frequency radar surface current data to predict the movement of surface drifters, Section 4 provides a comparison of velocities derived from drifter trajectories with corresponding data collected by the high frequency radar. Section 5 provides the associated estimates of dispersion coefficients based on the radar data. Predictions of the drifter trajectories were then made using a state of the art, search and rescue model (SARMAP; ASA, 2003), forced by the observed high frequency radar current fields (Section 6). Differences between the model predictions and observations were used to assess the dispersion coefficient required in SARMAP to ensure that the model predicted search area included the observed location of the drifters. Study conclusions are presented in Section 7 and references in Section 8.

## E.2 Hierarchy of stochastic particle models

The large number of scales participating in the motion makes modeling of the movement of particles (search and rescue objects) in the ocean complicated. For the search and rescue problem, these range from continental shelf to molecular scales. Since methods are not available to solve for all scales simultaneously, it is common practice (Taylor, 1921) to divide the flow into a mean field representing the large-scale flows, U, and turbulence representing the smaller scale flows (u’).

Following the work of Griffa (1996), Griffa et al, (1995), and Berloff and McWilliams (2002), it is proposed that the trajectories of objects drifting at sea be modeled by a hierarchy of progressively more complicated Markovian, stochastic particle models. These models are simple examples of the generalized, stochastic, nonlinear, Langevin equations for arbitrary dimensions (Risken, 1989). Markovian models are typically used to describe processes whose conditional probability density at time $t_n$ is solely dependent on values at an earlier time $t_{n-1.}$ They have been shown to be well suited for modeling the movement of drifters in the ocean (Dutkiewicz et al, 1994; Griffa, 1996; Bauer et al, 1998, 2002; Mariano et al, 2002). A complete derivation of the hierarchy of models is provided in appendices to Berloff and McWilliams (2002).

The lowest level model (Model 1, alternately referred to as the zeroth order Markov model) assumes that the particle position, **x,** is a Markov variable. This model assumes that the scales of acceleration and velocity are infinitesimal. This model can be shown to give solutions to the advective-diffusion equation (Csanady, 1973) and is widely known as a “random walk” model. The model is simple to implement and widely used in oceanographic studies. Model 1 is used in most search and rescue models to make trajectory predictions (Breivik et al, 2004; Spaulding and Howlett, 1996; Spaulding and Jayko, 1991; ASA, 2003). Model 2, often referred to as a “random flight” model (Thomson, 1986; van Dop et al, 1985), assumes that both the position, **x,** and the velocity, **u,** are jointly Markovian. The scale of acceleration is once again assumed infinitesimal. This model is well-suited to describe meso-scale particle motions in the upper ocean (Griffa, 1996). Finally, Model 3 assumes **x**, **u**, and **a** are jointly Markovian (Sawford, (1991), Pope, (1994)). This model is typically used when particles display strong looping or wave-like motion (Mariano et al, 2002). Berloff and McWilliams (2002) extend this internally consistent hierarchy to equations for the hyper-acceleration or the time derivative of the acceleration. This model is most useful if the particles move in vortex or ring-like structures with very long lives. This model is not considered here because it is well beyond the scope of the current state of practice, requires extensive supporting data, and is not justified since the potential areas of application do not have particle trajectories that display strong wave or looping like movements over the typical forecast periods.

The governing equations for each of the three Markovian models are presented below. Only one component is provided, as the other is analogous. The following assumptions have been made for the present application.

1. The velocity field is two-dimensional. This assumption is a natural result of focusing on the transport of particles floating at or very near the sea surface.
2. Models describe the motion of single, independent particles released in the flow field; the movements of individual particles are not correlated with each other.
3. The particles are dynamically passive (i.e. they don’t affect the fluid dynamic motion).
4. The turbulence velocity is homogenous in space and stationary in time. For the present application, it is assumed that temporal and spatial variations are accounted for by the temporally and spatially varying flow fields provided by the high frequency surface radar systems (horizontal spatial resolution on the order of 1 to 6 km and a temporal resolution of 1 to 3 hrs) or hydrodynamic models.
5. The two components of velocity are independent (i.e. spatial correlations of the velocity are zero).
6. Random forcing is Gaussian (or normal).

### E.2.1 Model 1: Markovian x

The governing equation for particle motion, in incremental form, for this model is

$$dx = Udt + dx' \qquad (1)$$

$$dx' = K^{1/2}\, dw \qquad (2)$$

with initial conditions x(t=0) = 0. dx is the total particle displacement during time interval dt, U (x, t) is the mean flow, dx' is the displacement due to the turbulent velocity field, and dw(t) is a random increment from a normal distribution (zero mean and second order moment of 2dt).

K is the turbulent diffusion coefficient and is given

$$K = \sigma_u^2 T \qquad (3)$$

Where $\sigma_u^2$ is the velocity variance ($cm^2/sec^2$) and T is the turbulence time scale. In order for $\sigma_u^2 = \langle(dx'/dt)^2\rangle$, T must be equal to dt/2.

Griffa (1996) presents the Fokker-Planck equation associated with Model 1 and shows that it provides a solution to the well-known, advective diffusion equation for the average concentration of a constituent, where K is the eddy diffusion coefficient.

Equation 1 shows that the movement of a particle is a result of contributions from the mean flow and turbulence. The latter is represented as a random stochastic process, uncorrelated from one time to the next. The particle hence receives a random pulse or input due to actions of the turbulence field, but retains no memory of the prior turbulent impulse it experienced at the earlier time step. For this model T, and hence dt, are small compared with temporal variations of U and with the actual time t. This model is therefore applicable for times when t >> T.

The dispersion, or mean squared separation of particles, $S_1^2 = \langle(x - \langle x\rangle)^2\rangle$, where the < > indicates the mean value, for this model is given by

$$S_1^2 = 2Kt \qquad (4)$$

where the subscript 1 refers to Model 1. The mean dispersion of particles is predicted to grow linearly with time, in agreement with the solution to the advective diffusion equation (Csanady, 1973).

### E.2.2 Model 2: Joint Markovian x and u

The incremental equations for particle motion for Model 2 are given by

$$dx = (U+u)dt \qquad (5)$$

$$du = -(1/T)udt + K^{*\,1/2}\, dw^* \qquad (6)$$

the initial conditions are $x(0) = 0$ and $u(0) = \hat{u}$, where $\hat{u}$ is drawn from a Gaussian distribution with a zero mean and variance of $\sigma_u^2$, dw* is a random increment with the same statistical characteristics as in Model 1 (Equation 2), and T is the turbulent time scale.

K* is the diffusion coefficient and can be expressed in terms of the velocity variance and the Model 1 diffusion coefficient, K, by

$$K^* = \sigma_u^2/T = K/T^2 \tag{7}$$

Model 2 (Equation 5) shows that perturbations of the velocity field at each time increment are composed of two components, a random impulse (dw*) and a loss of velocity (momentum) (-(1/T) u dt) as a result of the memory of the velocity from the prior time step. A particle hence retains a memory of its initial turbulent velocity over a finite time of order T.

T is typically derived from the velocity autocorrelation function, expressed as

$$R(\tau) = \sigma_u^{-2}\langle u(t)u(t+\tau)\rangle \tag{8}$$

where $\tau$ is the time lag. Numerous applications have shown that the autocorrelation function decays exponentially for meso-scale oceanographic problems (see Griffa, 1996) and hence R can be approximated by

$$R(\tau) = e^{-\tau/T} \tag{9}$$

where T is the integral time scale of the autocorrelation function.

Griffa (1996) and van Dop et al, (1985) present the Fokker-Planck equation for Model 2 and show that the equation includes a term that constitutes the memory of the velocity for a finite period of time.

Model 2 can represent transient processes with times $t < T$; as well as those where $t > T$, as in Model 1. Model 2 fails however at very small times since the acceleration has an infinitesimally small scale and Equation 5 is discontinuous at each step.

For the case of constant K and T, Equation 6 has an exact solution (van Dop et al, 1985).

The particle dispersion for Model 2, $S_2^2$, for this case is given by

$$S_2^2 = 2Kt- 2KT(1-e^{-t/T}) \tag{10}$$

Equation 10 shows that $S_2^2$ has an exponential like shape. This solution also shows that the velocity autocorrelation must have the exponential form given by Equation 9. Comparing $S_1$ and $S_2$, it is noted that Model 2 predicts a lower dispersion than Model 1 for $t < T$. The dispersion approaches that given by Model 1 for large values of t; however there is a permanent offset, with a value of 2KT.

### Model 3: Joint Markovian x, u, and a

The governing equations for Model 3, written in incremental form, are

$$dx = (U+u)dt \tag{11}$$

$$du = adt \tag{12}$$

$$da = -(1+ a\, T_a/T)dt/\, T_a - udt/(T\, T_a) + K^{**1/2}dw^{**} \tag{13}$$

where

$$K^{**} = (1/T_a)(\sigma_a^2(1+T_a/T)) \tag{14}$$

and

$$\sigma_a^2 = \sigma_u^2/(\, T\, T_a) \tag{15}$$

the initial conditions are x(0) = 0, u (0) = û, a (0) = â where the values for û and â are obtained from a Gaussian distribution, with zero mean and variances of $\sigma_u^2$ and $\sigma^2_a$, respectively. K** is the diffusion coefficient, $\sigma^2_a$ is the acceleration variance, and dw ** is a random increment with the same statistical characteristics as dw and dw* in Equations 2 and 5, respectively. Model 3 has two time scales, T and $T_a$, representing the velocity and acceleration time scales, respectively.

Assuming that the velocity and acceleration autocorrelations can be approximated by exponential relationships results in

$$R(\tau) = (e^{-\tau/T} - (T_a/T)\, e^{-\tau/T}a)/(1-T_a/T) \tag{16}$$

for the velocity autocorrelation function.

To understand the physical behavior of Model 3, as represented by Equations 11 - 13, let us assume there is a complete separation of the temporal scales of velocity and acceleration such that $T_a << T$. For long time lags ($\tau >> T_a$) R ($\tau$) reduces to Equation 9 (Model 2). For time lags on the order of $T_a$, R has a quadratic behavior in the vicinity of $\tau = 0$. The autocorrelation for acceleration has an approximate exponential dependence for short time lags and is given by

$$R_a(\tau) = e^{-\tau/T}a \tag{17}$$

## E.2.3 Extension to inhomogeneous and non-stationary turbulence

When turbulent parameters in the above models are spatially or temporally varying, the basic Langevin equations given above are not strictly correct. Errors manifest themselves in the form of particle distributions that are uncharacteristically high in areas of low turbulence. This problem has proven particularly important in particle transport problems where the temporal/spatial variations in the turbulence levels are strong. The typical strategy used to address this problem is the addition of a drift correction term to the velocity for Model 2 and to the velocity and acceleration for Model 3 (Berloff and McWilliams, 2002; Thomson, 1987;

Sawford and Yeung, 2000; Legg and Raupach, 1982). This term typically involves the spatial gradients of the velocity and acceleration variances. As an example, the simplest correction for Model 2, to account for inhomogeneous and non-stationary turbulence, is to add the following term to the right-hand side of Equation 6.

$$\frac{d\sigma^2_u\, dt}{dx}$$

This term introduces a mean acceleration acting on the particles directed toward the regions of higher variance. It serves to counterbalance the tendency of particles to concentrate in areas of lower variance. This adjustment ensures that particle distributions are well mixed.

Data collected by the high frequency radar system in the Block Island Sound study area indicate values of $\sigma^2_u$ ranging from 100 to 400 $cm^2/sec^2$ with a mean value of about 100 $cm^2/sec^2$ (Ullman et al, 2003). For the present study, mean variances in the range of 350 to 550 $cm^2/sec^2$ were observed in Block Island Sound and the Mid Atlantic Bight. The larger values of variance are observed at the outer edge of the radar footprint and are a result of the poor geometric resolution in the area, the reduced radial coverage at long ranges, and lower data recovery rates. The velocity variance however, is typically smoothly-varying over the central portion of the footprint. Given this situation, it will be assumed, as a first approximation, that inhomogeneous and non-stationary effects can be ignored.

### E.2.4 Numerical implementation

The procedure used to solve the governing equations presented is provided below. Since the method is the same for each model, the approach for Model 2 is presented, because it illustrates all the key steps and is less complicated than Model 3.

The strategy is to solve Equations 5 and 6 using a Monte Carlo technique. In this approach simulations are performed for discrete particles and the results of multiple simulations are ensemble-averaged to predict the advection and dispersion of the particles as a function of time.

Equations 5 and 6 are expanded in discrete, incremental form as

$$x^{n+1}_{i+1,\,j+1} = x_{i,\,j}^{\;n} + (U^{\,n}_{\;i,\,j} + u^{n}_{\;i,\,j})\,\Delta t \qquad (18)$$

$$u^{n+1}_{\;i+1\,,\,j+1} = u^{\,n}_{\;i\;,\,j} - (1/T)\,u^{\,n}_{\;i\;,\,j}\;\Delta t\; + (2\,\sigma_u^{\;2}/T)^{1/2}\,w^n * \qquad (19)$$

where the superscript, n, refers to the time, and is stepped in increments of Δt. The subscripts i and j refer to the two-dimensional horizontal location of the velocity. The location of the particle at n+1, $x^{n+1}_{i+1,\,j+1}$, is given subscript i+1, j+1 to note that the particle will be moved horizontally to a new position during the time increment, Δt. U is the mean velocity at the location (i, j) of the particle at time n and u is the turbulent fluctuating component of the velocity. U can be obtained directly from the output of the radar as the mean value of the velocity for each grid. $\sigma_u^{\;2}$ is the variance of the turbulent velocity. This value is available at each grid point from the radar data. It can be averaged over time at one grid point or all grid points can be averaged over both time and space. T is the integral time scale from the autocorrelation function (Equation 8) assuming that the function is exponential (Equation 9). T is available either as an average value over the radar footprint or for each observation point. Finally, $w^n$ * is a random increment from a normal distribution with zero mean and second order moment of 2dt. Equations 18 and 19 are the simplest approximations to time stepping of the particle position. More sophisticated integration procedures can be used, including predictor corrector and 4th order Runge-Kutta methods (Press et al, 1992). These methods become necessary if the time steps of the simulation become sufficiently large so that a particle is moved more than one grid in one time step.

In the computation cycle, one particle is selected and Equation 18 is solved to determine the location of that particle at time n+1. For the first step, $x^n$ is assumed to be zero, or some other prescribed value, and $u^n_{i,j}$ is selected at random from a normal distribution of velocity variance. Equation 19 is then solved to determine the value of the turbulent velocity component at n +1. In the next time step, this value is substituted in Equation 18 for $u^n_{i,j.}$ This sequence of calculations is repeated to predict the position of the particle in time. Similar simulations are performed for each additional particle. Finally, ensemble averages are computed using the results of numerous particle simulations to predict the mean position and dispersion of the particles at each time step.

In the present application, estimates of mean currents and associated estimates of the velocity fluctuations are available from the radar system at increments of 1 to 3 hours. The autocorrelation times are estimated to be on the order of 4 to 6 hrs. Simulation times are typically one to several days. The grid spacing for the Block Island Sound CODAR system is approximately 1.6 km and about 6 km for the Mid Atlantic Bight system. For a mean grid size of 1.6 km (6 km) and a peak current of 50 cm/sec, 0.89 hrs (3.3 hrs) are required for a particle to transit one grid. To take maximum advantage of the temporal variations of the data, the time step should be less than 1 hour. In addition, to ensure that the particles won't travel more than one grid in one time step, the time step should be less than 0.989 hrs for the Block Island Sound grid. We have therefore selected a time step of 15 minutes for all simulations. This time step ensures that particles will not transit more than one grid in one time step and allows us to take maximum advantage of all available data. This time step is also substantially less than the integral time scale of the autocorrelation function and hence allows us to evaluate any improvement in performance from considering the autocorrelation of the velocity field.

The present work is restricted to the application of Models 1 and 2 to predict the trajectories of particles. Application of Model 3 is premature and awaits the results of the evaluation of Models 1 and 2.

### E.2.5 Model testing

To verify that the numerical solutions for both Models 1 and 2 have been implemented correctly, simulations with fixed parameters for cases with available analytic solutions were performed. Model predictions of the mean squared separation of particles, $S^2 = <(x- <x>)^2>$ versus time were compared with the corresponding analytic solutions.

For the cases studied, the mean flow was set to zero (U = 0). The no flow case was selected because the only difference between Models 1 and 2 is in their treatment of the turbulent transport term. Simulations were performed for a period of 5 days with a time step, dt = 15 minutes (900 seconds). The diffusion coefficient (Model 1) was assumed at K = 1 $m^2$/sec (or $\sigma_u^2 = 2K/dt = 22.2\ cm^2/sec^2$).

### E.2.5.1 Model 1: Markovian x

Six simulations were performed increasing the number of particles used in the simulation from 100 to 50,000 (100, 500, 1000, 2000, 5000, and 50,000) and using the model parameters above. Ensemble-averaged model predictions of the mean displacement, $S_1^2 = \langle (x - \langle x \rangle)^2 \rangle$ are plotted versus time and against the analytic solution in Figure E-1. Only simulations for the 500, 5000, and 50,000 cases are shown for clarity in the figures. For Model-1, the analytic solution of the mean squared separation of particles is given by Equation 4, $S_1^2 = 2Kt$. Figures E-2 and E-3 show the percent error and cumulative error squared versus time, respectively, for the simulations shown in Figure E-1. The numerical solution approaches its analytic counterpart as the number of particles used in the simulation increases. Maximum errors for the 500 particle case are about 10 percent and decline to less than 1 percent for 50,000 particles (Figure E-2). The cumulative errors show similar behavior. Errors are observed to decrease rapidly with the initial increase in number of particles, and then more slowly as the number of particles increases.

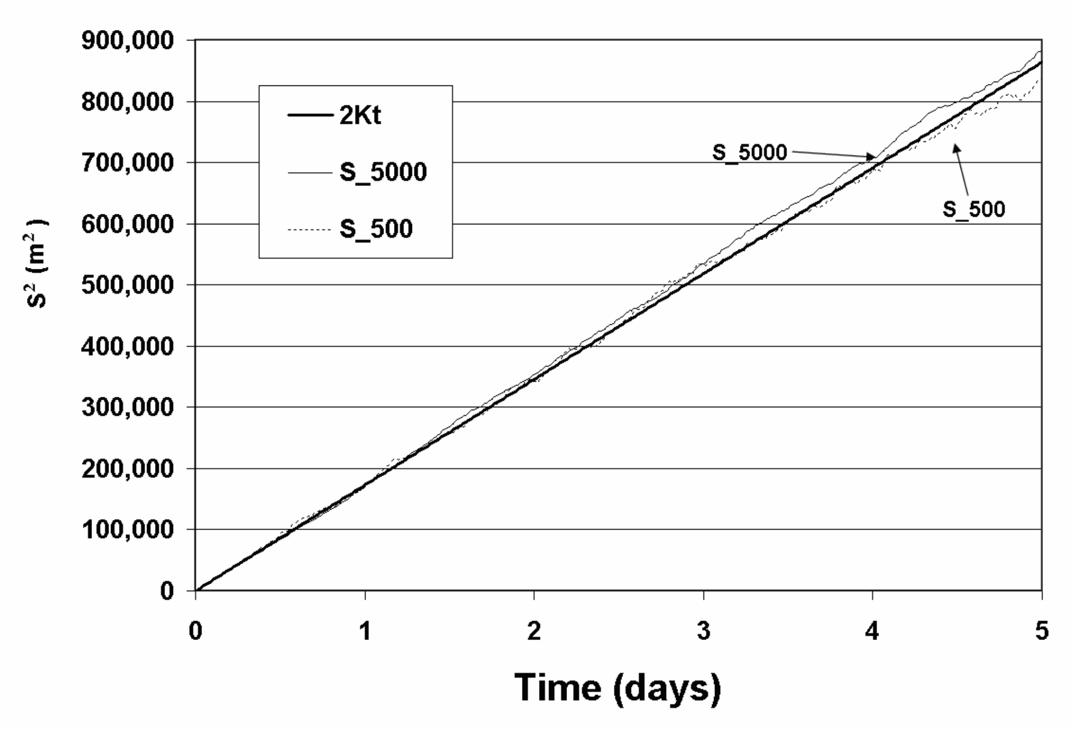

Figure E-1. Time series of the mean squared separation obtained using Model 1. **S_xxx, xxx** denotes the number of particles used.

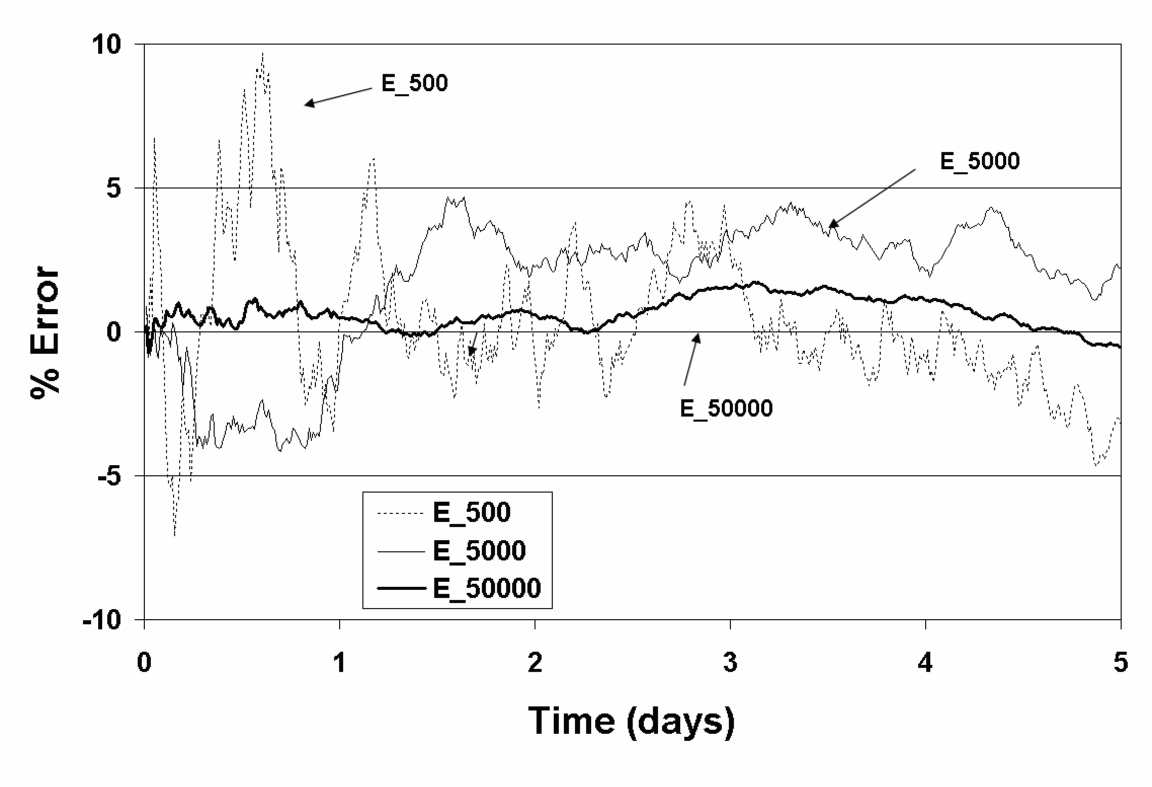

Figure E-2. Time series of percent error for Model 1. E_xxx, xxx denotes the number of particles used.

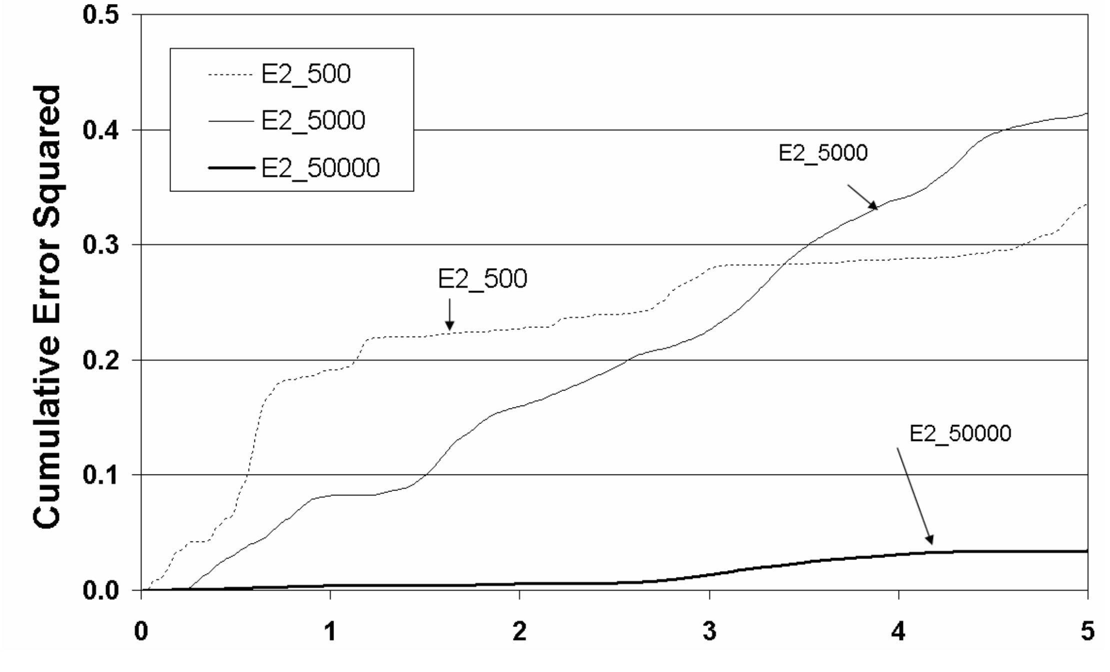

Figure E-3. Time series of the cumulative squared error for Model 1. E2_xxx, xxx denotes the number of particles used.

### E.2.5.2 Model 2: Joint Markovian x and u

Simulations, similar to those above, were repeated using Model 2, employing the same parameters and assuming an autocorrelation time scale of 1 day. The analytic solution for the mean squared separation of particles versus time is given by Equation 10, $S_2^2 = 2Kt - 2KT (1-e^{-t/T})$. Figure E-4 shows $S_2^2$ versus time for the model predicted (for varying number of particles) and analytic solution for this case. Also shown for reference is the analytic solution for Model 1. Figures E-4 and E-5 provide the percent error and cumulative error squared versus time, respectively, for the simulations shown in Figure E-3. Model performance, as a function of number of particles, shows similar trends as in Model 1, with the exception that the high frequency variations in the errors are dramatically reduced. This is a direct result of the reduced contribution of the random component to turbulent velocity fluctuations inherent in the random flight model. Using the random flight model clearly shows a reduction in the dispersion of particles compared to the random walk model. This reduction is observed over a time scale equivalent to the autocorrelation time. The two models show the same slope of the mean squared separation distance with time after the several days of simulation. Implementation of the random flight model results in an effective reduction (offset) of $S^2_2$ of 2KT.

Results from simulations using both Models 1 and 2 indicate that several thousand particles are required to obtain error levels below 5 percent. Error levels with 500 particles are on the order of 7.5 percent. Predictive performance can be improved beyond the 5 percent level but only by the use of a substantially increased number of particles, which adversely impacts computational times.

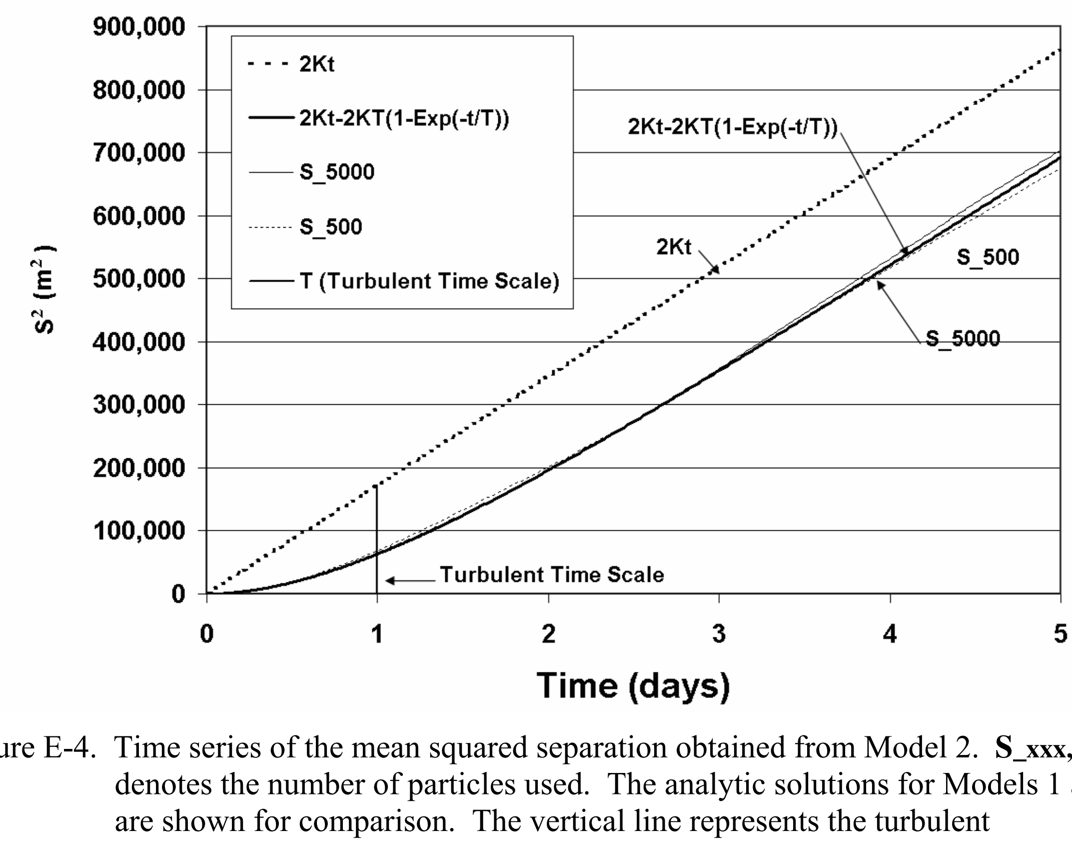

Figure E-4. Time series of the mean squared separation obtained from Model 2. **S_xxx, xxx** denotes the number of particles used. The analytic solutions for Models 1 and 2 are shown for comparison. The vertical line represents the turbulent autocorrelation time scale (1 day).

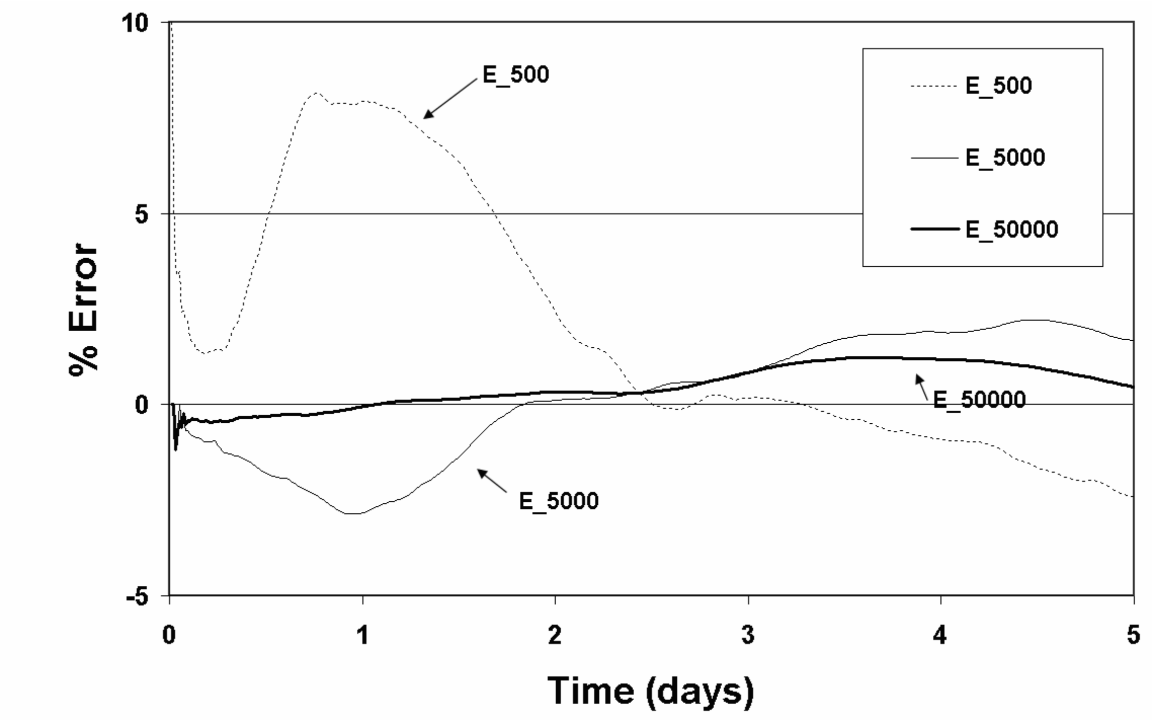

Figure E-5. Time series of percent error for the Model 2. E_**xxx, xxx** denotes the number of particles used.

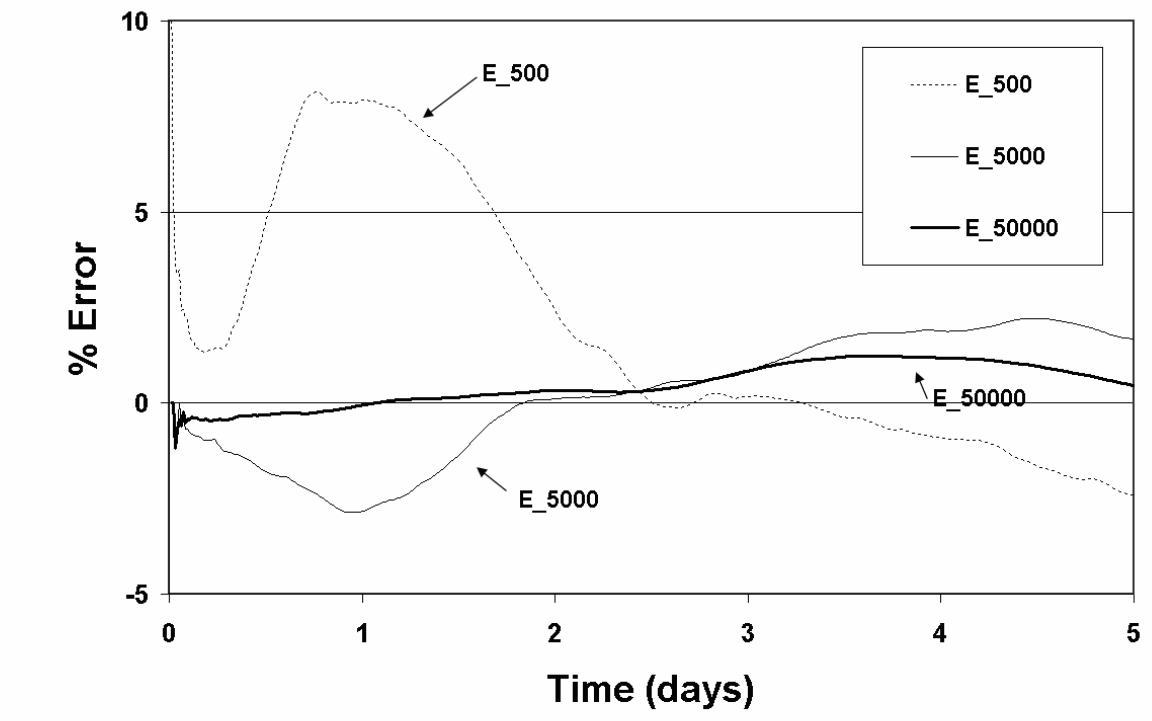

Figure E-6. Time series of cumulative squared error for Model 2. E2_**xxx, xxx** denotes the number of particles used.

### E.2.5.3. Parametric experiments

Parametric simulations were performed varying the diffusion coefficient (K) (1, 10, and 20 $m^2$/sec (corresponding to $\sigma_u^2$ = 22, 222, and 444 $cm^2/sec^2$), respectively for a 15 min. time step) and turbulent time scale (T) (0.5, 1, and 10 days) to show that the model is capable of accurate predictions over the range of K and T values typically observed in coastal waters.

Time series predictions of the mean squared separation, obtained from Model 1 and Model 2, for K= 1, 10, and 20 $m^2$/sec, together with corresponding analytic solutions, are shown in Figure E-7. The turbulent time scale (T) for Model 2 was maintained at 1 day. All simulations used 5,000 particles. Numerical model predictions are seen to be in very good agreement with the corresponding analytic solutions. The model performance declines slightly as the diffusion coefficient increases. The offset (2KT) between Model 1 and 2 predictions is clearly shown and increases linearly with the value of the diffusion coefficient selected.

The sensitivity of Model 2 predictions to variations in the autocorrelation time scale (T = 0.5, 1 and 10 days) is shown in Figure E-8. A diffusion coefficient of K = 1 $m^2$/sec and 5,000 particles were used in these simulations. Once again, model predictions are in very good agreement with the analytic solution. The offset increases linearly with the value of the autocorrelation time scale, as predicted by the analytic solution.

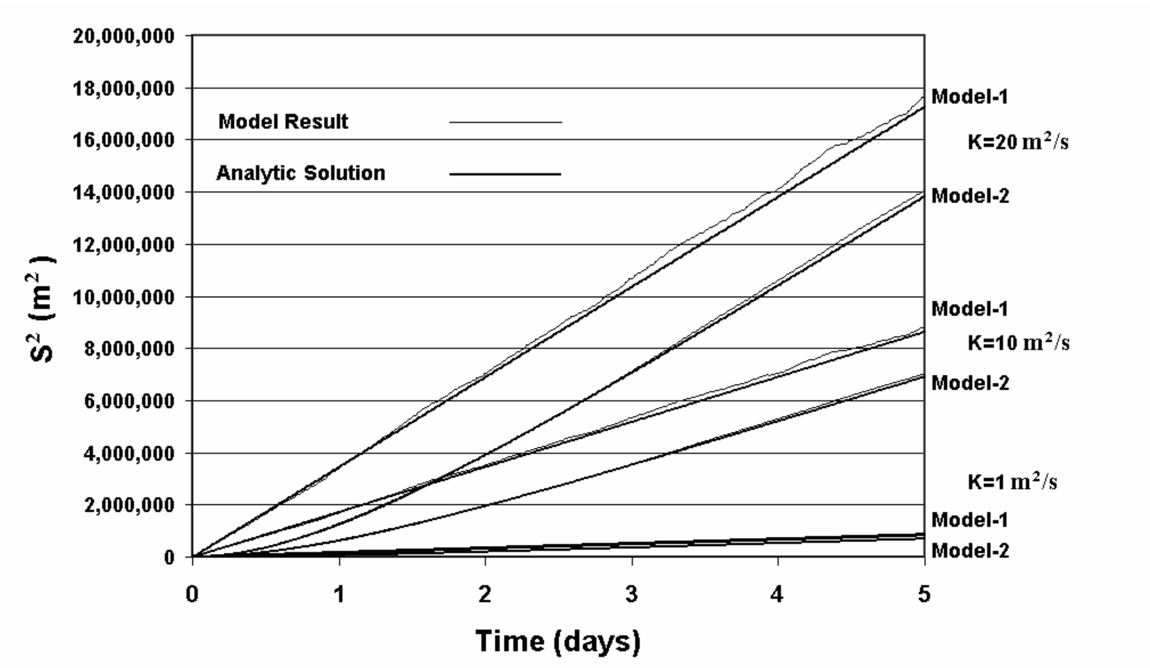

Figure E-7. Time series of the mean squared separation obtained for K= 1, 10, and 20 $m^2$/sec, using Models 1 and 2 (T= 1 day) and 5,000 particles. The analytic solutions for each case are also shown.

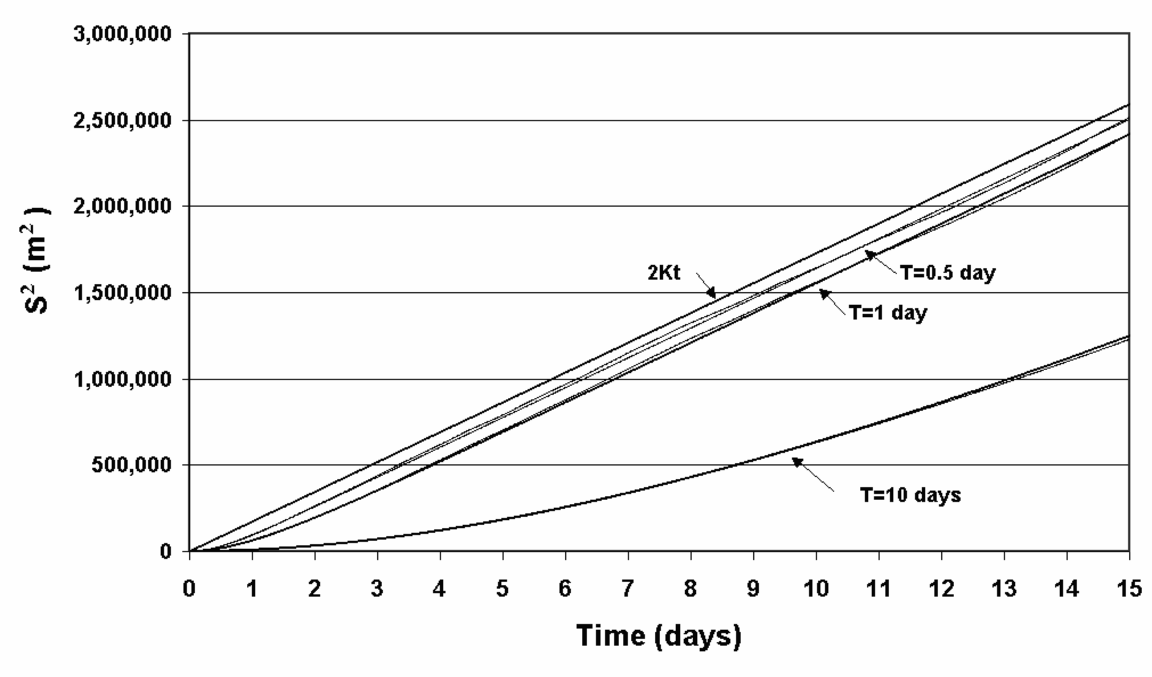

Figure E-8. Time series of the mean squared separation obtained for Model 2 (T= 0.5, 1, and 10 days), using K=1 $m^2$/sec and 5000 particles.

Some interesting insight can be gained on the application of Model 2 (random flight), relative to Model 1(random walk), for the search and rescue problem by studying the analytic solutions and assuming that the model parameters are constant. Specifically, we note that:

1. The predicted mean location of a drifting objective versus time is independent of the model selected, since the advective field and the associated integration to obtain particle position is exactly the same in both models.
2. Model 2 predicts a reduction in the effective search area (measured by $S^2$), relative to Model 1, beginning immediately after the initiation of the simulation and continuing with time. The difference in area becomes constant and scales as KT. For t >>T, the area ratio ($R_a$) of Model 2 to Model 1 can be approximated by $R_a$ = 1- T/t. The ratio of search area between the two hence decreases as time increases. As an example for T = 2 days, $R_a$ is 0.6 at t = 5 days; 0.8 at 10 days; and 0.1 at 20 days.

## E.3 Application of random walk and flight models to SDLMB drifter trajectories

The CG deployed three clusters of three SLDMBs: one set in Block Island Sound and the other two sets at the northern end of the Mid Atlantic Bight, in the general vicinity of the New York Bight. SLDMBs are air deployable, 7/10 size, Davis (1985) like surface drifters (70 cm draft, 1 m width) that are GPS tracked every half hour by the Argos satellite system. Table E-1 provides the drifter serial number, deployment time (EST) and location, and the cluster identifier name.

All drifters were released on July 27, 2004. Figures E-9a and b show the drifter trajectories for the duration of the 35-day experiment for the Block Island Sound and Mid Atlantic Bight releases, respectively.

Table E-1. Summary of SLDMBs deployed on July 27, 2004 by CG.

| Serial # | Time | Position | Cluster |
|---|---|---|---|
| 43049 | 0830 | N39-55.98 W72-40.28 | no data |
| 43061 | 0834 | N39-55.98 W72-40.28 | AB_B (five days) |
| 43062 | 0839 | N39-55.98 W72-40.28 | AB_B |
| 38867 | 0855 | N40-17.62 W73-34.40 | no data |
| 43057 | 0900 | N40-17.62 W73-34.40 | AB_A |
| 43060 | 0902 | N40-17.62 W73-34.40 | AB_A |
| 32779 | 1009 | N41-08.31 W71-44.72 | RI_A |
| 32773 | 1011 | N41-08.31 W71-44.72 | RI_A |
| 32776 | 1014 | N41-08.31 W71-44.72 | RI_A |

Drifters 43049 and 38867 ceased operation immediately after deployment and provided no useful data. 43061 provided data for the first 5 days only.

During the 35-day period in which the drifters were tracked, measurements of the near-sea surface currents were made by a three-station, short-range CODAR system covering the western end of Block Island Sound and the adjacent area south of Montauk Point and operated by the Universities of Rhode Island and Connecticut (Ullman et al, 2003; Ullman et al, 2004; Codiga and Rear, 2004) and by a two-station, long-range CODAR system operated by Rutgers University (Josh Kohut) for the Mid Atlantic Bight. The short-range system has a resolution of about 1.5 km and a range of 50 km (Ullman et al, 2003), while the long-range system has a resolution of 6 km and a range of 150 km (Josh Kohut).

All data were processed by the CODAR data analysis program, and provided hourly observations of the mean surface current and corresponding variances for each grid cell. The quality control protocol removed data where the signal to noise ratio was less than 5 dB or data for which the radial lines used to assemble the velocity estimates crossed at angles of 30 degrees (150 degrees) or smaller (larger). Plots of the percent data recovery (above and below 50 percent) over the experimental period are provided in Figure E-9. Recovery rates were generally good for the Block Island Sound system covering most of the radar footprint. Recovery rates for the Mid Atlantic Bight were much lower, with about half of the radar footprint giving less than 50 percent data returns. The Mid Atlantic Bight measurements showed significant diurnal variability reflecting the impacts of nighttime atmospheric conditions on the radar performance.

As a first step in the analysis, the three sets of drifter data were used to estimate the effective dispersion of the drifters over time. The three sets of cluster releases are referred to as:

| | |
|---|---|
| RI_A: | 3 buoys in Block Island Sound |
| AB_A: | 2 buoys near shore New York Bight |
| AB_B: | 2 buoys offshore New York Bight |

Wind time histories at the National Oceanic & Atmospheric Administration (NOAA)/National Data Buoy Center (NBDC) marine buoys on the Mid Atlantic shelf (44017, 44025), in the New York Bight Apex (ALSN6), and the entrance to Buzzard's Bay (BUZM3), are given in Figure E-10. Winds were spatially coherent throughout the study area, with mean speeds in the range of 4 to 6 m/sec.

All three sets of SLDMBs drifted in a southwesterly direction (generally shore parallel). The mean drift rates (Table E-2) were in the range of 5 to 8 km/day. The speeds were highly variable however, with standard deviations on the order of 60 percent of the average values. Maximum rates were 14 to 18 km/day. There was no statistically significant correlation between the wind and drifter speed, even in the wind-forced band. The impact of the predominantly semi-diurnal tidal currents is evident in all records, with excursions of about 2 km/day and oriented at 35/215 degrees in the Mid Atlantic Bight. The tidal currents are substantially stronger, with speeds above 50 cm/sec and oriented in a north/south direction on the southern boundary of Block Island Sound. Inertial oscillations (18.6 to 19 hour periods) are prevalent in the Mid Atlantic Bight drifter paths, as well as a lower frequency, large-scale looping motion. This looping motion is larger for cluster AB_B than AB_A.

Table E-2. Minimum, average, maximum, and standard deviation of SLDMB drifter speeds for each drifter.

| SLDMB ID Number | Minimum (km/day) | Average (km/day) | Maximum (km/day) | Standard Deviation (km/day) |
|---|---|---|---|---|
| 32773 | 0.2 | 6.3 | 15.6 | 3.9 |
| 32776 | 1.4 | 6.9 | 18.4 | 4.6 |
| 32779 | 0.5 | 6.3 | 14.2 | 4.0 |
| 43057 | 0.2 | 4.9 | 14.6 | 3.2 |
| 43060 | 0.9 | 5.1 | 12.2 | 2.9 |
| 43061 | 0.3 | 7.8 | 18.3 | 4.1 |
| 43062 | (Not examined due to short record) | | | |

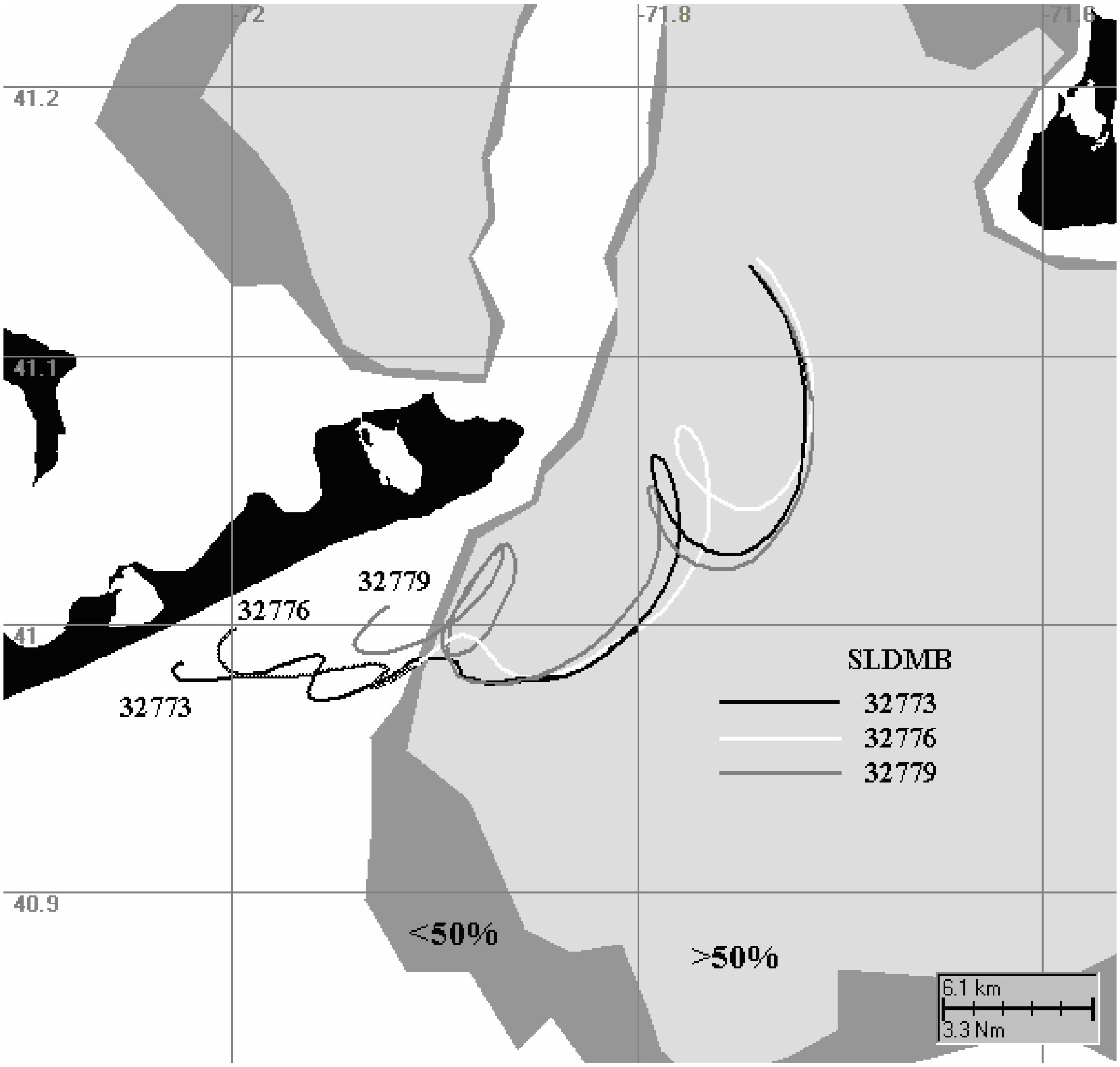

Figure E-9a. Trajectories of SLDMB drifters released in the Block Island Sound area. The drifter numbers are noted. The contours show the greater than 50 percent (light gray) and less than 50 percent (dark gray) data returns for the Universities of Rhode Island and Connecticut CODAR systems.

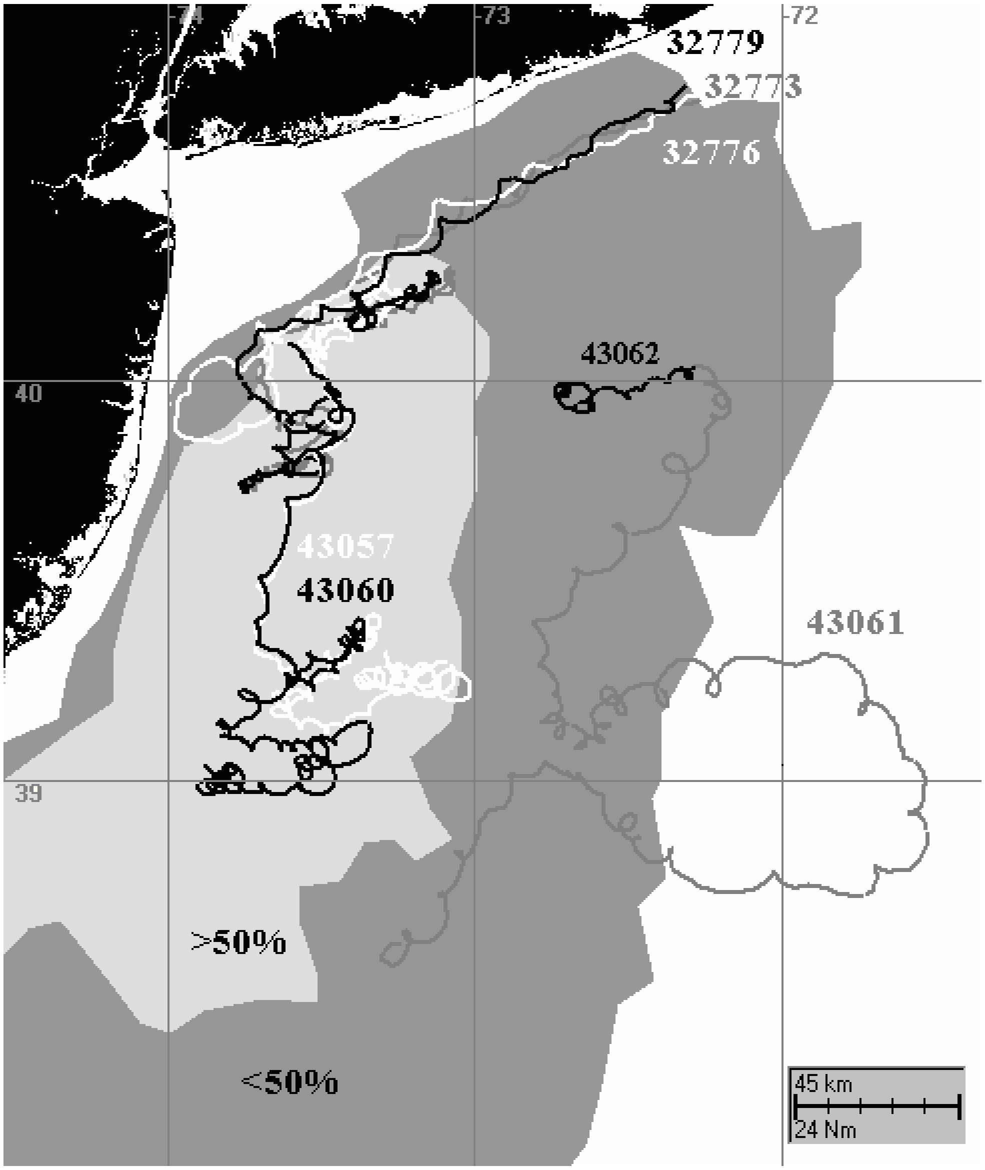

Figure E-9b. Trajectories of SLDMB drifters released in the Mid Atlantic Bight area. The drifter numbers are noted. The contours show the greater than 50 percent (light gray) and less than 50 percent (dark gray) data returns for the Rutgers University long range CODAR system.

Power spectra for the wind speed (buoy 44025) (upper panel) and the east/west and north/south components of the currents, based on data from SLDMB 43057, at CODAR cell 349 (location: 73.88669 Longitude, 39.33987 Latitude, cell with highest data return in MAB), and at the CODAR cells along the trajectory of 43057 (lower panels), are shown in Figure E-11a. A more detailed version of the power spectra, noting the principal diurnal, semi-diurnal and over-tide components is provided in Figure E-11b for buoy 43057 and its companion in cluster AB_A, 43061. The buoy data show that the most energy is found at the inertial oscillation period, followed by that in the semi-diurnal tidal band. Energies in the tidal harmonics and at periods typical of wind forcing (several days) (Figure E-10) are substantially smaller. The energy at the inertial oscillation period, based on the SLDMB and the corresponding CODAR data at the same locations, shows that the CODAR-based estimates have lower energies in the north/south direction than in the east/west direction, while they are comparable in the SLDMB observations. The CODAR measurements, hence, under represent the energy at the inertial oscillation period in the north/south direction. The energies at the semidiurnal tidal band, however, are comparable.

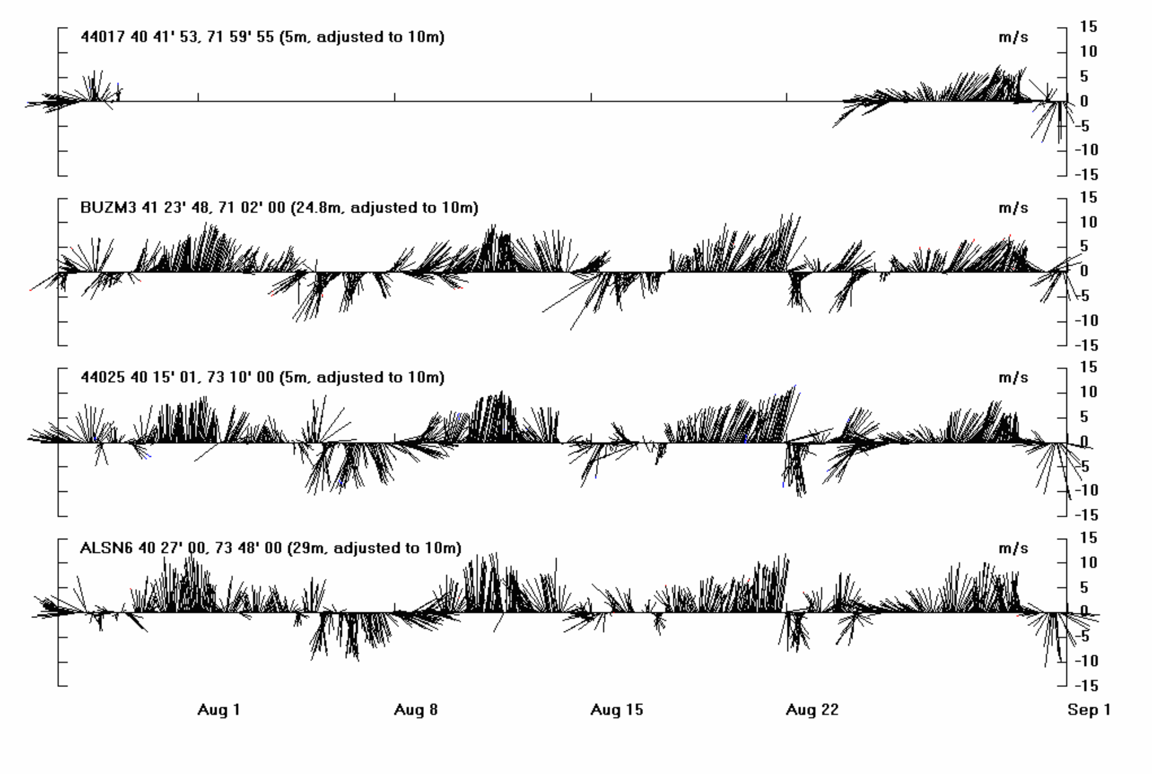

Figure E-10. Wind time series for July 27 to September 1, 2004 at NOAA/NBDC stations 44017, BUZM3, 44025, and ALSN6.

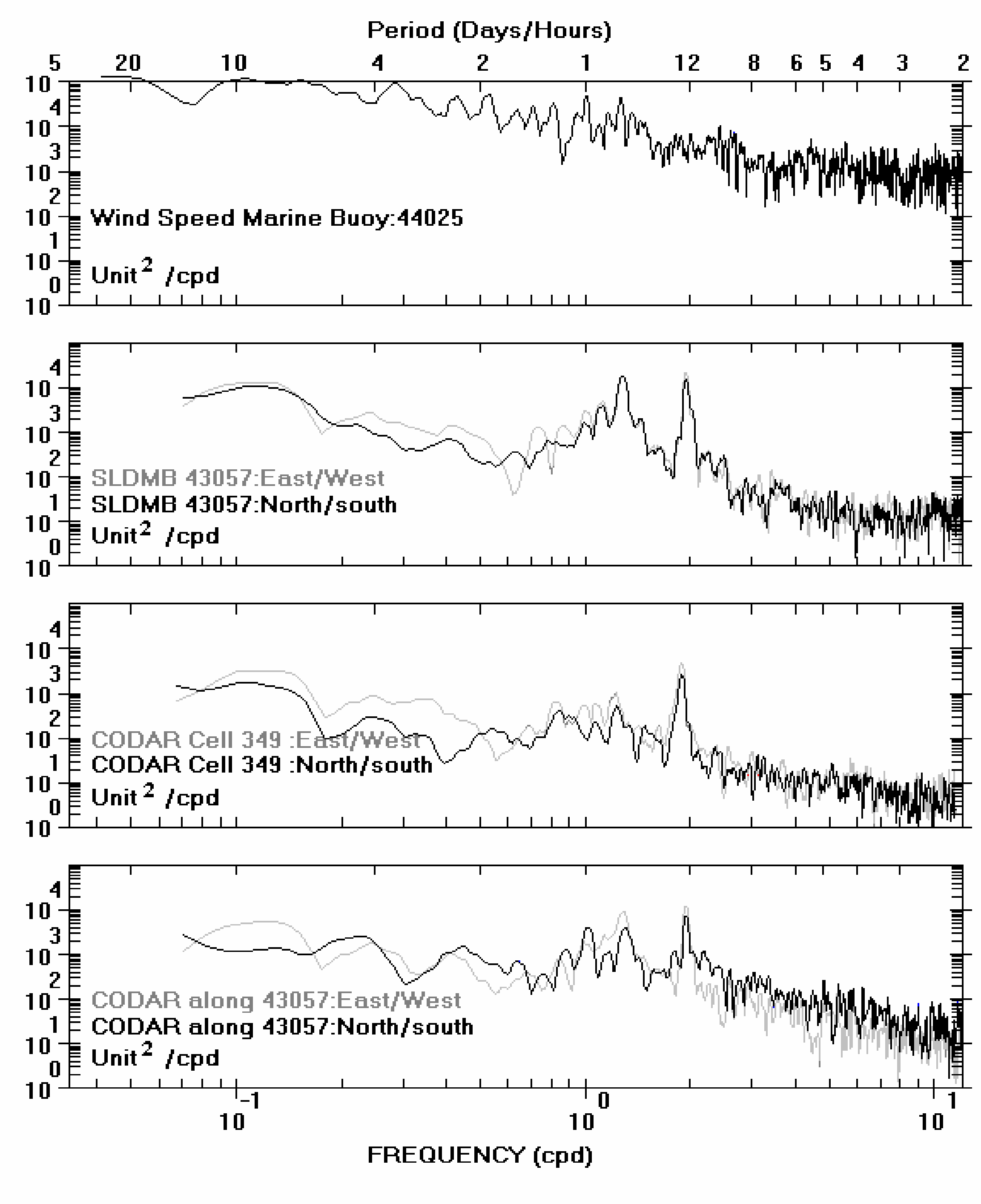

Figure E-11a. Power spectra of the wind (buoy 44025) and east/west and north/south components of the currents derived from the SLDMB 43057, from CODAR grid cell 349, and from CODAR along the trajectory of SLDMB 43057.

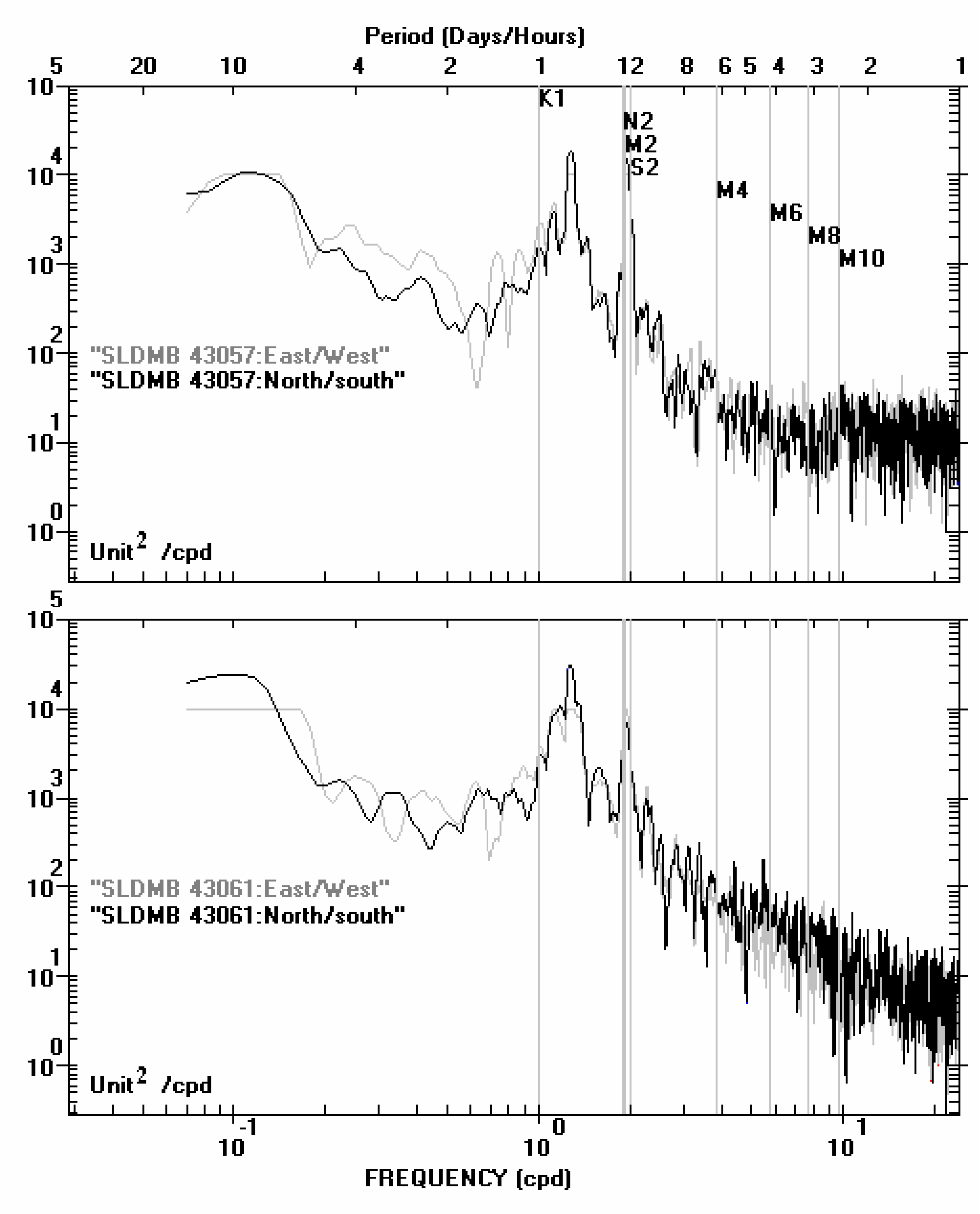

Figure E-11b. Power spectra for the east/west and north/south components of the currents derived from the SLDMB 43057 and 43061. The principal diurnal, semi-diurnal and harmonic tidal frequencies are noted.

For each cluster, the mean squared separation distances, $S^2$, were estimated by

$S^2$ ($m^2$) = (Drifter location - Center of the cluster) $^2$ / (Number of drifters)

Figure E-12 shows the mean squared separation distance (log scale) versus time for each cluster of drifters. Drifters released at both AB_A and AB_B stayed remarkably close together for the first 15 days, with separation variances of less than 1.0E6 to 5.0E6 $m^2$ (distances of 1 to 2.3 km).

Cluster AB_A started to disperse significantly after 25 days. The mean squared separation distance increased progressively throughout the experiment for cluster RI_A.

Assuming that the mean squared separation was approximated by either a random walk (Equation 4) or a random flight model (Equation 10), estimates of the dispersion coefficients were made for each cluster.

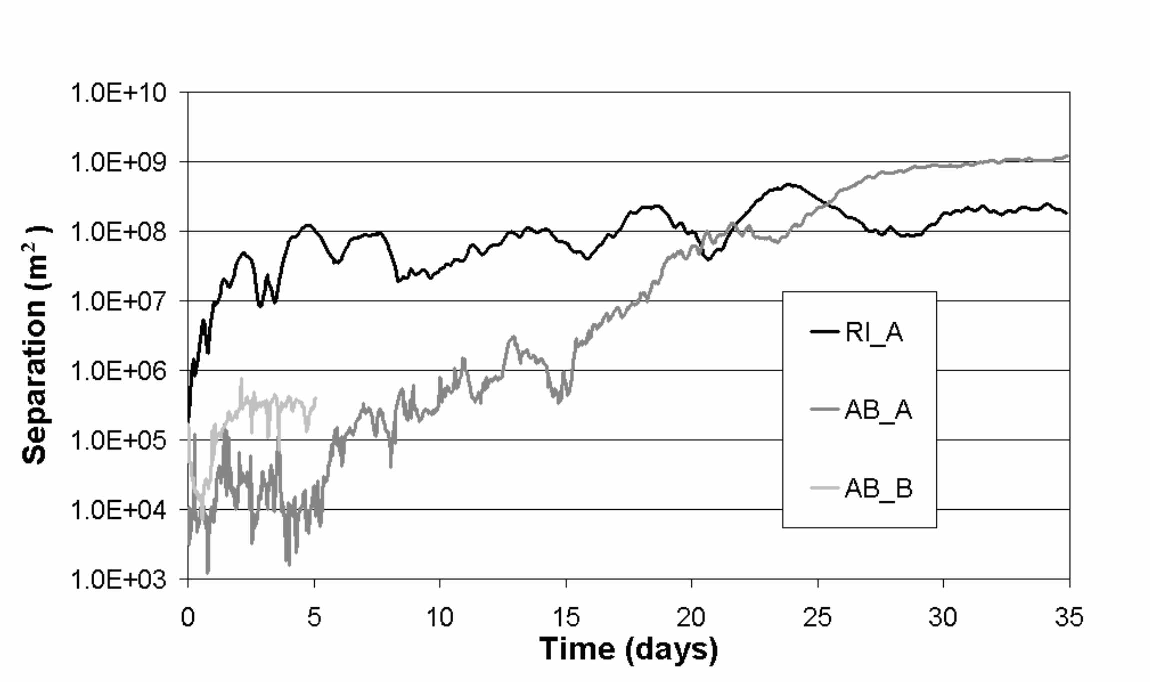

Figure E-12. Mean squared separation distance squared versus time for each cluster of drifters.

Figures E-13a and b show the mean squared separation distance versus time for cluster RI-A and AB_B, respectively. Results for cluster AB_B are not provided, since one drifter only provided data for the first 5 days of the experiment. Lower, mid, and upper bound fits of the random walk model to the data were made and resulted in the dispersion values shown in Figure E-13 and Table E-3. Restricting attention to the median values, cluster RI_A gave a dispersion coefficient of 40 m$^2$/sec, consistent with what one might expect on the shelf. The values for AB_A (85 m$^2$/sec) were about twice those for RI_A. A closer look at the mean squared separation distance for AB_A, however, shows that the dispersion estimate is dominated by the last 10 days of the record. If attention is restricted to the initial five days for AB_A and AB_B (Figure E-14), the dispersion coefficient is very low, on the order of 0.3 m$^2$/sec.

Table E-3. Dispersion values estimated from cluster separation statistics assuming a random walk model.

| Cluster | Dispersion coefficient (m$^2$/sec) | | |
|---|---|---|---|
| | RI_A | AB_A | AB_A & AB_B* |
| Lower: | 17 | 20 | 0.1 |
| Median: | 40 | 85 | 0.3 |
| Upper bound: | 110 | 185 | 0.75 |

For comparison to the values in Table E-3, Okubo's (1971) 4/3$^{rds}$ power law gives dispersion coefficients in the range of 20 to 200 m$^2$/sec for time scales from 5 to 30 days. These values are broadly consistent with, but larger than, those observed by the cluster analysis. Elliott et al, (1997) have recently analyzed data from short-term (less than 2 days) dye dispersion studies in coastal and estuarine waters, and find that the dispersion coefficient scales linearly with the current speed for these releases. For peak tidal current speeds in the range of 40 to 60 cm/sec for the present study areas, dispersion coefficients would be approximately 0.4 to 0.6 m$^2$/sec.

It is impossible to reconcile the differences in estimates of the dispersion coefficient from the cluster analysis given the very limited drifter data available.

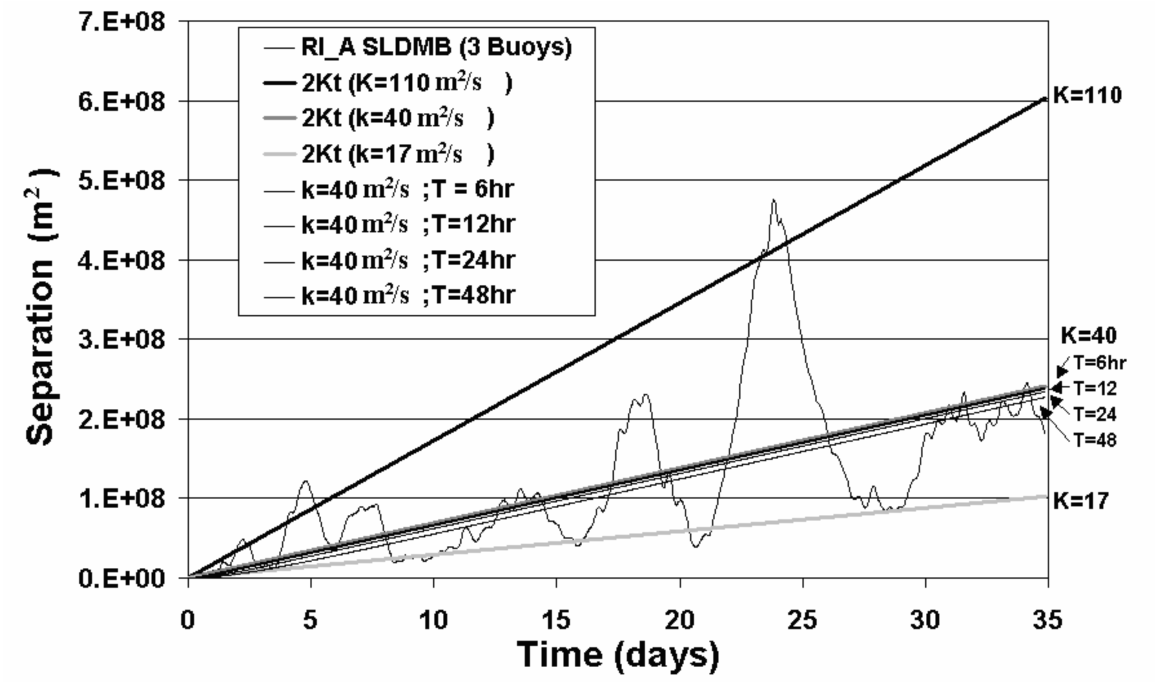

Figure E-13a. Mean squared separation distance versus time for cluster RI_A. Also shown are lower, mid and upper bound fits of random walk and random flight models with the parameter values given in the legend.

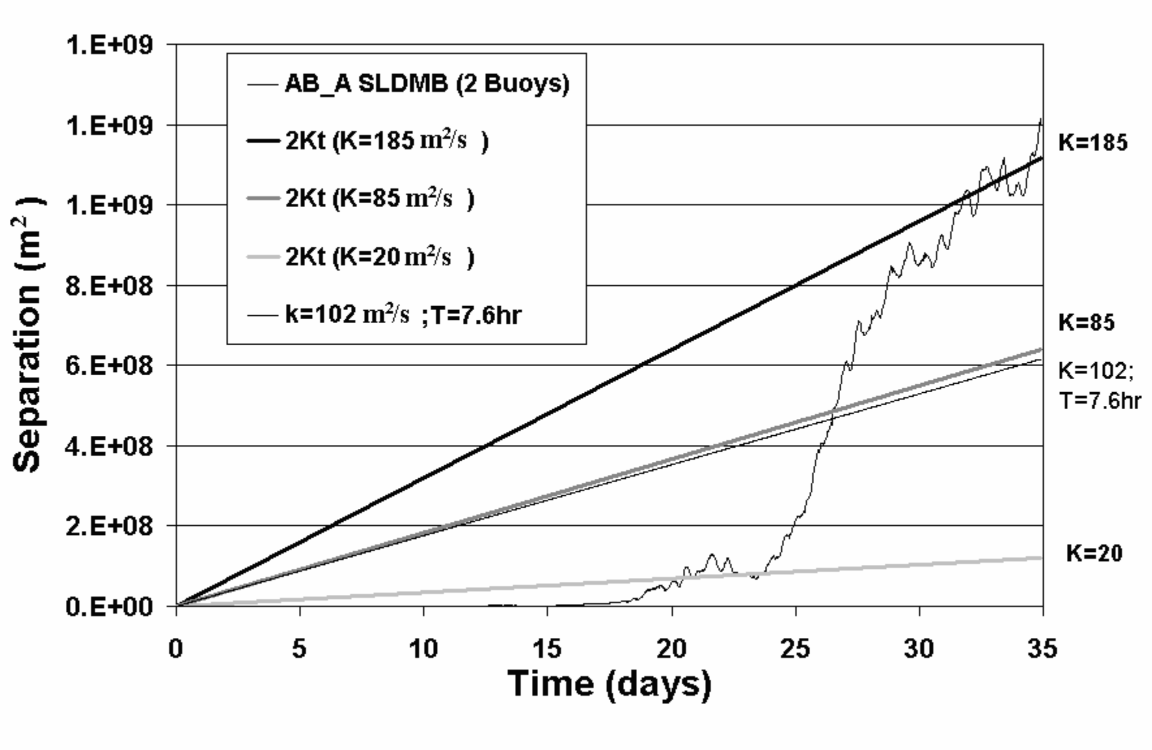

Figure E-13b. Mean squared separation distance versus time for cluster AB_A. Also shown are lower, mid, and upper bound fits of random walk and random flight models, with the parameter values given in the legend.

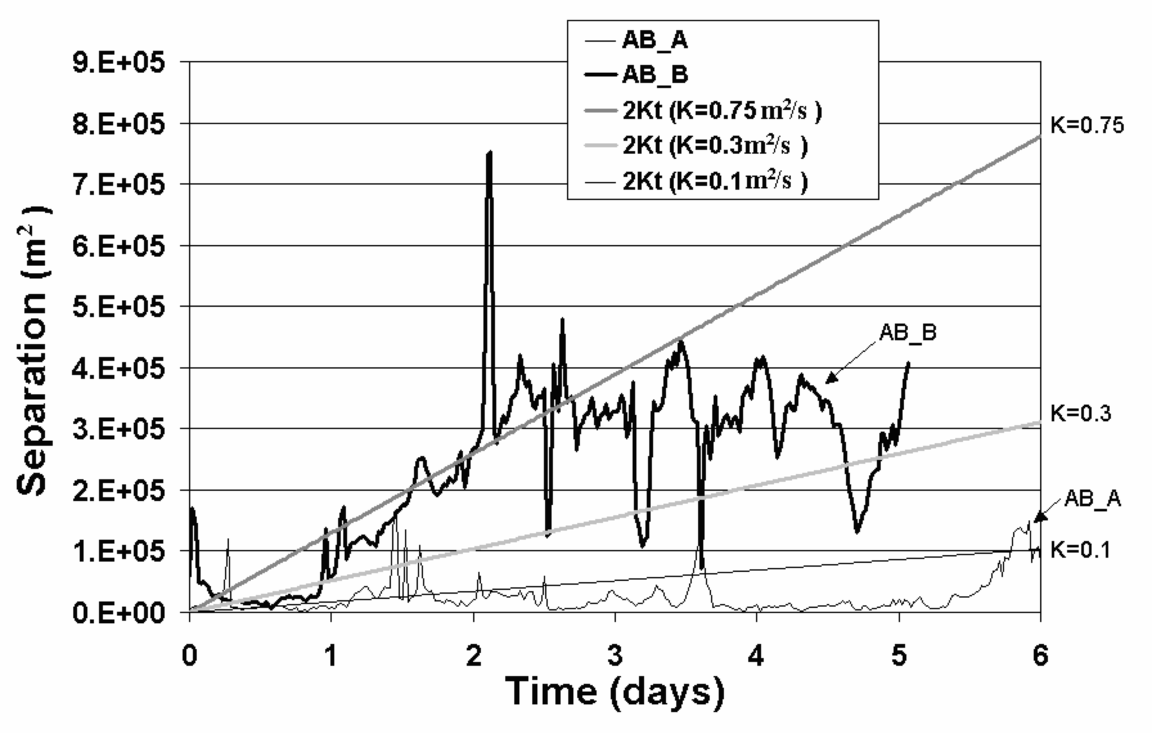

Figure E-14. Mean squared separation distance versus time for cluster AB_A and AB-B restricted to the first 5 days of the experiment. Also shown are lower, mid, and upper bound fits of a random walk model to the data, with the values of the dispersion coefficient given in the legend.

In order to apply the random flight model to the data, an estimate of the autocorrelation time scale is required. The autocorrelation function versus lag time for the east/west and north/south components of the velocity was estimated at that location with the largest number and best quality data return in the Mid Atlantic Bight footprint (Station 349, 73.88669 Longitude 39.33987 Latitude). The autocorrelation for the two components are shown in Figures E-15a and b. The analysis was performed using the hourly sampled CODAR data and with a corresponding de-tided data set where the eight largest tidal harmonics were removed. The tidal currents were dominated by the $M_2$, $S_2$, and $N_2$ constituents, with mean speeds of 11.3, 2.66 and 2.3 cm/sec and directions of 35, 57, and 28.8 degrees, respectively. Assuming that the autocorrelation function can be represented by an exponential relationship (Equation 9), the autocorrelation time scale (1/e folding time) is 3.5 hrs for the original record and 6.5 hrs for the de-tided record. Even when the de-tided record is used, the autocorrelation function shows evidence of a periodic variation. Estimates were made of the dispersion coefficient using Equation 3, with T based on the autocorrelation time scale. The east and north components gave dispersion coefficients of 170 and 106 $m^2$/sec, respectively, for the original record and 187 and 130 $m^2$/sec for the de-tided record. These values are comparable to those based on the analysis of drifter cluster AB_A above.

Estimates of the dispersion coefficient can also be made by directly integrating the autocorrelation function (Batchelor, 1953). In the present case, the estimate proved to be very sensitive to the length of the integration time since the autocorrelation function is quite variable at long lag times (Figure E-15). This is particularly true for the original record, which is strongly impacted by tidal variations. Ojo and Bonner (2000) had a similar experience in deriving dispersion coefficients from HF radar data collected in Corpus Christi and Matagorda Bay, Texas. The mean value of their dispersion coefficients was in the range of 1.5 to 4.5 m$^2$/sec, while peak values reached several thousand.

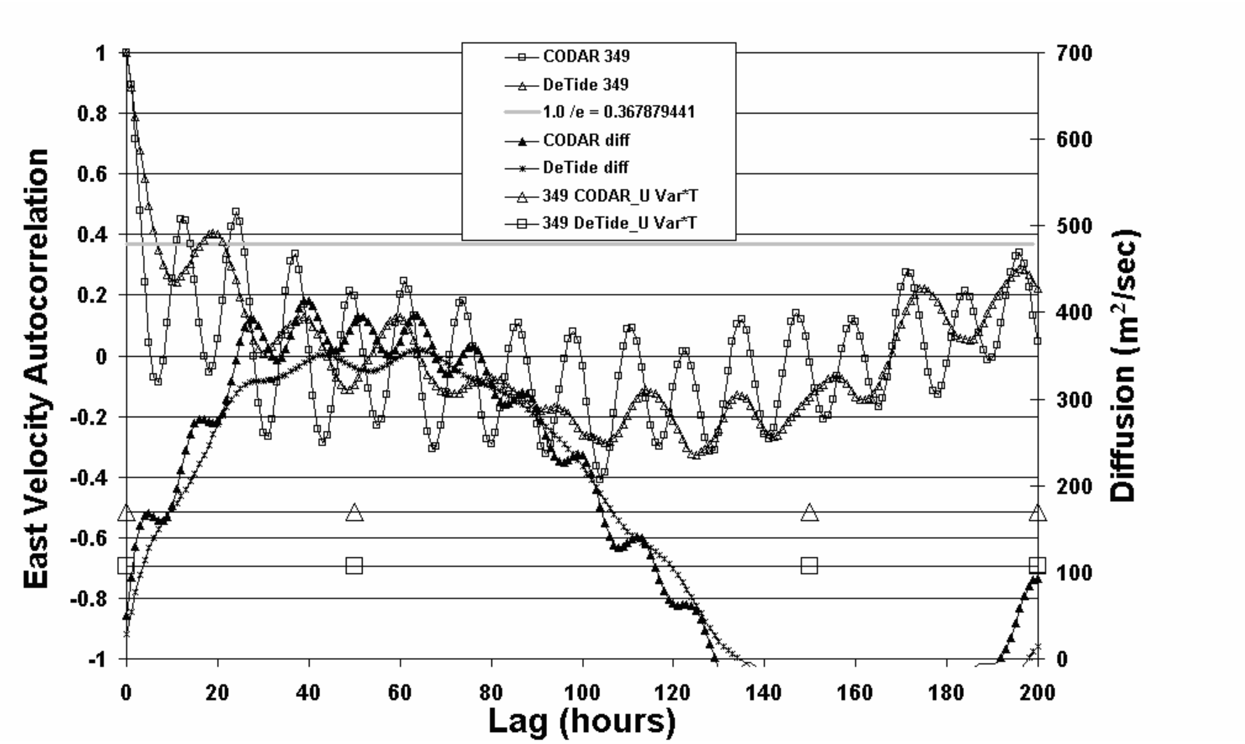

Figure E-15a. Autocorrelation of the east component of the velocity versus lag time for the original CODAR and de-tided CODAR data from location 349 in the Mid Atlantic Bight. Also shown are estimates of the dispersion coefficient based on the assumption that Equation 10 can represent the autocorrelation function.

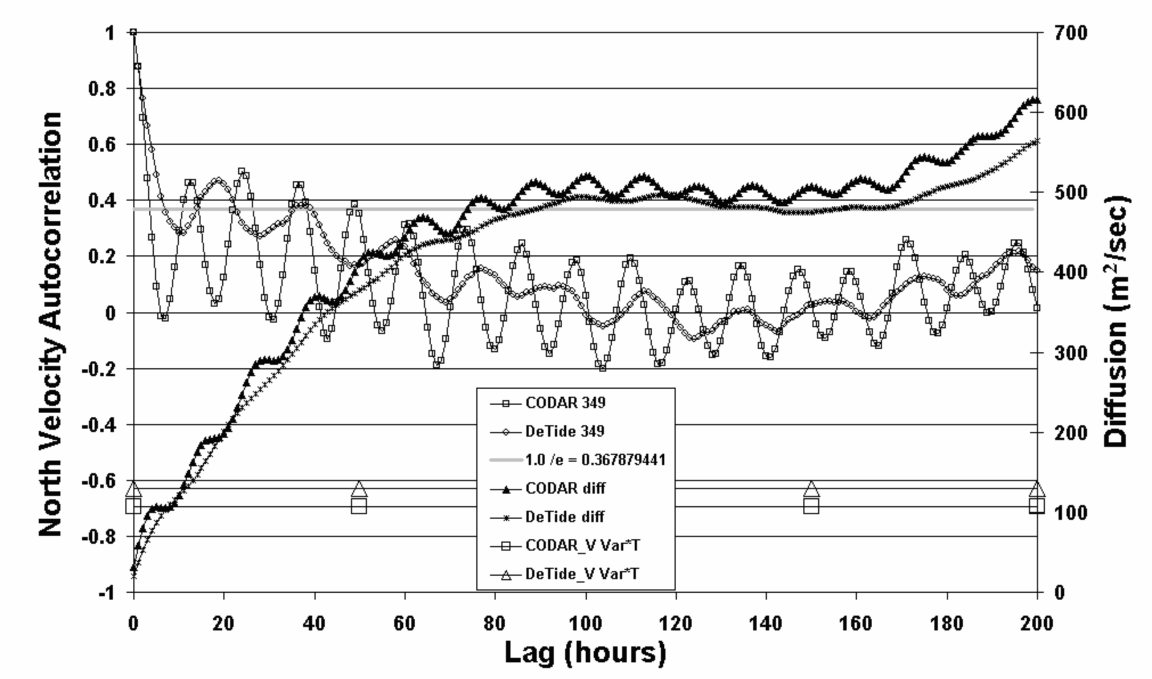

Figure E-15b. Autocorrelation of the north component of the velocity versus lag time for the original CODAR and de-tided CODAR data from location 349 in the Mid Atlantic Bight. Also shown are estimates of the dispersion coefficient based on the assumption that Equation 10 can represent the autocorrelation function.

With an estimate of the autocorrelation time scale, one can assess the impact of assuming that a random flight model approximates the dispersion of the drifters. Restricting attention to cluster RI_A, Figure E-13a shows a comparison of a random flight model fit to the mean squared separation distance data, assuming a median dispersion coefficient of 40 $m^2$/sec and autocorrelation time scales of 6, 12, 24, and 48 hours. Six hours is approximately the value determined from an analysis of the CODAR data (Figures E-15a and b). It is noted that the variations of the autocorrelation time scale over the range selected have very little impact on estimates of the mean squared separation distance. It is clear that there is insufficient data to estimate the improvements resulting from use of a random flight model. Application of an unconstrained two-dimensional optimization method gives a K=102 $m^2$/s and T=7.6 hr for cluster AB_A. Once again the use of a random flight model provides no benefit over a random walk approximation in the present application.

## E.4 Comparison of velocities derived from SLDMB versus CODAR

Anticipating the use of the CODAR data as input to a search and rescue model, it would be useful to compare the observed surface current data from the CODAR system and similar data derived from the SLDMB drifters. The velocities of the seven SLDMB drifters were therefore estimated at 1/2 hour time intervals by dividing the distance traveled by the elapsed time in the east/west and north/south directions. SLDMB data were available every half hour. These values were extremely erratic due to ubiquitous irregularities in the original position versus time files.

The data were edited to remove outliers, the majority of which were not contiguous in time. The effect of the editing was a smoother and more realistic velocity field. It was assumed that the drifters and CODAR data both represented the currents in the upper meter of the water column, and hence the two measurements could be compared directly.

The CODAR velocity at a particular SLDMB location and at a given time was estimated using inverse-distance weighting of the nearest five CODAR grid points in space and linear interpolation in time. If the distance to any CODAR grid point was greater than 4 km, the data were not used.

Figures E-9a and b show the SLDMB trajectories, as well as the CODAR data coverage (50 percent> and <50 percent) contours over the experimental period for the Block Island Sound and Mid Atlantic Bight areas, respectively. Comparison of the above and below 50 percent coverage in the two areas shows that the difference is minimal in the Block Island Sound and substantial in the Mid Atlantic Bight.

Time series plots were prepared to compare the CODAR-observed and SLDMB-derived currents, and are provided in Figures E-16a, b, and c for the Block Island Sound (a, b) and Mid Atlantic Bight (c) drifter clusters, respectively. The upper panels show the SLDMB (thick) and CODAR (thin) velocities, and the lower panel the corresponding differences. Figure E-17 provides scatter plots for the east (light gray) and north (black) velocity and the associated correlation coefficients.

In general, the difference in velocity between the drifter-derived currents and those from CODAR are similar in magnitude to their speed. The variance and the autocorrelation time of the difference (errors) are also similar for both SLDMB and CODAR velocities. Tidal variations are dominant in Block Island Sound and are clearly evident in both data sets. They are less prevalent in the Mid Atlantic Bight observations. For the three buoys released in Block Island Sound (32773, 32776, and 32779), the scatter plots (Figure E-17) show a correlation of less than 0.1 for the east component and greater than 0.6 for the north component. This is consistent with the dominant axis of the tidal current ellipses, which are generally north/south in the area of the releases. For the Mid Atlantic Bight buoys, the scatter plots show a correlation coefficient of greater than 0.75 for the east component (onshore-offshore) and less than about 0.4 for the north component. This behavior is just the opposite of the releases in Block Island Sound. The radar obtains a more accurate measure of the onshore-offshore flow than the along-shelf flows. Both correlation coefficients are observed to be lower in areas where the percent data return is below 50 percent (compare correlation coefficients for 43061 with those for 43057 and 43060).

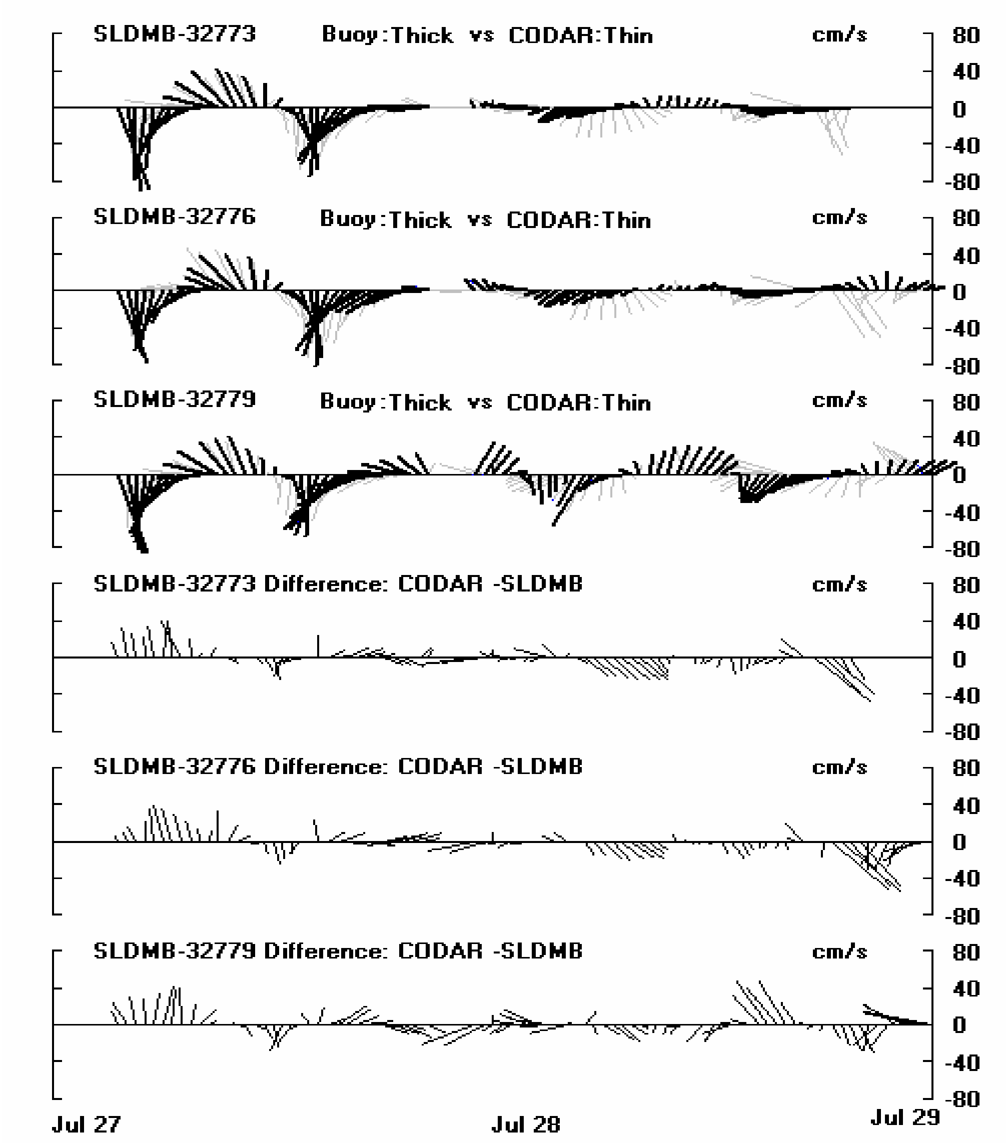

Figure E-16a. Time series of the SLDMB and CODAR derived currents (upper three) and the difference between the two (lower three) for drifters released in Block Island Sound (see Figure E-9a).

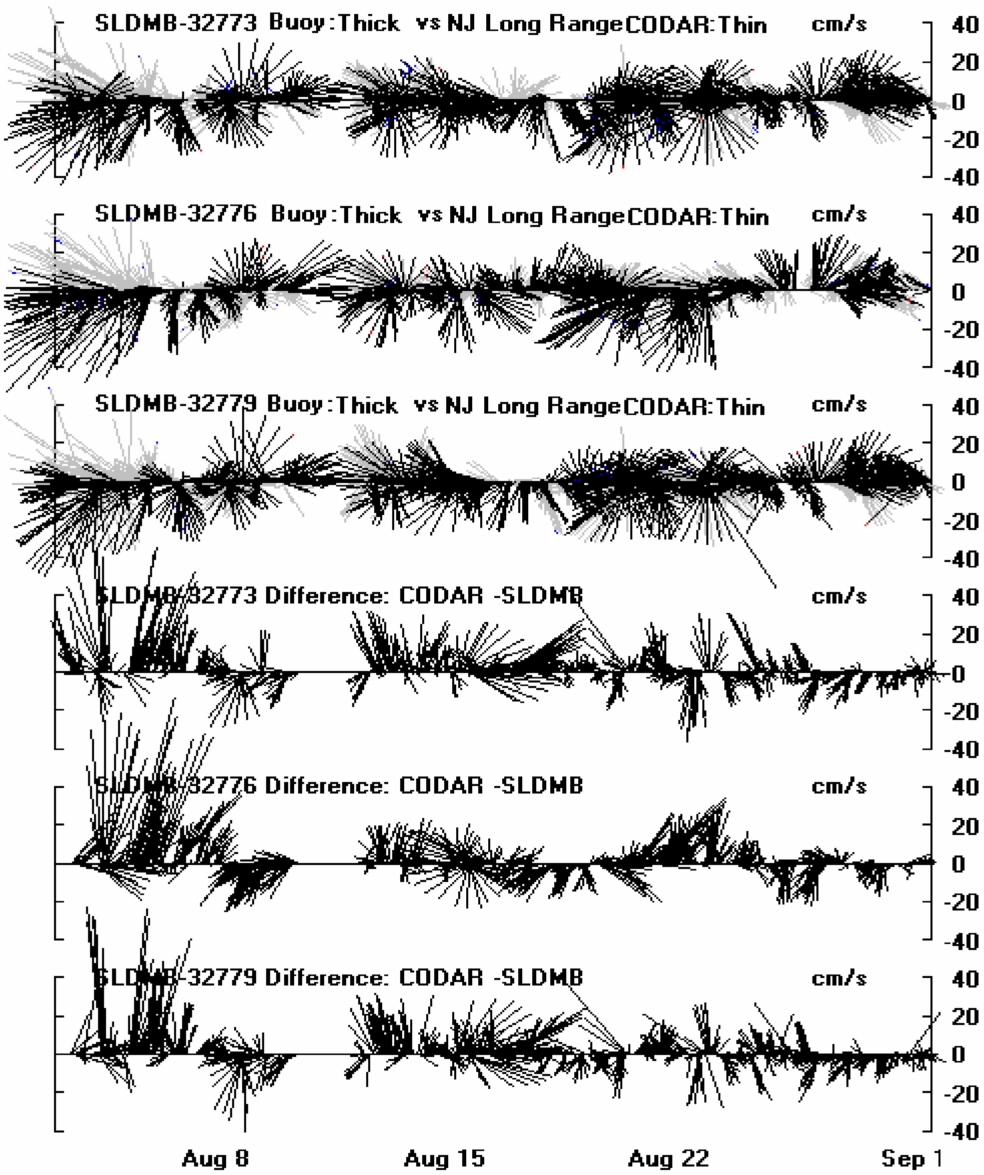

Figure E-16b. Time series of the SLDMB and CODAR derived currents (upper three) and the difference between the two (lower three) for drifters released in Block Island Sound and transported into the Mid Atlantic Bight (see Figures E-9a and b).

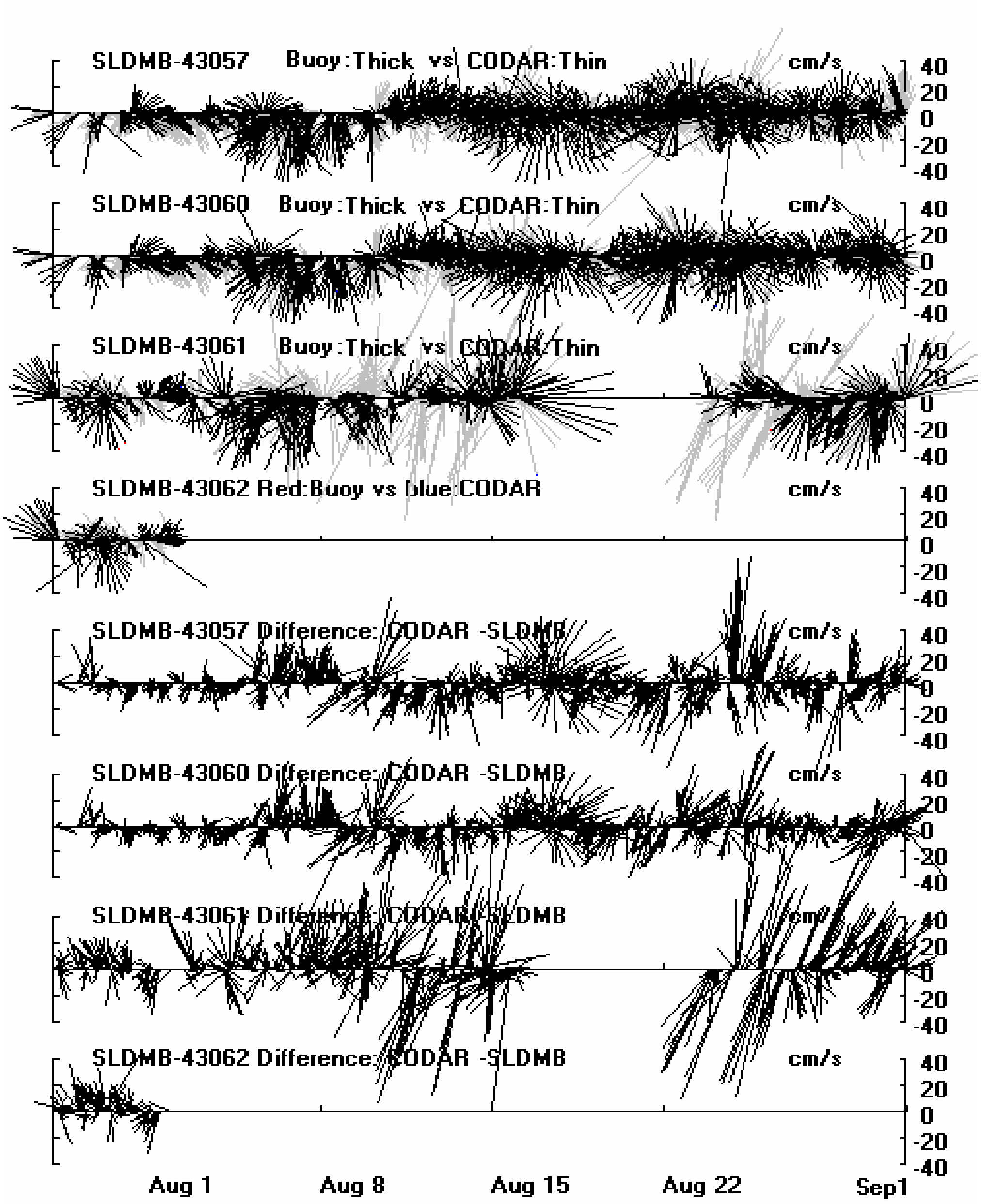

Figure E-16c. Time series of the SLDMB and CODAR derived currents (upper four) and the difference between the two (lower four) for drifters released in the Mid Atlantic Bight (See Figure E-9b).

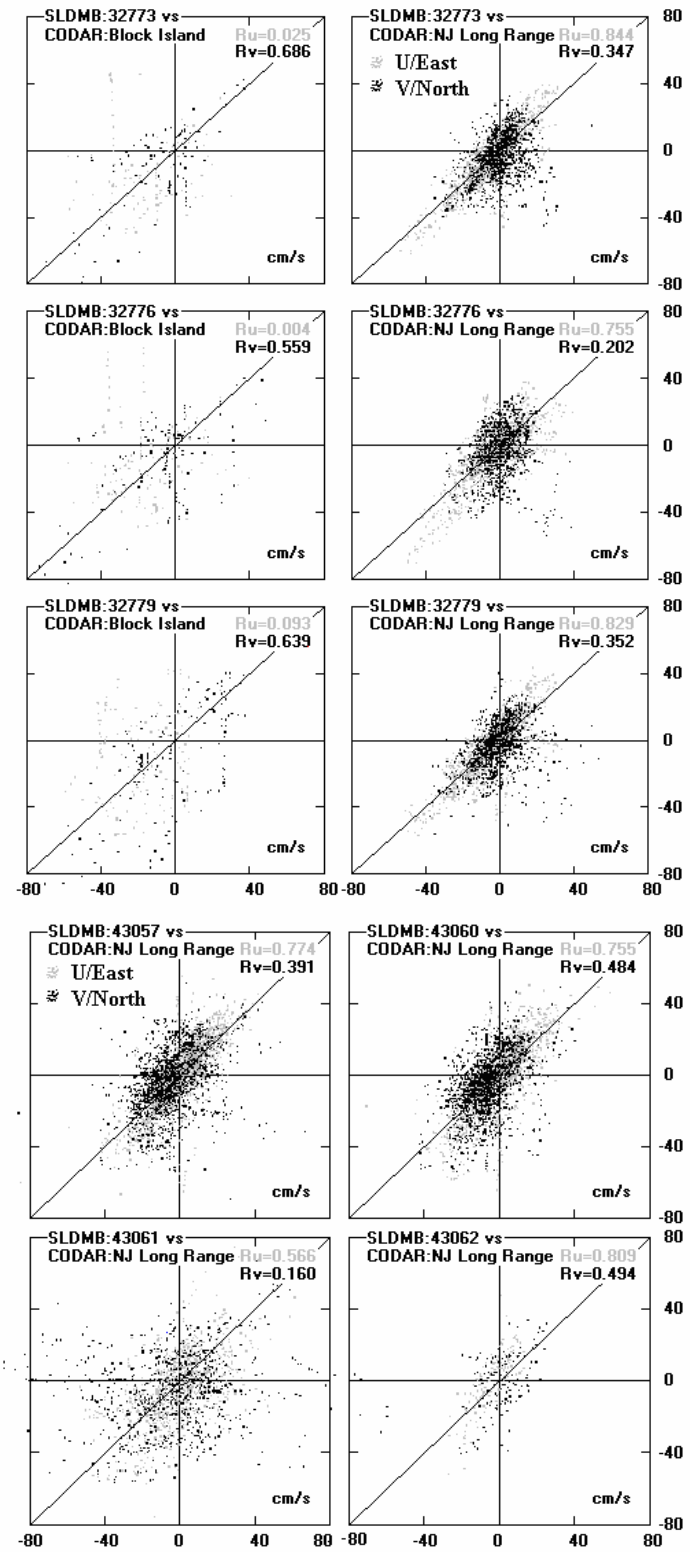

Figure E-17. Scatter plots for the east (u, light gray) and north (v, black) components of the velocity derived from the CODAR and SLDMB data, with associated correlation coefficient. The drifter number is provided in the top left corner of each plot.

## E.5 Estimates of dispersion coefficients based on CODAR data

Estimates of the dispersion coefficients for the Block Island Sound and Mid Atlantic Bight region were made based on an analysis of all the data collected over the SLDMB deployment period, where the CODAR data return was above 50 percent. Table E-4 summarizes the bulk-averaged, east/west and north/south velocity variance, average error variance, and the median autocorrelation time scale. The velocity variance and estimates of the velocity error were obtained directly from the CODAR data processing system. The dispersion coefficients were calculated using Equation 3, assuming that T is the autocorrelation time scale, which decreased exponentially with time. Dispersion coefficients based on both the velocity and errors variance are provided. Estimates based on the separation analysis presented above in Table E-3 are included for comparison.

Table E-4. Estimates of the dispersion coefficients based on CODAR data for Block Island Sound and Mid Atlantic Bight.

| | **Block Island Sound** | | **Mid Atlantic Bight** | |
|---|---|---|---|---|
| **Parameter** | **East/west** | **North/south** | **East/west** | **North/south** |
| Average variance ($cm^2/sec^2$) | 552.6 | 438.3 | 331.6 | 345.9 |
| Average error ($cm^2/sec^2$) | 45.3 | 29.8 | 107.3 | 217.0 |
| Median T* (hrs) | 3.7 | 2.8 | 5.0 | 5.0 |
| Dispersion coefficient ($m^2/sec$) | | | | |
| Based on variance | 726.2 | 441.8 | 596.8 | 622.6 |
| Based on error | 59.5 | 30.1 | 193.2 | 390.6 |
| Based on separation analysis | 40 | 85 | | |
| * T - autocorrelation time scale | | | | |

Using the velocity variances gives very large values of the dispersion coefficient for both areas, particularly for Block Island Sound. These large values are at least partially attributable to the horizontal shear in the tidal current fields in Block Island Sound. Replacing the variance with the CODAR velocity errors and using the autocorrelation time of the velocity reduces the dispersion to the range of separation analysis-based values.

## E.6 SARMAP simulations of SLDMB trajectories

SARMAP (ASA, 2003) simulations were performed using the CODAR data as input to predict the movement of the trajectories of the SLDMB drifters for the Mid Atlantic Bight releases (and for the Block Island releases as they drifted into the area covered by the Mid Atlantic Bight radar system). Each day-long simulation started at the reported SLDMB location at midnight. A 1-day simulation interval was used, as it is typical of the time scale of a search forecast period. Simulations were repeated with a new start at the current SLDMB position each succeeding day, with no overlap in time. Based on the availability of SLDMB data, 178 independent simulations (Table E-5) were performed.

Table E-5. Number of simulations performed for each SLDMB.

| SLDMB | Period (Y2004) | Simulations |
|---|---|---|
| 32773 | Aug 2 - Aug 31 | 30 |
| 32776 | Aug 2 - Aug 31 | 30 |
| 32779 | Aug 2 - Aug 31 | 30 |
| 43057 | Aug1 - Aug 31 | 31 |
| 43060 | Aug1 - Aug 31 | 31 |
| 43061 | Aug1 - Aug 31 | 26 |
| 43062 | (not used as the record is too short) | |
| | Total | 178 |

This series of simulations was performed to characterize the advection transport fields and hence, no diffusion/dispersion was used. A typical simulation ended with the predicted location of the drifter some distance away from the observed location. The difference in final location between the observed and model predictions is a result of errors in the buoy location and the CODAR estimated currents and the turbulence inherent both in the buoy movements and CODAR observations. Independent of the reasons, the difference in location provides an estimate of the equivalent diffusion value such that the observed location of the buoy was within the model predicted search area. With observed velocities in range of 5 to 18 km/day and CODAR grid resolutions of 6 km in the Mid Atlantic Bight, trajectory predictions sampled no more than a few grids of current data in the day-long simulations; hence, current shear cannot be an important contributing factor to the model-predicted position of the drifters.

Figure E-18 shows the trajectories of each buoy (continuous dark gray thick line) and the corresponding model predicted trajectories (black lines), at 1-day intervals. A circle is drawn for each simulation centered at the model-predicted buoy location at the end of one day with a radius equivalent to the distance from the predicted to the observed location at the end of the day. This circle represents the minimum area required so that the target (search object) is within the model-predicted search area. The above and below 50 percent CODAR data return are noted by the contour intervals. In general, the circle sizes approximately inversely reflect the CODAR percent coverage, the higher the coverage the smaller the circle size. The circle sizes are particularly large immediately south of Long Island. When CODAR returns are higher, better estimates of the velocity are obtained and reflected in lower differences between predictions and observations.

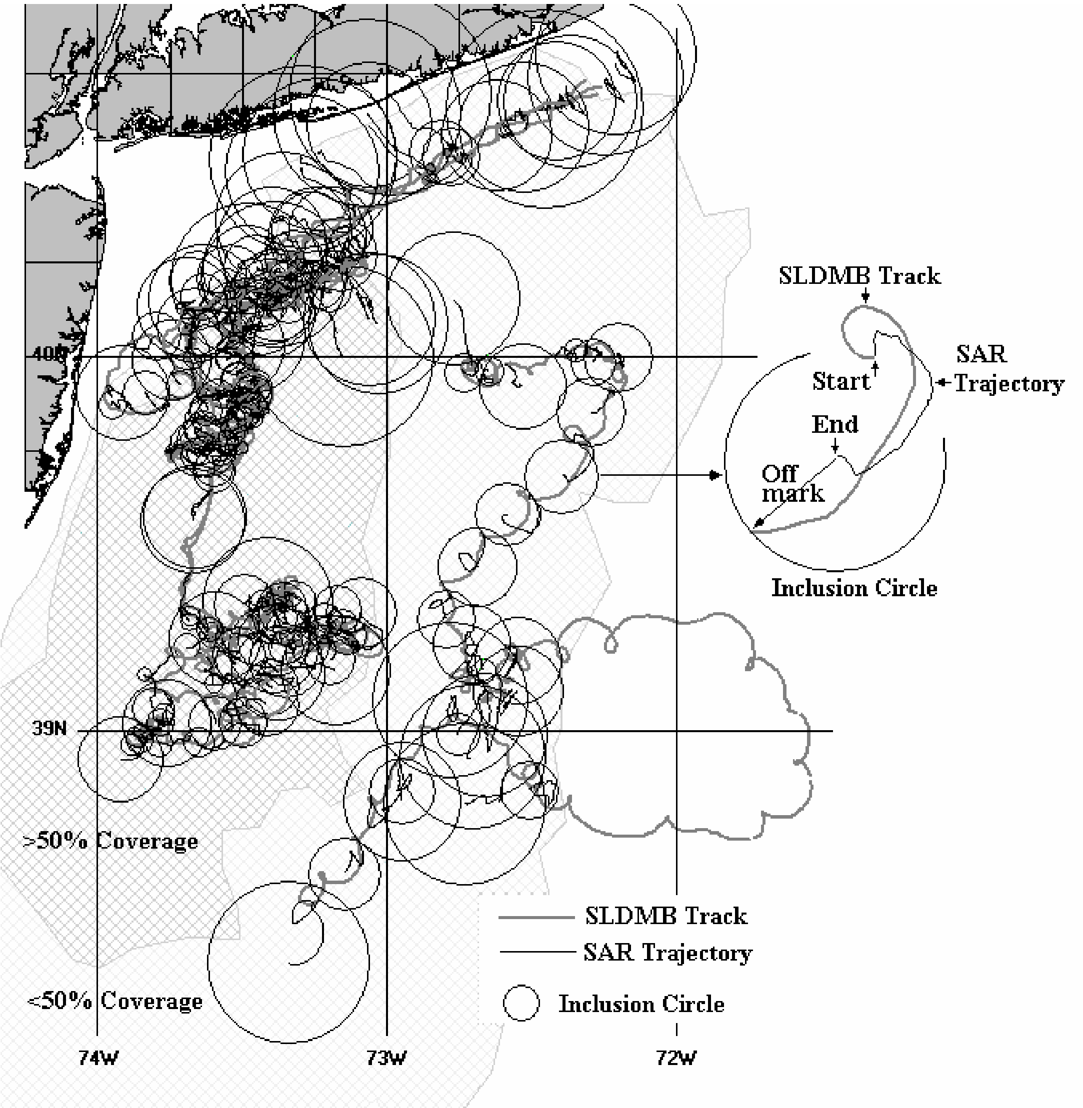

Figure E-18. Observed SLDMB trajectories and corresponding SARMAP predictions for 1-day simulations, restarted every day along the SLDMB path. Also shown is an inclusion circle, which is bounded by the ends of the observed and model predicted trajectories.

Figure E-19 provides histograms of the separation distance between the predicted and observed locations of the buoys at 3, 6, 12, and 24 hrs after the start of the simulation. The last panel is a repeat of the results at 24 hrs showing additional details of the frequency distribution as well as the cumulative distribution. Figure E-20 shows the same data but in terms of the average and 95th percentile separation distances versus time. Both plots show that the separation distance increases and the distribution gets broader and flatter with time. At the end of the simulations, the maximum separation distance is ~30 km. The maximum occurrence distance is in the range of 3 to 4 km. The median distance is 7 km and the average is 9.3 km. The 95th percentile separation distance is 23 km. These results are consistent with similar analyses performed on CODAR data and SDLMB buoy deployment in Middle Atlantic Bight by Ullman et al, (2002), which show 95th percentile separation distances at the end of 1 day of 25 km.

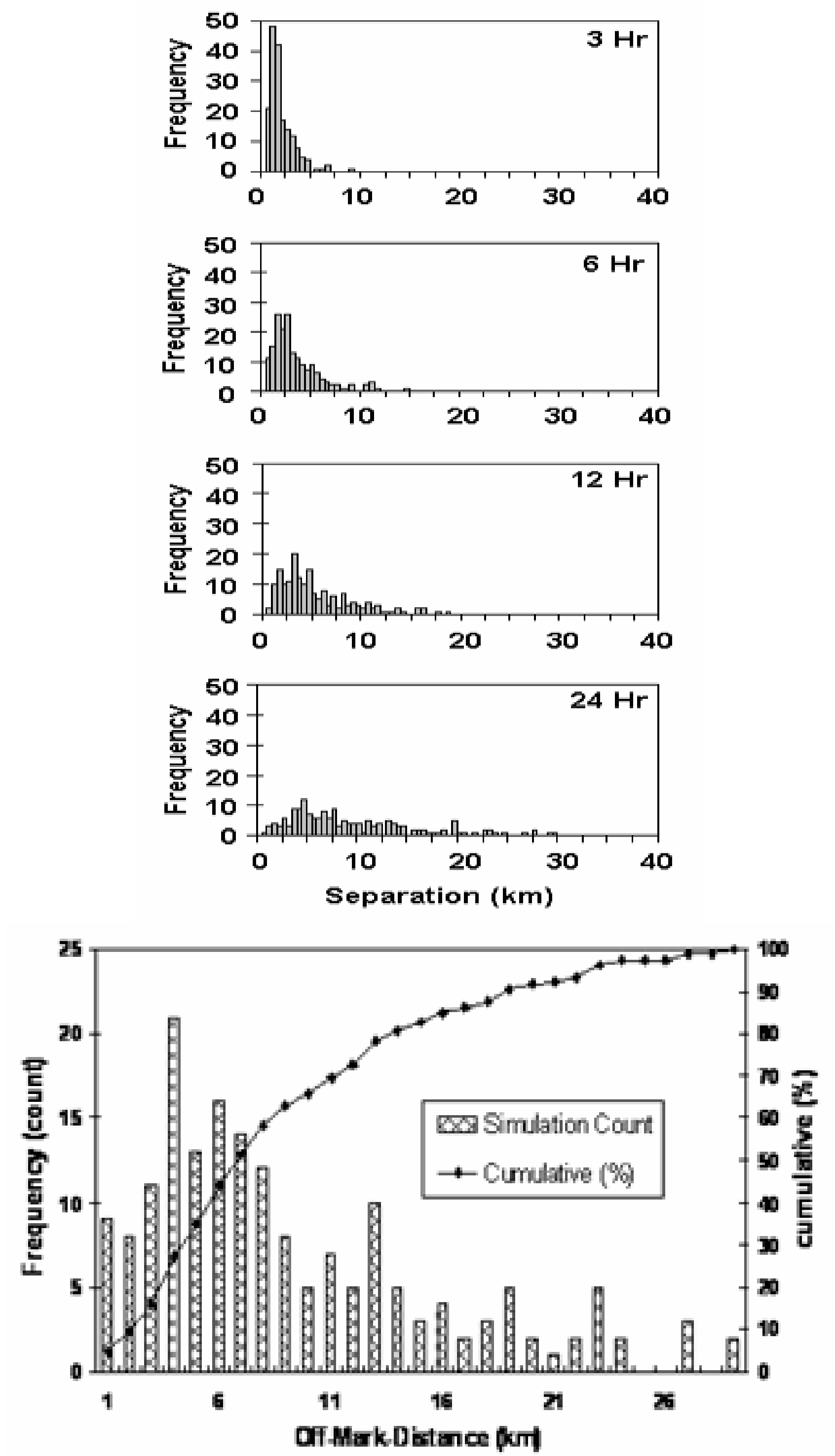

Figure E-19. Histograms of the separation distance between model-predicted and observed for the SLDMBs at 3, 6, 12, and 24 hrs after the start of the simulation. The last panel shows the distribution and cumulative separation distance distribution at the end of 1 day.

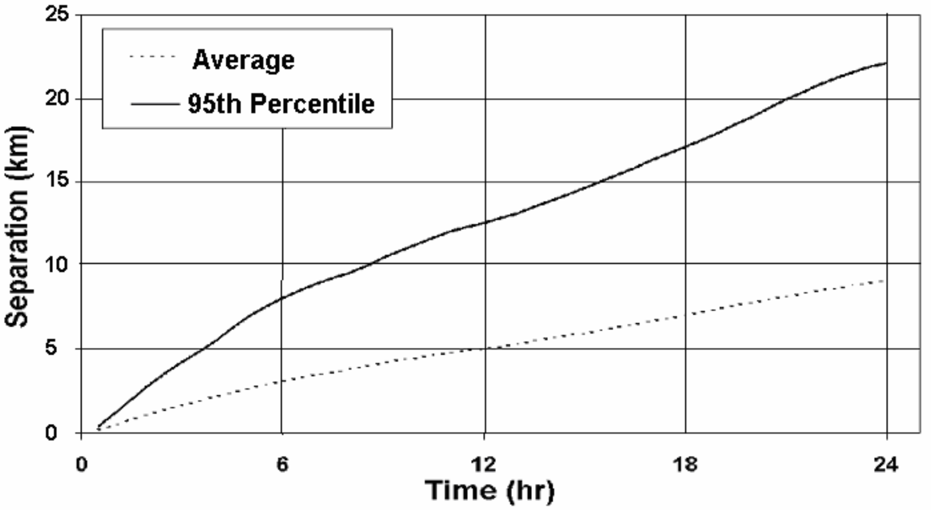

Figure E-20. Average and 95$^{th}$ percentile separation distance as a function of time from the start of the simulation.

Figure E-21 shows a plot of the separation distance at the end of the day versus the SLDMB drift speed for that day. In general, the trend, while statistically very weak, shows that the separation distance increases as the mean drift speed increases. The separation distance is approximately 80% of the observed buoy movement over 1 day.

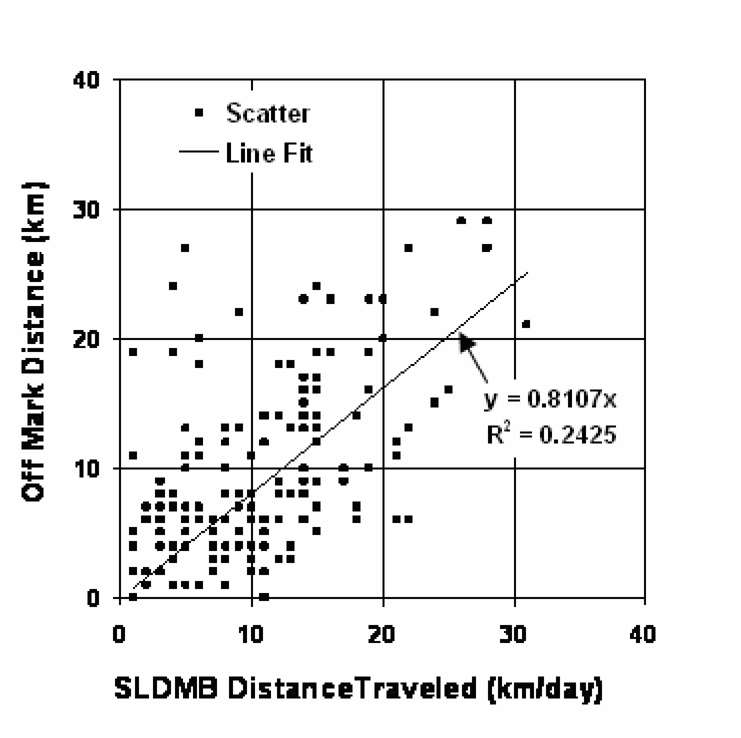

Figure E-21. Separation distance between predicted and observed locations of the SLDMB at the end of each day versus distance traveled by the SLDMB during that day. A linear curve fit to the data is provided (solid line) with the corresponding correlation coefficient.

Using Equation 4 (random walk model) and assuming that t is the time from release and the separation distance is equivalent to $S_1$, an estimate can be made of the dispersion coefficient that must be used in the search and rescue model in order to ensure that model predictions give a search area that includes the observed location of the buoy. Figure E-22 shows a histogram of the dispersion coefficients based on this analysis.

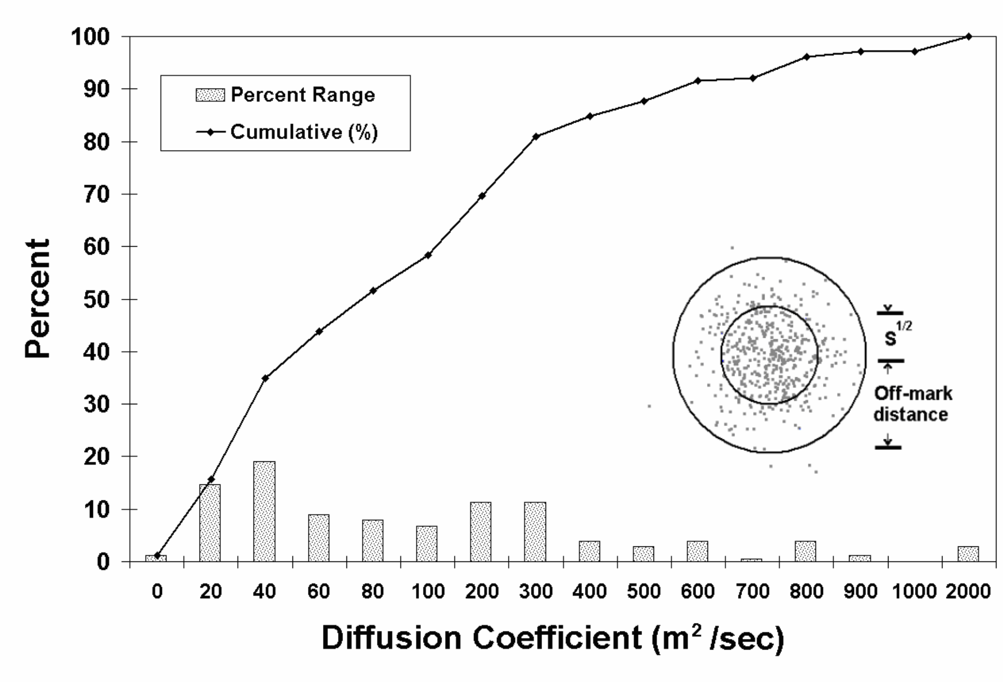

Figure E-22. Histogram of dispersion coefficients based on an application of a random walk model to the separation distances at the end of 1-day simulation.

A diffusion coefficient of 40 $m^2$/sec is the most frequent match (~20 percent) and represents up to 35 percent of the simulations and 100 $m^2$/sec up to 60 percent. The larger values of dispersion (greater than 500 $m^2$/sec) occur in areas of low radar data returns and are not representative. The values of the dispersion coefficients from this estimate are consistent with those estimated using the SLDMB cluster analysis above.

If the diffusion coefficient were kept the same and the random flight were employed, the search radius would be expected to shrink and miss the target depending on the autocorrelation time, or conversely, the diffusion coefficient must be larger than the values shown in Figure E-22.

## E.7 Conclusions

A review of stochastic particle models is presented and shows a well-established hierarchy with position, velocity and acceleration progressively described as Markovian processes. The governing equations for each are provided. Numerical implementation and testing against an analytic solution for diffusive spreading of both random walk and flight models are presented. The numerical model is shown to give predictions in good agreement with the analytic solution when the results are based on 2,000 or more independent simulations. Parameteric studies show that the random flight model predicts a smaller search area, compared to the random walk model beginning immediately after the initiation of the simulation and continuing with time. The difference in area becomes constant and scales as the diffusion coefficient, K, times the velocity autocorrelation time scale, T. For time >>T, the search area ratio ($R_a$) can be approximated by $R_a = 1- T/t$. The ratio of the search areas hence decreases as time increases. The random flight model is therefore expected to have the largest impact in reducing the size of the search area at time scales shorter than T.

Based on the drifter cluster analysis, dispersion coefficients of 40 to 85 $m^2$/sec were estimated for the 35-day experiments by fitting the observations to a random walk model. The variability in these estimates was very large however, covering a range from 20 to almost 200 $m^2$/sec. These dispersion coefficients are broadly consistent with Okubo's (1971) $4/3^{rds}$ power law and within the range of variability of his curve fit to field data. The high level of uncertainty in the estimates is clearly a result of the very limited number of drifter trajectories available to perform the analysis. One surprising finding was that several of the drifters in the Mid Atlantic Bight region tracked very closely with one another over a period of almost 25 days. The upper bound separation distances were in the range of 1 to 3 km. This implies very low dispersion (0.5 $m^2$/sec) for this particular cluster of drifters.

Random flight models were applied to the drifter data to determine their impact on dispersion of the drifters. The autocorrelation time scale was estimated using CODAR data and gave values in the range of 3.5 to 6.5 hrs for the Mid Atlantic Bight when the original and de-tided data, respectively, were used. No improvement was observed in the ability of a random flight model to predict the dispersion of the drifters because of the large uncertainty in the dispersion coefficient. Based on the present results, there is no motivation to implement higher order stochastic trajectory models for search and rescue until better estimates of turbulent dispersion become available.

Direct comparisons of the velocities derived from the drifters and CODAR observations showed that the differences are similar in magnitude to their speed. The variance and the autocorrelation time of the difference (errors) are also similar. Semi-diurnal tidal variations are clearly evident in both data sets; dominant in Block Island Sound, but much smaller in the Mid Atlantic Bight. Inertial oscillations, with periods of about 19 hrs, are dominant in the Mid Atlantic Bight, but not observed in Block Island Sound. Scatter plots for the Block Island Sound cluster show a correlation of less than 0.1 for the east/west component and greater than 0.6 for the north/south component. For the Mid Atlantic Bight clusters the scatter plots show a correlation coefficient of greater than 0.75 for the east/west component (onshore-offshore) and less than about 0.4 for the north/south component. This behavior is just the opposite of the Block Island Sound cluster. Correlation coefficients are observed to be much lower in areas where the percent data return is below 50 percent.

Estimates of the dispersion coefficients for both north/south and east/west components were made using the CODAR variance and error data and the median autocorrelation time scale for Block Island Sound and the Mid Atlantic Bight. The dispersion coefficients, based on the velocity variances, were comparable in the two directions in both areas with values in the range of 450 to 700 $m^2$/sec. Using velocity errors, the dispersion coefficients were in the range of 30 to 60 $m^2$/sec in Block Island Sound and 200 to 400 $m^2$/sec in the Mid Atlantic Bight. These compare to median values of 40 and 85 $m^2$/sec for Block Island Sound and Mid Atlantic Bight, respectively, based on the cluster analysis.

A total of 178 statistically independent simulations was performed using SARMAP to predict the daylong trajectories at successive locations along the paths of the seven SLDMB in the Mid

Atlantic Bight. Comparison of the model predicted and observed locations at the end of one day showed a median separation distance of 7 km, an averaged distance of 9.3 km, a maximum distance of 30 km and the most frequent occurrence distance of 3 to 4 km. The error in location was roughly comparable (about 80 percent) to the distance the drifter traveled in 1 day (5 to 18 km/day). Errors in predictions were significantly higher in areas where the CODAR data return rates were less than 50 percent (immediately south of Long Island and near the shelf break). Estimates of the dispersion coefficients necessary as input to the model, to ensure that the predicted and observed locations were within the model predicted search area, were made for each simulation. The resulting dispersion coefficients ranged from 20 to 2,000 $m^2$/sec, with most in the range of 20 to 300 $m^2$/sec. The median value was about 90 $m^2$/sec and the most frequent values 40 to 60 $m^2$/sec. The largest dispersion coefficients were associated with areas where the CODAR data returns were lowest and hence, not representative.

Estimates of the median horizontal dispersion coefficient based on cluster analysis, CODAR velocity errors, and SARMAP trajectory analysis give values of 40 $m^2$/sec, 30 to 60 $m^2$/sec, and (no trajectory analysis in Block Island Sound), respectively for Block Island Sound. Similar values for the Mid Atlantic Bight were 85, 200 to 400, and 90 $m^2$/sec. This range of values is consistent with Okubo's $4/3^{rds}$ power law, which gives values in the range of 20 to 200 $m^2$/sec, for time scales of 5 to 30 days.

## E.8 References

Allen, A. A., 1999. Leeway divergence, US Coast Guard Research and Development Center, Groton, CT, Report CG-D-XX-99.

Allen, A. A. and J. V. Plourde, 1999. Review of leeway: field experience and implementation, US Coast Guard Research and Development Center, Groton, CT, Report CG-D-08-99.

Applied Science Associates, Inc (ASA), 2003, SARMAP User's and Technical Manual, Applied Science Associates, Inc, Narragansett, RI 02882.

Batchelor, G. K., 1953. *Homogeneous Turbulence*, Cambridge University Press, Cambridge,UK, 197p.

Bauer, S., M. Swenson, A. Griffa, A. Mariano, and K. Owens, 1998. Eddy mean flow decomposition and eddy diffusivity estimates in the tropical Pacific Ocean: Methodology, Journal of Geophysical Research, Vol. 103, No: C13, 30,855-30,871, December 15, 1988.

Bauer, S., M. Swenson, and A. Griffa, 2002. Eddy mean flow decomposition and eddy diffusivity estimates in the tropical Pacific Ocean: 2. Results, Journal of Geophysical Research, Vol. 110, No: C10, 3154.

Berloff, P., J. C. McWilliams, and A. Bracco, 2002. Material transport in ocean gyres: Part I Phenomenology, Journal of Physical Oceanography, Vol. 32, 764-796. March 2002.

Berloff, P. and J. C. McWilliams, 2002. Material transport in ocean gyres: Part II hierarchy of stochastic models, Journal of Physical Oceanography, Vol. 32, 797-830. March 2002.

Breivik, O., A. Allen, C. Wettre, O. Saetra, and K. Roang, 2004. An operational search and rescue model for the Norwegian Sea and the North Sea, Norwegian Meteorological Institute, Bergen, Norway. 36 p.

Codiga, D. L., and L. V. Rear, 2004. Observed tidal currents outside Block Island Sound: Offshore decay and effects of estuarine outflow, J. Geophys. Res., 109, C07S05, doi:10.1029/2003JC001804.

Csanady, G. T., 1973. *Turbulent Diffusion in the Environment*, D. Reidel Publishing Company, Boston, MA, 248 p.

Davis, R. E., 1985. Drifter observations of coastal surface currents during CODE: The method and descriptive view, Journal of Geophysical Research, 90, 4741-4755.

Davis, R. E., 1987. Modeling eddy transport of passive tracers, Journal of Marine Research, 45, 635-666.

Dutkiewicz, S., A. Griffa, and D. Olson, 1994. Particle diffusion in a meandering jet, Journal of Geophysical Research, 98, 16,487-16,500.

Elliott, A. J., A. J. Barr, and D. Kennan, 1997. Diffusion in Irish coastal waters, Estuarine, Coastal and Shelf Science, 44 (Supplement A), 15-23.

Griffa, A., K. Owens, L. Piterberg, and B. Rozovski, 1995. Estimates of turbulence parameters from Lagrangian data using a stochastic particle model, Journal of Marine Research, 53, 371-401.

Griffa, A., 1996. Applications of stochastic particle models to oceanographic problems, in *Stochastic Modeling in Physical Oceanography*, edited by R. Adler, P. Mueller, and B. Rozovski, pp. 114-140, Birkhauser, Boston, MA.

Legg, B. J. and M. R. Raupach, 1982. Markov chain simulation of particle dispersion in homogeneous flows: The mean drift velocity induced by a gradient in the Eulerian velocity variance, Boundary Layer Meteorology, 24, 3-13.

Mariano, A., A. Griffa, T. Ozgokmen, and E. Zambianchi, 2002. Lagrangian analysis and predictability of coastal and ocean dynamics 2000. Journal of Atmospheric and Oceanic Technology, Vol. 19, 1114-1126, July 2002.

Ojo, T. O. and J. Bonner, 2000. Three dimensional self-calibrating coastal oil spill trajectory tracking and contaminant transport using HF radar, Proceedings of Arctic Marine Oil Spill Program Technical Seminar.

Okubo, A., 1971. Oceanic diffusion diagrams, Deep Sea Research, 18, 789-802.

Ozgokmen, A. Griffa, A. Mariano, and L. Piterbarg, 1999. On the predictability of Lagrangian trajectories in the ocean. Journal of Atmospheric and Oceanic Technology, Vol. 17, 336-383.

Pope, S. B., 1994. Lagrangian PDF methods for turbulent flows, Annual Review Fluid Mechanics, 26, 23-63.

Press, W. H., S. A. Teukolsky, W. T. Vetterling, and B. P. Flannnery, 1992. Numerical Recipes in FORTRAN: The Art of Scientific Computing, 2nd Edition, Cambridge University Press, Cambridge, UK, 963 p.

Risken, H, 1989. *The Fokker Planck Equations: Methods of Solution and Applications*, Springer Verlag, New York, NY, 472 p.

Sawford, B. L., 1991. Reynolds number effects in Lagrangian stochastic models of turbulent dispersion, Physics of Fluids, A 3(6), 1577-1585.

Sawford, B. L. and P. Yeung, 2000. Eulerian acceleration statistics as a discriminator between Lagrangian stochastic models in uniform shear flows, Physics of Fluids, 12, 2033-2045.

Spaulding, M. L. and E. Howlett, 1996. Application of SARMAP to estimate probable search area for objects lost at sea, Marine Technology Society Journal, Vol. 30, No. 2, Summer 1996, p. 17-25.

Spaulding, M. L. and K. Jayko, 1991. Estimating the search area of the New England Airlines crash site off Block Island, Marine Technology Society Journal, Vol. 25, No. 2, p. 43-48.

Taylor, G. I., 1921. Diffusion by continuous movement, Proc. London Math. Soc. 20, 196-212.

Thomson, D. J., 1986. A random walk model of dispersion in turbulent flows and its application to dispersion in a valley, Quart. J. Roy. Meteor. Soc., 112, 511-529.

Thomson, D. J., 1987. Criteria for the selection of stochastic models of particle trajectories in turbulent flows, Journal of Fluid Mechanics, 180, 529-556.

Ullman, D., J. O'Donnell, C. Edwards, T. Fake, D. Morschauser, M. Sprague, A. Allen, and B. Krenzien, 2002, Appendix B, STPS/CODAR error analysis, US Coast Guard Research and Development Center, Groton, CT.

Ullman, D., J. O'Donnell, C. Edwards, T. Fake, D. Morschauser, M. Sprague, A. Allen, and B. Krenzien, 2003. Use of coastal ocean dynamics application radar (CODAR), technology in US Coast Guard search and rescue planning, US Coast Guard Research and Development Center, Groton, CT, Report CG-D-09-03.

Ullman, D. S., and D. L. Codiga, 2004. Seasonal variation of a coastal jet in the Long Island Sound outflow region based on HF radar and Doppler current observations, J. Geophys. Res., 109, C07S06, doi:10.1029/2002JC001660.

van Dop, H. F., F. T. M. Nieuwstadt, and J. C. R. Hunt, 1985. Random walk models for particle displacements in inhomogeneous unsteady turbulent flows, Physics of Fluids, 28 (6), 1639-1653.